DESIGN AND RIGOROUS ANALYSIS OF GENERALIZED AXIALLY-SYMMETRIC DUAL-REFLECTOR ANTENNAS

by

Fernando J. S. Moreira

A Dissertation Presented to the

FACULTY OF THE GRADUATE SCHOOL

UNIVERSITY OF SOUTHERN CALIFORNIA

In Partial Fulfillment of the

Requirements for the Degree

DOCTOR OF PHILOSOPHY

(Electrical Engineering)

August 1997

UNIVERSITY OF SOUTHERN CALIFORNIA
THE GRADUATE SCHOOL
UNIVERSITY PARK
LOS ANGELES, CALIFORNIA 90007

This dissertation, written by

FERNANDO J.S. MOREIRA

*under the direction of h*is *Dissertation Committee, and approved by all its members, has been presented to and accepted by The Graduate School, in partial fulfillment of requirements for the degree of*

DOCTOR OF PHILOSOPHY

Dean of Graduate Studies

Date August 15, 1997

DISSERTATION COMMITTEE

Chairperson

To my parents, Armênio and Maria;
brothers, Antonio and Paulo;
and wife, Luciana.

ACKNOWLEDGMENTS

Thanks are due to the following people and organizations:

. My academic advisor Professor Aluizio Prata, Jr., for his friendship and advice during the past five years.

. Professors Hans H. Kuehl and John S. Nodvik, members of the dissertation committee.

. CNPq (Conselho Nacional de Desenvolvimento Científico e Tecnológico—Brasil) for the Doctoral Fellowship.

. Professor David C. Jenn, Dr. Odilon M. C. Pereira Filho, and Marcos G. C. Branco for providing several of the used references.

. Dr. Michael R. Barclay for assembling the LaTeX thesis-style option used in typesetting this dissertation.

. My wife Luciana for her generous support during the completion of this dissertation.

. And finally to my parents Armênio and Maria Moreira for *everything*.

TABLE OF CONTENTS

LIST OF FIGURES

LIST OF TABLES

Chapter 1
INTRODUCTION

Since the early studies of electromagnetic waves conducted by Hertz [1], reflector antennas have been widely used in countless communication applications, ranging from the large radio-telescopes used in deep-space probing [2] to the compact base stations of mobile communications [3]. The major appeal of these antennas resides in the collimating properties of the reflector surfaces, which provide high performance with a cost-effective geometry [4]–[7].

The analysis and synthesis of reflector antennas have been successfully accomplished in terms of the approximations provided by the Physical Optics (PO) [8] and the Geometrical Theory of Diffraction (GTD) [9] techniques, specially for reflector surfaces with large electrical dimensions. However, these techniques can not efficiently account for the mutual interactions among the several antenna components (i.e., reflector surfaces, feeding and supporting structures, etc.), which reduce the overall antenna efficiency and increase the sidelobe levels of the radiation pattern. As the current state of the art in telecommunication technology pushes for highly efficient antennas designed to satisfy a steadily increasing number of electrical re-

strictions, the antenna synthesis must then be grounded in an accurate analysis tool, capable of accounting for all relevant effects.

The rigorous simulation of the antenna electromagnetic properties can be assembled in terms of integral equations (together with the appropriate boundary conditions over the antenna surfaces), which can then be numerically solved using the Method of Moments (MoM) [10]–[13]. Although this technique models the antenna electrical characteristics with an extreme accuracy, its numerical implementation requires excessive amounts of computer memory and time, which generally preclude the analysis of antenna systems with large electrical dimensions. Recently, while pushing current numerical limits, the three-dimensional MoM analysis of the plane-wave scattering from a square thin plate with only 6 wavelengths in size has been reported [14]. This indicates that the possibility of a similar analysis of large and general reflector antennas remains in the future, waiting for enhancements in computer hardware and/or analysis methods. However, for the particular case of reflector antennas with axial symmetry, the MoM analysis can be reduced into the complexity of a two-dimensional one [15]–[20], yielding an overwhelming decrease in the computational burden. This brings the rigorous modeling of large axially-symmetric reflector antennas into feasibility [17]–[20]. In the present dissertation, which is devoted to the analysis and design of axially-symmetric dual-reflector antennas, configurations with main-reflector diameters up to 200 wavelengths are entirely analyzed using the MoM technique. The formulation to be

presented also enables the inclusion of a circularly-symmetric feed structure into the rigorous antenna analysis, avoiding the inaccuracies associated with using a spherical-wave point source to excite the reflector antenna—a drawback present in previous works [17]–[20].

A highly efficient reflector antenna is accomplished by implementing, as close as possible, uniform amplitude and phase distributions for the electromagnetic field at the antenna aperture [21]. The simultaneous control of both aperture amplitude and phase distributions is only possible if at least two reflector surfaces are used to transform the feed radiation into the desired aperture illumination. A clear aperture with uniform illumination intrinsically requires an offset reflector configuration to avoid blockage [5]—this is never possible in an axially-symmetric dual-reflector geometry due to the presence of the subreflector in front of the main reflector. However, the axially-symmetric geometry is inherently simpler and, consequently, less expensive to manufacture. This fact makes it specially attractive for commercial applications. Besides, the axial symmetry enables a rigorous analysis of the antenna system using MoM, simplifying the corresponding engineering development process. For antenna configurations with extremely large main reflectors (which may preclude a complete MoM analysis due to computer-memory restrictions), accurate hybrid techniques based on MoM and PO can still be applied to their analysis [22]–[24].

The most commonly used axially-symmetric dual-reflector configurations are the classical Cassegrain and Gregorian [25],[26]. In these geometries part of the energy radiated by the main reflector impinges back on the subreflector, creating several undesirable effects (e.g., efficiency decrease, sidelobe level increase, etc.). However, reduction of the main-reflector scattering towards the subreflector can be accomplished by appropriately shaping both reflector surfaces [27] or by using alternative classical configurations [28]–[31]. In this dissertation both approaches are investigated. It is shown that, for sufficiently large reflectors, antenna efficiencies beyond 90% can be achieved by some alternative classical configurations. These efficiencies can be further improved by shaping the reflector surfaces to provide an almost-uniform aperture illumination.

However, depending on the particular application and the associated sidelobe requirements, the specification of a uniform amplitude distribution for the aperture field (desirable for high efficiency) may generate intolerable sidelobe levels. Aperture distributions capable of controlling the sidelobe envelope have been investigated by Ludwig [32]. However, Ludwig's aperture distribution does not yield antenna efficiencies beyond 80% [32]. In this dissertation, an alternative amplitude distribution is proposed for the aperture field. This distribution is capable of controlling the sidelobe levels while providing high efficiencies. Also, the GTD approximations are used to yield useful insights and closed-form expressions to control the forward- and backward-spillover impacts upon the antenna sidelobes, as well

as to investigate the effects of the subreflector-edge diffraction on the aperture illumination.

The objective of this dissertation is to present a detailed formulation for the design and rigorous analysis of generalized axially-symmetric dual-reflector antennas, aiming a highly efficient performance with a prescribed sidelobe envelope. The work is discussed in the following order. Chapter 2 presents the necessary formulation for the rigorous electromagnetic analysis of perfectly-conducting axially-symmetric reflector antennas, based on the MoM technique. At this stage, the antenna system is excited by a spherical-wave point source (e.g., a raised-cosine feed model, Hertz dipole, etc.) located at the symmetry axis. The MoM formulation adopted is based on Ref. [16]. However, in order to provide the necessary basis for the inclusion of the feed structure in the antenna analysis (discussed in Chapter 3), a complete discussion of the MoM formulation and its numerical implementation is conducted. Also, complete expressions for the electric and magnetic near- and far-zone fields are presented.

Note that this dissertation does not consider the presence of the feed/subreflector supporting struts in the antenna analysis. The struts destroy the axial symmetry of the antenna configuration and thus require special treatments, specially for the modeling of the junction between the strut and the axially-symmetric reflector surface. Previous works have dealt with this problem by simulating the struts as infinitely thin wires [17] or strips [33]. However, theses formulations are applicable

only to infinitely thin struts, and hence further improvements are still required to model struts with arbitrary cross sections [33].

Chapter 3 presents an integral-equation formulation that includes a circularly-symmetric feed structure in the analysis, enabling the complete antenna to be handled. The excitation is provided by equivalent currents and charges located inside the circular waveguide connected to the feed horn. These equivalent sources are specified to excite the fundamental TE_{11} mode towards the feed boresight direction [34]. Also, Impedance Boundary Conditions (IBC) are incorporated into the formulation, enabling the simulation of horn-flare corrugations and perfectly matched waveguides [35]. The simulation of the horn corrugations permits an accurate analysis of the feed radiation characteristics without the hassle of modeling the corrugation geometries (this reduces the numerical burden of the feed analysis). Both the simulation of matched waveguides using an IBC and the TE_{11}-mode excitation yield the evaluation of the feed return loss in a single computer run. The present formulation is then an improvement over previously reported works, where Hertz dipoles were used to excite the fundamental TE_{11} mode and the feed return loss could not be directly obtained [35],[36]. Furthermore, Chapter 3 also presents expressions for the radiated near- and far-zone fields (associated with the IBC). Although the present formulation only permits the analysis of mono-modal axially-symmetric feed structures, most of the feeds applied in practical reflector-antenna applications fall into this category [37]–[39].

After the presentation of the necessary tools for the rigorous analysis of axially-symmetric dual-reflector antennas, this dissertation goes into their design details. The approach is based on the concept that the design process should always start from a (simpler) classical configuration. So, Chapter 4 introduces generalized classical axially-symmetric dual-reflector antennas capable of reducing the main-reflector radiation towards the subreflector while providing a uniform phase distribution for the aperture field [28]–[31]. The expression *generalized classical* is used to stress that all possible configurations (there are four distinct geometries) are investigated in a unified way and that their reflector surfaces are generated by conic sections. Based on Geometrical Optics (GO) concepts, closed-form expressions are derived to design all possible classical configurations, and to obtain the corresponding aperture fields [31]. Parametric comparisons among these generalized antenna types are conducted, and it is demonstrated that some of these configurations yield efficiencies beyond 90% (under a GO perspective). However, higher efficiencies (up to 98%) are obtained by shaping the reflector surfaces [27] (discussed in Chapter 5), in which case the classical geometries may be applied as the starting point for the shaping process.

However, as previously mentioned, depending on the application a practical antenna design must aim not only towards high efficiency but also the satisfaction of a required sidelobe envelope. With this motivation, Chapter 5 proposes a useful distribution for the aperture electric-field amplitude, capable of controlling the antenna

sidelobe envelope while providing high efficiencies. The reflector-antenna surfaces yielding the proposed aperture distribution are obtained through an efficient GO-shaping algorithm [40]. Also, the forward and backward spillovers are investigated and controlled using asymptotic approximations provided by GTD [9], which then leeds to the study of the diffraction effects to the aperture illumination. Chapter 5 concludes with the design of a shaped axially-symmetric Cassegrain antenna (main-reflector and subreflector diameters of 100 and 15 wavelengths, respectively) with 80% efficiency while satisfying current ITU sidelobe-envelope requirements for earth-station antennas operating with geostationary satellites [41].

Throughout this work the complex $e^{+j\omega t}$ time dependence is implicitly assumed for all fields, currents, and charges, where $j = \sqrt{-1}$, $\omega = 2\pi f$, and f is the electromagnetic radiation frequency. An arrow, a hat, and a double bar on the top of a variable are used to represent a vector, a unit vector, and a dyadic, respectively.

Chapter 2

SCATTERING FROM PERFECTLY CONDUCTING BODIES OF REVOLUTION

The objective of this chapter is to present the required formulation for the rigorous numerical analysis of axially-symmetric reflector-antenna systems. The reflectors are assumed made of perfectly-conducting (PEC) infinitely-thin open shells and the numerical analysis is performed using the Electric Field Integral Equation (EFIE) [10]–[13],[16]. Although this dissertation is devoted to axially-symmetric reflector-antenna applications, the formulation to be presented is general enough to be applied to any PEC axially-symmetric geometry (e.g., metallic spheres). Herein the axially-symmetric configurations are referred to as bodies of revolution (BOR), and their geometries obtained by rotating generating curves about a single axis of symmetry, as illustrated in Fig. 2.1.

The geometrical representation of the BOR generating curve is presented in Sect. 2.1. The EFIE formulation used to analyze the PEC-BOR configurations is briefly discussed in Sect. 2.2. The EFIE is then numerically solved using the Method of Moments (MoM), which is presented in Sect. 2.3. Afterwards, the radiated near-

and far-zone fields are obtained from the resulting induced currents, as formulated in Sects. 2.4 and 2.5, respectively. Finally, two validation test cases are discussed in Sect. 2.6: the near-zone field produced inside and outside a PEC sphere illuminated by a Hertz dipole and the radiated far-zone field of a paraboloidal reflector.

In the present chapter, the PEC-BOR configurations are illuminated by simple spherical-wave sources, such as the Hertz dipole. However, the accurate analysis of real antenna systems must include more complex feeds. To account for such possibility, in Chapter 3 the EFIE formulation is extended to BOR geometries with an impedance boundary condition (IBC), which allows the consideration of more realistic feeds. So, although the MoM formulation of the present chapter is based on Ref. [16], its derivation is conducted in detail to provide the required basis for the formulation of Chapter 3.

2.1 The Body-of-Revolution Geometry

The surface of a BOR is defined by its generating curve rotated about the BOR axis of symmetry, as shown in Fig. 2.1. In the present work, the axis of symmetry is always assumed to coincide with the z-axis of the principal coordinate system. Furthermore, it is convenient to define an orthogonal curvilinear coordinate system over the BOR surface. This coordinate system is characterized by the orthonormal base vectors $\hat{t}$, $\hat{\phi}$, and $\hat{n}$, where $\hat{t}$ is the unit vector tangent to the surface and pointing along the generating curve, $\hat{\phi}$ is the unit vector tangent to the surface

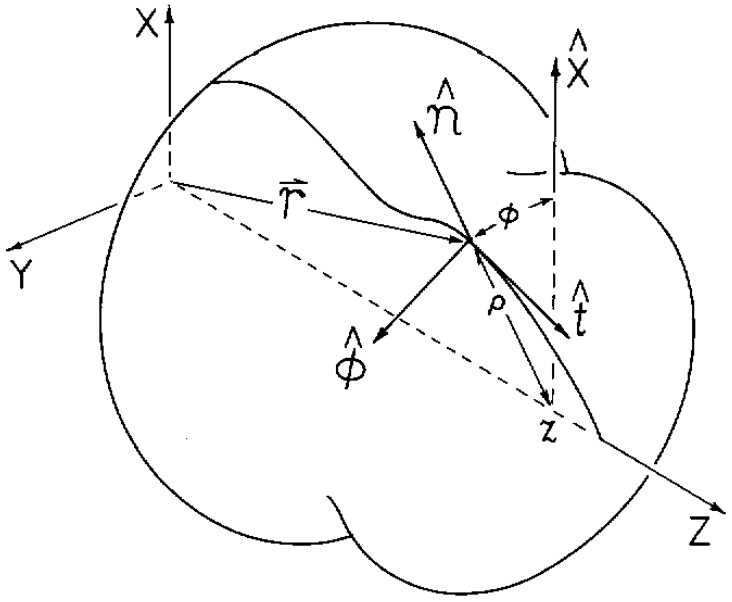

a) Three-Dimensional View

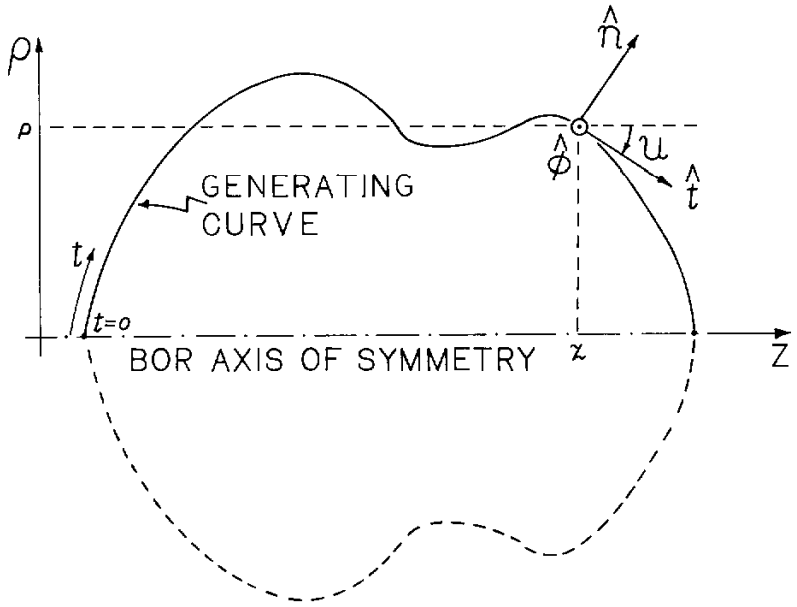

b) Generating Curve

Figure 2.1: The BOR Geometry.

and pointing along the circumferential direction, and $\hat{n}$ is the unit vector normal to the BOR surface, such that $\hat{n} = \hat{\phi} \times \hat{t}$ (see Fig. 2.1). It is very important to observe here that the formulation presented in this work always assume that $\hat{n}$ points outwards a closed BOR surface (i.e., towards the region where the excitation sources are located). For an open surface (like the reflector surfaces to be studied), the ambiguity on the orientation of $\hat{n}$ is irrelevant.

These unit directions are related to the usual cylindrical coordinates of the principal coordinate system by

$$\hat{t} = \sin u \ \hat{\rho} + \cos u \ \hat{z}, \tag{2.1}$$

$$\hat{n} = \hat{\phi} \times \hat{t} = \cos u \ \hat{\rho} - \sin u \ \hat{z}, \tag{2.2}$$

where u is the angle between $\hat{t}$ and $\hat{z}$, as illustrated in Fig. 2.1.

For the numerical evaluation of the EFIE, it is also convenient to describe the BOR generating curve by straight-line segments and, consequently, the BOR surface by rings, as illustrated in Fig. 2.2. Notice that over each generating-curve segment, the corresponding angle u is constant.

2.2 The Electric Field Integral Equation

Assuming a linear, homogeneous, and isotropic medium, the electromagnetic field at a given observation point outside a closed and finite region can be entirely determined by the prior knowledge of the electromagnetic behavior over the closed-region

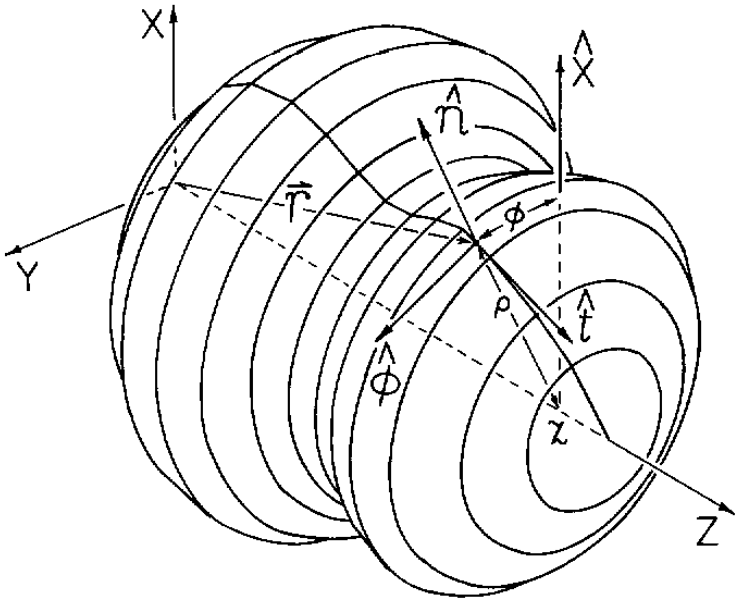

a) Three-Dimensional View

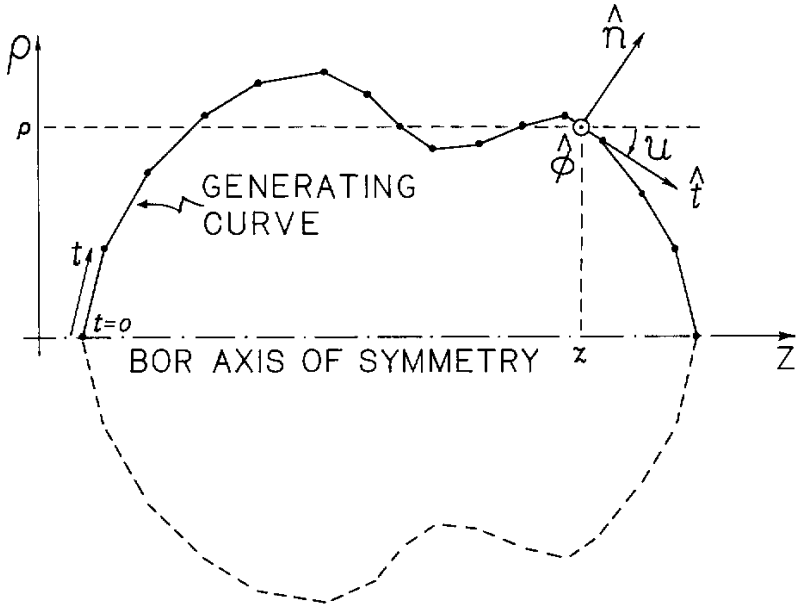

b) Segmented Generating Curve

Figure 2.2: Representation of the BOR Generating Curve by Straight Segments.

surface plus the radiation characteristics of any source located outside the closed region. This is accomplished by the Stratton-Chu formula [42], where the closed region is defined by the BOR surface in this work. For the electric field, this formula is known as the EFIE and given by [11]

$$\begin{aligned}\vec{E}(\vec{r}) &= \Gamma\vec{E}^{inc}(\vec{r}) - \frac{\Gamma}{4\pi}\oint_{S'}\Big\{j\omega\mu_o\left[\hat{n}'\times\vec{H}(\vec{r}')\right]\Psi - \left[\hat{n}'\times\vec{E}(\vec{r}')\right]\times\nabla'\Psi \\ &- \left[\hat{n}'\cdot\vec{E}(\vec{r}')\right]\nabla'\Psi\Big\}\,ds', \end{aligned} \tag{2.3}$$

where S' represents one or more disconnected BOR closed surfaces, $\vec{r}$ locates the observation point, $\vec{r}'$ locates the source point over S', $\vec{E}(\vec{r})$ is the total electric field at $\vec{r}$, $\vec{E}^{inc}(\vec{r})$ is the incident electric field at $\vec{r}$ produced by external sources, $\vec{E}(\vec{r}')$ is the total electric field at $\vec{r}'$, $\vec{H}(\vec{r}')$ is the total magnetic field at $\vec{r}'$, $\hat{n}'$ is the unit surface normal at $\vec{r}'$ pointing towards the region where the external sources are located, and

$$\Psi = \frac{e^{-jk_oR}}{R}, \tag{2.4}$$

where $R = |\vec{r} - \vec{r}'|$ and $k_o = 2\pi/\lambda = \omega\sqrt{\mu_o\epsilon_o}$ with λ being the electromagnetic radiation wavelength. In this work, the configurations to be analyzed are always surrounded by the free space, which has permittivity $\epsilon_o = 8.854\times10^{-12}$ F/m and permeability $\mu_o = 4\pi\times10^{-7}$ H/m. In Eq. 2.3, the parameter Γ is equal to 1 if $\vec{r}$ is outside the surface S' and is equal to 2 if $\vec{r}$ is over a smooth surface S' [11]. It is important to observe that Eq. 2.3 has removable singularities whenever $\vec{r} = \vec{r}'$. The singularity remotion depends on the approach used to solve Eq. 2.3.

Furthermore, it is convenient to substitute the original problem where the BOR is physically present by an equivalent configuration where electric and magnetic currents (radiating in free space) are placed over the BOR-surface location. This is known as the equivalence principle [34], which is illustrated in Fig. 2.3. In the equivalent problem, the electric and magnetic equivalent currents are defined as

$$\hat{n} \times \vec{H}(\vec{r}) = \vec{J}(\vec{r}), \tag{2.5}$$

$$\hat{n} \times \vec{E}(\vec{r}) = -\vec{M}(\vec{r}), \tag{2.6}$$

respectively. The definition of these equivalent currents transfer the boundary-condition information from the original problem to the equivalent one, such that the electromagnetic fields outside the BOR region are identical on both problems.

Assuming the observation point $\vec{r}$ located over the smooth BOR surface S' ($\Gamma = 2$), taking the cross product of Eq. 2.3 with respect to the unit surface normal $\hat{n}$ at $\vec{r}$, using the relation derived from the continuity equation [11]

$$\hat{n}' \cdot \vec{E}(\vec{r}') = \frac{j}{\omega \epsilon_o} \nabla' \cdot \left[\hat{n}' \times \vec{H}(\vec{r}')\right], \tag{2.7}$$

and solving the equivalent problem by substituting Eqs. 2.5 and 2.6 into Eq. 2.3, the following EFIE is obtained:

$$\begin{aligned} \hat{n} \times \vec{E}^{inc}(\vec{r}) = & -\frac{\vec{M}(\vec{r})}{2} + \frac{j}{4\pi\omega\epsilon_o}\, \hat{n} \times \oint_{S'} \Big\{ k_o^2 \vec{J}(\vec{r}')\Psi - j\omega\epsilon_o \vec{M}(\vec{r}') \times \nabla'\Psi \\ & - \left[\nabla' \cdot \vec{J}(\vec{r}')\right] \nabla'\Psi \Big\}\, ds'. \end{aligned} \tag{2.8}$$

However, for a PEC surface, the boundary conditions at S' state that the tangential electric field and, from Eq. 2.6, $\vec{M}(\vec{r}')$ are both zero over S'. In this case, Eq. 2.8

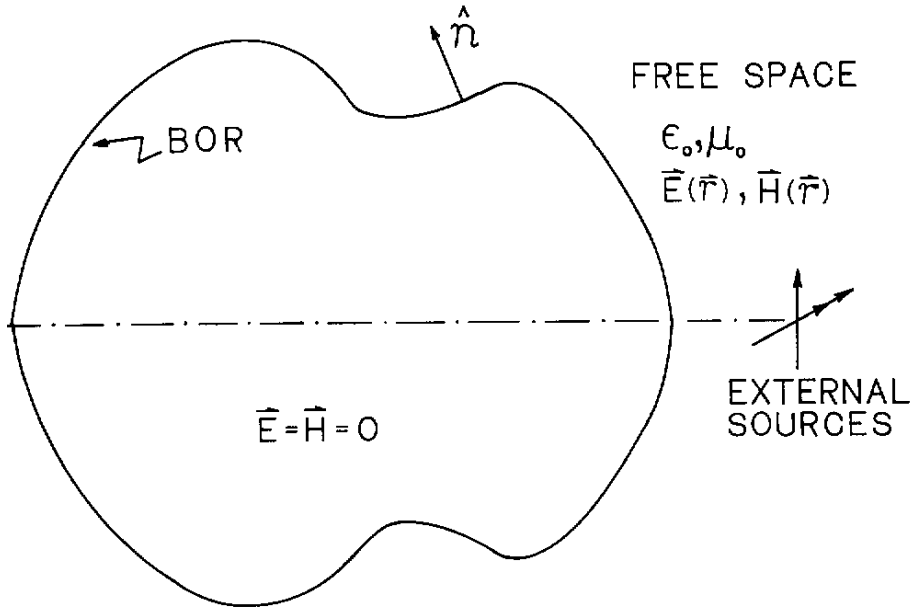

a) Original Problem

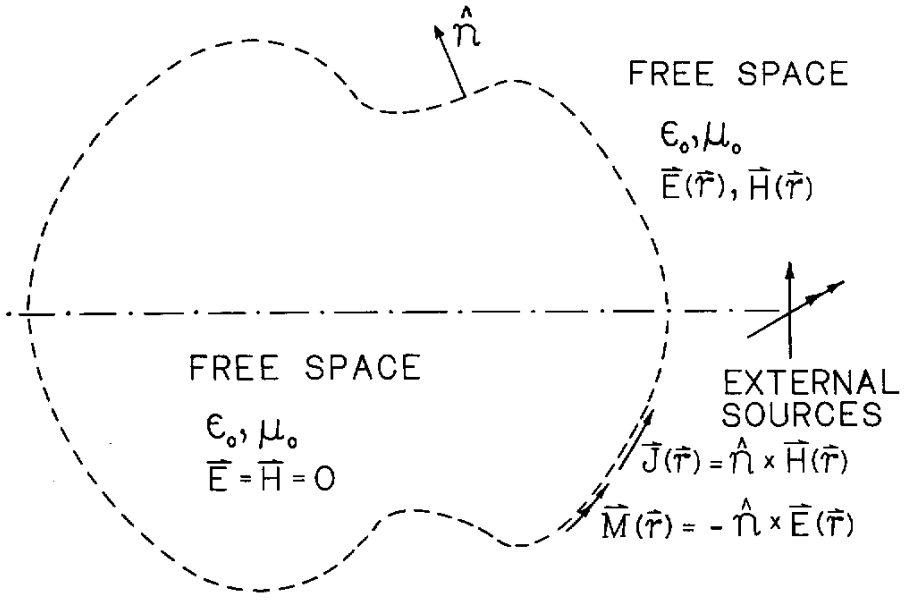

b) Equivalent Problem

Figure 2.3: The Equivalence Principle.

can be rewritten as

$$\hat{n} \times \vec{E}^{inc}(\vec{r}) \;=\; \frac{j}{4\pi\omega\epsilon_o}\,\hat{n} \times \int\limits_{S'} \left\{ k_o^2 \vec{J}(\vec{r}\,')\Psi - \left[\nabla' \cdot \vec{J}(\vec{r}\,')\right] \nabla'\Psi \right\}\, ds', \qquad (2.9)$$

where the unknown quantity is the electric current $\vec{J}(\vec{r}\,')$, which may be obtained using the MoM technique [10]–[13],[16].

In Eq. 2.9, when the closed BOR surface is shrunk into an open and infinitely thin surface (e.g., reflector surface), $\vec{J}(\vec{r}\,')$ then represents the summation of the electric currents on both sides of S' at the corresponding point $\vec{r}\,'$ [11]. Nevertheless, in Chapter 3 an impedance boundary condition (IBC) will be applied over portions of S' in order to allow the analysis of feed structures. The IBC actually represents a boundary relation between $\vec{J}(\vec{r}\,')$ and $\vec{M}(\vec{r}\,')$ over the surface. Consequently, over the portions of S' where the IBC is present $\vec{M}(\vec{r}\,')$ will no longer be zero and Eq. 2.8 must be used instead of Eq. 2.9. In such cases, the surfaces containing the IBC must be closed [11].

2.3 The Method of Moments

In this section, the MoM technique is applied to the numerical solution of Eq. 2.9 for a PEC BOR. This technique basically consists in transforming the integral equation into a system of linear algebraic equations [10]–[13],[16].

2.3.1 The Matrix Equation

To transform the EFIE into an equation amenable to numerical solution, first the unknown current $\vec{J}(\vec{r}\,')$ of Eq. 2.9 is represented by a finite summation of known basis functions $\vec{J}_j(\vec{r}\,')$ respectively multiplied by unknown complex coefficients I_j as follows:

$$\vec{J}(\vec{r}\,') \;=\; \sum_{j}^{N} I_j\, \vec{J}_j(\vec{r}\,'), \tag{2.10}$$

where N is the total number of basis functions and $\vec{J}_j(\vec{r}\,')$ must be judiciously chosen in order to correctly represent the electromagnetic behavior of the electric current, ensuring the proper convergence of the numerical solution (discussed in Sect. 2.3.2). The substitution of Eq. 2.10 into Eq. 2.9 yields

$$\hat{n} \times \vec{E}^{inc}(\vec{r}) \;=\; \sum_{j}^{N} I_j\, L(\vec{J}_j), \tag{2.11}$$

where

$$L(\vec{J}_j) \;=\; \frac{j}{4\pi\omega\epsilon_o}\, \hat{n} \times \int_{S'} \left\{ k_o^2 \vec{J}_j(\vec{r}\,')\Psi - \left[\nabla' \cdot \vec{J}_j(\vec{r}\,')\right] \nabla'\Psi \right\}\, ds'. \tag{2.12}$$

Next, to obtain the unknown coefficients I_j, the solution of Eq. 2.11 is enforced over S' by means of weighting functions $\vec{W}_i(\vec{r})$. These weighting functions are defined over the BOR surface S and an inner product is taken on both sides of Eq. 2.11 for each one of the N functions $\vec{W}_i(\vec{r})$ [10]–[13],[16]:

$$\int_S \vec{W}_i(\vec{r}) \cdot \left[\hat{n} \times \vec{E}^{inc}(\vec{r})\right]\, ds \;=\; \sum_{j}^{N} I_j \int_S \vec{W}_i(\vec{r}) \cdot L(\vec{J}_j)\, ds, \tag{2.13}$$

where S and the unprimed coordinates refer to the observation point $\vec{r}$, and S' and the primed coordinates refer to the source point $\vec{r}'$ (S and S' actually represent the same BOR surface). Anticipating that the basis and weighting functions are to be chosen tangent to the surface and, consequently, perpendicular to the surface normals $\hat{n}'$ and $\hat{n}$, respectively, Eq. 2.13 may be rewritten as [16]

$$\begin{aligned} \int_S \vec{W}_i(\vec{r}) \cdot \vec{E}^{inc}(\vec{r})\, ds &= \frac{j}{4\pi\omega\epsilon_o} \sum_j^N I_j \int_S \int_{S'} \vec{W}_i(\vec{r}) \cdot \Big\{ k_o^2 \vec{J}_j(\vec{r}\,')\Psi \\ &- \Big[\nabla' \cdot \vec{J}_j(\vec{r}\,')\Big] \nabla'\Psi \Big\}\, ds'\, ds. \end{aligned} \tag{2.14}$$

Now, from Eq. 2.4 one obtains the useful result

$$\nabla'\Psi = -\nabla\Psi. \tag{2.15}$$

Also useful is the following vector identity:

$$\oint_S \vec{W}_i(\vec{r}) \cdot \nabla\Psi\, ds = \oint_S \nabla \cdot \Big[\Psi \vec{W}_i(\vec{r})\Big]\, ds - \oint_S \Psi\, \nabla \cdot \vec{W}_i(\vec{r})\, ds, \tag{2.16}$$

where the first integral of the right-hand side of Eq. 2.16 is zero, as a consequence of the two-dimensional divergence theorem. The substitution of Eqs. 2.15 and 2.16 into Eq. 2.14 yields

$$\begin{aligned} \int_S \vec{W}_i(\vec{r}) \cdot \vec{E}^{inc}(\vec{r})\, ds &= \frac{j}{4\pi\omega\epsilon_o} \sum_j^N I_j \int_S \int_{S'} \Big\{ k_o^2\, \vec{W}_i(\vec{r}) \cdot \vec{J}_j(\vec{r}\,') \\ &- \Big[\nabla \cdot \vec{W}_i(\vec{r})\Big] \Big[\nabla' \cdot \vec{J}_j(\vec{r}\,')\Big] \Big\}\, \Psi\, ds'\, ds. \end{aligned} \tag{2.17}$$

From Eq. 2.17, which must be applied to each weighting function $\vec{W}_i(\vec{r})$, one finally obtains the matrix equation

$$[V] = [Z]\,[I], \tag{2.18}$$

where the i-th element of the column matrix $[V]$ is given by

$$V_i = \frac{1}{\eta_o} \int_S \vec{W}_i(\vec{r}) \cdot \vec{E}^{inc}(\vec{r})\, ds \tag{2.19}$$

(where the free-space impedance $\eta_o = \sqrt{\mu_o/\epsilon_o}$), the elements of the N-element square matrix $[Z]$ are given by

$$Z_{ij} = \frac{j}{4\pi k_o} \int_S \int_{S'} \left\{ k_o^2 \vec{W}_i(\vec{r}) \cdot \vec{J}_j(\vec{r}\,') - \left[\nabla \cdot \vec{W}_i(\vec{r})\right] \left[\nabla' \cdot \vec{J}_j(\vec{r}\,')\right] \right\} \Psi\, ds'\, ds, \tag{2.20}$$

and the j-th element of the column matrix $[I]$ is the unknown coefficient I_j. Due to the physical units of the respective elements, the matrices $[V]$, $[Z]$, and $[I]$ are known as the *voltage*, *impedance*, and *current* matrices, respectively. Once the linear system of Eq. 2.18 is solved for the unknown coefficients I_j, the electric current $\vec{J}(\vec{r}\,')$ is immediately obtained from Eq. 2.10.

2.3.2 Basis and Weighting Functions

The correct choice of the basis and weighting functions is fundamental for the proper convergence of the MoM technique. For reflector-antenna applications composed of smooth and well-behaved surfaces, local and/or entire-domain basis and weighting functions may be used. The advantage of the entire-domain functions is to permit the analysis of large reflector antennas with a relatively small number N of functions [18],[19]. This tremendously reduces the number of impedance-matrix elements (see Eq. 2.18), which is equal to N^2. However, as the evaluation of each impedance-matrix element is proportional to N^2 in this case, the time spent in

obtaining the entire matrix is then proportional to N^4, yielding a highly time consuming algorithm. To overcome this difficulty, spatial-frequency localized functions may be used [20]. In this procedure, a relatively small number N (still, bigger than the one for the entire-domain functions) may be used and the time spent on the numerical evaluation of each impedance-matrix element is now independent on N. However, both the entire-domain and spatial-frequency localized functions can not efficiently analyze configurations with complex geometries (such as the feed structures to be studied in Chapter 3).

In the present work, the basis and weighting functions [$\vec{J}_j(\vec{r}')$ and $\vec{W}_i(\vec{r})$, respectively] used are the local triangle and pulse functions of Refs. [16] and [17] (see Fig. 2.4). Although a higher number N of functions must be used, their versatileness enables the analysis of practically any geometry representing the reflector and feed surfaces of the antenna. Likewise the spatial-frequency localized functions, the numerical evaluation of each impedance-matrix element is independent on N, but the integrals associated with the present formulation are somewhat simpler.

The above choice for the local triangle and pulse functions are primarily based on the requirements of the impedance-boundary-condition (IBC) formulation presented in Chapter 3 to model the feed structure. Whenever a discontinuity of the IBC is present over the BOR surface, the boundary conditions stablish a continuity and a discontinuity on the electric surface current flowing along the $\hat{t}$- and $\hat{\phi}$-directions, respectively. So, the $\hat{t}$-oriented electric currents are represented by

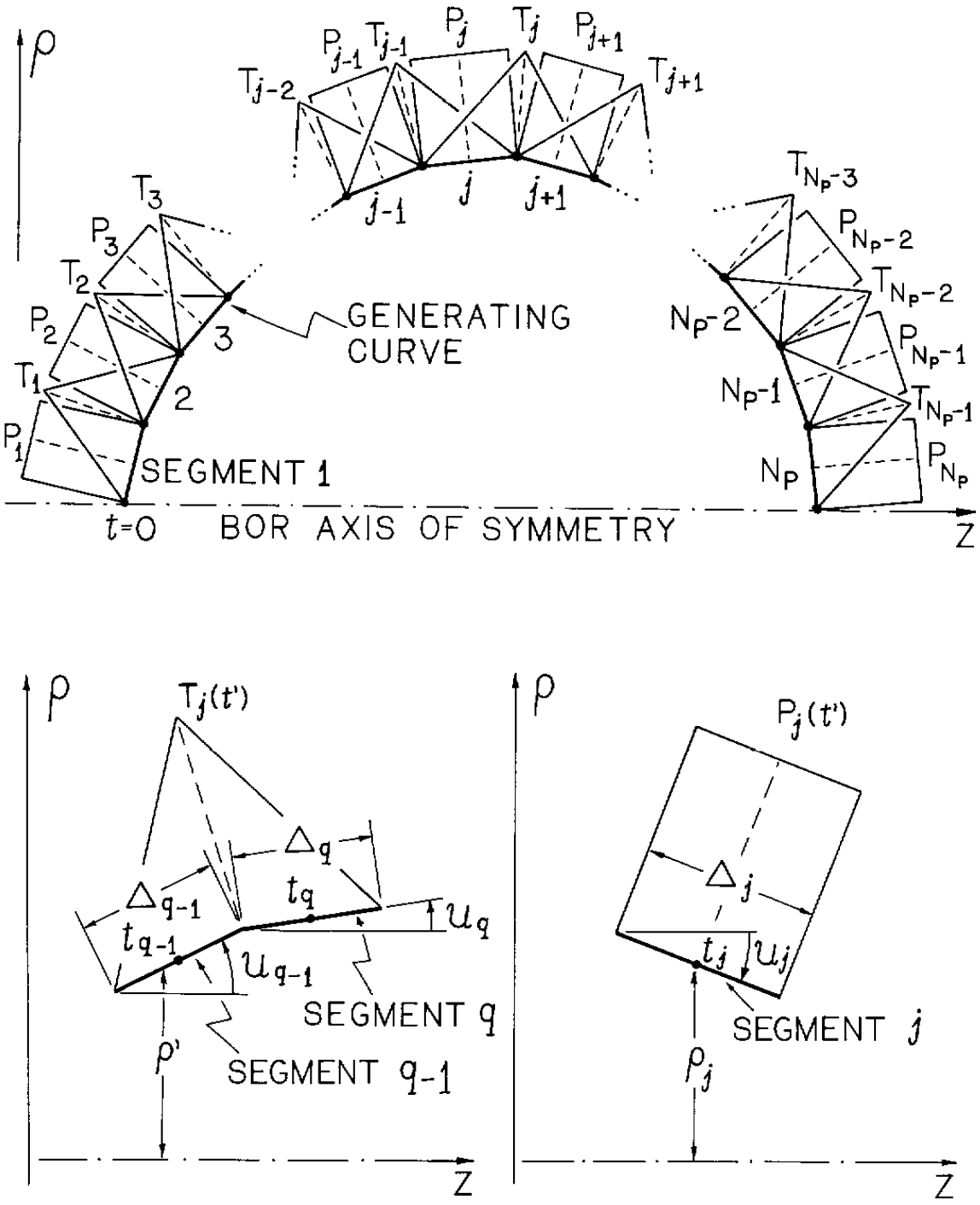

Figure 2.4: Triangle and Pulse Basis Functions.

triangle basis functions to ensure their continuity from one segment to an adjacent one over the BOR generating curve, while the $\hat{\phi}$-oriented electric currents are represented by pulse basis functions to account for any possible discontinuity (see Fig. 2.4). This representation also enables the correct modeling of the currents at the rim of a PEC reflector surface, as the $\hat{t}$-oriented electric current dies to zero at the rim while the $\hat{\phi}$-oriented one reaches very large values.

Accordingly to Ref. [16], the electric current is then represented as

$$\vec{J}(\vec{r}\,') = \sum_{n=-\infty}^{\infty} \left\{ \sum_{j=1}^{N_T} I_{nj}^{T} \frac{T_j(t')}{\rho'} e^{jn\phi'} \hat{t}' + \sum_{j=1}^{N_P} I_{nj}^{P} \frac{P_j(t')}{\rho_j} e^{jn\phi'} \hat{\phi}' \right\}, \qquad (2.21)$$

where $\hat{t}'$ and $\hat{\phi}'$ are the unit vectors at the source point $\vec{r}\,'$ over the surface S', t' and ϕ' are the corresponding coordinates locating $\vec{r}\,'$, $T_j(t')$ and $P_j(t')$ are the triangle and pulse basis functions, respectively, N_T and N_P are the total number of triangle and pulse basis functions, respectively, I_{nj}^{T} and I_{nj}^{P} are the unknown complex coefficients associated with $T_j(t')$ and $P_j(t')$, respectively, ρ' is the radial distance from $\vec{r}\,'$ to the z-axis, and ρ_j is the radial distance from the middle point of segment j to the z-axis. Herein, the BOR generating-curve segments associated with $T_j(t')$ and $P_j(t')$ are called the *source segments*.

With the assistance of Fig. 2.4, each triangle basis function $T_j(t')$ is defined over two consecutive source segments. Throughout this work, for each $T_j(t')$ the subscript $q-1$ is used to identify the associated source segment where $T_j(t')$ has a positive first derivative, while the subscript q identifies the remaining source seg-

ment (where the derivative is negative). In Eq. 2.21, the division of $T_j(t')$ by ρ' avoids numerical problems whenever ρ' is close to zero (this point will become clear later). As illustrated in Fig. 2.4, in the first and last segments of the generating curve representing one of the BOR surfaces only one triangle function will be present (i.e., no half-triangles will be used). Half-triangles can be used to ensure the proper modeling of the current behavior at the generating-curve extremes. However, these extremes will correspond either to the point where the BOR intercepts the symmetry axis [in which case the proper current behavior is taken into account by the pulse function $P_j(t')$ representing the $\hat{\phi}$-oriented current] or to the rim of the BOR surface (where the $\hat{t}$-oriented current naturally dies to zero). Furthermore, the pulse function $P_j(t')$ is defined over a single source segment, which is simply represented by the subscript j. In Eq. 2.21, the division of $P_j(t')$ by ρ_j is used to maintain the same unit for both t- and ϕ-current representations (no numerical singularity is introduced by this division since ρ_j will never be zero). From Eq. 2.21, a sinusoidal behavior is chosen for the azimuthal ϕ' variation on both current elements, where n is an integer number.

To represent the weighting functions $\vec{W}_i(\vec{r})$, Galerkin's method is employed as explained in Ref. [16]. The application of Galerkin's method to the MoM technique generally yields more accurate and rapidly convergent solutions [12]. In this case:

$$\vec{W}_i(\vec{r}) \;=\; \sum_{m=-\infty}^{\infty} \left[\frac{T_i(t)}{\rho}\,\hat{t} \;+\; \frac{P_i(t)}{\rho_i}\,\hat{\phi} \right] e^{-jm\phi}, \tag{2.22}$$

where now the unprimed vectors and coordinates are used to represent the observation point $\vec{r}$. The definition of the triangle and pulse weighting functions $T_i(t)$ and $P_i(t)$ exactly follows the one of the triangle and pulse basis functions $T_j(t')$ and $P_j(t')$ of Eq. 2.21, where now the BOR generating-curve segments associated with the weighting functions are called the *observation segments*. To remove any ambiguities between the source and observation segments, the subscripts $p-1$, p, and i are used for the observation-segment representation, instead of the previously used subscripts $q-1$, q, and j, respectively. In Eq. 2.22 the sinusoidal azimuthal variation is established by the integer number m.

As two different basis functions $[T_j(t')$ and $P_j(t')]$ and two different weighting functions $[T_i(t)$ and $P_i(t)]$ are used, the matrix equation of Eq. 2.18 is written as

$$\begin{bmatrix} V^T \\ V^P \end{bmatrix} = \begin{bmatrix} Z^{TT} & Z^{TP} \\ Z^{PT} & Z^{PP} \end{bmatrix} \begin{bmatrix} I^T \\ I^P \end{bmatrix}, \tag{2.23}$$

where, from Eqs. 2.19 and 2.22, the elements of the sub-matrices V^T and V^P are given by

$$V_i^T = \frac{1}{\eta_o} \int_S \frac{T_i(t)}{\rho} e^{-jm\phi} \; \hat{t} \cdot \vec{E}^{inc}(\vec{r}) \, ds, \qquad i = 1, ..., N_T, \tag{2.24}$$

$$V_i^P = \frac{1}{\eta_o} \int_S \frac{P_i(t)}{\rho_i} e^{-jm\phi} \; \hat{\phi} \cdot \vec{E}^{inc}(\vec{r}) \, ds, \qquad i = 1, ..., N_P, \tag{2.25}$$

respectively, from Eqs. 2.20–2.22 the elements of the sub-matrices Z^{TT}, Z^{TP}, Z^{PT},

and Z^{PP} are given by

$$Z_{ij}^{TT} = \frac{j}{4\pi k_o} \int_S \int_{S'} \left\{ k_o^2 \frac{T_i(t)}{\rho} \frac{T_j(t')}{\rho'} e^{j(n\phi'-m\phi)} \hat{t} \cdot \hat{t}' - \nabla \cdot \left[\frac{T_i(t)}{\rho} e^{-jm\phi} \hat{t} \right] \right.$$
$$\left. \times \nabla' \cdot \left[\frac{T_j(t')}{\rho'} e^{jn\phi'} \hat{t}' \right] \right\} \Psi \, ds' \, ds, \; i = 1, ..., N_T \text{ and } j = 1, ..., N_T, \quad (2.26)$$

$$Z_{ij}^{TP} = \frac{j}{4\pi k_o} \int_S \int_{S'} \left\{ k_o^2 \frac{T_i(t)}{\rho} \frac{P_j(t')}{\rho_j} e^{j(n\phi'-m\phi)} \hat{t} \cdot \hat{\phi}' - \nabla \cdot \left[\frac{T_i(t)}{\rho} e^{-jm\phi} \hat{t} \right] \right.$$
$$\left. \times \nabla' \cdot \left[\frac{P_j(t')}{\rho_j} e^{jn\phi'} \hat{\phi}' \right] \right\} \Psi \, ds' \, ds, \; i = 1, ..., N_T \text{ and } j = 1, ..., N_P, \quad (2.27)$$

$$Z_{ij}^{PT} = \frac{j}{4\pi k_o} \int_S \int_{S'} \left\{ k_o^2 \frac{P_i(t)}{\rho_i} \frac{T_j(t')}{\rho'} e^{j(n\phi'-m\phi)} \hat{\phi} \cdot \hat{t}' - \nabla \cdot \left[\frac{P_i(t)}{\rho_i} e^{-jm\phi} \hat{\phi} \right] \right.$$
$$\left. \times \nabla' \cdot \left[\frac{T_j(t')}{\rho'} e^{jn\phi'} \hat{t}' \right] \right\} \Psi \, ds' \, ds, \; i = 1, ..., N_P \text{ and } j = 1, ..., N_T, \quad (2.28)$$

$$Z_{ij}^{PP} = \frac{j}{4\pi k_o} \int_S \int_{S'} \left\{ k_o^2 \frac{P_i(t)}{\rho_i} \frac{P_j(t')}{\rho_j} e^{j(n\phi'-m\phi)} \hat{\phi} \cdot \hat{\phi}' - \nabla \cdot \left[\frac{P_i(t)}{\rho_i} e^{-jm\phi} \hat{\phi} \right] \right.$$
$$\left. \times \nabla' \cdot \left[\frac{P_j(t')}{\rho_j} e^{jn\phi'} \hat{\phi}' \right] \right\} \Psi \, ds' \, ds, \; i = 1, ..., N_P \text{ and } j = 1, ..., N_P, \quad (2.29)$$

respectively, and the elements of the sub-matrices I_T and I_P are the unknown coefficients I_{nj}^T and I_{nj}^P of Eq. 2.21, respectively. The numerical evaluation of the impedance-matrix elements given by Eqs. 2.26–2.29 is discussed in Sects. 2.3.3 and 2.3.4, while the evaluation of the voltage-matrix elements given by Eqs. 2.24 and 2.25 is presented in Sect. 2.3.5.

2.3.3 Impedance-Matrix Evaluation

The numerical evaluation of the impedance-matrix elements discussed in this section follows the procedure of Ref. [16]. Although the material here presented is not new, for the sake of completeness the formulation is detailed below in order to

introduce the notation used throughout this work as well as to provide a reference for the evaluation of the impedance-matrix elements related to the IBC formulation (discussed in Chapter 3).

The evaluation of the surface integrals of Eqs. 2.26–2.29 is better accomplished using the orthogonal curvilinear coordinate system defined in Sect. 2.1, in which case [16]

$$ds \;=\; \rho\, dt\, d\phi, \tag{2.30}$$

where ρ is the distance from the observation point $\vec{r}$ to the z-axis (see Fig. 2.2). Using the primed coordinates of the source point $\vec{r}\,'$ instead, Eq. 2.30 can also be used to write ds' as $ds' = \rho'\, dt'\, d\phi'$. Using the relations

$$\hat{t}\cdot\hat{t}' \;=\; \sin u\, \sin u'\, \cos(\phi-\phi') \,+\, \cos u\, \cos u', \tag{2.31}$$

$$\hat{t}\cdot\hat{\phi}' \;=\; \sin u\, \sin(\phi-\phi'), \tag{2.32}$$

$$\hat{\phi}\cdot\hat{t}' \;=\; -\sin u'\, \sin(\phi-\phi'), \tag{2.33}$$

$$\hat{\phi}\cdot\hat{\phi}' \;=\; \cos(\phi-\phi'), \tag{2.34}$$

$$\nabla\cdot\vec{F} \;=\; \frac{1}{\rho}\frac{\partial}{\partial t}(\rho F_t) \,+\, \frac{1}{\rho}\frac{\partial}{\partial \phi}(F_\phi), \tag{2.35}$$

$$R \;=\; \left[(\rho-\rho')^2 + (z-z')^2 + 4\rho\rho'\sin^2\left(\frac{\phi-\phi'}{2}\right)\right]^{\frac{1}{2}}, \tag{2.36}$$

Eqs. 2.26–2.29 are rewritten as

$$\begin{aligned} Z_{ij}^{TT} \;=\; \frac{j}{4\pi}\int_0^{2\pi}\int_t^{2\pi}\int_0^{2\pi}\int_{t'} \Big\{ & k_o^2\, T_i(t)\, T_j(t')\, [\sin u\, \sin u'\, \cos(\phi-\phi') \,+\, \cos u\, \cos u'] \\ -\; & T_i'(t)\, T_j'(t') \Big\}\; e^{j(n\phi'-m\phi)}\; \frac{e^{-jk_oR}}{k_oR}\; dt'\, d\phi'\, dt\, d\phi, \end{aligned} \tag{2.37}$$

$$Z_{ij}^{TP} = \frac{j}{4\pi} \int_0^{2\pi}\int_t\int_0^{2\pi}\int_{t'} \left\{ k_o^2\, T_i(t)\, P_j(t')\, \frac{\rho'}{\rho_j}\, \sin u\, \sin(\phi-\phi') \right.$$
$$\left. - \; jn\, T_i'(t)\, \frac{P_j(t')}{\rho_j} \right\} e^{j(n\phi'-m\phi)}\, \frac{e^{-jk_oR}}{k_oR}\; dt'\, d\phi'\, dt\, d\phi, \tag{2.38}$$

$$Z_{ij}^{PT} = \frac{-j}{4\pi} \int_0^{2\pi}\int_t\int_0^{2\pi}\int_{t'} \left\{ k_o^2\, P_i(t)\, T_j(t')\, \frac{\rho}{\rho_i}\, \sin u'\, \sin(\phi-\phi') \right.$$
$$\left. - \; jm\, \frac{P_i(t)}{\rho_i}\, T_j'(t') \right\} e^{j(n\phi'-m\phi)}\, \frac{e^{-jk_oR}}{k_oR}\; dt'\, d\phi'\, dt\, d\phi, \tag{2.39}$$

$$Z_{ij}^{PP} = \frac{j}{4\pi} \int_0^{2\pi}\int_t\int_0^{2\pi}\int_{t'} \left\{ k_o^2\, P_i(t)\, P_j(t')\, \frac{\rho\rho'}{\rho_i\rho_j}\, \cos(\phi-\phi') \right.$$
$$\left. - \; mn\, \frac{P_i(t)}{\rho_i}\, \frac{P_j(t')}{\rho_j} \right\} e^{j(n\phi'-m\phi)}\, \frac{e^{-jk_oR}}{k_oR}\; dt'\, d\phi'\, dt\, d\phi, \tag{2.40}$$

where $T'(t) = \partial T/\partial t$ and the limits of the integrals with respect to t and t' will depend on the weighting and basis functions, respectively.

From Eqs. 2.36–2.40 one observes that all functions of ϕ and ϕ' are periodic over the 0–2π interval. In this case, the following relation applies:

$$\int_0^{2\pi} F(\phi-\phi')\, e^{j(n\phi'-m\phi)}\, d\phi' = \int_0^{2\pi} F(\phi)\, e^{j[(n-m)\phi'-m\phi]}\, d\phi'$$
$$= F(\phi)\, e^{-jm\phi} \times \begin{cases} 2\pi, & m = n, \\ 0, & m \neq n. \end{cases} \tag{2.41}$$

Equation 2.41 then indicates that the impedance-matrix elements are zero whenever $m \neq n$ and, consequently, Eq. 2.23 may be separated into several independent systems, one for each different mode $m = n$. The modes m to be excited will depend on the incident electric field $\vec{E}^{inc}(\vec{r})$ radiated by the external sources and, consequently, on the voltage matrix of Eq. 2.23 (discussed in Sect. 2.3.5).

Substituting Eq. 2.41 into Eqs. 2.37–2.40 for each independent mode m, these equations are rewritten as

$$Z_{ij}^{TT} = j \int_t \int_{t'} \Big\{ k_o^2\, T_i(t)\, T_j(t')\, [\sin u \sin u'\, G_5(t,t') + \cos u \cos u'\, G_7(t,t')] - T_i'(t)\, T_j'(t')\, G_7(t,t') \Big\}\, dt'\, dt, \quad (2.42)$$

$$Z_{ij}^{TP} = \int_t \int_{t'} \frac{P_j(t')}{\rho_j} \Big[k_o^2\, T_i(t)\, \rho' \sin u\, G_6(t,t') + m\, T_i'(t)\, G_7(t,t') \Big]\, dt'\, dt, \quad (2.43)$$

$$Z_{ij}^{PT} = -\int_t \int_{t'} \frac{P_i(t)}{\rho_i} \Big[k_o^2\, T_j(t')\, \rho \sin u'\, G_6(t,t') + m\, T_j'(t')\, G_7(t,t') \Big]\, dt'\, dt, \quad (2.44)$$

$$Z_{ij}^{PP} = j \int_t \int_{t'} \frac{P_i(t)}{\rho_i} \frac{P_j(t')}{\rho_j} \Big[k_o^2\, \rho\, \rho'\, G_5(t,t') - m^2\, G_7(t,t') \Big]\, dt'\, dt, \quad (2.45)$$

where the integrals with respect to ϕ are given by

$$G_5(t,t') = \frac{1}{2} \int_0^{2\pi} \cos\phi\; e^{-jm\phi}\; \frac{e^{-jk_oR}}{k_oR}\, d\phi = \int_0^{\pi} \cos\phi\; \cos m\phi\; \frac{e^{-jk_oR}}{k_oR}\, d\phi, \quad (2.46)$$

$$G_6(t,t') = \frac{j}{2} \int_0^{2\pi} \sin\phi\; e^{-jm\phi}\; \frac{e^{-jk_oR}}{k_oR}\, d\phi = \int_0^{\pi} \sin\phi\; \sin m\phi\; \frac{e^{-jk_oR}}{k_oR}\, d\phi, \quad (2.47)$$

$$G_7(t,t') = \frac{1}{2} \int_0^{2\pi} e^{-jm\phi}\; \frac{e^{-jk_oR}}{k_oR}\, d\phi = \int_0^{\pi} \cos m\phi\; \frac{e^{-jk_oR}}{k_oR}\, d\phi, \quad (2.48)$$

with, from Eq. 2.36,

$$R = \left[(\rho - \rho')^2 + (z - z')^2 + 4\, \rho\, \rho' \sin^2 \frac{\phi}{2} \right]^{\frac{1}{2}}. \quad (2.49)$$

It should be noted in Eqs. 2.46–2.48 that the integrals $G_v(t,t')$ are defined with $v = 5$, 6, and 7, respectively, as they belong to a family of similar integrals (to be shown later) where $v = 1, ..., 12$.

To evaluate the integrals with respect to t and t' one recalls that, accordingly to the notation of Sect. 2.3.2, the basis function $T_j(t')$ is defined over two consecutive

segments of the BOR generating curve and the basis function $P_j(t')$ is defined over a single one. Furthermore, it is convenient to define the parameter α to represent the basis functions. This parameter is related to the source coordinates t', ρ', and z' accordingly to:

$$t' = t_l + \alpha \frac{\Delta_l}{2} , \tag{2.50}$$

$$\rho' = \rho_l + \alpha \frac{\Delta_l}{2} \sin u_l , \tag{2.51}$$

$$z' = z_l + \alpha \frac{\Delta_l}{2} \cos u_l , \tag{2.52}$$

where $\alpha = -1$ and 1 represent the point where the source segment l starts and ends, respectively, u_l is the constant angle u associated with the source segment l, t_l, ρ_l, z_l are the t', ρ', and z' coordinates of the middle point of the source segment l, respectively, and throughout this work the subscript l represents any of the subscripts $q-1$, q, and j associated with the source segments. Using the parameter α and from Fig. 2.4, $T_j(t')$ is conveniently written at the source segment $q-1$ as

$$T_j(t') = \frac{1+\alpha}{2}, \tag{2.53}$$

$$T_j'(t') = \frac{1}{\Delta_{q-1}}, \tag{2.54}$$

where Δ_{q-1} is the length of the source segment $q-1$ and α is defined accordingly to Eqs. 2.50–2.52 for $l = q-1$. Similarly, when $l = q$, $T_j(t')$ is expressed as

$$T_j(t') = \frac{1-\alpha}{2}, \tag{2.55}$$

$$T_j'(t') = \frac{-1}{\Delta_q}, \tag{2.56}$$

where now the parameters are associated with the source segment q. Furthermore, the basis function $P_j(t')$ associated with the source segment j is simply given by

$$P_j(t') \;=\; 1\,, \tag{2.57}$$

where now Eqs. 2.50–2.52 are applied with $l = j$. For the weighting functions $T_i(t)$ and $P_i(t)$ the same procedure is adopted and Eqs. 2.50–2.57 are used for their definition with the primed source coordinates replaced by the unprimed observation coordinates and the source-segment subscripts l, $q-1$, q, and j replaced by the observation-segment subscripts k, $p-1$, p, and i, respectively.

Following Ref. [16], the integrals with respect to t are evaluated by the approximation

$$\int\limits_{segment\ k} F(t)\,dt \;\approx\; F(\alpha = 0)\;\Delta_k, \tag{2.58}$$

where throughout this work the subscript k represents any of the subscripts $p-1$, p, and i associated with the observation segments. Substituting Eqs. 2.50–2.57 [for the weighting functions $T_i(t)$ and $P_i(t)$] and 2.58 into Eqs. 2.42–2.45, one obtains the following relations:

$$\begin{aligned} Z_{ij}^{TT} \;=\; & j \int\limits_{t'} \sum_{k=p-1}^{p} \left\{ k_o^2\,\frac{\Delta_k}{2}\,T_j(t')\,\left[\sin u_k\,\sin u'\,G_5(t_k,t') \;+\; \cos u_k\,\cos u'\,G_7(t_k,t')\right]\right. \\ & +\; \left.(-1)^{p-k}\,T_j'(t')\,G_7(t_k,t')\right\} dt', \end{aligned} \tag{2.59}$$

$$Z_{ij}^{TP} \;=\; \int\limits_{t'} \frac{P_j(t')}{\rho_j} \sum_{k=p-1}^{p} \left[k_o^2\,\frac{\Delta_k}{2}\,\rho'\,\sin u_k\,G_6(t_k,t') - (-1)^{p-k}\,m\,G_7(t_k,t')\right] dt', \tag{2.60}$$

$$Z_{ij}^{PT} \;=\; -\,\Delta_i \int\limits_{t'} \left[k_o^2\,T_j(t')\,\sin u'\,G_6(t_i,t') + \frac{m}{\rho_i}\,T_j'(t')\,G_7(t_i,t')\right] dt', \tag{2.61}$$

$$Z_{ij}^{PP} = j\,\Delta_i \int_{t'} \frac{P_j(t')}{\rho_j}\left[k_o^2\,\rho'\,G_5(t_i,t') - \frac{m^2}{\rho_i}\,G_7(t_i,t')\right]dt', \tag{2.62}$$

where the distance R in Eqs. 2.46–2.49 is now given by

$$R = \left[(\rho_k-\rho')^2 + (z_k-z')^2 + 4\,\rho_k\,\rho'\,\sin^2\frac{\phi}{2}\right]^{\frac{1}{2}}, \tag{2.63}$$

and $(-1)^{p-k} = -1$ and 1 when $k = p-1$ and p, respectively.

Using Eqs. 2.50–2.57, the variable of integration t' can be transformed into α and after straightforward algebraic manipulations Eqs. 2.59–2.62 may be finally rewritten as

$$\begin{aligned} Z_{ij}^{TT} = {} & \frac{j}{2}\sum_{k=p-1}^{p}\sum_{l=q-1}^{q}\left\{k_o^2\,\frac{\Delta_k\,\Delta_l}{4}\left[\sin u_k\,\sin u_l\,\left[G_{5a}(t_k,t_l) - (-1)^{q-l}G_{5b}(t_k,t_l)\right]\right.\right. \\ & + \left.\left.\cos u_k\,\cos u_l\,\left[G_{7a}(t_k,t_l) - (-1)^{q-l}G_{7b}(t_k,t_l)\right]\right] \right. \\ & - \left.(-1)^{p-k}(-1)^{q-l}\,G_{7a}(t_k,t_l)\right\}, \end{aligned} \tag{2.64}$$

$$\begin{aligned} Z_{ij}^{TP} = {} & \frac{\Delta_j}{2}\sum_{k=p-1}^{p}\left\{k_o^2\,\frac{\Delta_k}{2}\,\sin u_k\,\left[G_{6a}(t_k,t_j) + \frac{\Delta_j\,\sin u_j}{2\,\rho_j}\,G_{6b}(t_k,t_j)\right]\right. \\ & - \left.(-1)^{p-k}\,\frac{m}{\rho_j}\,G_{7a}(t_k,t_j)\right\}, \end{aligned} \tag{2.65}$$

$$\begin{aligned} Z_{ij}^{PT} = {} & \frac{-\Delta_i}{2}\sum_{l=q-1}^{q}\left\{k_o^2\,\frac{\Delta_l}{2}\,\sin u_l\,\left[G_{6a}(t_i,t_l) - (-1)^{q-l}G_{6b}(t_i,t_l)\right]\right. \\ & - \left.(-1)^{q-l}\,\frac{m}{\rho_i}\,G_{7a}(t_i,t_l)\right\}, \end{aligned} \tag{2.66}$$

$$\begin{aligned} Z_{ij}^{PP} = {} & j\,\frac{\Delta_i\,\Delta_j}{2}\left\{k_o^2\,\left[G_{5a}(t_i,t_j) + \frac{\Delta_j\,\sin u_j}{2\,\rho_j}\,G_{5b}(t_i,t_j)\right)\right] \\ & - \left.\frac{m^2}{\rho_i\,\rho_j}\,G_{7a}(t_i,t_j)\right\}, \end{aligned} \tag{2.67}$$

where the integrals with respect to α are given by

$$G_{va}(t_k, t_l) = \int_{-1}^{1} G_v(t_k, t_l)\, d\alpha, \qquad v = 5, 6, 7\,, \tag{2.68}$$

$$G_{vb}(t_k, t_l) = \int_{-1}^{1} G_v(t_k, t_l)\, \alpha\, d\alpha, \qquad v = 5, 6, 7\,, \tag{2.69}$$

with $G_v(t_k, t_l)$ given by Eqs. 2.46–2.48 for $v = 5$, 6, and 7, respectively, the distance R given by Eq. 2.63, and ρ' and z' given by Eqs. 2.51 and 2.52, respectively.

It is important to notice that a one by one (i.e., one element at each time) evaluation of the impedance-matrix elements given by Eqs. 2.64–2.66 is very inefficient due to the overlapping integration regions. Many of the numerical calculations present on a given pair of segments k and l are repeated and, thus, must be stored for further reuse. To take advantage of this, the best approach is to fill the impedance matrix with a one by one contribution from each pair of segments k and l [16]. On doing so, the integrals of Eqs. 2.46–2.48, 2.68, and 2.69 are evaluated just once for each pair of segments. As each segment has two triangles (except for those at the generating-curve extremes) and one pulse function, this procedure reduces the computational effort by a factor of about 4.5. Furthermore, Eqs. 2.64–2.69 yield

$$\left(Z_{ij}^{TT}\right)_m = \left(Z_{ij}^{TT}\right)_{-m}, \tag{2.70}$$

$$\left(Z_{ij}^{TP}\right)_m = -\left(Z_{ij}^{TP}\right)_{-m}, \tag{2.71}$$

$$\left(Z_{ij}^{PT}\right)_m = -\left(Z_{ij}^{PT}\right)_{-m}, \tag{2.72}$$

$$\left(Z_{ij}^{PP}\right)_m = \left(Z_{ij}^{PP}\right)_{-m}, \tag{2.73}$$

such that the results for a positive mode m may be used to obtain the terms corresponding to the negative mode $-m$, further reducing the computational effort.

2.3.4 Numerical Evaluation of the Impedance-Matrix Integrals

The numerical evaluation of the double integrals of Eqs. 2.68 and 2.69 will follow the procedure adopted in Ref. [16]. First of all, due to the singularities present on the integrand of Eq. 2.48, which are difficult to be numerically removed, it is more appropriate to express $G_7(t,t')$ as

$$G_7(t,t') \;=\; G_4(t,t') \;+\; G_5(t,t'), \tag{2.74}$$

where $G_5(t,t')$ is given by Eq. 2.46 and

$$G_4(t,t') \;=\; \frac{1}{2}\int_0^{2\pi}(1-\cos\phi)\;e^{-jm\phi}\;\frac{e^{-jk_oR}}{k_oR}\,d\phi \;=\; 2\int_0^{\pi}\sin^2\frac{\phi}{2}\;\cos m\phi\;\frac{e^{-jk_oR}}{k_oR}\,d\phi. \tag{2.75}$$

Consequently, from Eqs. 2.68, 2.69, and 2.74 one obtains

$$G_{7a}(t_k,t_l) \;=\; G_{4a}(t_k,t_l) \;+\; G_{5a}(t_k,t_l), \tag{2.76}$$

$$G_{7b}(t_k,t_l) \;=\; G_{4b}(t_k,t_l) \;+\; G_{5b}(t_k,t_l), \tag{2.77}$$

where $G_{4a}(t_k,t_l)$ and $G_{4b}(t_k,t_l)$ are given by Eqs. 2.68 and 2.69, respectively, with $\upsilon = 4$.

The integrals with respect to α in Eqs. 2.68 and 2.69 may be numerically evaluated in terms of a n_α-point Gaussian quadrature [43], in which case one obtains

the expressions

$$G_{va}(t_k,t_l) = \sum_{\xi=1}^{n_\alpha} A_\xi \, G_v(t_k,t_l), \qquad v=4,5,6\,, \tag{2.78}$$

$$G_{vb}(t_k,t_l) = \sum_{\xi=1}^{n_\alpha} A_\xi \, \alpha_\xi \, G_v(t_k,t_l), \qquad v=4,5,6\,, \tag{2.79}$$

where A_ξ and α_ξ are the weights and abscissas of the n_α-point Gaussian quadrature, respectively. The value $n_\alpha = 2$ is used throughout this work, in which case $A_1 = A_2 = 1$ and $-\alpha_1 = \alpha_2 = 1/\sqrt{3}$ [43]. Similarly, the integrals of Eqs. 2.46, 2.47, and 2.75 may be numerically evaluated using a n_ϕ-point Gaussian quadrature, in which case:

$$G_4(t_k,t_l) = \pi \sum_{\beta=1}^{n_\phi} A_\beta \, \sin^2\frac{\phi_\beta}{2} \, \cos m\phi_\beta \, \frac{e^{-jk_oR}}{k_oR}, \tag{2.80}$$

$$G_5(t_k,t_l) = \frac{\pi}{2} \sum_{\beta=1}^{n_\phi} A_\beta \, \cos\phi_\beta \, \cos m\phi_\beta \, \frac{e^{-jk_oR}}{k_oR}, \tag{2.81}$$

$$G_6(t_k,t_l) = \frac{\pi}{2} \sum_{\beta=1}^{n_\phi} A_\beta \, \sin\phi_\beta \, \sin m\phi_\beta \, \frac{e^{-jk_oR}}{k_oR}, \tag{2.82}$$

where

$$\phi_\beta = \frac{\pi}{2}\,(x_\beta + 1)\,, \tag{2.83}$$

A_β and x_β are the weights and abscissas of the n_ϕ-point Gaussian quadrature, respectively, and from Eqs. 2.51, 2.52, and 2.63

$$R = \left[(\rho_k-\rho')^2 + (z_k-z')^2 + 4\,\rho_k\,\rho'\,\sin^2\frac{\phi_\beta}{2}\right]^{\frac{1}{2}}, \tag{2.84}$$

$$\rho' = \rho_l + \alpha_\xi \frac{\Delta_l}{2}\sin u_l, \tag{2.85}$$

$$z' = z_l + \alpha_\xi \frac{\Delta_l}{2}\cos u_l. \tag{2.86}$$

The required n_ϕ value for a given accuracy depends on the integrand behavior of Eqs. 2.46, 2.47, and 2.75. From these equations and for a small value of $|m|$ (anticipating that only the modes $m = \pm 1$ are excited by the external sources used throughout this work, as discussed in Sects. 2.3.5 and 3.2.4), the highest oscillatory term present in the integrals is e^{-jk_oR}. To estimate n_ϕ, one must first find the value $\phi = \phi_{max}$ where the exponential argument k_oR has its maximum variation and, consequently, its second derivative with respect to ϕ is zero. From Eq. 2.49 one obtains that

$$\frac{\partial^2(k_oR)}{\partial\phi^2} = \frac{k_o\rho\rho'}{R^2}\left[R\cos\phi - \frac{\rho\rho'\sin^2\phi}{R}\right] = 0, \tag{2.87}$$

which provides

$$R^2\cos\phi_{max} = \rho\,\rho'\,\sin^2\phi_{max}\,. \tag{2.88}$$

Furthermore, from Eqs. 2.49 and 2.88 one obtains that

$$\cos\phi_{max} = \frac{\gamma - \sqrt{\gamma^2 - (2\rho\rho')^2}}{2\rho\rho'}, \qquad \phi_{max} \in [0,\pi]\,, \tag{2.89}$$

where

$$\gamma = \rho^2 + \rho'^2 + (z - z')^2. \tag{2.90}$$

Finally, the number of integrand oscillations (NO) in the interval from $\phi_1 = \phi_{max} - \delta$ to $\phi_2 = \phi_{max} + \delta$ (where $\delta = \pi/36$ is adopted in this work) is obtained from:

$$NO \approx \frac{k_o\,\Delta R}{2\pi}\,\frac{\pi}{(\phi_2 - \phi_1)} = \frac{\pi\,\Delta R}{2\,\lambda\,\delta}\,, \tag{2.91}$$

where $\Delta R = R(\phi = \phi_2) - R(\phi = \phi_1)$ is a positive number. In this work,

$$n_\phi \;=\; 4\,NO \tag{2.92}$$

proved sufficient to ensure the required accuracy. Nevertheless, it is also useful to determine the maximum n_ϕ value that a given geometry will require. By inspection of Eq. 2.49 the maximum n_ϕ value is associated with $z = z'$ and $\rho = \rho' = \rho_{max}$, where ρ_{max} is the maximum radial dimension of the geometry being analyzed. In such case, from Eqs. 2.89 and 2.90 one obtains that $\phi_{max} = 0$ and from Eq. 2.49:

$$\Delta R \;=\; R(\phi = \delta) \;-\; R(\phi = -\delta) \;=\; 4\,\rho_{max}\,\sin\frac{\delta}{2}\,. \tag{2.93}$$

Finally, substituting Eq. 2.93 into Eqs. 2.91 and 2.92 and taking the limit when $\delta \to 0$, the maximum number $n_\phi = n_\phi|_{max}$ required for a given geometry is

$$n_\phi|_{max} \;=\; \frac{4\pi\rho_{max}}{\lambda}. \tag{2.94}$$

For example, in the analysis of a single paraboloidal reflector with 100λ in diameter, $n_\phi|_{max} \approx 630$. To avoid several calculations of the weights A_β and abscissas x_β, a pre-defined set with several different n_ϕ-point Gaussian-quadrature weights and abscissas may be determined, stored, and used accordingly to the results of Eqs. 2.92 and 2.94.

The numerical evaluation of the double integrals of Eqs. 2.68 and 2.69 must deal with the singularities present whenever the observation point $\vec{r}$ is near the source point $\vec{r}'$. In these cases Eqs. 2.78–2.82 can not be used in their present format.

Three different numerical methods are employed to remove the singularities, and they are detailed below.

The first, Method 1, is applied when the distance between the middle points of segments k and l is smaller than Δ_l and bigger than $0.1\rho_l$. In this case, the singularity elimination is applied to the integral with respect to α. From Eqs. 2.46, 2.47, 2.68, 2.69, and 2.75, the required α-integrals are

$$G_a^E = \int_{-1}^{1} \frac{e^{-jk_oR}}{k_oR}\, d\alpha, \tag{2.95}$$

$$G_b^E = \int_{-1}^{1} \frac{e^{-jk_oR}}{k_oR}\, \alpha\, d\alpha. \tag{2.96}$$

The above integrals can be rewritten as

$$G_a^E = G_{a1}^E + G_{a2}^E, \tag{2.97}$$

$$G_b^E = G_{b1}^E + G_{b2}^E, \tag{2.98}$$

where

$$G_{a1}^E = \int_{-1}^{1} \frac{e^{-jk_oR} - 1}{k_oR}\, d\alpha, \tag{2.99}$$

$$G_{a2}^E = \int_{-1}^{1} \frac{1}{k_oR}\, d\alpha, \tag{2.100}$$

$$G_{b1}^E = \int_{-1}^{1} \frac{e^{-jk_oR} - 1}{k_oR}\, \alpha\, d\alpha, \tag{2.101}$$

$$G_{b2}^E = \int_{-1}^{1} \frac{\alpha}{k_oR}\, d\alpha. \tag{2.102}$$

Equations 2.99 and 2.101 have no singularities and can be numerically evaluated using a n_α-point Gaussian quadrature in the same manner as Eqs. 2.78 and 2.79.

In this case, the following relation proves useful:

$$\frac{e^{-jk_oR}-1}{k_oR} = -\frac{\sin\frac{k_oR}{2}}{\frac{k_oR}{2}}\left(\sin\frac{k_oR}{2}+j\,\cos\frac{k_oR}{2}\right). \tag{2.103}$$

Equations 2.100 and 2.102 are evaluated in closed form. First, Eqs. 2.51 and 2.52 are substituted into Eq. 2.63 to obtain:

$$R = \left[\left(\alpha\,\frac{\Delta_l}{2}+\alpha_0\right)^2 + d^2\right]^{\frac{1}{2}}, \tag{2.104}$$

where

$$\alpha_0 = (\rho_l-\rho_k)\sin u_l + (z_l-z_k)\cos u_l + 2\,\rho_k\,\sin u_l\,\sin^2\frac{\phi}{2}, \tag{2.105}$$

$$d^2 = (\rho_l-\rho_k)^2 + (z_l-z_k)^2 + 4\,\rho_k\,\rho_l\,\sin^2\frac{\phi}{2} - \alpha_0^2. \tag{2.106}$$

Substituting Eq. 2.104 into Eqs. 2.100 and 2.102, and using Eqs. 2.271.4 and 2.271.7 of Ref. [44], one obtains

$$G_{a2}^E = \frac{2}{k_o\,\Delta_l}\,I_G^E, \tag{2.107}$$

$$G_{b2}^E = \frac{2\,\alpha_0}{k_o\,\Delta_l}\left(\frac{4}{\alpha_4^E+\alpha_5^E} - \frac{2}{\Delta_l}\,I_G^E\right), \tag{2.108}$$

where

$$I_G^E = \begin{cases} \ln\left(\frac{\alpha_1^E}{\alpha_2^E}\right), & |\alpha_0| \geq \frac{\Delta_l}{2}, \\ \ln\left(\frac{\alpha_1^E\,\alpha_3^E}{d^2}\right), & |\alpha_0| < \frac{\Delta_l}{2}, \end{cases} \tag{2.109}$$

$$\alpha_1^E = |\alpha_0| + \frac{\Delta_l}{2} + \alpha_4^E, \tag{2.110}$$

$$\alpha_2^E = |\alpha_0| - \frac{\Delta_l}{2} + \alpha_5^E, \tag{2.111}$$

$$\alpha_3^E = \frac{\Delta_l}{2} - |\alpha_0| + \alpha_5^E, \tag{2.112}$$

$$\alpha_4^E = \sqrt{\left(|\alpha_0| + \frac{\Delta_l}{2}\right)^2 + d^2}, \tag{2.113}$$

$$\alpha_5^E = \sqrt{\left(|\alpha_0| - \frac{\Delta_l}{2}\right)^2 + d^2}. \tag{2.114}$$

Finally, convenient forms for the numerical computation of Eqs. 2.68 and 2.69 are obtained using a n_ϕ-point Gaussian quadrature to the integrations with respect to ϕ, in the same manner as in Eqs. 2.80–2.82:

$$G_{4a,b}(t_k, t_l) = \pi \sum_{\beta=1}^{n_\phi} A_\beta \, G_{a,b}^E \, \sin^2 \frac{\phi_\beta}{2} \, \cos m\phi_\beta, \tag{2.115}$$

$$G_{5a,b}(t_k, t_l) = \frac{\pi}{2} \sum_{\beta=1}^{n_\phi} A_\beta \, G_{a,b}^E \, \cos\phi_\beta \, \cos m\phi_\beta, \tag{2.116}$$

$$G_{6a,b}(t_k, t_l) = \frac{\pi}{2} \sum_{\beta=1}^{n_\phi} A_\beta \, G_{a,b}^E \, \sin\phi_\beta \, \sin m\phi_\beta, \tag{2.117}$$

where ϕ_β is given by Eq. 2.83 and both G_a^E and G_b^E (given by Eqs. 2.95–2.114) are evaluated at $\phi = \phi_\beta$.

The second method, Method 2, is applied when the distance between the middle points of segments k and l is smaller than $0.1\rho_l$. In this case, the singularity elimination is applied to the integral with respect to ϕ. Since in this situation the integrand of Eqs. 2.47 and 2.75 is well behaved, Method 2 is only used for Eq. 2.46, where the singularity problems occur near the point $\phi = 0$. In this region, the integrand of Eq. 2.46 can be approximated by

$$\lim_{\phi \to 0} \left[\cos\phi \, \cos m\phi \, \frac{e^{-jk_o R}}{k_o R}\right] \approx \frac{1}{k_o} \left[(\rho' - \rho_k)^2 + (z' - z_k)^2 + \rho_k \rho' \phi^2\right]^{-\frac{1}{2}}. \tag{2.118}$$

Method 2 calculates $G_5(t_k, t_l)$ using Eq. 2.81, then subtracts a n_ϕ-point Gaussian quadrature of Eq. 2.118 in order to cancel any possible numerical error from

Eq. 2.81, and finally adds back the closed-form integration of Eq. 2.118. The final result is

$$\begin{aligned} G_5(t_k,t_l) &= \frac{\pi}{2}\sum_{\beta=1}^{n_\phi} A_\beta \cos\phi_\beta \cos m\phi_\beta \frac{e^{-jk_oR}}{k_oR} + I_5 \\ &- \frac{\pi}{2}\sum_{\beta=1}^{n_\phi} \frac{A_\beta}{k_o}\left[(\rho'-\rho_k)^2+(z'-z_k)^2+\rho_k\rho'\phi_\beta^2\right]^{-\frac{1}{2}} , \end{aligned} \tag{2.119}$$

where, from Eq. 2.271.4 of Ref. [44]

$$\begin{aligned} I_5 &= \int_0^\pi \frac{1}{k_o}\left[(\rho'-\rho_k)^2+(z'-z_k)^2+\rho_k\rho'\phi^2\right]^{-\frac{1}{2}} d\phi \\ &= \frac{1}{k_o\sqrt{\rho_k\rho'}} \ln\left(v_1+\sqrt{1+v_1^2}\right), \end{aligned} \tag{2.120}$$

$$v_1 = \pi\sqrt{\frac{\rho_k\rho'}{(\rho'-\rho_k)^2+(z'-z_k)^2}} , \tag{2.121}$$

and ϕ_β, R, ρ', and z' are respectively given by Eqs. 2.83–2.86. So, when Method 2 is applied, Eqs. 2.78 and 2.79 with $\upsilon = 5$ (i.e., the integrals associated with G_5) are calculated using Eq. 2.119 instead of Eq. 2.81.

The last method, Method 3, is applied whenever the observation segment k coincides with the source segment l (i.e., $k = l$). Method 3 is only applied to the evaluation of $G_{5a}(t_k,t_l)$, which is the only integral with a non-bounded integrand [16]. In this case, from Eq. 2.68 with $\upsilon = 5$, the singularity problems occur near the region where $\alpha = \phi = 0$. In this region, the integrand of $G_{5a}(t_k,t_l)$ has the approximate behavior

$$\lim_{\alpha,\phi\to 0}\left[\cos\phi\cos m\phi\frac{e^{-jk_oR}}{k_oR}\right] \approx \frac{1}{k_o}\left[\left(\alpha\frac{\Delta_k}{2}\right)^2+(\rho_k\phi)^2\right]^{-\frac{1}{2}} . \tag{2.122}$$

Similarly to Method 2, Method 3 calculates $G_{5a}(t_k, t_l)$ from Eqs. 2.78 and 2.81, then subtracts a n_α- and n_ϕ-point Gaussian quadratures (with respect to α and ϕ, respectively) of Eq. 2.122 in order to cancel any possible numerical error from Eqs. 2.78 and 2.81, and finally adds back the closed-form integrations of Eq. 2.122 with respect to α and ϕ. The final result is

$$\begin{aligned} G_{5a}(t_k, t_l) &= \frac{\pi}{2} \sum_{\beta=1}^{n_\phi} A_\beta \cos\phi_\beta \cos m\phi_\beta \sum_{\xi=1}^{n_\alpha} A_\xi \frac{e^{-jk_o R}}{k_o R} + I_{5a} \\ &- \frac{\pi}{2} \sum_{\beta=1}^{n_\phi} A_\beta \sum_{\xi=1}^{n_\alpha} \frac{A_\xi}{k_o} \left[\left(\alpha_\xi \frac{\Delta_k}{2} \right)^2 + (\rho_k \phi_\beta)^2 \right]^{-\frac{1}{2}} , \end{aligned} \tag{2.123}$$

where [16]

$$\begin{aligned} I_{5a} &= \int_{-1}^{1} \int_{0}^{\pi} \frac{1}{k_o} \left[\left(\alpha \frac{\Delta_k}{2} \right)^2 + (\rho_k \phi)^2 \right]^{-\frac{1}{2}} d\phi \; d\alpha \\ &= \frac{2}{k_o \rho_k} \left[\ln\left(v_2 + \sqrt{1 + v_2^2} \right) + v_2 \ln\left(\frac{1}{v_2} + \sqrt{1 + \frac{1}{v_2^2}} \right) \right], \end{aligned} \tag{2.124}$$

$$v_2 = \frac{2\pi \rho_k}{\Delta_k} , \tag{2.125}$$

and ϕ_β and R are respectively given by Eqs. 2.83 and 2.84. So, when Method 3 is applied, $G_{5a}(t_k, t_l)$ is calculated from Eq. 2.123 instead of Eqs. 2.78 and 2.81.

2.3.5 Voltage-Matrix Evaluation for a Spherical-Wave Source

From Eqs. 2.24 and 2.25, the elements of the voltage sub-matrices V_i^T and V_i^P depend on the incident electric field $\vec{E}^{inc}(\vec{r})$ produced by the external sources. They will determine which modes m are present in the formulation and what linear systems of Eq. 2.23 should be solved.

It is well known that the electromagnetic radiation of a horn feed can be accurately modeled as being produced by a spherical-wave source located at the feed phase center. So, in this section $\vec{E}^{inc}(\vec{r})$ is assumed to be excited by a spherical-wave point source located over the BOR axis of symmetry (z-axis) to account for the feed radiation. Expressions are derived for the Hertz dipole (an extremely useful Maxwellian source) as well as for the raised-cosine feed (RCF) model (capable of modeling the radiation characteristics of most the feeds used in antenna applications). However, the formulation to be presented in Chapter 3 will allow the inclusion of the actual feed structure into the antenna analysis, enabling the correct determination of the mutual coupling among the several antenna components.

Referring to Fig. 2.5, the $\vec{E}^{inc}(\vec{r})$ radiated by an $\hat{x}$-polarized spherical-wave source located on the z-axis at $z = z_S$ is generalized as

$$\begin{aligned} \vec{E}^{inc}(\vec{r}) &= \Big[F_r(r_F,\theta_F)\,\cos\phi_F\,\hat{r}_F + F_\theta(r_F,\theta_F)\,\cos\phi_F\,\hat{\theta}_F \\ &+ F_\phi(r_F,\theta_F)\,\sin\phi_F\,\hat{\phi}_F\Big]\,\frac{e^{-jk_o r_F}}{r_F}\,, \end{aligned} \tag{2.126}$$

where r_F, θ_F, and ϕ_F are the usual spherical coordinates corresponding to the feed coordinate system centered at $z = z_S$ and $F_r(r_F,\theta_F)$, $F_\theta(r_F,\theta_F)$, and $F_\phi(r_F,\theta_F)$ represent the radiation pattern of the spherical-wave source. For example, if the feed is represented by an $\hat{x}$-polarized RCF model radiating towards the positive z-direction [21]:

$$F_r(r_F,\theta_F) = 0\,, \tag{2.127}$$

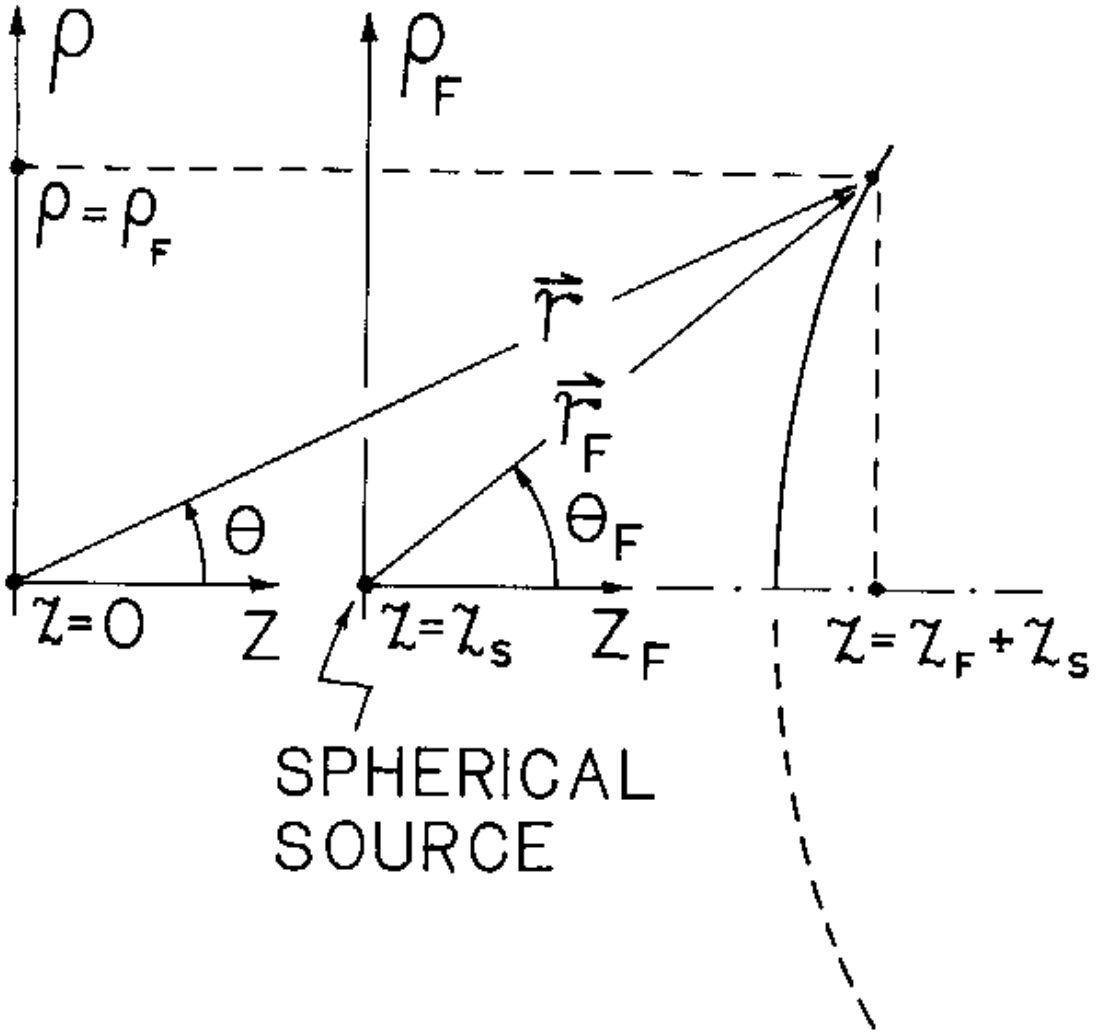

Figure 2.5: Geometry for the Spherical-Wave Source Excitation.

$$F_\theta(r_F,\theta_F) = \begin{cases} \cos^e\theta_F\,, & 0 \le \theta_F \le \frac{\pi}{2}\,, \\ 0\,, & \frac{\pi}{2} < \theta_F \le \pi\,, \end{cases} \tag{2.128}$$

$$F_\phi(r_F,\theta_F) = \begin{cases} -\cos^h\theta_F\,, & 0 \le \theta_F \le \frac{\pi}{2}\,, \\ 0\,, & \frac{\pi}{2} < \theta_F \le \pi\,, \end{cases} \tag{2.129}$$

where e and h control the RCF pattern at its E- and H-planes, respectively. Instead, if an $\hat{x}$-polarized Hertz dipole is used [21]:

$$F_r(r_F,\theta_F) = -j\eta_o \frac{(I\ell)}{\lambda} \frac{1+jk_or_F}{(k_or_F)^2} \sin\theta_F\,, \tag{2.130}$$

$$F_\theta(r_F,\theta_F) = j\eta_o \frac{(I\ell)}{2\lambda} \frac{[1+jk_or_F-(k_or_F)^2]}{(k_or_F)^2} \cos\theta_F\,, \tag{2.131}$$

$$F_\phi(r_F,\theta_F) = -j\eta_o \frac{(I\ell)}{2\lambda} \frac{[1+jk_or_F-(k_or_F)^2]}{(k_or_F)^2}\,, \tag{2.132}$$

where $(I\ell)$ is the dipole moment of the source.

To numerically evaluate the integrals of Eqs. 2.24 and 2.25, a procedure similar to the one adopted in Sect. 2.3.3 is used. From Fig. 2.5, one observes that

$$\hat{r}_F = \sin\theta_F\,\hat{\rho} + \cos\theta_F\,\hat{z}\,, \tag{2.133}$$

$$\hat{\theta}_F = \cos\theta_F\,\hat{\rho} - \sin\theta_F\,\hat{z}\,, \tag{2.134}$$

$$\hat{\phi}_F = \hat{\phi}\,, \tag{2.135}$$

where

$$\sin\theta_F = \frac{\rho}{r_F}\,, \tag{2.136}$$

$$\cos\theta_F = \frac{(z-z_S)}{r_F}\,, \tag{2.137}$$

$$r_F = \sqrt{\rho^2 + (z-z_S)^2}\,, \tag{2.138}$$

and ρ, ϕ, and z are the cylindrical coordinates of the principal coordinate system locating the observation point $\vec{r}$ over the BOR surface S. From Eqs. 2.1 and 2.133–2.135, one obtains the relations

$$\hat{t} \cdot \hat{r}_F = \sin u \sin\theta_F + \cos u \cos\theta_F , \tag{2.139}$$

$$\hat{t} \cdot \hat{\theta}_F = \sin u \cos\theta_F - \cos u \sin\theta_F , \tag{2.140}$$

$$\hat{t} \cdot \hat{\phi}_F = \hat{\phi} \cdot \hat{r}_F = \hat{\phi} \cdot \hat{\theta}_F = 0 , \tag{2.141}$$

$$\hat{\phi} \cdot \hat{\phi}_F = 1 , \tag{2.142}$$

which are substituted into Eqs. 2.24 and 2.25 (together with Eqs. 2.30 and 2.126) to yield

$$\begin{aligned} V_i^T &= \frac{1}{\eta_o} \int_t T_i(t)\ F_i^T(t) \int_0^{2\pi} \cos\phi\ e^{-jm\phi}\ d\phi\ dt \\ &= \begin{cases} \frac{\pi}{\eta_o} \int_t T_i(t)\ F_i^T(t)\ dt , & m = \pm 1 , \\ 0 , & m \neq \pm 1 , \end{cases} \end{aligned} \tag{2.143}$$

$$\begin{aligned} V_i^P &= \frac{1}{\eta_o} \int_t P_i(t)\ \frac{\rho}{\rho_i}\ F_i^P(t) \int_0^{2\pi} \sin\phi\ e^{-jm\phi}\ d\phi\ dt \\ &= \begin{cases} \frac{-jm\pi}{\eta_o} \int_t P_i(t)\ \frac{\rho}{\rho_i}\ F_i^P(t)\ dt , & m = \pm 1 , \\ 0 , & m \neq \pm 1 , \end{cases} \end{aligned} \tag{2.144}$$

where

$$\begin{aligned} F_i^T(t) &= [F_r(r_F, \theta_F)\ (\sin u \sin\theta_F + \cos u \cos\theta_F) \\ &+ F_\theta(r_F, \theta_F)\ (\sin u \cos\theta_F - \cos u \sin\theta_F)]\ \frac{e^{-jk_o r_F}}{r_F} , \end{aligned} \tag{2.145}$$

$$F_i^P(t) = F_\phi(r_F, \theta_F)\ \frac{e^{-jk_o r_F}}{r_F} , \tag{2.146}$$

and the limits of integration depend on the weighting functions $T_i(t)$ and $P_i(t)$. It is important to observe from Eqs. 2.143 and 2.144 that only the modes $m = \pm 1$ are excited when $\vec{E}^{inc}(\vec{r})$ is given by Eq. 2.126. Applying Eqs. 2.50–2.57 [for the weighting functions $T_i(t)$ and $P_i(t)$] and the procedure used in Sect. 2.3.3, Eqs. 2.143 and 2.144 are finally rewritten as

$$V_i^T = \frac{\pi}{4\eta_o} \sum_{k=p-1}^{p} \Delta_k \left[\left(F_k^T\right)_a - (-1)^{p-k} \left(F_k^T\right)_b \right], \quad m = \pm 1, \tag{2.147}$$

$$V_i^P = \frac{-jm\pi}{2\eta_o} \Delta_i \left[\left(F_i^P\right)_a + \frac{\Delta_i \sin u_i}{2\,\rho_i} \left(F_i^P\right)_b \right], \quad m = \pm 1, \tag{2.148}$$

where

$$\left(F_k^T\right)_a = \int_{-1}^{1} F_i^T(t_k)\, d\alpha, \quad k = p-1, p, \tag{2.149}$$

$$\left(F_k^T\right)_b = \int_{-1}^{1} F_i^T(t_k)\, \alpha\, d\alpha, \quad k = p-1, p, \tag{2.150}$$

$$\left(F_i^P\right)_a = \int_{-1}^{1} F_i^P(t_i)\, d\alpha, \tag{2.151}$$

$$\left(F_i^P\right)_b = \int_{-1}^{1} F_i^P(t_i)\, \alpha\, d\alpha, \tag{2.152}$$

$F_i^T(t_k)$ is given by Eq. 2.145 with $u = u_k$, $F_i^P(t_i)$ is given by Eq. 2.146, r_F and θ_F are given by Eqs. 2.136–2.138, and ρ and z are given by

$$\rho = \rho_k + \alpha \frac{\Delta_k}{2} \sin u_k, \tag{2.153}$$

$$z = z_k + \alpha \frac{\Delta_k}{2} \cos u_k, \tag{2.154}$$

where the subscript k represents the observation segments $p-1$, p, and i, as explained in Sect. 2.3.3.

Similarly to the procedure of Sect. 2.3.4, the integrals with respect to α in Eqs. 2.149–2.152 are numerically evaluated applying a n_α-point Gaussian quadrature (in this work $n_\alpha = 2$):

$$\left(F_k^T\right)_a = \sum_{\xi=1}^{n_\alpha} A_\xi \, F_i^T(t_k) \, , \qquad k = p-1, p \, , \tag{2.155}$$

$$\left(F_k^T\right)_b = \sum_{\xi=1}^{n_\alpha} A_\xi \, \alpha_\xi \, F_i^T(t_k) \, , \qquad k = p-1, p \, , \tag{2.156}$$

$$\left(F_i^P\right)_a = \sum_{\xi=1}^{n_\alpha} A_\xi \; F_i^P(t_i) \, , \tag{2.157}$$

$$\left(F_i^P\right)_b = \sum_{\xi=1}^{n_\alpha} A_\xi \, \alpha_\xi \, F_i^P(t_i) \, , \tag{2.158}$$

where $F_i^T(t_k)$ and $F_i^P(t_i)$ are evaluated at $\alpha = \alpha_\xi$. As far as the spherical-wave source is not very close to the BOR surfaces, no singularity problems will occur. Finally, from Eqs. 2.147–2.152 one observes that

$$\left(V_i^T\right)_{m=1} = \left(V_i^T\right)_{m=-1} , \tag{2.159}$$

$$\left(V_i^P\right)_{m=1} = - \left(V_i^P\right)_{m=-1} , \tag{2.160}$$

in which case, from Eqs. 2.21, 2.23, and 2.70–2.73, the following relations apply to the current coefficients:

$$I_{1j}^T = I_{-1j}^T \, , \tag{2.161}$$

$$I_{1j}^P = - \, I_{-1j}^P \, . \tag{2.162}$$

So, for a $\vec{E}^{inc}(\vec{r})$ given by Eq. 2.126, only the coefficients corresponding to the mode $m = 1$ need to be calculated from the linear system of Eq. 2.23, while the

coefficients corresponding to $m = -1$ are readily obtained from Eqs. 2.161 and 2.162.

2.4 Radiated Near-Zone Fields

Once the coefficients of Eq. 2.21 are determined, the total electric and magnetic near-zone fields radiated by the PEC BOR are obtained from

$$\vec{E}_{NF}(\vec{r}) = \vec{E}^{J}_{NF}(\vec{r}) + \vec{E}^{inc}_{NF}(\vec{r}) , \tag{2.163}$$

$$\vec{H}_{NF}(\vec{r}) = \vec{H}^{J}_{NF}(\vec{r}) + \vec{H}^{inc}_{NF}(\vec{r}) , \tag{2.164}$$

where $\vec{E}^{inc}_{NF}(\vec{r})$ and $\vec{H}^{inc}_{NF}(\vec{r})$ are the electric and magnetic fields produced by the external sources, respectively, and $\vec{E}^{J}_{NF}(\vec{r})$ and $\vec{H}^{J}_{NF}(\vec{r})$ are the electric and magnetic fields radiated by the electric current $\vec{J}(\vec{r}\,')$, respectively. The later are given by, from Eqs. 120 and 121 in Chap. 3 of Ref. [21],

$$\vec{E}^{J}_{NF}(\vec{r}) = \frac{-j}{4\pi\omega\epsilon_o} \int_{S'} \left\{ \left[\vec{J}(\vec{r}\,') \cdot \nabla' \right] \nabla'\Psi + k_o^2 \, \vec{J}(\vec{r}\,') \, \Psi \right\} ds' , \tag{2.165}$$

$$\vec{H}^{J}_{NF}(\vec{r}) = \frac{1}{4\pi} \int_{S'} \vec{J}(\vec{r}\,') \times \nabla'\Psi \, ds' , \tag{2.166}$$

where Ψ is given by Eq. 2.4,

$$\begin{aligned} \left[\vec{J}(\vec{r}\,') \cdot \nabla' \right] \nabla'\Psi &= \left\{ \left(\frac{-k_o^2}{R^2} + \frac{j3k_o}{R^3} + \frac{3}{R^4} \right) \left[\vec{J}(\vec{r}\,') \cdot \vec{R} \right] \vec{R} \right. \\ &\quad \left. - \left(jk_o + \frac{1}{R} \right) \frac{\vec{J}(\vec{r}\,')}{R} \right\} \frac{e^{-jk_oR}}{R} , \end{aligned} \tag{2.167}$$

$$\vec{J}(\vec{r}\,') \times \nabla'\Psi = \vec{J}(\vec{r}\,') \times \vec{R} \left(\frac{jk_o}{R} + \frac{1}{R^2} \right) \frac{e^{-jk_oR}}{R} , \tag{2.168}$$

and $\vec{R} = \vec{r} - \vec{r}'$. Applying the relations

$$\vec{J}(\vec{r}') = J_t(\vec{r}')\,\hat{t}' + J_\phi(\vec{r}')\,\hat{\phi}' , \tag{2.169}$$

$$\vec{R} = \rho\,\hat{\rho} - \rho'\,\hat{\rho}' + (z - z')\,\hat{z} , \tag{2.170}$$

$$\hat{t}' = \sin u'\,\hat{\rho}' + \cos u'\,\hat{z} , \tag{2.171}$$

$$\hat{\rho}' = \cos(\phi' - \phi)\,\hat{\rho} + \sin(\phi' - \phi)\,\hat{\phi} , \tag{2.172}$$

$$\hat{\phi}' = -\sin(\phi' - \phi)\,\hat{\rho} + \cos(\phi' - \phi)\,\hat{\phi} , \tag{2.173}$$

into Eqs. 2.165–2.168 one obtains that

$$\vec{E}^J_{NF}(\vec{r}) = E^J_{NF\rho}\,\hat{\rho} + E^J_{NF\phi}\,\hat{\phi} + E^J_{NFz}\,\hat{z} , \tag{2.174}$$

$$\vec{H}^J_{NF}(\vec{r}) = H^J_{NF\rho}\,\hat{\rho} + H^J_{NF\phi}\,\hat{\phi} + H^J_{NFz}\,\hat{z} , \tag{2.175}$$

where

$$\begin{aligned} E^J_{NF\rho} &= \frac{-j\eta_o k_o^2}{4\pi} \int_{S'} \Big\{ J_t(\vec{r}') \Big[\sin u' \cos(\phi' - \phi)\,(G_E - G_H) + k_o^2 \left[\rho - \rho' \cos(\phi' - \phi)\right] \\ &\times \Big[\sin u' \Big(\rho\,\cos(\phi' - \phi) - \rho' \Big) - \cos u'\,(z' - z) \Big]\, G_{EH} \Big] - J_\phi(\vec{r}') \Big[\sin(\phi' - \phi) \\ &\times (G_E - G_H) + k_o^2 \rho \sin(\phi' - \phi)\,\left[\rho - \rho' \cos(\phi' - \phi)\right]\, G_{EH} \Big] \Big\}\, ds' , \end{aligned} \tag{2.176}$$

$$\begin{aligned} E^J_{NF\phi} &= \frac{-j\eta_o k_o^2}{4\pi} \int_{S'} \Big\{ J_t(\vec{r}') \Big[\sin u' \sin(\phi' - \phi)\,(G_E - G_H) - k_o^2 \rho' \sin(\phi' - \phi) \\ &\times \Big[\sin u' \Big(\rho\,\cos(\phi' - \phi) - \rho' \Big) - \cos u'\,(z' - z) \Big]\, G_{EH} \Big] + J_\phi(\vec{r}') \Big[\cos(\phi' - \phi) \\ &\times (G_E - G_H) + k_o^2 \rho\,\rho' \sin^2(\phi' - \phi)\, G_{EH} \Big] \Big\}\, ds' , \end{aligned} \tag{2.177}$$

$$E^J_{NFz} = \frac{-j\eta_o k_o^2}{4\pi} \int_{S'} \Big\{ J_t(\vec{r}\,') \Big[\cos u' \; (G_E - G_H) - k_o^2 (z' - z) \times \Big[\sin u' \Big(\rho \cos(\phi' - \phi) - \rho' \Big) - \cos u' \; (z' - z) \Big] G_{EH} \Big] + J_\phi(\vec{r}\,') \; k_o^2 \rho \, (z' - z) \, \sin(\phi' - \phi) \, G_{EH} \Big\} \, ds' \; , \tag{2.178}$$

$$H^J_{NF\rho} = \frac{k_o^3}{4\pi} \int_{S'} \Big\{ J_t(\vec{r}\,') \; [\rho' \cos u' - (z' - z) \, \sin u'] \, \sin(\phi' - \phi) - J_\phi(\vec{r}\,') \; (z' - z) \, \cos(\phi' - \phi) \Big\} \, G_H \, ds' \; , \tag{2.179}$$

$$H^J_{NF\phi} = \frac{-k_o^3}{4\pi} \int_{S'} \Big\{ J_t(\vec{r}\,') \; \Big[[\rho' \cos u' - (z' - z) \, \sin u'] \cos(\phi' - \phi) - \rho \cos u' \Big] + J_\phi(\vec{r}\,') \; (z' - z) \, \sin(\phi' - \phi) \Big\} \, G_H \, ds' \; , \tag{2.180}$$

$$H^J_{NFz} = \frac{-k_o^3}{4\pi} \int_{S'} \Big\{ J_t(\vec{r}\,') \; \rho \, \sin u' \, \sin(\phi' - \phi) + J_\phi(\vec{r}\,') \; [\rho \cos(\phi' - \phi) - \rho'] \Big\} \, G_H \, ds' \; , \tag{2.181}$$

and

$$G_E = \frac{e^{-jk_o R}}{k_o R} \; , \tag{2.182}$$

$$G_H = \left[\frac{1 + jk_o R}{(k_o R)^2} \right] \frac{e^{-jk_o R}}{k_o R} \; , \tag{2.183}$$

$$G_{EH} = \left[\frac{3 + j3k_o R - (k_o R)^2}{(k_o R)^4} \right] \frac{e^{-jk_o R}}{k_o R} = \frac{3 \, G_H - G_E}{(k_o R)^2} \; . \tag{2.184}$$

Substituting Eq. 2.21 into Eqs. 2.174–2.181 (with the modal parameter n in Eq. 2.21 conveniently changed into m) and solving the two-dimension integrals using the procedure adopted in Sects. 2.3.3 and 2.3.4, after straightforward algebraic

manipulations one obtains that

$$\vec{E}^J_{NF}(\vec{r}) = \sum_{m=-\infty}^{\infty} \left\{ \sum_{j=1}^{N_T} I^T_{mj} \left[\left(E^J_{NF\rho}\right)^T_{mj} \hat{\rho} + \left(E^J_{NF\phi}\right)^T_{mj} \hat{\phi} + \left(E^J_{NFz}\right)^T_{mj} \hat{z} \right] + \sum_{j=1}^{N_P} I^P_{mj} \left[\left(E^J_{NF\rho}\right)^P_{mj} \hat{\rho} + \left(E^J_{NF\phi}\right)^P_{mj} \hat{\phi} + \left(E^J_{NFz}\right)^P_{mj} \hat{z} \right] \right\}, \quad (2.185)$$

$$\vec{H}^J_{NF}(\vec{r}) = \sum_{m=-\infty}^{\infty} \left\{ \sum_{j=1}^{N_T} I^T_{mj} \left[\left(H^J_{NF\rho}\right)^T_{mj} \hat{\rho} + \left(H^J_{NF\phi}\right)^T_{mj} \hat{\phi} + \left(H^J_{NFz}\right)^T_{mj} \hat{z} \right] + \sum_{j=1}^{N_P} I^P_{mj} \left[\left(H^J_{NF\rho}\right)^P_{mj} \hat{\rho} + \left(H^J_{NF\phi}\right)^P_{mj} \hat{\phi} + \left(H^J_{NFz}\right)^P_{mj} \hat{z} \right] \right\}, \quad (2.186)$$

where

$$\begin{aligned}
\left(E^J_{NF\rho}\right)^T_{mj} = \frac{-j\eta_o k_o^2}{8\pi} e^{jm\phi} \sum_{l=q-1}^{q} \Delta_l \Big\{ & \sin u_l \left[G_{5a}(\vec{r}, t_l) - G_{2a}(\vec{r}, t_l) \right. \\
& \left. - (-1)^{q-l} \left[G_{5b}(\vec{r}, t_l) - G_{2b}(\vec{r}, t_l) \right] \right] + k_o^2 \Big[(\rho_l - \rho) \Big((\rho_l - \rho) \sin u_l \\
& + (z_l - z) \cos u_l \Big) + \frac{\rho \rho_l}{2} \sin u_l \Big] \left[G_{8a}(\vec{r}, t_l) - (-1)^{q-l} G_{8b}(\vec{r}, t_l) \right] \\
& + k_o^2 \frac{\Delta_l}{2} \left[\rho_l - \rho + \sin u_l \left(\left(\rho_l - \frac{\rho}{2} \right) \sin u_l + (z_l - z) \cos u_l \right) \right] \left[G_{8b}(\vec{r}, t_l) \right. \\
& \left. - (-1)^{q-l} G_{8c}(\vec{r}, t_l) \right] + \left(k_o \frac{\Delta_l}{2} \right)^2 \sin u_l \left[G_{8c}(\vec{r}, t_l) - (-1)^{q-l} G_{8d}(\vec{r}, t_l) \right] \\
& - k_o^2 \frac{\rho \rho_l}{2} \sin u_l \Big[G_{10a}(\vec{r}, t_l) - (-1)^{q-l} G_{10b}(\vec{r}, t_l) \\
& + \frac{\Delta_l \sin u_l}{2 \rho_l} \left[G_{10b}(\vec{r}, t_l) - (-1)^{q-l} G_{10c}(\vec{r}, t_l) \right] \Big] \\
& - k_o^2 \rho \left[\frac{3\rho_l}{2} \sin u_l + (z_l - z) \cos u_l \right] \left[G_{12a}(\vec{r}, t_l) - (-1)^{q-l} G_{12b}(\vec{r}, t_l) \right] \\
& - k_o^2 \frac{\rho \Delta_l}{2} \left(1 + \frac{\sin^2 u_l}{2} \right) \left[G_{12b}(\vec{r}, t_l) - (-1)^{q-l} G_{12c}(\vec{r}, t_l) \right] \Big\}, \quad (2.187)
\end{aligned}$$

$$\left(E^J_{NF\phi}\right)^T_{mj} = \frac{\eta_o k_o^2}{8\pi}\, e^{jm\phi} \sum_{l=q-1}^{q} \Delta_l \left\{ \sin u_l \left[G_{6a}(\vec{r},t_l) - G_{3a}(\vec{r},t_l) \right.\right.$$
$$\left. - (-1)^{q-l} \left[G_{6b}(\vec{r},t_l) - G_{3b}(\vec{r},t_l) \right] \right] + k_o^2\, \rho_l \left[\rho_l \sin u_l + (z_l - z) \cos u_l \right]$$
$$\times \left[G_{9a}(\vec{r},t_l) - (-1)^{q-l} G_{9b}(\vec{r},t_l) \right] + k_o^2 \frac{\Delta_l}{2} \left[\rho_l \left(1 + \sin^2 u_l \right) \right.$$
$$\left. + (z_l - z) \cos u_l \sin u_l \right] \left[G_{9b}(\vec{r},t_l) - (-1)^{q-l} G_{9c}(\vec{r},t_l) \right]$$
$$+ \left(k_o \frac{\Delta_l}{2} \right)^2 \sin u_l \left[G_{9c}(\vec{r},t_l) - (-1)^{q-l} G_{9d}(\vec{r},t_l) \right]$$
$$- k_o^2 \frac{\rho \rho_l}{2} \sin u_l \left[G_{11a}(\vec{r},t_l) - (-1)^{q-l} G_{11b}(\vec{r},t_l) \right.$$
$$\left. \left. + \frac{\Delta_l \sin u_l}{2\,\rho_l} \left[G_{11b}(\vec{r},t_l) - (-1)^{q-l} G_{11c}(\vec{r},t_l) \right] \right] \right\}, \tag{2.188}$$

$$\left(E^J_{NFz}\right)^T_{mj} = \frac{-j\eta_o k_o^2}{8\pi}\, e^{jm\phi} \sum_{l=q-1}^{q} \Delta_l \left\{ \cos u_l \left[G_{7a}(\vec{r},t_l) - G_{1a}(\vec{r},t_l) - G_{2a}(\vec{r},t_l) \right.\right.$$
$$\left. - (-1)^{q-l} \left[G_{7b}(\vec{r},t_l) - G_{1b}(\vec{r},t_l) - G_{2b}(\vec{r},t_l) \right] \right] + k_o^2 \left(z_l - z \right)$$
$$\times \left[\rho_l \sin u_l + (z_l - z) \cos u_l \right] \left[G_{12a}(\vec{r},t_l) - (-1)^{q-l} G_{12b}(\vec{r},t_l) \right]$$
$$+ k_o^2 \frac{\Delta_l}{2} \left[z_l - z + \cos u_l \left(\rho_l \sin u_l + (z_l - z) \cos u_l \right) \right] \left[G_{12b}(\vec{r},t_l) \right.$$
$$\left. - (-1)^{q-l} G_{12c}(\vec{r},t_l) \right] + \left(k_o \frac{\Delta_l}{2} \right)^2 \cos u_l \left[G_{12c}(\vec{r},t_l) - (-1)^{q-l} G_{12d}(\vec{r},t_l) \right]$$
$$+ k_o^2 \left(z_l - z \right) \left[(\rho_l - \rho) \sin u_l + (z_l - z) \cos u_l \right] \left[G_{8a}(\vec{r},t_l) \right.$$
$$\left. - (-1)^{q-l} G_{8b}(\vec{r},t_l) \right] + k_o^2 \frac{\Delta_l}{2} \left[z_l - z + \cos u_l \left((\rho_l - \rho) \sin u_l \right.\right.$$
$$\left. \left. + (z_l - z) \cos u_l \right) \right] \left[G_{8b}(\vec{r},t_l) - (-1)^{q-l} G_{8c}(\vec{r},t_l) \right]$$
$$\left. + \left(k_o \frac{\Delta_l}{2} \right)^2 \cos u_l \left[G_{8c}(\vec{r},t_l) - (-1)^{q-l} G_{8d}(\vec{r},t_l) \right] \right\}, \tag{2.189}$$

$$\left(E^J_{NF\rho}\right)^P_{mj} = \frac{\eta_o k_o^2}{4\pi}\, e^{jm\phi}\, \Delta_j \left\{ G_{3a}(\vec{r},t_j) - G_{6a}(\vec{r},t_j) + \frac{\Delta_j \sin u_j}{2\,\rho_j}\, [G_{3b}(\vec{r},t_j) \right.$$
$$- G_{6b}(\vec{r},t_j)] - (k_o\rho)^2 \left[G_{9a}(\vec{r},t_j) + \frac{\Delta_j \sin u_j}{2\,\rho_j}\, G_{9b}(\vec{r},t_j) \right]$$
$$+ k_o^2\, \frac{\rho\rho_j}{2} \left[G_{11a}(\vec{r},t_j) + 2\, \frac{\Delta_j \sin u_j}{2\,\rho_j}\, G_{11b}(\vec{r},t_j) \right.$$
$$\left. \left. + \left(\frac{\Delta_j \sin u_j}{2\,\rho_j} \right)^2 G_{11c}(\vec{r},t_j) \right] \right\}, \tag{2.190}$$

$$\left(E^J_{NF\phi}\right)^P_{mj} = \frac{-j\eta_o k_o^2}{4\pi}\, e^{jm\phi}\, \Delta_j \left\{ G_{5a}(\vec{r},t_j) - G_{2a}(\vec{r},t_j) + \frac{\Delta_j \sin u_j}{2\,\rho_j}\, [G_{5b}(\vec{r},t_j) \right.$$
$$- G_{2b}(\vec{r},t_j)] + k_o^2\, \frac{\rho\rho_j}{2} \left[G_{8a}(\vec{r},t_j) + G_{12a}(\vec{r},t_j) - G_{10a}(\vec{r},t_j) \right.$$
$$+ 2\, \frac{\Delta_j \sin u_j}{2\,\rho_j} \left(G_{8b}(\vec{r},t_j) + G_{12b}(\vec{r},t_j) - G_{10b}(\vec{r},t_j) \right)$$
$$\left. \left. + \left(\frac{\Delta_j \sin u_j}{2\,\rho_j} \right)^2 \left(G_{8c}(\vec{r},t_j) + G_{12c}(\vec{r},t_j) - G_{10c}(\vec{r},t_j) \right) \right] \right\}, \tag{2.191}$$

$$\left(E^J_{NFz}\right)^P_{mj} = \frac{\eta_o k_o^2}{4\pi}\, e^{jm\phi}\, \Delta_j\, k_o^2\, \rho \left\{ (z_j - z) \left[G_{9a}(\vec{r},t_j) + \frac{\Delta_j \sin u_j}{2\,\rho_j}\, G_{9b}(\vec{r},t_j) \right] \right.$$
$$\left. + \frac{\Delta_j}{2} \cos u_j \left[G_{9b}(\vec{r},t_j) + \frac{\Delta_j \sin u_j}{2\,\rho_j}\, G_{9c}(\vec{r},t_j) \right] \right\}, \tag{2.192}$$

$$\left(H^J_{NF\rho}\right)^T_{mj} = \frac{j k_o^3}{8\pi}\, e^{jm\phi} \sum_{l=q-1}^{q} \Delta_l\, [\rho_l \cos u_l - (z_l - z) \sin u_l]$$
$$\times \left[G_{3a}(\vec{r},t_l) - (-1)^{q-l} G_{3b}(\vec{r},t_l) \right], \tag{2.193}$$

$$\left(H^J_{NF\phi}\right)^T_{mj} = \frac{k_o^3}{8\pi}\, e^{jm\phi} \sum_{l=q-1}^{q} \Delta_l \left\{ \rho \cos u_l \left[G_{1a}(\vec{r},t_l) - (-1)^{q-l} G_{1b}(\vec{r},t_l) \right] - [(\rho_l - \rho) \right.$$
$$\left. \times \cos u_l - (z_l - z) \sin u_l] \left[G_{2a}(\vec{r},t_l) - (-1)^{q-l} G_{2b}(\vec{r},t_l) \right] \right\}, \tag{2.194}$$

$$\left(H^J_{NFz}\right)^T_{mj} = \frac{-j k_o^3}{8\pi}\, e^{jm\phi}\, \rho \sum_{l=q-1}^{q} \Delta_l \sin u_l \left[G_{3a}(\vec{r},t_l) - (-1)^{q-l} G_{3b}(\vec{r},t_l) \right], \tag{2.195}$$

$$\left(H^J_{NF\rho}\right)^P_{mj} = \frac{-k_o^3}{4\pi}\, e^{jm\phi}\, \Delta_j \left\{ (z_j - z) \left[G_{2a}(\vec{r},t_j) + \frac{\Delta_j \sin u_j}{2\,\rho_j}\, G_{2b}(\vec{r},t_j) \right] \right.$$
$$\left. + \frac{\Delta_j}{2} \cos u_j \left[G_{2b}(\vec{r},t_j) + \frac{\Delta_j \sin u_j}{2\,\rho_j}\, G_{2c}(\vec{r},t_j) \right] \right\}, \tag{2.196}$$

$$\left(H^J_{NF\phi}\right)^P_{mj} = \frac{-jk_o^3}{4\pi}\, e^{jm\phi}\, \Delta_j \left\{ (z_j - z) \left[G_{3a}(\vec{r}, t_j) + \frac{\Delta_j \sin u_j}{2\,\rho_j}\, G_{3b}(\vec{r}, t_j) \right] \right.$$
$$\left. + \frac{\Delta_j}{2} \cos u_j \left[G_{3b}(\vec{r}, t_j) + \frac{\Delta_j \sin u_j}{2\,\rho_j}\, G_{3c}(\vec{r}, t_j) \right] \right\}, \tag{2.197}$$

$$\left(H^J_{NFz}\right)^P_{mj} = \frac{k_o^3}{4\pi}\, e^{jm\phi}\, \Delta_j\, \rho_j \left\{ G_{1a}(\vec{r}, t_j) + G_{2a}(\vec{r}, t_j) + 2\,\frac{\Delta_j \sin u_j}{2\,\rho_j} \right.$$
$$\times \left[G_{1b}(\vec{r}, t_j) + G_{2b}(\vec{r}, t_j) \right] + \left(\frac{\Delta_j \sin u_j}{2\,\rho_j} \right)^2 \left[G_{1c}(\vec{r}, t_j) + G_{2c}(\vec{r}, t_j) \right]$$
$$\left. - \frac{\rho}{\rho_j} \left[G_{2a}(\vec{r}, t_j) + \frac{\Delta_j \sin u_j}{2\,\rho_j}\, G_{2b}(\vec{r}, t_j) \right] \right\}, \tag{2.198}$$

the two-dimension integrals are given by

$$G_{va}(\vec{r}, t_l) = \int_{-1}^{1} G_v(\vec{r}, t_l)\, d\alpha\,, \qquad v = 1, ..., 12\,, \tag{2.199}$$

$$G_{vb}(\vec{r}, t_l) = \int_{-1}^{1} G_v(\vec{r}, t_l)\, \alpha\, d\alpha\,, \quad v = 1, ..., 12\,, \tag{2.200}$$

$$G_{vc}(\vec{r}, t_l) = \int_{-1}^{1} G_v(\vec{r}, t_l)\, \alpha^2\, d\alpha\,, \quad v = 1, 2, 3, 8, ..., 12\,, \tag{2.201}$$

$$G_{vd}(\vec{r}, t_l) = \int_{-1}^{1} G_v(\vec{r}, t_l)\, \alpha^3\, d\alpha\,, \quad v = 8, 9, 12\,, \tag{2.202}$$

$$G_1(\vec{r}, t_l) = 2 \int_0^{\pi} \sin^2 \frac{\pi}{2}\, \cos m\phi\, G_H\, d\phi\,, \tag{2.203}$$

$$G_2(\vec{r}, t_l) = \int_0^{\pi} \cos\phi\, \cos m\phi\, G_H\, d\phi\,, \tag{2.204}$$

$$G_3(\vec{r}, t_l) = \int_0^{\pi} \sin\phi\, \sin m\phi\, G_H\, d\phi\,, \tag{2.205}$$

$$G_4(\vec{r}, t_l) = 2 \int_0^{\pi} \sin^2 \frac{\pi}{2}\, \cos m\phi\, G_E\, d\phi\,, \tag{2.206}$$

$$G_5(\vec{r}, t_l) = \int_0^{\pi} \cos\phi\, \cos m\phi\, G_E\, d\phi\,, \tag{2.207}$$

$$G_6(\vec{r},t_l) = \int_0^{\pi} \sin\phi \, \sin m\phi \, G_E \, d\phi \, , \tag{2.208}$$

$$G_7(\vec{r},t_l) = G_4(\vec{r},t_l) + G_5(\vec{r},t_l) \, , \tag{2.209}$$

$$G_8(\vec{r},t_l) = \int_0^{\pi} \cos\phi \, \cos m\phi \, G_{EH} \, d\phi \, , \tag{2.210}$$

$$G_9(\vec{r},t_l) = \int_0^{\pi} \sin\phi \, \sin m\phi \, G_{EH} \, d\phi \, , \tag{2.211}$$

$$G_{10}(\vec{r},t_l) = \int_0^{\pi} \cos 2\phi \, \cos m\phi \, G_{EH} \, d\phi \, , \tag{2.212}$$

$$G_{11}(\vec{r},t_l) = \int_0^{\pi} \sin 2\phi \, \sin m\phi \, G_{EH} \, d\phi \, , \tag{2.213}$$

$$G_{12}(\vec{r},t_l) = 2 \int_0^{\pi} \sin^2 \frac{\pi}{2} \, \cos m\phi \, G_{EH} \, d\phi \, , \tag{2.214}$$

G_E, G_H, and G_{EH} are given by Eqs. 2.182–2.184, respectively, with

$$R = \left[\left(\rho - \rho_l - \alpha \frac{\Delta_l}{2} \sin u_l \right)^2 + \left(z - z_l - \alpha \frac{\Delta_l}{2} \cos u_l \right)^2 + 4\,\rho \left(\rho_l + \alpha \frac{\Delta_l}{2} \sin u_l \right) \sin^2 \frac{\phi}{2} \right]^{\frac{1}{2}} \, , \tag{2.215}$$

where ρ and z are the cylindrical coordinates of the observation point $\vec{r}$, and the subscript l represents the source segments $q-1$, q, and j (accordingly to the notation of Sect. 2.3.2).

The integrals with respect to α and ϕ in Eqs. 2.199–2.214 may be numerically evaluated using n_α- and n_ϕ-point Gaussian quadratures, respectively, as discussed in Sect. 2.3.4. If the observation point $\vec{r}$ is not close to the source currents, no singularity problems will occur during the numerical evaluation of these integrals.

From Eqs. 2.187–2.214, one obtains the following relations:

$$\left(E^J_{NF\rho}\right)^T_{mj}\ e^{-jm\phi} = \left(E^J_{NF\rho}\right)^T_{-mj}\ e^{jm\phi}\,, \tag{2.216}$$

$$\left(E^J_{NF\phi}\right)^T_{mj}\ e^{-jm\phi} = -\left(E^J_{NF\phi}\right)^T_{-mj}\ e^{jm\phi}\,, \tag{2.217}$$

$$\left(E^J_{NFz}\right)^T_{mj}\ e^{-jm\phi} = \left(E^J_{NFz}\right)^T_{-mj}\ e^{jm\phi}\,, \tag{2.218}$$

$$\left(E^J_{NF\rho}\right)^P_{mj}\ e^{-jm\phi} = -\left(E^J_{NF\rho}\right)^P_{-mj}\ e^{jm\phi}\,, \tag{2.219}$$

$$\left(E^J_{NF\phi}\right)^P_{mj}\ e^{-jm\phi} = \left(E^J_{NF\phi}\right)^P_{-mj}\ e^{jm\phi}\,, \tag{2.220}$$

$$\left(E^J_{NFz}\right)^P_{mj}\ e^{-jm\phi} = -\left(E^J_{NFz}\right)^P_{-mj}\ e^{jm\phi}\,, \tag{2.221}$$

$$\left(H^J_{NF\rho}\right)^T_{mj}\ e^{-jm\phi} = -\left(H^J_{NF\rho}\right)^T_{-mj}\ e^{jm\phi}\,, \tag{2.222}$$

$$\left(H^J_{NF\phi}\right)^T_{mj}\ e^{-jm\phi} = \left(H^J_{NF\phi}\right)^T_{-mj}\ e^{jm\phi}\,, \tag{2.223}$$

$$\left(H^J_{NFz}\right)^T_{mj}\ e^{-jm\phi} = -\left(H^J_{NFz}\right)^T_{-mj}\ e^{jm\phi}\,, \tag{2.224}$$

$$\left(H^J_{NF\rho}\right)^P_{mj}\ e^{-jm\phi} = \left(H^J_{NF\rho}\right)^P_{-mj}\ e^{jm\phi}\,, \tag{2.225}$$

$$\left(H^J_{NF\phi}\right)^P_{mj}\ e^{-jm\phi} = -\left(H^J_{NF\phi}\right)^P_{-mj}\ e^{jm\phi}\,, \tag{2.226}$$

$$\left(H^J_{NFz}\right)^P_{mj}\ e^{-jm\phi} = \left(H^J_{NFz}\right)^P_{-mj}\ e^{jm\phi}\,, \tag{2.227}$$

which allow the results of a positive mode m to be used to obtain the terms corresponding to a negative mode $-m$. Notice that, for $\vec{E}^{inc}(\vec{r})$ given by Eq. 2.126, only the modes $m = \pm 1$ are present.

The electric near-zone field $\vec{E}^{inc}_{NF}(\vec{r})$ radiated by the external spherical-wave source is readily given by Eqs. 2.126–2.138 using the cylindrical coordinates ρ, ϕ, and z associated with $\vec{r}$ (where the field is being calculated). However, notice that

the RCF model given by Eqs.2.127–2.129 only satisfies Maxwell's equations when r_F and, consequently, $|\vec{r}|$ have infinite values. So, whenever this model is used, one should only expect reasonable results at an observation point $\vec{r}$ sufficiently away from the source location.

From Eqs. 2.126 and 2.130–2.132, the magnetic near-zone field produced by the $\hat{x}$-polarized Hertz dipole is given by

$$\begin{aligned} \vec{H}_{NF}^{inc}(\vec{r}) &= \frac{j}{\omega\mu_o}\,\nabla^F \times \vec{E}_{NF}^{inc}(\vec{r}) \;=\; -\,\frac{(I\ell)}{2\lambda}\left(\frac{1+jk_or_F}{k_or_F}\right) \\ &\times \left(\sin\phi_F\,\hat{\theta}_F \;+\; \cos\theta_F\,\cos\phi_F\,\hat{\phi}_F\right)\frac{e^{-jk_or_F}}{r_F} \end{aligned} \tag{2.228}$$

together with Eqs. 2.133–2.138, where ∇^F indicates that the operation is performed in the coordinate system of the spherical-wave source. For the RCF model, the TEM approximation

$$\vec{H}_{NF}^{inc}(\vec{r}) \;=\; -\,\frac{1}{\eta_o}\left[F_\phi(r_F,\theta_F)\,\sin\phi_F\,\hat{\theta}_F \;-\; F_\theta(r_F,\theta_F)\,\cos\phi_F\,\hat{\phi}_F\right]\frac{e^{-jk_or_F}}{r_F} \tag{2.229}$$

may be used together with Eqs. 2.127–2.129 and 2.133–2.138, recalling that the observation point $\vec{r}$ must be sufficiently away from the spherical-wave source location as the TEM approximation is only valid in the far zone.

2.5 Radiated Far-Zone Fields

In the same manner as the radiated near-zone field derived in Sect. 2.4, the electric and magnetic far-zone fields radiated by a PEC BOR are obtained from the electric

current $\vec{J}(\vec{r}\,')$ and the excitation sources:

$$\vec{E}_{FF}(\vec{r}) \;=\; \vec{E}^{J}_{FF}(\vec{r}) \;+\; \vec{E}^{inc}_{FF}(\vec{r})\;, \tag{2.230}$$

$$\vec{H}_{FF}(\vec{r}) \;=\; \frac{1}{\eta_o}\,\hat{r}\times\vec{E}_{FF}(\vec{r})\;, \tag{2.231}$$

where $\hat{r}$ is the unit vector pointing towards the far-zone observation direction, $\vec{E}^{inc}_{FF}(\vec{r})$ is the electric far-zone field radiated by the external sources, and $\vec{E}^{J}_{FF}(\vec{r})$ is the electric far-zone field radiated by $\vec{J}(\vec{r}\,')$ and obtained from Eq. 128 in Chap. 3 of Ref. [21] as

$$\vec{E}^{J}_{FF}(\vec{r}) \;=\; \frac{-j\omega\mu_o}{4\pi}\,\frac{e^{-jk_o r}}{r}\int\limits_{S'}\Big\{\vec{J}(\vec{r}\,') \;-\; \Big[\vec{J}(\vec{r}\,')\cdot\hat{r}\Big]\,\hat{r}\Big\}\;e^{jk_o\,\vec{r}\,'\cdot\hat{r}}\;\;ds'\,. \tag{2.232}$$

From Eqs. 2.171–2.173 one obtains the relations

$$\begin{aligned}\hat{t}' \;&=\; [\sin u'\,\sin\theta\,\cos(\phi'-\phi) \;+\; \cos u'\,\cos\theta]\;\hat{r} \;+\; [\sin u'\,\cos\theta\,\cos(\phi'-\phi)\\ &-\; \cos u'\,\sin\theta]\;\hat{\theta} \;+\; \sin u'\,\sin(\phi'-\phi)\;\hat{\phi}\;,\end{aligned} \tag{2.233}$$

$$\hat{\phi}' \;=\; -\,\sin(\phi'-\phi)\;\Big(\sin\theta\;\hat{r} \;+\; \cos\theta\;\hat{\theta}\Big) \;+\; \cos(\phi'-\phi)\;\hat{\phi}\;, \tag{2.234}$$

$$\vec{r}\,'\cdot\hat{r} \;=\; \rho'\,\sin\theta\,\cos(\phi'-\phi) \;+\; z'\,\cos\theta\;, \tag{2.235}$$

which, together with Eq. 2.169, allow Eq. 2.232 to be rewritten as

$$\vec{E}^{J}_{FF}(\vec{r}) \;=\; E^{J}_{FF\theta}\;\hat{\theta} \;+\; E^{J}_{FF\phi}\;\hat{\phi}\;, \tag{2.236}$$

where

$$E^J_{FF\theta} = \frac{-j\omega\mu_o}{4\pi}\frac{e^{-jk_or}}{r}\int\limits_{S'}\Big\{J_t(\vec{r}\,')\ [\sin u'\cos\theta\cos(\phi'-\phi)\ -\ \cos u'\sin\theta] - J_\phi(\vec{r}\,')\cos\theta\sin(\phi'-\phi)\Big\}\ e^{jk_o[\rho'\sin\theta\cos(\phi'-\phi)+z'\cos\theta]}\,ds' \quad (2.237)$$

$$E^J_{FF\phi} = \frac{-j\omega\mu_o}{4\pi}\frac{e^{-jk_or}}{r}\int\limits_{S'}\Big[J_t(\vec{r}\,')\sin u'\sin(\phi'-\phi)\ +\ J_\phi(\vec{r}\,')\cos(\phi'-\phi)\Big] \times\ e^{jk_o[\rho'\sin\theta\cos(\phi'-\phi)+z'\cos\theta]}\,ds' \quad (2.238)$$

and r, θ, and ϕ are the spherical coordinates of the far-zone point $\vec{r}$.

Substituting Eq. 2.21 into Eqs. 2.236–2.238 (with the modal parameter n in Eq. 2.21 conveniently changed into m), solving the integrals with respect to ϕ' in closed form, and solving the integrals with respect to t' using the same procedure of Sects. 2.3.3 and 2.3.4, after straightforward algebraic manipulations one obtains

$$\vec{E}^J_{FF}(\vec{r}) = \sum_{m=-\infty}^{\infty}\left\{\sum_{j=1}^{N_T} I^T_{mj}\left[\left(E^J_{FF\theta}\right)^T_{mj}\ \hat{\theta}\ +\ \left(E^J_{FF\phi}\right)^T_{mj}\ \hat{\phi}\right] + \sum_{j=1}^{N_P} I^P_{mj}\left[\left(E^J_{FF\theta}\right)^P_{mj}\ \hat{\theta}\ +\ \left(E^J_{FF\phi}\right)^P_{mj}\ \hat{\phi}\right]\right\}, \quad (2.239)$$

where

$$\left(E^J_{FF\theta}\right)^T_{mj} = \frac{-j\eta_ok_o}{8}\left(je^{j\phi}\right)^m\frac{e^{-jk_or}}{r}\sum_{l=q-1}^{q}\Delta_l\left\{\frac{j}{2}\sin u_l\cos\theta \times\left[F_{m+1,a}(t_l)-F_{m-1,a}(t_l)-(-1)^{q-l}\left[F_{m+1,b}(t_l)-F_{m-1,b}(t_l)\right]\right] - \cos u_l\sin\theta\left[F_{m,a}(t_l)-(-1)^{q-l}F_{m,b}(t_l)\right]\right\}, \quad (2.240)$$

$$\left(E^J_{FF\phi}\right)^T_{mj} = \frac{-j\eta_ok_o}{8}\left(je^{j\phi}\right)^m\frac{e^{-jk_or}}{r}\sum_{l=q-1}^{q}\frac{\Delta_l}{2}\sin u_l\left\{F_{m+1,a}(t_l)+F_{m-1,a}(t_l) - (-1)^{q-l}[F_{m+1,b}(t_l)+F_{m-1,b}(t_l)]\right\}, \quad (2.241)$$

$$\left(E^J_{FF\theta}\right)^P_{mj} = \frac{j\eta_o k_o}{8}\left(je^{j\phi}\right)^m \frac{e^{-jk_o r}}{r}\Delta_j \cos\theta \left\{F_{m+1,a}(t_j) + F_{m-1,a}(t_j) + \frac{\Delta_j \sin u_j}{2\,\rho_j}\left[F_{m+1,b}(t_j) + F_{m-1,b}(t_j)\right]\right\}, \quad (2.242)$$

$$\left(E^J_{FF\phi}\right)^P_{mj} = \frac{\eta_o k_o}{8}\left(je^{j\phi}\right)^m \frac{e^{-jk_o r}}{r}\Delta_j \left\{F_{m+1,a}(t_j) - F_{m-1,a}(t_j) + \frac{\Delta_j \sin u_j}{2\,\rho_j}\left[F_{m+1,b}(t_j) - F_{m-1,b}(t_j)\right]\right\}, \quad (2.243)$$

the integrals with respect to α are given by

$$F_{n,a}(t_l) = \int_{-1}^{1} J_n(k_o\rho' \sin\theta)\, e^{jk_o z' \cos\theta}\, d\alpha\,, \qquad n = m-1, m, m+1\,, \quad (2.244)$$

$$F_{n,b}(t_l) = \int_{-1}^{1} J_n(k_o\rho' \sin\theta)\, e^{jk_o z' \cos\theta}\, \alpha\, d\alpha\,, \quad n = m-1, m, m+1\,, \quad (2.245)$$

$J_n(k_o\rho' \sin\theta)$ is the Bessel function of order n with argument $k_o\rho' \sin\theta$, ρ' and z' are given by Eqs. 2.51 and 2.52, respectively, and the subscript l characterizes the source segments $q-1$, q, and j (accordingly to the notation of Sect. 2.3.2). The integrals of Eqs. 2.244 and 2.245 can be numerically evaluated using a n_α-point Gaussian quadrature in a similar manner as in Sect. 2.3.4. As before, $n_\alpha = 2$ is adopted.

From Eqs. 2.240–2.245, one obtains the following relations:

$$\left(E^J_{FF\theta}\right)^T_{mj}\left(je^{j\phi}\right)^{-m} = (-1)^m \left(E^J_{FF\theta}\right)^T_{-mj}\left(je^{j\phi}\right)^m\,, \quad (2.246)$$

$$\left(E^J_{FF\phi}\right)^T_{mj}\left(je^{j\phi}\right)^{-m} = (-1)^{m+1} \left(E^J_{FF\phi}\right)^T_{-mj}\left(je^{j\phi}\right)^m\,, \quad (2.247)$$

$$\left(E^J_{FF\theta}\right)^P_{mj}\left(je^{j\phi}\right)^{-m} = (-1)^{m+1} \left(E^J_{FF\theta}\right)^P_{-mj}\left(je^{j\phi}\right)^m\,, \quad (2.248)$$

$$\left(E^J_{FF\phi}\right)^P_{mj}\left(je^{j\phi}\right)^{-m} = (-1)^m \left(E^J_{FF\phi}\right)^P_{-mj}\left(je^{j\phi}\right)^m\,, \quad (2.249)$$

from which the results for a positive mode m can be used to obtain the terms corresponding to a negative mode $-m$. Notice that for the $\vec{E}^{inc}(\vec{r})$ given by Eq. 2.126 only the modes $m = \pm 1$ are present.

The electric far-zone field $\vec{E}^{inc}_{FF}(\vec{r})$ radiated by the external spherical-wave source is readily obtained from Eqs. 2.126–2.138 by keeping only the terms of order $1/r$. For the RCF model given by Eqs. 2.127–2.129:

$$\vec{E}^{inc}_{FF}(\vec{r}) \;=\; \left[\cos^e\theta\,\cos\phi\;\hat{\theta} \;-\; \cos^h\theta\,\sin\phi\;\hat{\phi}\right]\;\frac{e^{-jk_o r}}{r}\;, \qquad \theta \in \left[0, \frac{\pi}{2}\right]\;, \tag{2.250}$$

which satisfies Maxwell's equations only in the far-zone region. For the $\hat{x}$-polarized Hertz dipole given by Eqs. 2.130–2.132 one has

$$\vec{E}^{inc}_{FF}(\vec{r}) \;=\; -j\eta_o\,\frac{(I\ell)}{2\lambda}\,\left[\cos\theta\,\cos\phi\;\hat{\theta} \;-\; \sin\phi\;\hat{\phi}\right]\;\frac{e^{-jk_o r}}{r}\;. \tag{2.251}$$

2.6 Numerical Examples

A computer code implementing the formulation presented in this chapter was created and its results successfully compared with several examples available in Refs. [16] and [17]. In this section two illustrative validation cases are discussed: the electric and magnetic near-zone fields inside and outside a PEC sphere illuminated by a Hertz dipole and the electric far-zone field scattered by a paraboloidal reflector. These validation cases, together with several other test cases successfully accomplished, provide the confidence that the present formulation as well as its numerical implementation are correct.

2.6.1 Metallic Sphere Illuminated by a Hertz Dipole

Figure 2.6 depicts a PEC sphere centered on the z-axis at $z = 0.64\lambda$, with a diameter of 0.64λ (no internal resonances are present for this diameter), and illuminated by an $\hat{x}$-polarized Hertz dipole given by Eqs. 2.126 and 2.130–2.132 (located at $z_S = 0$). In this example, the dipole moment $(I\ell)$ is such that

$$-j\eta_o \frac{(I\ell)}{2\lambda} = 1 \, . \tag{2.252}$$

The sphere generating curve starts at $z = 0.32\lambda$ $(t = 0)$ and ends at $z = 0.96\lambda$ $(t = 1.0053\lambda)$, such that the unit surface normal $\hat{n}$ points towards the region where the Hertz dipole is present. A total of 20 segments was used to represent the generating curve. Consequently, $N_T = 19$ and $N_P = 20$.

For this configuration, the total electric and magnetic fields computed from the results of Sect. 2.4 are given in Fig. 2.7. In these plots, the observation point $\vec{r}$ is located at the plane $\phi = 45°$ with $|\vec{r}| = 0.64\lambda$ (see Fig. 2.6). From Fig. 2.7, it is observed that the near-zone fields inside the PEC sphere ($\theta < 28.955°$) are negligible, as expected. At the region where the observation point is close to the PEC surface, one observes that the electric field components reach very large values while the magnetic ones have the expected behavior. This is due to the numerical evaluations of Eqs. 2.199–2.214. For the integrals corresponding to $v = 8, ..., 12$, the singularities where not removed (which is not a problem since in practical cases the observation point is away from the BOR surface). However, for $v = 4, ..., 7$,

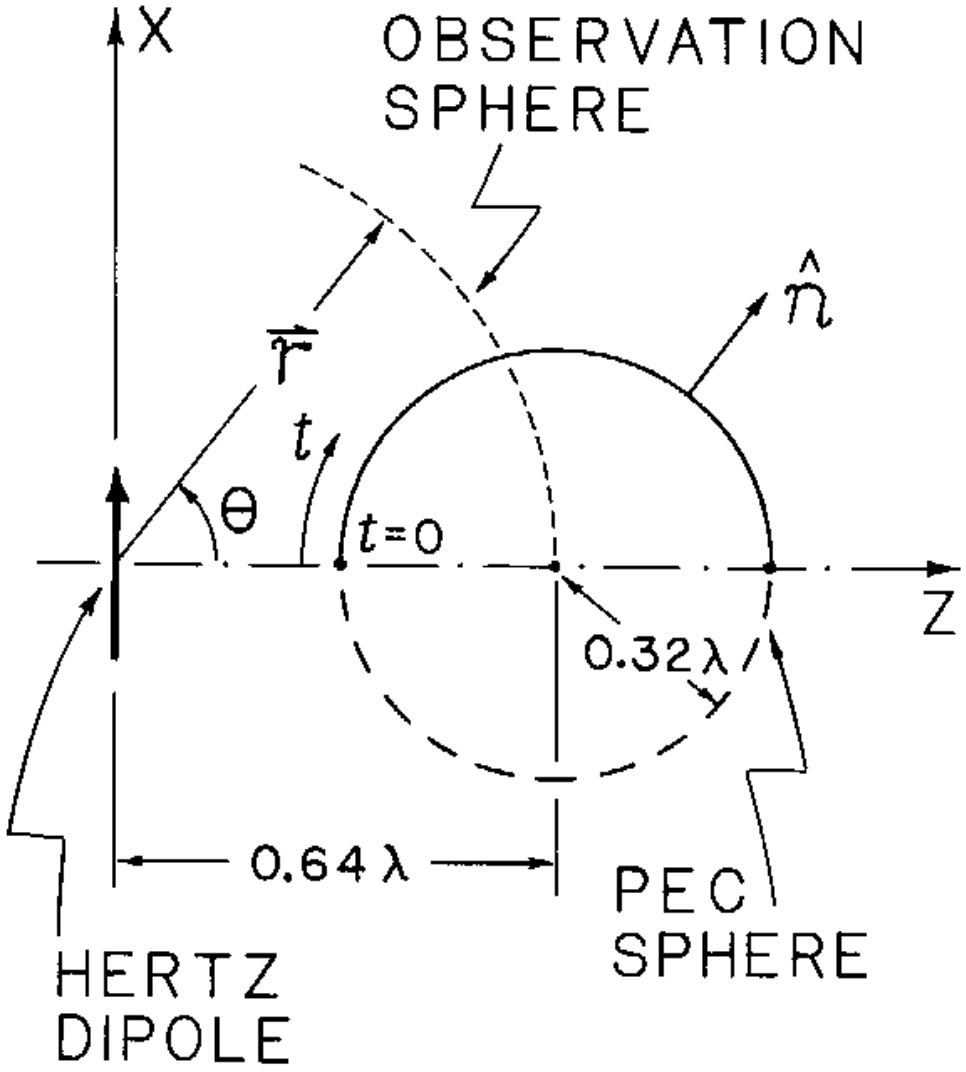

Figure 2.6: Geometry of the PEC Sphere Illuminated by a Hertz Dipole.

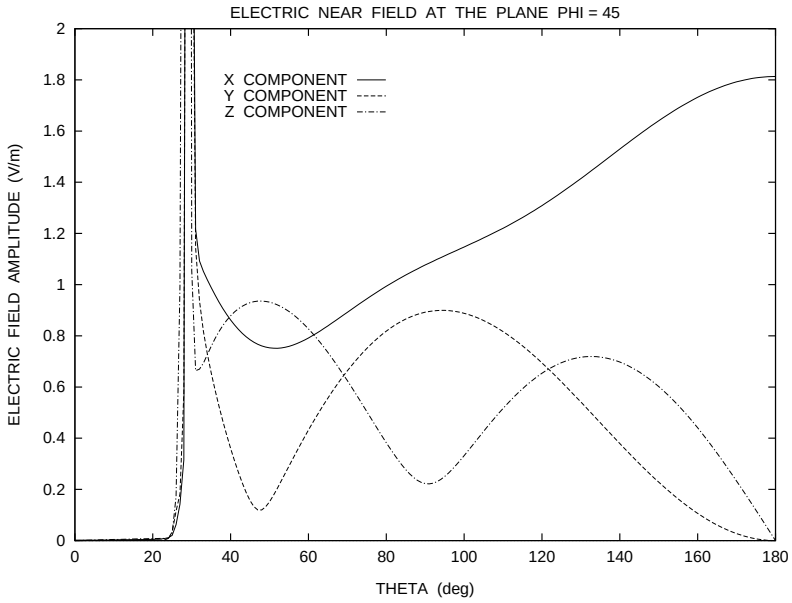

a) Electric Near-Zone Field Components (Plane $\phi = 45°$)

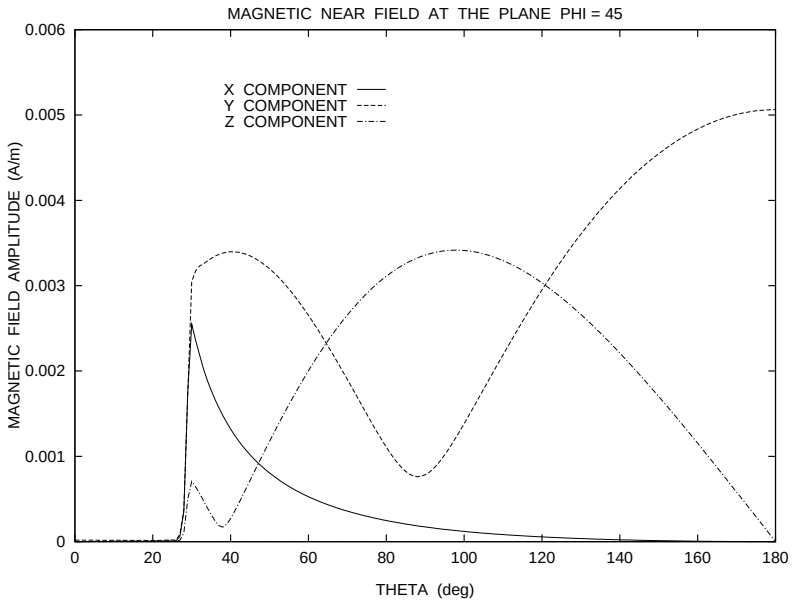

b) Magnetic Near-Zone Field Components (Plane $\phi = 45°$)

Figure 2.7: Near-Zone Fields of the PEC Sphere Illuminated by a Hertz Dipole.

the integrals are similar to the ones discussed in Sect. 2.3.4 and Methods 1 and 2 were used to remove the singularities. The same was done for the integrals corresponding to $v = 1, 2, 3$, but in this case the singularity remotion will be explained in Chapter 3. At the PEC surface ($\theta = 28.955°$), the computer code gives

$$\vec{H}_{NF}(\vec{r}) \;=\; (2.78 \angle -74.1° \; \hat{x} \;+\; 3.12 \angle 108° \; \hat{y} \;+\; 0.80 \angle 125.1° \; \hat{z}) \;\; 10^{-3} \; A/m \; , \tag{2.253}$$

which is readily verified to be perpendicular to the spherical surface unit normal

$$\hat{n} \;=\; 0.685 \; (\hat{x} \;+\; \hat{y}) \;-\; 0.250 \; \hat{z} \tag{2.254}$$

at $\theta = 28.955°$. Extrapolating the code results, it was verified that the total electric field is normal to the PEC spherical surface, as expected.

2.6.2 Paraboloidal Reflector Illuminated by a Raised-Cosine Feed Model

The paraboloidal-reflector geometry is depicted in Fig 2.8. The paraboloidal reflector has a diameter of 200λ, a focal length of 60λ, and an edge angle of 79.61°. Its focus is located at the origin of the principal coordinate system, as illustrated in Fig. 2.8. This reflector is illuminated by an $\hat{x}$-polarized RCF model radiating towards the negative $\hat{z}$-direction and located at the paraboloid focus. In this case, the feed radiation is given by Eqs. 2.126–2.129, with the angle θ_F substituted by $\pi - \theta_F$ ($\theta_F \in [\pi/2, \pi]$) in Eqs. 2.128 and 2.129. It was desired to illuminate the reflector

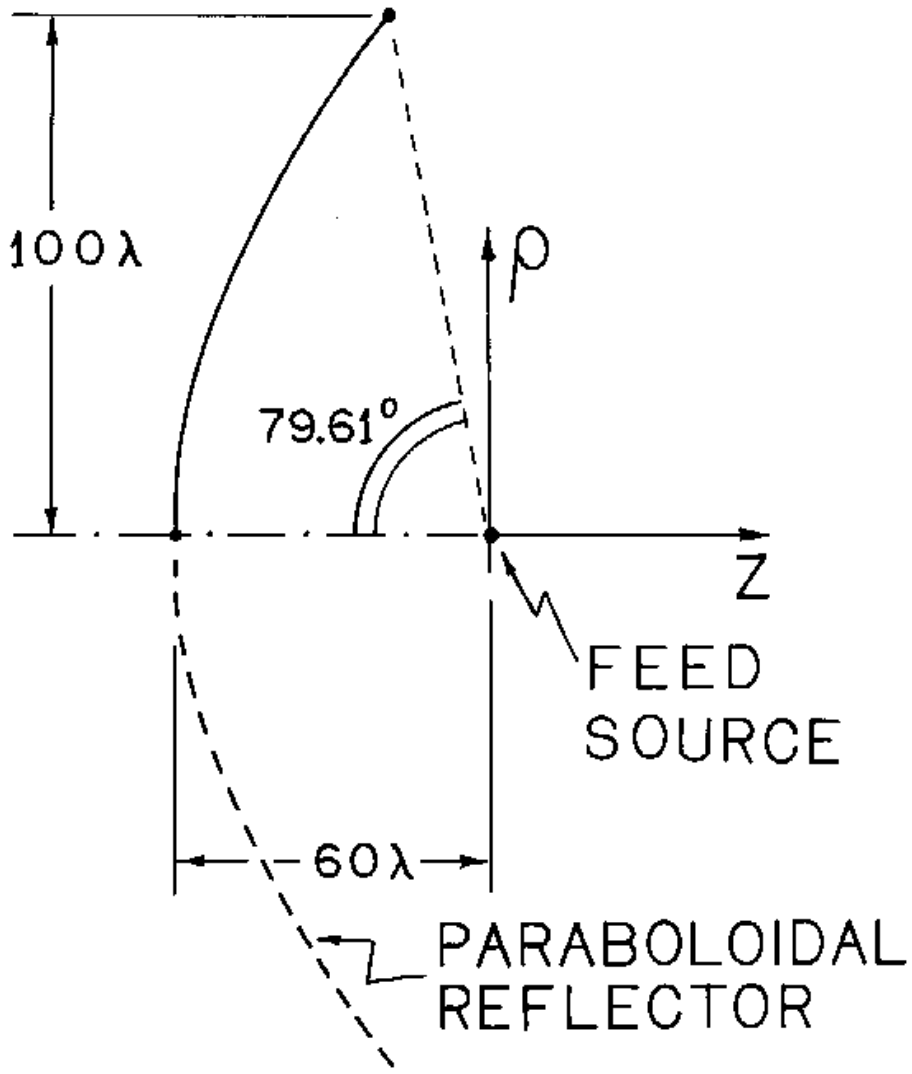

Figure 2.8: Geometry of the PEC Paraboloidal Reflector.

with a 10 dB taper towards the rim, in which case the parameters $e = h = 0.6721$ were used in Eqs. 2.128 and 2.129. A total of 1000 segments were used to represent the reflector generating curve (about 10 segments per wavelength), in which case $N_T = 999$ and $N_P = 1000$.

The antenna far-zone patterns at the plane $\phi = 45°$ (obtained from the results of Sect. 2.5) are shown in Fig. 2.9. In this figure, the results obtained from the MoM formulation are compared with the ones obtained from the Physical Optics (PO) approximation [8]. The co- and cross-polarizations are defined accordingly to Ludwig Third definition [45]. The excellent agreement between the results is expected since the paraboloidal reflector has a smoothly curved surface with large electric dimensions. The boresight gain obtained from the MoM analysis is 55.08 dBi, while the PO analysis obtains 55.01 dBi. Also, the MoM technique gives a cross-polarization peak level 7.34 dB higher than the one predicted by the PO approximation.

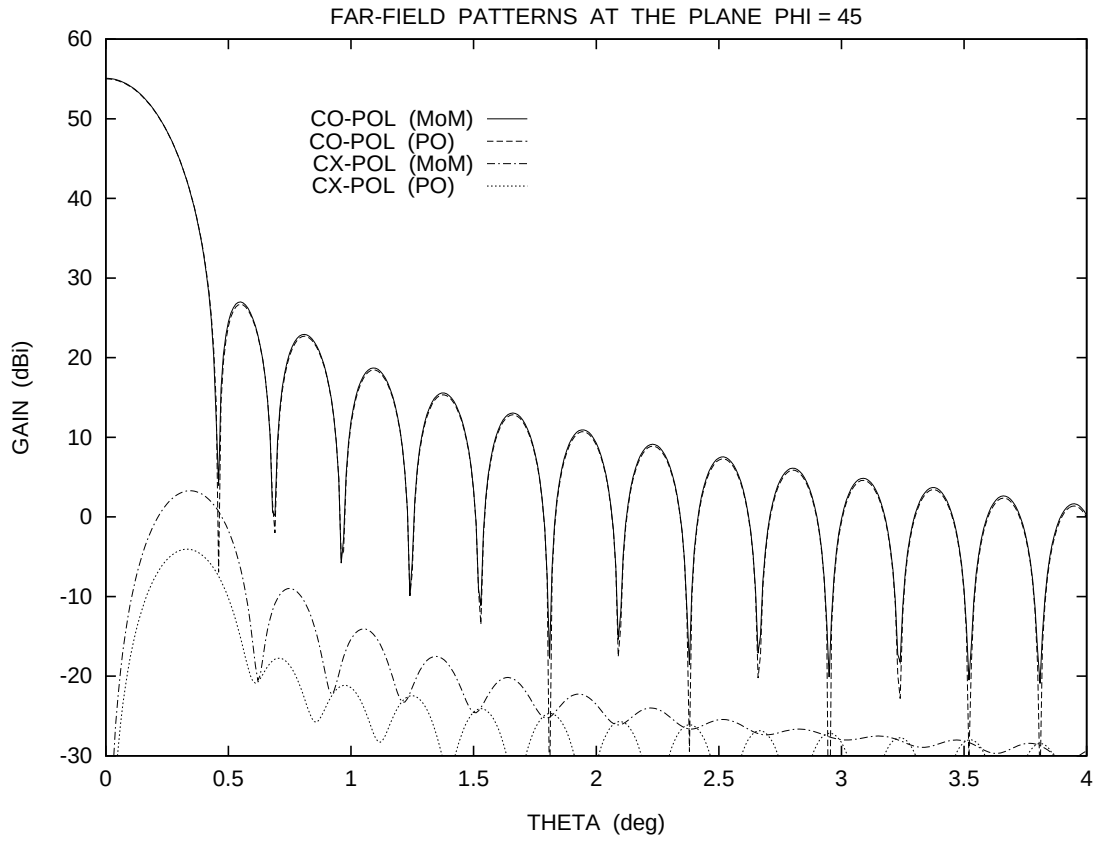

Figure 2.9: Far-Zone Patterns (Plane $\phi = 45°$) of the PEC Paraboloidal Reflector Illuminated by a RCF Model.

Chapter 3

SCATTERING FROM BODIES OF REVOLUTION WITH AN IMPEDANCE BOUNDARY CONDITION

Chapter 2 presented a technique for the rigorous (in a numerical sense) analysis of PEC axially-symmetric antennas, and the excitation was assumed to be a spherical-wave point source. However, to accomplish a more accurate analysis of the reflector-antenna system, the radiation effects of the feed structure must be included. One of the highest-performance feed used in reflector-antenna applications is the corrugated-horn feed (see Fig. 3.1). The corrugations present over the interior horn surface create an anisotropic surface impedance that enables the propagation of a balanced hybrid mode inside the horn up to its aperture, producing a circularly-symmetric feed pattern [37]–[39]. This circularly-symmetric pattern reduces the cross-polarization levels of the antenna radiation, produces a more uniform illumination of the reflector surfaces, and, consequently, improves the overall antenna performance [4].

The analysis of corrugated horns may be performed using the procedure of Chapter 2, with a proper excitation. However, to achieve the desired numerical

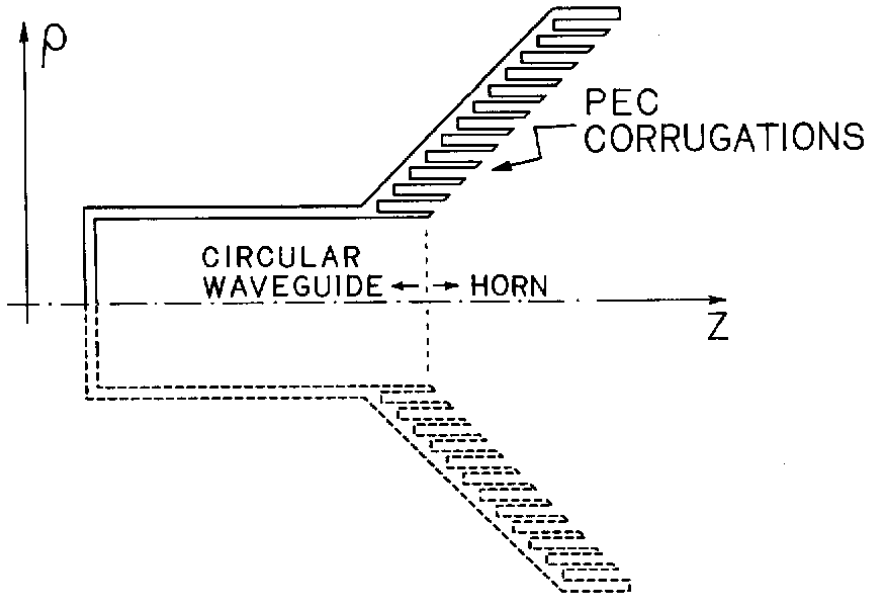

a) Horn with the PEC Corrugations

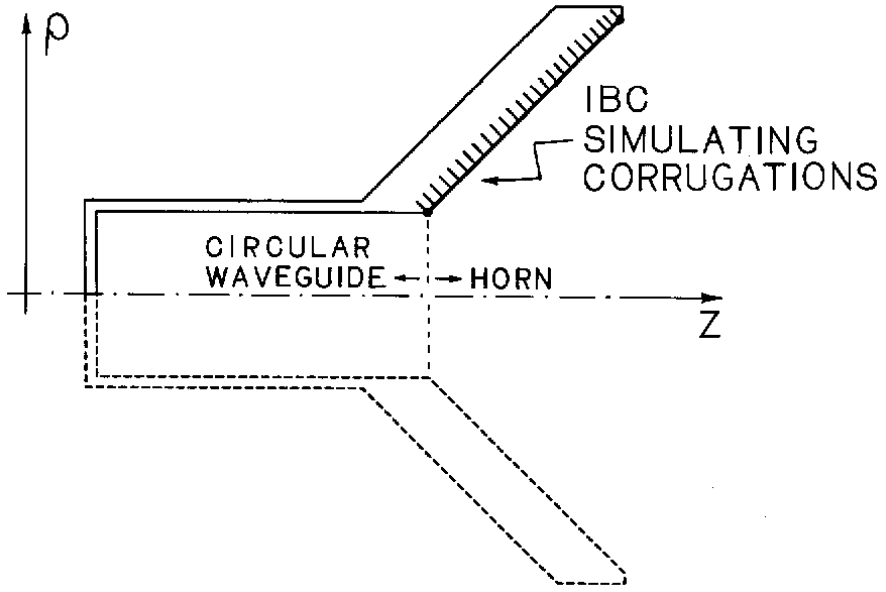

b) Horn with the IBC Approximation

Figure 3.1: Basic Geometry of a Corrugated Horn.

accuracy, an extremely large number of segments must be employed to describe the corrugations over the horn generating curve (see Fig. 3.1). A more efficient and accurate way to analyze such horns is to apply the scattering matrix technique [46]. This technique is capable of analyzing a large variety of waveguide and horn components within the the measurements accuracy, but its numerical implementation is somewhat involving.

A different approach in the analysis of corrugated horns is to use the Impedance Boundary Condition (IBC) technique together with the EFIE [35]. The IBC may be used to simulate the anisotropic boundary conditions created by the corrugations over the interior surface of the horn. It may also be used to simulate a matched load for the feed [35]. This technique can successfully predict the radiation characteristics of the corrugated horn without the hassle of using a large number of segments to describe the horn contour (see Fig. 3.1), providing a useful numerical tool for the antenna design. However, due to the fact that the IBC can not accurately model the mode conversion at the horn throat (specially in an oversized waveguide), this corrugation simulation precludes the correct prediction of the reflection losses related to the energy that is radiated back into the feed circular waveguide (as illustrated in Sect. 3.6.2). In this case, the scattering matrix technique may be used or the PEC corrugations correctly represented by a large number of segments. As the present work is primarily concerned with the radiation characteristics of axially-symmetric

reflector-antenna systems, the IBC technique suffices for many applications and hence it is presented in this chapter.

The IBC is presented in Sect. 3.1. The EFIE including the IBC is then formulated and numerically solved using the MoM technique, as discussed in Sect. 3.2. The equations of the near- and far-zone fields radiated by a BOR with an IBC are presented in Sects. 3.3 and 3.4, respectively. The calculation of the feed return loss is discussed in Sect. 3.5. Finally, Sect. 3.6 presents two illustrative test cases: the propagation of the fundamental TE_{11} mode inside a circular waveguide and the radiation characteristics of a corrugated-horn feed.

The formulation of the present chapter, built over the basis provided throughout Chapter 2, constitutes an improvement with respect to Ref. [35]. Instead of using only triangle functions [35], the present triangle/pulse representation of the induced electric currents is more accurate and, consequently, yields a stabler numerical procedure (as discussed in Sect. 2.3.2).

3.1 The Impedance Boundary Condition

The IBC represents the relation between the tangential components of the electric and magnetic fields over a surface. In this work, to simulate either the anisotropic surface impedance created by corrugations (discussed in Sect. 3.6.2) or a matched load for the feed waveguide (discussed in Sect. 3.5), the required relations for the

tangential field components over a BOR surface are described in terms of IBCs as:

$$\mathcal{Z}_t^{IBC} = \frac{-E_t}{H_\phi}, \tag{3.1}$$

$$\mathcal{Z}_\phi^{IBC} = \frac{E_\phi}{H_t}, \tag{3.2}$$

where the subscripts t and ϕ associate the several terms with respect to the curvilinear orthonormal coordinate system illustrated in Fig. 2.1. Using vector algebra and with the help of Fig. 2.1, Eqs. 3.1 and 3.2 can be conveniently formulated as

$$-\hat{n} \times \vec{E}(\vec{r}) = \overline{\overline{\mathcal{Z}}}_{IBC} \cdot \left\{ \hat{n} \times \left[\hat{n} \times \vec{H}(\vec{r}) \right] \right\}, \tag{3.3}$$

where $\hat{n}$ is the unit normal at the BOR surface and $\overline{\overline{\mathcal{Z}}}_{IBC}$ is the IBC dyadic given by

$$\overline{\overline{\mathcal{Z}}}_{IBC} = \mathcal{Z}_t^{IBC}\, \hat{\phi}\hat{\phi} + \mathcal{Z}_\phi^{IBC}\, \hat{t}\hat{t}. \tag{3.4}$$

To define an equivalent problem in terms of the equivalence principle, the boundary-condition information contained in Eqs. 3.1–3.4 must be transfered into the definition of the equivalent currents over the BOR surface (see Fig. 2.3). From Eqs. 2.5, 2.6, and 3.1–3.4, the equivalent currents are defined such that

$$\vec{M}(\vec{r}) = \mathcal{Z}_\phi^{IBC}\, J_\phi(\vec{r})\, \hat{t} - \mathcal{Z}_t^{IBC}\, J_t(\vec{r})\, \hat{\phi}, \tag{3.5}$$

where $J_t(\vec{r})$ and $J_\phi(\vec{r})$ are the components of $\vec{J}(\vec{r})$. This equation indicates that $\vec{M}(\vec{r})$ is related to $\vec{J}(\vec{r})$ through the IBC. For a PEC BOR, $\mathcal{Z}_t^{IBC} = \mathcal{Z}_\phi^{IBC} = 0$ and, consequently, $\vec{M}(\vec{r})$ is not present.

3.2 The Method of Moments with an Impedance Boundary Condition

The EFIE in the presence of an IBC is given by Eq. 2.8, with $\vec{M}(\vec{r})$ obtained from Eq. 3.5. The MoM solution of Eq. 2.8 follows exactly the same steps presented in Sect. 2.3, with the exception that now some extra terms related to $\vec{M}(\vec{r})$ are present at the impedance matrix of Eq. 2.23. The basis and weighting functions to be used are still the same ones given by Eqs. 2.21 and 2.22.

It is extremely important to observe here that Eq. 2.8 can not be used in the analysis of infinitely thin open shells [11]. This is due to the fact that, as the closed surface is shrunk into an infinitely thin one, the term $\vec{M}(\vec{r})$ appearing outside the integral in Eq. 2.8 will correspond to the summation between the magnetic currents at both sides of the surface (at point $\vec{r}$), while the one inside the integral will correspond to the difference. As the magnetic currents at both sides of the open surface can not be combined into a single one, the proper solution of Eq. 2.8 requires a finite thickness (i.e., closed surface). However, the PEC reflector surfaces may still be represented by infinitely thin shells, since at these surfaces $\vec{M}(\vec{r}) = 0$ and Eq. 2.8 reduces to Eq. 2.9.

3.2.1 The IBC Matrix Equation

The matrix equation to be solved is still the one of Eq. 2.23, where the elements of the sub-matrices V^T and V^P are given by Eqs. 2.24 and 2.25, respectively, and the elements of the sub-matrices I_T and I_P are the unknown coefficients I_{nj}^T and I_{nj}^P of Eq. 2.21, respectively. Following Sect. 2.3.1 (where now the EFIE to be used is the one of Eq 2.8), the impedance-matrix elements including the terms related to $\vec{M}(\vec{r})$ are obtained from

$$\begin{aligned} Z_{ij} &= \frac{j}{4\pi k_o} \int_S \int_{S'} \left\{ k_o^2 \, \vec{W}_i(\vec{r}) \cdot \vec{J}_j(\vec{r}\,') - \left[\nabla \cdot \vec{W}_i(\vec{r})\right] \left[\nabla' \cdot \vec{J}_j(\vec{r}\,')\right] \right\} \Psi \, ds' \, ds \\ &- \frac{1}{2\eta_o} \int_S \vec{W}_i(\vec{r}) \cdot \left[\vec{M}_j(\vec{r}) \times \hat{n}\right] \, ds \\ &+ \frac{1}{4\pi\eta_o} \int_S \int_{S'} \vec{W}_i(\vec{r}) \cdot \left[\vec{M}_j(\vec{r}\,') \times \nabla' \Psi\right] \, ds' \, ds \,, \end{aligned} \tag{3.6}$$

instead of Eq. 2.20. From Eqs. 2.21, 2.22, 3.5 and 3.6 one obtains the terms of the impedance matrix of Eq. 2.23 when the IBC is present, which is now rewritten as

$$[Z] = \begin{bmatrix} Z_{IBC}^{TT} & Z_{IBC}^{TP} \\ Z_{IBC}^{PT} & Z_{IBC}^{PP} \end{bmatrix} , \tag{3.7}$$

where the sub-matrix elements are given by

$$Z_{IBC}^{TT}|_{ij} = Z_{ij}^{TT} + Y_{ij}^{TT} \,, \tag{3.8}$$

$$Z_{IBC}^{TP}|_{ij} = Z_{ij}^{TP} + Y_{ij}^{TP} \,, \tag{3.9}$$

$$Z_{IBC}^{PT}|_{ij} = Z_{ij}^{PT} + Y_{ij}^{PT} \,, \tag{3.10}$$

$$Z_{IBC}^{PP}|_{ij} = Z_{ij}^{PP} + Y_{ij}^{PP} \,, \tag{3.11}$$

with Z_{ij}^{TT}, Z_{ij}^{TP}, Z_{ij}^{PT}, and Z_{ij}^{PP} given by Eqs. 2.26–2.29, respectively, and the terms corresponding to $\vec{M}(\vec{r})$ given by

$$
\begin{aligned}
Y_{ij}^{TT} &= \frac{-1}{2\eta_o} \int_S \mathcal{Z}_{tj}^{IBC} \frac{T_i(t)}{\rho} \frac{T_j(t)}{\rho} e^{j(n-m)\phi} \, ds \\
&- \frac{1}{4\pi\eta_o} \int_S \int_{S'} \mathcal{Z}_{tj}^{IBC} \frac{T_i(t)}{\rho} \frac{T_j(t')}{\rho'} e^{j(n\phi'-m\phi)} \\
&\times \hat{t} \cdot \left(\hat{\phi}' \times \nabla' \Psi \right) \, ds' \, ds, \quad i = 1, ..., N_T \text{ and } j = 1, ..., N_T, \qquad (3.12) \\
Y_{ij}^{TP} &= \frac{1}{4\pi\eta_o} \int_S \int_{S'} \mathcal{Z}_{\phi j}^{IBC} \frac{T_i(t)}{\rho} \frac{P_j(t')}{\rho_j} e^{j(n\phi'-m\phi)} \\
&\times \hat{t} \cdot \left(\hat{t}' \times \nabla' \Psi \right) \, ds' \, ds, \quad i = 1, ..., N_T \text{ and } j = 1, ..., N_P, \qquad (3.13) \\
Y_{ij}^{PT} &= \frac{-1}{4\pi\eta_o} \int_S \int_{S'} \mathcal{Z}_{tj}^{IBC} \frac{P_i(t)}{\rho_i} \frac{T_j(t')}{\rho'} e^{j(n\phi'-m\phi)} \\
&\times \hat{\phi} \cdot \left(\hat{\phi}' \times \nabla' \Psi \right) \, ds' \, ds, \quad i = 1, ..., N_P \text{ and } j = 1, ..., N_T, \qquad (3.14) \\
Y_{ij}^{PP} &= \frac{-1}{2\eta_o} \int_S \mathcal{Z}_{\phi j}^{IBC} \frac{P_i(t)}{\rho_i} \frac{P_j(t)}{\rho_j} e^{j(n-m)\phi} \, ds \\
&+ \frac{1}{4\pi\eta_o} \int_S \int_{S'} \mathcal{Z}_{\phi j}^{IBC} \frac{P_i(t)}{\rho_i} \frac{P_j(t')}{\rho_j} e^{j(n\phi'-m\phi)} \\
&\times \hat{\phi} \cdot \left(\hat{t}' \times \nabla' \Psi \right) \, ds' \, ds, \quad i = 1, ..., N_P \text{ and } j = 1, ..., N_P. \qquad (3.15)
\end{aligned}
$$

In Eqs. 3.12–3.15, the unprimed and primed coordinates refer to the observation point $\vec{r}$ over the surface S and to the source point $\vec{r}\,'$ over the surface S', respectively, and $\mathcal{Z}_{tj}^{IBC}$ and $\mathcal{Z}_{\phi j}^{IBC}$ correspond to the $\mathcal{Z}_t^{IBC}$ associated with the triangle basis function $T_j(t')$ and to the $\mathcal{Z}_\phi^{IBC}$ associated with the pulse basis function $P_j(t')$, respectively. Obviously, when $\mathcal{Z}_t^{IBC} = \mathcal{Z}_\phi^{IBC} = 0$ the present formulation reduces to the one of Sect. 2.3.3 for a PEC BOR.

The numerical evaluation of Eqs. 3.12–3.15 is discussed in Sects. 3.2.2 and 3.2.3, where it will be shown that the impedance-matrix elements with $m \neq n$ are zero and, consequently, Eq. 2.23 (with the impedance matrix now given by Eq. 3.7) may be decomposed into several independent matrix systems for each different mode $m = n$. The evaluation of the voltage-matrix elements for the proper feed excitation is discussed in Sect. 3.2.4.

3.2.2 Impedance-Matrix Evaluation for the IBC Terms

The evaluation of the surface integrals of Eqs. 3.12–3.15 will follow the same steps done for Eqs. 2.26–2.29 in Sect. 2.3.3. From Eqs. 2.1 and 2.170–2.173, one obtains the following relations:

$$\hat{t} \cdot \left(\hat{t}' \times \vec{R}\right) = \{\rho \sin u' \cos u - [\rho' \cos u' - (z' - z) \sin u'] \sin u\} \sin(\phi - \phi'), \quad (3.16)$$

$$\hat{\phi} \cdot \left(\hat{t}' \times \vec{R}\right) = \rho \cos u' - [\rho' \cos u' - (z' - z) \sin u'] \cos(\phi - \phi'), \quad (3.17)$$

$$\hat{t} \cdot \left(\hat{\phi}' \times \vec{R}\right) = \rho' \cos u - [\rho \cos u + (z' - z) \sin u] \cos(\phi - \phi'), \quad (3.18)$$

$$\hat{\phi} \cdot \left(\hat{\phi}' \times \vec{R}\right) = (z' - z) \sin(\phi - \phi'). \quad (3.19)$$

Using Eqs. 2.30, 2.168, and 3.16–3.19, Eqs. 3.12–3.15 may be rewritten as

$$\begin{aligned} Y_{ij}^{TT} = & \frac{-1}{2\eta_o} \int_0^{2\pi} \int_t \frac{\mathcal{Z}_{tj}^{IBC}}{\rho} T_i(t)\, T_j(t)\, e^{j(n-m)\phi}\ dt\ d\phi \\ & - \frac{k_o^3}{4\pi\eta_o} \int_0^{2\pi} \int_t \int_0^{2\pi} \int_{t'} \mathcal{Z}_{tj}^{IBC}\, T_i(t)\, T_j(t')\, e^{j(n\phi' - m\phi)} \Big\{\rho' \cos u \\ & - [\rho \cos u + (z' - z) \sin u] \cos(\phi - \phi')\Big\}\ G_H\ dt'\, d\phi'\, dt\, d\phi, \end{aligned} \quad (3.20)$$

$$Y_{ij}^{TP} = \frac{k_o^3}{4\pi\eta_o} \int_0^{2\pi}\int_t \int_0^{2\pi}\int_{t'} \mathcal{Z}_{\phi j}^{IBC}\, T_i(t)\, P_j(t')\, \frac{\rho'}{\rho_j}\, e^{j(n\phi'-m\phi)} \Big\{\rho \sin u' \cos u - [\rho' \cos u' - (z'-z)\sin u']\sin u\Big\} \sin(\phi-\phi')\; G_H\; dt'\, d\phi'\, dt\, d\phi, \quad (3.21)$$

$$Y_{ij}^{PT} = \frac{-k_o^3}{4\pi\eta_o} \int_0^{2\pi}\int_t \int_0^{2\pi}\int_{t'} \mathcal{Z}_{tj}^{IBC}\, P_i(t)\, T_j(t')\, \frac{\rho}{\rho_i}\, e^{j(n\phi'-m\phi)}\, (z'-z)\, \sin(\phi-\phi') \times\; G_H\; dt'\, d\phi'\, dt\, d\phi, \quad (3.22)$$

$$Y_{ij}^{PP} = \frac{-1}{2\eta_o} \int_0^{2\pi}\int_t \frac{\mathcal{Z}_{\phi j}^{IBC}\,\rho}{\rho_i\,\rho_j}\, P_i(t)\, P_j(t)\, e^{j(n-m)\phi}\; dt\, d\phi + \frac{k_o^3}{4\pi\eta_o} \int_0^{2\pi}\int_t \int_0^{2\pi}\int_{t'} \mathcal{Z}_{\phi j}^{IBC}\, P_i(t)\, P_j(t')\, \frac{\rho\,\rho'}{\rho_i\rho_j}\, e^{j(n\phi'-m\phi)} \Big\{\rho\cos u' - [\rho'\cos u' - (z'-z)\sin u']\cos(\phi-\phi')\Big\}\; G_H\; dt'\, d\phi'\, dt\, d\phi, \quad (3.23)$$

where G_H is given by Eq. 2.183, R is given by Eq. 2.36, and the integration limits t and t' will depend on the weighting and basis functions being used, respectively. From Eq. 2.41 one observes that Eqs. 3.20–3.23 are equal to zero whenever $m \neq n$ and, consequently, the matrix equation given by Eq. 2.23 (with the impedance matrix given by Eq. 3.7) may be decomposed into several ones for each different mode $m = n$. For a particular mode m and from Eq. 2.41, Eqs. 3.20–3.23 may be rewritten as

$$Y_{ij}^{TT} = \frac{-\pi}{\eta_o}\, F_{ij}^{T} - \frac{k_o^3}{\eta_o} \int_t \int_{t'} \mathcal{Z}_{tj}^{IBC}\, T_i(t)\, T_j(t') \Big\{\rho' \cos u\; G_1(t,t') + [(\rho'-\rho)\cos u - (z'-z)\sin u]\; G_2(t,t')\Big\}\; dt'\, dt, \quad (3.24)$$

$$Y_{ij}^{TP} = \frac{-jk_o^3}{\eta_o} \int_t \int_{t'} \mathcal{Z}_{\phi j}^{IBC}\, T_i(t)\, P_j(t')\, \frac{\rho'}{\rho_j} \Big\{\rho \sin u' \cos u - [\rho' \cos u' - (z'-z)\sin u']\sin u\Big\}\; G_3(t,t')\; dt'\, dt, \quad (3.25)$$

$$Y_{ij}^{PT} = \frac{j k_o^3}{\eta_o} \int_t \int_{t'} \mathcal{Z}_{tj}^{IBC}\, P_i(t)\, T_j(t')\, \frac{\rho}{\rho_i}\, (z'-z)\;\; G_3(t,t')\;\; dt'\, dt, \tag{3.26}$$

$$\begin{aligned} Y_{ij}^{PP} = {} & \frac{-\pi}{\eta_o} F_{ij}^{P} + \frac{k_o^3}{\eta_o} \int_t \int_{t'} \mathcal{Z}_{\phi j}^{IBC}\, P_i(t)\, P_j(t')\, \frac{\rho\, \rho'}{\rho_i \rho_j} \Big\{ \rho \cos u' \;\; G_1(t,t') \\ & - \;\; [(\rho'-\rho)\cos u' - (z'-z)\sin u']\;\; G_2(t,t') \Big\} \;\; dt'\, dt, \end{aligned} \tag{3.27}$$

where

$$F_{ij}^{T} = \int_t \mathcal{Z}_{tj}^{IBC}\, T_i(t)\, T_j(t)\, \frac{1}{\rho}\, dt\,, \tag{3.28}$$

$$F_{ij}^{P} = \int_t \mathcal{Z}_{\phi j}^{IBC}\, P_i(t)\, P_j(t)\, \frac{\rho}{\rho_i\, \rho_j}\, dt\,, \tag{3.29}$$

$$G_1(t,t') = \frac{1}{2} \int_0^{2\pi} (1-\cos\phi)\;\; e^{-jm\phi}\, G_H\, d\phi \;=\; 2 \int_0^{\pi} \sin^2 \frac{\phi}{2}\;\; \cos m\phi\, G_H\, d\phi, \tag{3.30}$$

$$G_2(t,t') = \frac{1}{2} \int_0^{2\pi} \cos\phi\; e^{-jm\phi}\, G_H\, d\phi \;=\; \int_0^{\pi} \cos\phi\;\; \cos m\phi\, G_H\;\; d\phi\,, \tag{3.31}$$

$$G_3(t,t') = \frac{j}{2} \int_0^{2\pi} \sin\phi\; e^{-jm\phi}\, G_H\, d\phi \;=\; \int_0^{\pi} \sin\phi\;\; \sin m\phi\, G_H\;\; d\phi\,, \tag{3.32}$$

and R is now given by Eq. 2.49.

The integrals F_{ij}^T and F_{ij}^P in Eqs. 3.28 and 3.29, respectively, can be evaluated in closed form. When $T_i(t)$ and $T_j(t)$ do not overlap then $F_{ij}^T = 0$. However, three types of overlaps occur, as illustrated in Fig. 3.2. When $T_j(t)$ coincides with $T_{i+1}(t)$, the overlapping occurs at the observation segment p related to $T_i(t)$. In this case, from Eqs. 2.50–2.56,

$$F_{ij}^{T} = \frac{\mathcal{Z}_{t,p}^{IBC}\, \Delta_p}{8} \int_{-1}^{1} \frac{(1-\alpha)(1+\alpha)}{\rho_p + \alpha \frac{\Delta_p}{2} \sin u_p}\, d\alpha \;=\; F_1^T(t_p) - F_3^T(t_p)\,. \tag{3.33}$$

When $T_j(t)$ coincides with $T_i(t)$, the overlapping occurs at both $p-1$ and p obser-

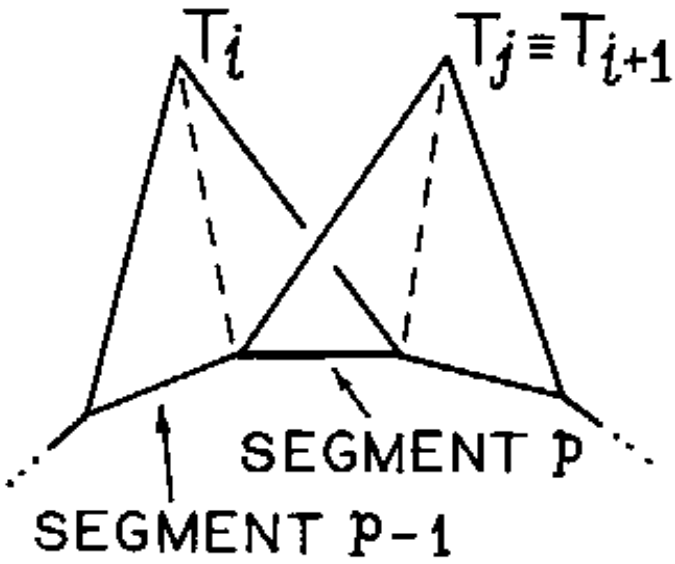

a) $T_j = T_{i+1}$

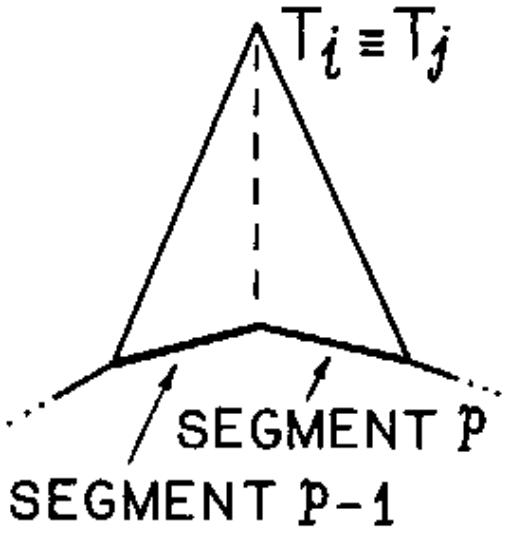

b) $T_j = T_i$

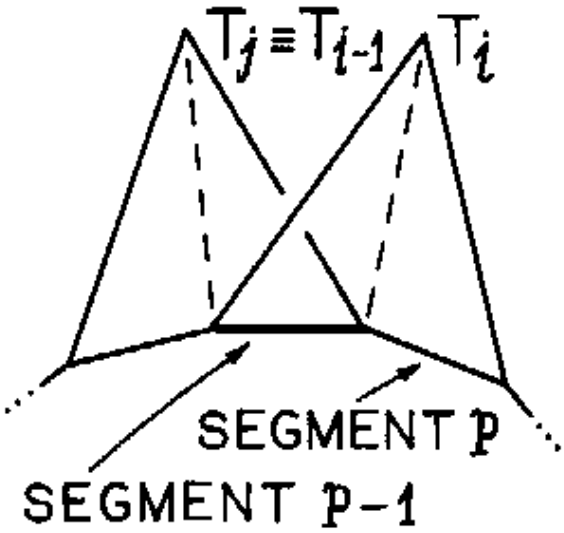

c) $T_j = T_{i-1}$

Figure 3.2: Different Overlapping Situations for the Triangle Functions.

vation segments and

$$F_{ij}^{T} = \frac{\mathcal{Z}_{t,p-1}^{IBC}\,\Delta_{p-1}}{8}\int_{-1}^{1}\frac{(1+\alpha)^2\ d\alpha}{\rho_{p-1}+\alpha\,\frac{\Delta_{p-1}}{2}\sin u_{p-1}} + \frac{\mathcal{Z}_{t,p}^{IBC}\Delta_p}{8}\int_{-1}^{1}\frac{(1-\alpha)^2\ d\alpha}{\rho_p+\alpha\,\frac{\Delta_p}{2}\sin u_p}$$
$$= F_1^T(t_{p-1}) + F_1^T(t_p) + F_2^T(t_{p-1}) - F_2^T(t_p) + F_3^T(t_{p-1}) + F_3^T(t_p)\,. \qquad (3.34)$$

When $T_j(t)$ coincides with $T_{i-1}(t)$, the overlapping occurs at the observation segment $p-1$ and

$$F_{ij}^{T} = \frac{\mathcal{Z}_{t,p-1}^{IBC}\,\Delta_{p-1}}{8}\int_{-1}^{1}\frac{(1+\alpha)(1-\alpha)\ d\alpha}{\rho_{p-1}+\alpha\,\frac{\Delta_{p-1}}{2}\sin u_{p-1}} = F_1^T(t_{p-1}) - F_3^T(t_{p-1})\,. \qquad (3.35)$$

In Eqs. 3.33–3.35,

$$F_1^T(t_k) = \frac{\mathcal{Z}_{t,k}^{IBC}\Delta_k}{8}\int_{-1}^{1}\frac{d\alpha}{\rho_k+\alpha\,\frac{\Delta_k}{2}\sin u_k} = \begin{cases} \frac{\mathcal{Z}_{t,k}^{IBC}}{4\sin u_k}\ \ln\left[\frac{\rho_k+\frac{\Delta_k}{2}\sin u_k}{\rho_k-\frac{\Delta_k}{2}\sin u_k}\right], \\ 0\,, \quad \text{if}\ \ \rho_k = \pm\,\frac{\Delta_k}{2}\sin u_k\,, \\ \frac{\mathcal{Z}_{t,k}^{IBC}\,\Delta_k}{4\,\rho_k}\,, \quad \text{if}\ \ \sin u_k = 0\,, \end{cases} \qquad (3.36)$$

$$F_2^T(t_k) = \frac{\mathcal{Z}_{t,k}^{IBC}\Delta_k}{4}\int_{-1}^{1}\frac{\alpha\ d\alpha}{\rho_k+\alpha\,\frac{\Delta_k}{2}\sin u_k} = \begin{cases} \frac{\mathcal{Z}_{t,k}^{IBC}}{\sin u_k}\ \left[1-\frac{4\,\rho_k}{\Delta_k}\,F_1^T(t_k)\right], \\ 0\,, \qquad \text{if}\ \ \sin u_k = 0\,, \end{cases} \qquad (3.37)$$

$$F_3^T(t_k) = \frac{\mathcal{Z}_{t,k}^{IBC}\Delta_k}{8}\int_{-1}^{1}\frac{\alpha^2\ d\alpha}{\rho_k+\alpha\,\frac{\Delta_k}{2}\sin u_k} = \begin{cases} \frac{-\mathcal{Z}_{t,k}^{IBC}\,\rho_k}{\Delta_k\sin u_k}\ F_2^T(t_k)\,, \\ \frac{\mathcal{Z}_{t,k}^{IBC}\,\Delta_k}{12\,\rho_k}\,, \quad \text{if}\ \ \sin u_k = 0\,, \end{cases} \qquad (3.38)$$

where the subscript k represents the observation segments $p-1$ and p associated with $T_i(t)$. For the integral F_{ij}^P in Eq. 3.29, applying Eqs. 2.51 and 2.57 one obtains

$$F_{ij}^{P} = \begin{cases} \frac{\mathcal{Z}_{\phi,i}^{IBC}\,\Delta_i}{2\,\rho_i^2}\int_{-1}^{1}\left(\rho_i + \alpha\,\frac{\Delta_i}{2}\sin u_i\right)\,d\alpha = \frac{\mathcal{Z}_{\phi,i}^{IBC}\,\Delta_i}{\rho_i}\,, & i = j\,, \\ 0\,, & i \neq j\,, \end{cases} \qquad (3.39)$$

where the subscript i characterizes the observation segment related to $P_i(t)$.

For the remaining integrals on Eqs. 3.24–3.27, the integrals with respect to t are evaluated using the approximation given by Eq. 2.58 and the integration variable t' is transformed into α using Eqs. 2.50–2.57. After straightforward algebraic manipulations, Eqs. 3.24–3.27 are finally rewritten as

$$
\begin{aligned}
Y_{ij}^{TT} = & \frac{-\pi}{\eta_o} F_{ij}^{T} - \frac{k_o^3}{8\eta_o} \sum_{k=p-1}^{p} \sum_{l=q-1}^{q} \left\{ \mathcal{Z}_{t,l}^{IBC} \Delta_k \Delta_l \left[[(\rho_l - \rho_k)\cos u_k - (z_l - z_k)\sin u_k] \right.\right. \\
& \times \left[G_{2a}(t_k, t_l) - (-1)^{q-l} G_{2b}(t_k, t_l) \right] + \frac{\Delta_l}{2} (\cos u_k \sin u_l - \sin u_k \cos u_l) \\
& \times \left[G_{2b}(t_k, t_l) - (-1)^{q-l} G_{2c}(t_k, t_l) \right] + \rho_l \cos u_k \left[G_{1a}(t_k, t_l) \right. \\
& \left.\left.\left. - (-1)^{q-l} G_{1b}(t_k, t_l) + \frac{\Delta_l \sin u_l}{2\,\rho_l} \left[G_{1b}(t_k, t_l) - (-1)^{q-l} G_{1c}(t_k, t_l) \right] \right] \right] \right\}, \qquad (3.40)
\end{aligned}
$$

$$
\begin{aligned}
Y_{ij}^{TP} = & \frac{j k_o^3}{4\eta_o} \mathcal{Z}_{\phi,j}^{IBC} \Delta_j \sum_{k=p-1}^{p} \left\{ \Delta_k \left[\rho_j \sin u_k \cos u_j - [\rho_k \cos u_k \right.\right. \\
& \left.\left. + (z_j - z_k)\sin u_k] \sin u_j \right] \left[G_{3a}(t_k, t_j) + \frac{\Delta_j \sin u_j}{2\,\rho_j} G_{3b}(t_k, t_j) \right] \right\}, \qquad (3.41)
\end{aligned}
$$

$$
\begin{aligned}
Y_{ij}^{PT} = & \frac{j k_o^3}{4\eta_o} \Delta_i \sum_{l=q-1}^{q} \left\{ \mathcal{Z}_{t,l}^{IBC} \Delta_l \left[(z_l - z_i) \left[G_{3a}(t_i, t_l) - (-1)^{q-l} G_{3b}(t_i, t_l) \right] \right.\right. \\
& \left.\left. + \frac{\Delta_l}{2} \cos u_l \left[G_{3b}(t_i, t_l) - (-1)^{q-l} G_{3c}(t_i, t_l) \right] \right] \right\}, \qquad (3.42)
\end{aligned}
$$

$$
\begin{aligned}
Y_{ij}^{PP} = & \frac{-\pi}{\eta_o} F_{ij}^{P} - \frac{k_o^3}{2\eta_o} \mathcal{Z}_{\phi,j}^{IBC} \Delta_i \Delta_j \left\{ \left[(\rho_j - \rho_i)\cos u_j - (z_j - z_i)\sin u_j \right] \right. \\
& \times \left[G_{2a}(t_i, t_j) + \frac{\Delta_j \sin u_j}{2\,\rho_j} G_{2b}(t_i, t_j) \right] \\
& \left. - \rho_i \cos u_j \left[G_{1a}(t_i, t_j) + \frac{\Delta_j \sin u_j}{2\,\rho_j} G_{1b}(t_i, t_j) \right] \right\}, \qquad (3.43)
\end{aligned}
$$

where $\mathcal{Z}_{t,l}^{IBC}$ and $\mathcal{Z}_{\phi,l}^{IBC}$ are located over the source segment l, $G_{va}(t_k, t_l)$ and $G_{vb}(t_k, t_l)$ are given by Eqs. 2.68 and 2.69 (with $v = 1, 2, 3$), respectively, $G_{vc}(t_k, t_l)$

is given by

$$G_{vc}(t_k, t_l) \;=\; \int_{-1}^{1} G_v(t_k, t_l)\; \alpha^2 \; d\alpha, \qquad v = 1, 2, 3\,, \tag{3.44}$$

and the distance R of G_H on Eqs. 3.30–3.32 is given by Eqs. 2.51, 2.52, and 2.63.

From Eqs. 3.40–3.43, one observes that for a particular mode m

$$\left(Y_{ij}^{TT}\right)_m \;=\; \left(Y_{ij}^{TT}\right)_{-m}, \tag{3.45}$$

$$\left(Y_{ij}^{TP}\right)_m \;=\; -\left(Y_{ij}^{TP}\right)_{-m}, \tag{3.46}$$

$$\left(Y_{ij}^{PT}\right)_m \;=\; -\left(Y_{ij}^{PT}\right)_{-m}, \tag{3.47}$$

$$\left(Y_{ij}^{PP}\right)_m \;=\; \left(Y_{ij}^{PP}\right)_{-m}, \tag{3.48}$$

such that the results for a positive mode m may be used to obtain the terms corresponding to the negative mode $-m$.

3.2.3 Numerical Evaluation of the IBC Impedance-Matrix Integrals

The numerical evaluation of the double integrals of Eqs. 3.40–3.43 follows the procedure adopted in Sect. 2.3.4. The integrals with respect to α and ϕ are evaluated using a n_α- and n_ϕ-Gaussian quadratures, respectively. On doing so, $G_{va}(t_k, t_l)$ and $G_{vb}(t_k, t_l)$ are evaluated from Eqs. 2.78 and 2.79 (with $v = 1, 2, 3$), respectively, and $G_{vc}(t_k, t_l)$ is given by

$$G_{vc}(t_k, t_l) \;=\; \sum_{\xi=1}^{n_\alpha} A_\xi \; \alpha_\xi^2 \; G_v(t_k, t_l), \qquad v = 1, 2, 3\,. \tag{3.49}$$

Furthermore, Eqs. 3.30–3.32 are evaluated from

$$G_1(t_k, t_l) = \pi \sum_{\beta=1}^{n_\phi} A_\beta \sin^2 \frac{\phi_\beta}{2} \cos m\phi_\beta \, G_H, \tag{3.50}$$

$$G_2(t_k, t_l) = \frac{\pi}{2} \sum_{\beta=1}^{n_\phi} A_\beta \cos\phi_\beta \cos m\phi_\beta \, G_H, \tag{3.51}$$

$$G_3(t_k, t_l) = \frac{\pi}{2} \sum_{\beta=1}^{n_\phi} A_\beta \sin\phi_\beta \sin m\phi_\beta \, G_H, \tag{3.52}$$

where ϕ_β is given by Eq. 2.83 and the distance R of G_H is given by Eqs. 2.84–2.86. As in Sect. 2.3.4, $n_\alpha = 2$ and n_ϕ is calculated from Eq. 2.92.

Numerical singularities arise in the evaluation of the above mentioned integrals whenever the observation point $\vec{r}$ is sufficiently close to the source point $\vec{r}'$. The singularities are removed using the three methods previously explained in Sect. 2.3.4. In the present case and when required, Method 1 is applied to the following α-integrals (see Eqs. 2.68, 2.69, 3.30–3.32, and 3.44):

$$G_a^H = \int_{-1}^{1} G_H \, d\alpha = G_{a1}^H + G_{a2}^H, \tag{3.53}$$

$$G_b^H = \int_{-1}^{1} G_H \, \alpha \, d\alpha = G_{b1}^H + G_{b2}^H, \tag{3.54}$$

$$G_c^H = \int_{-1}^{1} G_H \, \alpha^2 \, d\alpha = G_{c1}^H + G_{c2}^H, \tag{3.55}$$

where

$$G_{a1}^H = \int_{-1}^{1} \left(G_H - G_\Delta^H \right) d\alpha, \tag{3.56}$$

$$G_{a2}^H = \int_{-1}^{1} G_\Delta^H \, d\alpha, \tag{3.57}$$

$$G_{b1}^H = \int_{-1}^{1} \left(G_H - G_\Delta^H\right) \alpha \, d\alpha, \tag{3.58}$$

$$G_{b2}^H = \int_{-1}^{1} G_\Delta^H \, \alpha \, d\alpha, \tag{3.59}$$

$$G_{c1}^H = \int_{-1}^{1} \left(G_H - G_\Delta^H\right) \alpha^2 \, d\alpha, \tag{3.60}$$

$$G_{c2}^H = \int_{-1}^{1} G_\Delta^H \, \alpha^2 \, d\alpha, \tag{3.61}$$

G_H is given by Eq. 2.183, and

$$G_\Delta^H = \frac{1}{(k_o R)^3} + \frac{1}{2k_o R} - \frac{j}{3}. \tag{3.62}$$

The integrals of Eqs. 3.56, 3.58, and 3.60 do not present any singularities and may be numerically evaluated using a n_α-point Gaussian quadrature. In this case, the following relation is useful:

$$\begin{aligned} G_H - G_\Delta^H &= \frac{1 + jk_oR}{(k_oR)^3} e^{-jk_oR} - \frac{1}{(k_oR)^3} - \frac{1}{2k_oR} + \frac{j}{3} \\ &= \frac{\cos k_oR - 1 + \frac{(k_oR)^2}{2}}{(k_oR)^3} - j\left[\frac{\sin k_oR - k_oR + \frac{(k_oR)^3}{6}}{(k_oR)^3}\right] \\ &+ j\left[\frac{\cos k_oR - 1 + \frac{(k_oR)^2}{2}}{(k_oR)^2}\right] + \frac{\sin k_oR - k_oR}{(k_oR)^2}, \end{aligned} \tag{3.63}$$

from which one observes that no singularity is present when $R \to 0$. The integrals of Eqs. 3.57, 3.59, and 3.61 can be evaluated in closed form applying Eqs. 2.271 and 2.272 of Ref. [44]:

$$G_{a2}^H = \frac{2}{k_o \, \Delta_l} \alpha_1^H - j\frac{2}{3}, \tag{3.64}$$

$$G_{b2}^H = \left(\frac{2}{k_o \Delta_l}\right)^2 \left(\alpha_2^H - k\,\alpha_0\,\alpha_1^H\right), \tag{3.65}$$

$$G_{c2}^H = \left(\frac{2}{k_o \Delta_l}\right)^3 \left[\alpha_3^H - k\,\alpha_0 \left(\alpha_2^H - k\,\alpha_0\,\alpha_1^H\right)\right] - j\,\frac{2}{9}, \tag{3.66}$$

where

$$\alpha_1^H = \frac{\Delta_l}{2(k_o d)^2}\,\frac{1}{\alpha_4^E\,\alpha_5^E}\left[\alpha_4^E + \alpha_5^E - \frac{4\,\alpha_0^2}{\alpha_4^E + \alpha_5^E}\right] + \frac{1}{2}\,I_G^E, \tag{3.67}$$

$$\alpha_2^H = \frac{2k_o\alpha_0\Delta_l}{\alpha_4^E + \alpha_5^E}\left(\frac{1}{2} + \frac{1}{k_o^2\,\alpha_4^E\,\alpha_5^E}\right), \tag{3.68}$$

$$\alpha_3^H = \frac{\Delta_l}{2}\left[\left(\alpha_4^E + \alpha_5^E\right)\left(\frac{k_o^2}{4} - \frac{1}{\alpha_4^E\alpha_5^E}\right) - \frac{(k_o\alpha_0)^2}{\alpha_4^E + \alpha_5^E}\right] + \left[1 - \frac{(k_o d)^2}{4}\right] I_G^E, \tag{3.69}$$

and α_0, d^2, I_G^E, α_4^E, and α_5^E are given by Eqs. 2.105, 2.106, 2.109, 2.113, and 2.114, respectively. Finally, when Method 1 is required the integrals with respect to ϕ in Eqs. 2.68, 2.69, and 3.44 (with $\upsilon = 1, 2, 3$) are evaluated using the following n_ϕ-point Gaussian quadrature:

$$G_{1a,b,c}(t_k, t_l) = \pi \sum_{\beta=1}^{n_\phi} A_\beta\, G_{a,b,c}^H\, \sin^2\frac{\phi_\beta}{2}\, \cos m\phi_\beta, \tag{3.70}$$

$$G_{2a,b,c}(t_k, t_l) = \frac{\pi}{2} \sum_{\beta=1}^{n_\phi} A_\beta\, G_{a,b,c}^H\, \cos\phi_\beta\, \cos m\phi_\beta, \tag{3.71}$$

$$G_{3a,b,c}(t_k, t_l) = \frac{\pi}{2} \sum_{\beta=1}^{n_\phi} A_\beta\, G_{a,b,c}^H\, \sin\phi_\beta\, \sin m\phi_\beta, \tag{3.72}$$

where ϕ_β is given by Eq. 2.83 and G_a^H, G_b^H, and G_c^H are given by Eqs. 3.53–3.69 with $\phi = \phi_\beta$.

When Method 2 is required (see Sect. 2.3.4), the singularity elimination is applied to the integrals with respect to ϕ in Eqs. 3.30–3.32, where the singularities occur near the point $\phi = 0$. At this region, the integrand of Eq. 3.30 has the

approximate behavior

$$\lim_{\phi\to 0}\left[2\,\sin^2\frac{\phi}{2}\,\cos m\phi\,G_H\right] \;\approx\; \frac{\phi^2}{2k_o^3}\left[(\rho'-\rho_k)^2+(z'-z_k)^2+\rho_k\rho'\phi^2\right]^{-\frac{3}{2}}, \quad (3.73)$$

and, following the concepts explained in Sect. 2.3.4, $G_1(t_k,t_l)$ is then calculated by (from Eqs. 3.50 and 3.73):

$$\begin{aligned} G_1(t_k,t_l) \;&=\; \pi\sum_{\beta=1}^{n_\phi} A_\beta\,\sin^2\frac{\phi_\beta}{2}\,\cos m\phi_\beta\,G_H \;+\; \frac{1}{2}\,I_1 \\ &-\; \frac{\pi}{4}\sum_{\beta=1}^{n_\phi}\frac{A_\beta\phi_\beta^2}{k_o^3}\left[(\rho'-\rho_k)^2+(z'-z_k)^2+\rho_k\rho'\phi_\beta^2\right]^{-\frac{3}{2}}, \end{aligned} \quad (3.74)$$

where, from Eq. 2.272.4 of Ref. [44]

$$\begin{aligned} I_1 \;&=\; \int_0^\pi \frac{\phi^2}{k_o^3}\left[(\rho'-\rho_k)^2+(z'-z_k)^2+\rho_k\rho'\phi^2\right]^{-\frac{3}{2}}\,d\phi \\ &=\; \frac{1}{(k_o^2\rho_k\rho')^{\frac{3}{2}}}\left[\ln\left(v_1+\sqrt{1+v_1^2}\right)-\frac{v_1}{\sqrt{1+v_1^2}}\right], \end{aligned} \quad (3.75)$$

and ϕ_β, R, ρ', z', v_1, and G_H are given by Eqs. 2.83–2.86, 2.121, and 2.183, respectively. Similarly, the integrand of Eq. 3.31 is approximated as

$$\lim_{\phi\to 0}\left[\cos\phi\,\cos m\phi\,G_H\right] \;\approx\; \frac{1}{k_o^3}\left[(\rho'-\rho_k)^2+(z'-z_k)^2+\rho_k\rho'\phi^2\right]^{-\frac{3}{2}}, \quad (3.76)$$

and, from Eqs. 3.51 and 3.76, $G_2(t_k,t_l)$ is given by:

$$\begin{aligned} G_2(t_k,t_l) \;&=\; \frac{\pi}{2}\sum_{\beta=1}^{n_\phi} A_\beta\,\cos\phi_\beta\,\cos m\phi_\beta\,G_H \;+\; I_2 \\ &-\; \frac{\pi}{2}\sum_{\beta=1}^{n_\phi}\frac{A_\beta}{k_o^3}\left[(\rho'-\rho_k)^2+(z'-z_k)^2+\rho_k\rho'\phi_\beta^2\right]^{-\frac{3}{2}}, \end{aligned} \quad (3.77)$$

where, from Eq. 2.271.5 of Ref. [44]

$$\begin{aligned} I_2 &= \int_0^{\pi} \frac{1}{k_o^3} \left[(\rho' - \rho_k)^2 + (z' - z_k)^2 + \rho_k \rho' \phi^2\right]^{-\frac{3}{2}} \, d\phi \\ &= \frac{\pi}{k_o^3} \frac{\left[(\rho' - \rho_k)^2 + (z' - z_k)^2\right]^{-\frac{3}{2}}}{\sqrt{1 + v_1^2}} . \end{aligned} \tag{3.78}$$

Finally, the approximation for the integrand of Eq. 3.32 is

$$\lim_{\phi \to 0} \left[\sin\phi \, \sin m\phi \, G_H\right] \approx \frac{m\,\phi^2}{k_o^3} \left[(\rho' - \rho_k)^2 + (z' - z_k)^2 + \rho_k \rho' \phi^2\right]^{-\frac{3}{2}} , \tag{3.79}$$

and, from Eqs. 3.52 and 3.79, $G_3(t_k, t_l)$ is evaluated from:

$$\begin{aligned} G_3(t_k, t_l) &= \frac{\pi}{2} \sum_{\beta=1}^{n_\phi} A_\beta \, \sin\phi_\beta \, \sin m\phi_\beta \, G_H + m\, I_1 \\ &- \frac{m\pi}{2} \sum_{\beta=1}^{n_\phi} \frac{A_\beta \phi_\beta^2}{k_o^3} \left[(\rho' - \rho_k)^2 + (z' - z_k)^2 + \rho_k \rho' \phi_\beta^2\right]^{-\frac{3}{2}} , \end{aligned} \tag{3.80}$$

where I_1 is obtained from Eq. 3.75. So, when Method 2 is required, Eqs. 2.78, 2.79, and 3.49 (with $\upsilon = 1, 2, 3$) are evaluated using Eqs. 3.74, 3.77, and 3.80 instead of Eqs. 3.50–3.52.

Method 3 is applied whenever the observation segment k coincides with the source segment l (i.e., $k = l$). From Eqs. 2.68, 2.69, and 3.44 (with $\upsilon = 1, 2, 3$) one observes that the only integrals with a non-bounded integrand are $G_{1a}(t_k, t_l)$, $G_{2a}(t_k, t_l)$, $G_{3a}(t_k, t_l)$, $G_{2b}(t_k, t_l)$, and $G_{2c}(t_k, t_l)$. However, from Eqs. 3.40–3.43, $G_{2a}(t_k, t_l)$, $G_{3a}(t_k, t_l)$, $G_{2b}(t_k, t_l)$, and $G_{2c}(t_k, t_l)$ are multiplied by terms that vanish to zero whenever $k = l$ and, consequently, these integrals do not need to be calculated. So, Method 3 is only used in the evaluation of $G_{1a}(t_k, t_l)$. Following

the concepts of Sect. 2.3.4, at the region where both α and ϕ are close to zero, the integrand of $G_{1a}(t_k, t_l)$ is approximated as [from Eq. 2.68 (with $\upsilon = 1$) and 3.30]

$$\lim_{\alpha,\phi\to 0}\left[2\,\sin^2\frac{\phi}{2}\,\cos m\phi\,G_H\right] \;\approx\; \frac{\phi^2}{2k_o^3}\left[\left(\alpha\,\frac{\Delta_k}{2}\right)^2+(\rho_k\phi)^2\right]^{-\frac{3}{2}}, \tag{3.81}$$

and $G_{1a}(t_k, t_l)$ evaluated from

$$\begin{aligned} G_{1a}(t_k,t_l) &= \pi\sum_{\beta=1}^{n_\phi}A_\beta\,\sin^2\frac{\phi_\beta}{2}\,\cos m\phi_\beta\sum_{\xi=1}^{n_\alpha}A_\xi\,G_H\;+\;I_{1a} \\ &- \frac{\pi}{4}\sum_{\beta=1}^{n_\phi}A_\beta\,\phi_\beta^2\sum_{\xi=1}^{n_\alpha}\frac{A_\xi}{k_o^3}\left[\left(\alpha_\xi\,\frac{\Delta_k}{2}\right)^2+(\rho_k\phi_\beta)^2\right]^{-\frac{3}{2}}, \end{aligned} \tag{3.82}$$

where

$$\begin{aligned} I_{1a} &= \int_{-1}^{1}\int_{0}^{\pi}\frac{\phi^2}{2k_o^3}\left[\left(\alpha\,\frac{\Delta_k}{2}\right)^2+(\rho_k\phi)^2\right]^{-\frac{3}{2}}\,d\phi\;\,d\alpha \\ &= \frac{1}{(k_o\rho_k)^3}\,\ln\left(v_2+\sqrt{1+v_2^2}\right), \end{aligned} \tag{3.83}$$

and ϕ_β, R, v_2, and G_H are given by Eqs. 2.83, 2.84, 2.125, and 2.183, respectively. So, when Method 3 is required, $G_{1a}(t_k, t_l)$ is evaluated from Eq. 3.82 instead of Eqs. 2.78 (with $\upsilon = 1$) and 3.50.

3.2.4 Voltage-Matrix Evaluation for the Fundamental Mode of a Circular Waveguide

The purpose of the IBC introduced in this chapter is to provide a tool for modeling a corrugated horn feed. In the present work, the horn feed and, consequently, the PEC reflector surfaces of the antenna system are excited by the fundamental TE_{11}

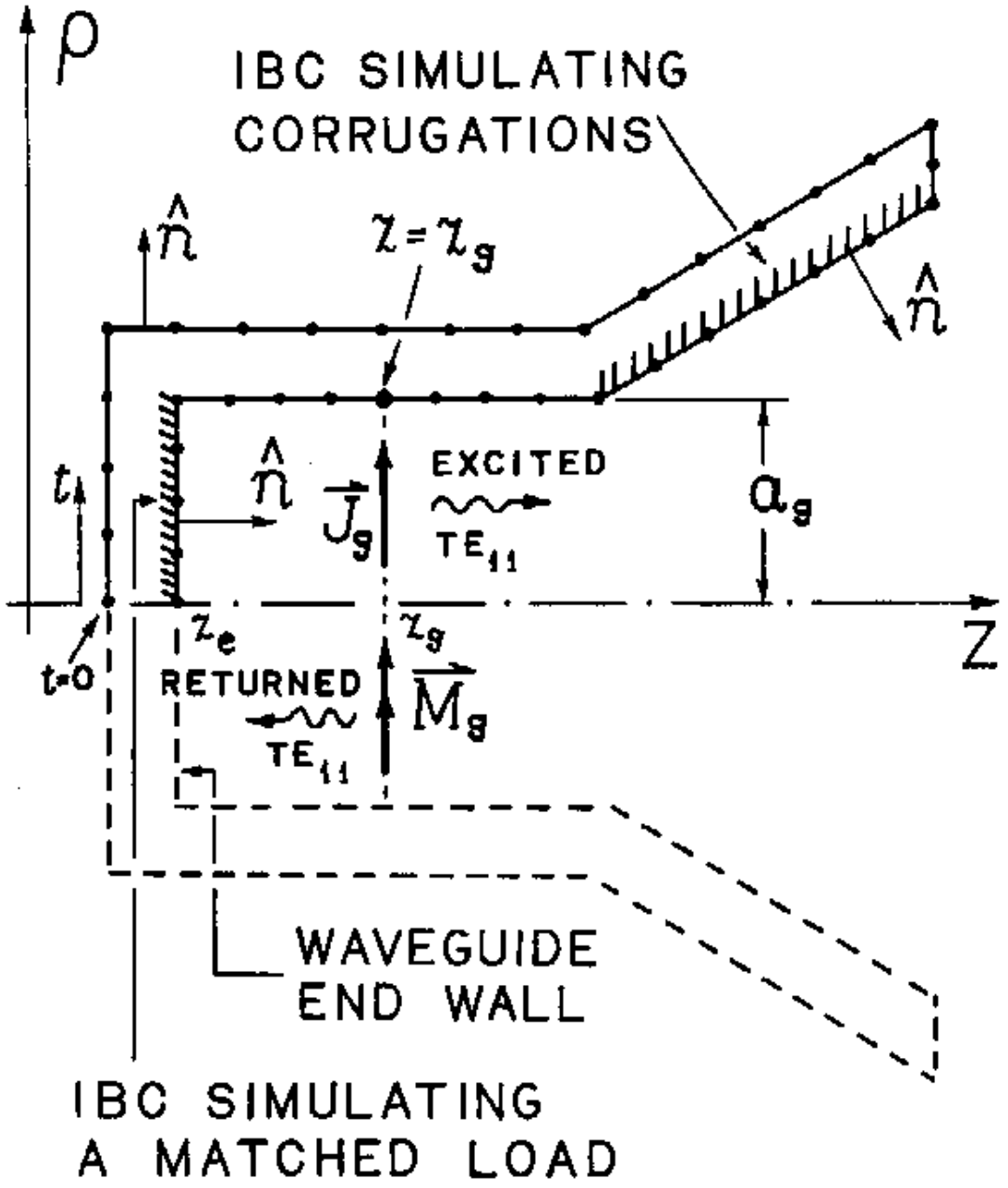

Figure 3.3: Equivalent Modal Currents Inside a Corrugated Horn.

mode of the circular waveguide connected to the horn throat (see Fig. 3.3). This circular waveguide has a cross-section radius a_g and is assumed to only allow the propagation of the TE_{11} mode. The formulation presented below also assumes that the feed points towards the positive $\hat{z}$-direction.

Accordingly to Ref. [34], the TE_{11} excitation may be simulated by a distribution of equivalent electric and magnetic currents represented as $\vec{J}_g(\vec{r})$ and $\vec{M}_g(\vec{r})$, respectively. These currents are placed inside the circular waveguide, over the cross-section plane located at $z = z_g$ (see Fig. 3.3). The currents are defined such that they only excite the fundamental TE_{11} mode towards the positive $\hat{z}$-direction at $z > z_g$ and no fields towards the negative $\hat{z}$-direction at $z < z_g$ (see Fig. 3.3).

The electromagnetic field of a $\hat{x}$-polarized TE_{11} mode is [47]

$$\begin{aligned}
\vec{E}_{TE_{11}}\Big|_{-}^{+} &= E_\rho\Big|_{-}^{+}\ \hat{\rho} + E_\phi\Big|_{-}^{+}\ \hat{\phi} \\
&= \frac{k_\rho}{\Lambda}\left[-\frac{J_1(k_\rho\,\rho)}{k_\rho\,\rho}\cos\phi\ \hat{\rho} + J_1'(k_\rho\,\rho)\sin\phi\ \hat{\phi}\right] e^{\mp j\sqrt{k_o^2-k_\rho^2}\,z}\,, \qquad (3.84) \\
\vec{H}_{TE_{11}}\Big|_{-}^{+} &= H_\rho\Big|_{-}^{+}\ \hat{\rho} + H_\phi\Big|_{-}^{+}\ \hat{\phi} + H_z\Big|_{-}^{+}\ \hat{z} \\
&= \pm\frac{1}{\mathcal{Z}_{TE}}\left(-E_\phi\Big|_{-}^{+}\ \hat{\rho} + E_\rho\Big|_{-}^{+}\ \hat{\phi}\right) \\
&\quad - \frac{jk_\rho^2}{\Lambda\omega\mu_o}J_1(k_\rho\,\rho)\sin\phi\ e^{\mp j\sqrt{k_o^2-k_\rho^2}\,z}\,, \qquad (3.85)
\end{aligned}$$

where the positive and negative indices correspond to the TE_{11} mode propagating towards the positive and negative $\hat{z}$-direction, respectively,

$$\Lambda = J_1(k_\rho\,a_g)\sqrt{\frac{\pi}{4}\,\frac{(k_\rho\,a_g)^2-1}{\mathcal{Z}_{TE}}}\,, \qquad (3.86)$$

$$\mathcal{Z}_{TE} = \frac{\omega\mu_o}{\sqrt{k_o^2 - k_\rho^2}} = \frac{k_o\eta_o}{\sqrt{k_o^2 - k_\rho^2}}\,, \tag{3.87}$$

$$k_\rho = \frac{1.84118}{a_g}\,, \tag{3.88}$$

$$J_1(k_\rho\, a_g) = 0.58187\,, \tag{3.89}$$

$J_1(x)$ is the Bessel function of the first order, and $J_1'(x)$ its first derivative with respect to the argument x. The field components of Eqs. 3.84 and 3.85 have been normalized by the parameter Λ such that the power associated with the TE_{11} mode is 1 Watt. From Ref. [34] and Eqs. 3.84 and 3.85, the modal currents $\vec{J}_g(\vec{r})$ and $\vec{M}_g(\vec{r})$ are derived using equivalence and given by

$$\begin{aligned}\vec{J}_g(\vec{r}) &= \hat{z}\times\vec{H}^+_{TE_{11}} = \frac{k_\rho}{\Lambda\mathcal{Z}_{TE}}\left[\frac{J_1(k_\rho\,\rho)}{k_\rho\,\rho}\,\cos\phi\;\hat{\rho}\right.\\ &- \left. J_1'(k_\rho\,\rho)\,\sin\phi\;\hat{\phi}\right] e^{-j\sqrt{k_o^2-k_\rho^2}\,z_g}\,, \qquad \rho\le a_g\,,\end{aligned} \tag{3.90}$$

$$\vec{M}_g(\vec{r}) = -\hat{z}\times\vec{E}^+_{TE_{11}} = \mathcal{Z}_{TE}\;\hat{z}\times\vec{J}_g(\vec{r})\,, \qquad \rho\le a_g\,. \tag{3.91}$$

Once the horn feed and the reflector surfaces are substituted by their equivalent surface currents $\vec{J}(\vec{r}\,')$ and $\vec{M}(\vec{r}\,')$ [where $\vec{M}(\vec{r}\,')$ is only present over the horn-surface regions with an IBC], the EFIE (Eq. 2.8) can be used with $\vec{E}^{inc}(\vec{r})$ produced by the above $\vec{J}_g(\vec{r})$ and $\vec{M}_g(\vec{r})$ radiating in free space. From Eq. 116a in Chap. 3 of Ref. [21]:

$$\vec{E}^{inc}(\vec{r}) = \frac{-j}{4\pi\omega\epsilon_o}\int_{S_g}\left[j\omega\,\rho_E(\vec{r}\,')\,\nabla'\Psi + k_o^2\,\vec{J}_g(\vec{r}\,')\,\Psi - j\omega\epsilon_o\,\vec{M}_g(\vec{r}\,')\times\nabla'\Psi\right]\,ds', \tag{3.92}$$

where S_g is the circular area of radius a_g at $z = z_g$ containing the equivalent modal

currents and $\rho_E(\vec{r}\,')$ is the electric charge density [present along the rim of S_g and caused by the abrupt termination of $\vec{J}_g(\vec{r}\,')$ at the waveguide wall]. Although the continuity equation could be used to express $\rho_E(\vec{r}\,')$ directly in terms of $\vec{J}_g(\vec{r}\,')$ in Eq. 3.92, the resulting expression turns out to be arduous to solve numerically [21]. On the contrary, the continuity equation is used to represent $\rho_E(\vec{r}\,')$ only along the rim of S_g as [21]

$$\rho_E(\vec{r}\,') \;=\; \frac{-j}{\omega}\,\hat{\rho}\cdot\vec{J}_g(\rho'=a_g,z'=z_g) \;=\; \frac{j}{\omega}\,H_\phi^+(\rho'=a_g,z'=z_g)\,, \tag{3.93}$$

where H_ϕ^+ is given by Eq. 3.85. The substitution of Eq. 3.93 into Eq. 3.92 yields

$$\begin{aligned}\vec{E}^{inc}(\vec{r}) \;&=\; \frac{-j}{4\pi\omega\epsilon_o}\int\limits_{S_g}\Big[k_o^2\,\vec{J}_g(\vec{r}\,')\,\Psi - j\omega\epsilon_o\,\vec{M}_g(\vec{r}\,')\times\nabla'\Psi\Big]\,ds' \\ &+\; \frac{j}{4\pi\omega\epsilon_o}\int\limits_{C_g} H_\phi^+\,\nabla'\Psi\,d\ell'\,,\end{aligned} \tag{3.94}$$

where C_g represents the rim of the surface S_g. Applying Eqs. 2.170, 2.172, 2.173, 3.90, and 3.91 to Eq. 3.94 one obtains

$$\begin{aligned}\vec{E}^{inc}(\vec{r}) \;&=\; \frac{j\eta_o k_o^2}{4\pi}\int_0^{2\pi}\!\!\int_0^{a_g}\Bigg\{\Big[G_E+\frac{jk_o\mathcal{Z}_{TE}}{\eta_o}\,(z_g-z)\,G_H\Big]\Big[\Big[H_\rho^+\sin(\phi'-\phi) \\ &+\; H_\phi^+\cos(\phi'-\phi)\Big]\hat{\rho}+\Big[H_\phi^+\sin(\phi'-\phi)-H_\rho^+\cos(\phi'-\phi)\Big]\hat{\phi}\Big] \\ &-\; \frac{jk_o\mathcal{Z}_{TE}}{\eta_o}\Big[H_\phi^+\,[\rho'-\rho\cos(\phi'-\phi)]-H_\rho^+\,\rho\sin(\phi'-\phi)\Big]G_H\,\hat{z}\Bigg\}\,\rho'\,d\rho'\,d\phi' \\ &+\; \frac{j\eta_o k_o^2}{4\pi}\int_0^{2\pi} H_\phi^+\Big\{[\rho-a_g\cos(\phi'-\phi)]\,\hat{\rho}-a_g\sin(\phi'-\phi)\,\hat{\phi} \\ &-\; (z_g-z)\,\hat{z}\Big\}\,G_H\,a_g\,d\phi'\,,\end{aligned} \tag{3.95}$$

where the unprimed coordinates refer to the observation point $\vec{r}$, H_ρ^+ is given by Eq. 3.85, and G_E and G_H are given by Eqs. 2.182 and 2.183, respectively. The

magnetic field radiated by the equivalent modal currents will be also required in Sect. 3.3 to obtain the expressions for the total field radiated by the horn feed. So, from Eq. 116b in Chap. 3 of Ref. [21] and proceeding in the same way done to obtain Eq. 3.95, the magnetic field radiated by $\vec{J}_g(\vec{r}\,')$ and $\vec{M}_g(\vec{r}\,')$ is given by

$$\begin{aligned}
\vec{H}^{inc}(\vec{r}) &= \frac{-j}{4\pi\omega\mu_o}\int\limits_{S_g}\Big[k_o^2\,\vec{M}_g(\vec{r}\,')\,\Psi + j\omega\mu_o\,\vec{J}_g(\vec{r}\,')\times\nabla'\Psi\Big]\;ds' \\
&= \frac{-jk_o^2}{4\pi}\int\limits_0^{2\pi}\int\limits_0^{a_g}\Bigg\{\left[\frac{\mathcal{Z}_{TE}}{\eta_o}\,G_E + jk_o\,(z_g-z)\,G_H\right]\Big[\Big[H_\phi^+\sin(\phi'-\phi) \\
&- H_\rho^+\cos(\phi'-\phi)\Big]\,\hat{\rho} - \Big[H_\rho^+\sin(\phi'-\phi) + H_\phi^+\cos(\phi'-\phi)\Big]\,\hat{\phi}\Big] \\
&+ jk_o\,H_z^+\Big[[\rho-\rho'\cos(\phi'-\phi)]\,\hat{\rho} - \rho'\sin(\phi'-\phi)\,\hat{\phi} - (z_g-z)\,\hat{z}\Big]\,G_H \\
&+ jk_o\Big[H_\rho^+\,[\rho'-\rho\cos(\phi'-\phi)] + H_\phi^+\,\rho\sin(\phi'-\phi)\Big]G_H\,\hat{z}\Bigg\}\rho'\,d\rho'\,d\phi', \qquad (3.96)
\end{aligned}$$

where H_z^+ is given by Eq. 3.85. Notice from Eq. 3.91 that $\hat{\rho}\cdot\vec{M}_g(\vec{r}\,')$ is zero at $\rho' = a_g$ and for this reason Eq. 3.96 has no contributions from equivalent magnetic charge distributions over C_g.

One obtains the voltage matrix of Eq. 2.23 by substituting Eq. 3.95 into Eqs. 2.24 and 2.25 to get

$$\begin{aligned}
V_i^T &= \frac{jk_o^2}{4\pi}\int\limits_0^{2\pi}\int\limits_t\int\limits_0^{2\pi}\int\limits_0^{a_g} T_i(t)\,e^{-jm\phi}\Bigg\{\left[G_E + \frac{jk_o\mathcal{Z}_{TE}}{\eta_o}\,(z_g-z)\,G_H\right]\Big[\Big[H_\rho^+\sin(\phi'-\phi) \\
&+ H_\phi^+\cos(\phi'-\phi)\Big]\,\sin u - \frac{jk_o\mathcal{Z}_{TE}}{\eta_o}\Big[H_\phi^+\,[\rho'-\rho\cos(\phi'-\phi)] - H_\rho^+\,\rho\sin(\phi'-\phi)\Big] \\
&\times G_H\,\cos u\Bigg\}\rho'\,d\rho'\,d\phi'\,dt\,d\phi \;+\; \frac{jk_o^2}{4\pi}\int\limits_0^{2\pi}\int\limits_t\int\limits_0^{2\pi} T_i(t)\,e^{-jm\phi}\,G_H\;H_\phi^+ \\
&\times\Big\{[\rho - a_g\cos(\phi'-\phi)]\,\sin u - (z_g-z)\,\cos u\Big\}\,a_g\,d\phi'\,dt\,d\phi\,, \qquad (3.97)
\end{aligned}$$

$$V_i^P = \frac{jk_o^2}{4\pi} \int_0^{2\pi} \int_t^{2\pi} \int_0^{2\pi} \int_0^{a_g} P_i(t)\, \frac{\rho}{\rho_i}\, e^{-jm\phi} \left[G_E + \frac{jk_o \mathcal{Z}_{TE}}{\eta_o} (z_g - z)\, G_H \right]$$
$$\times \left[H_\phi^+ \sin(\phi' - \phi) - H_\rho^+ \cos(\phi' - \phi) \right] \rho'\, d\rho'\, d\phi'\, dt\, d\phi$$
$$- \frac{jk_o^2}{4\pi} \int_0^{2\pi} \int_t^{2\pi} \int_0^{2\pi} P_i(t)\, \frac{\rho}{\rho_i}\, e^{-jm\phi}\, G_H\, H_\phi^+\, \sin(\phi' - \phi)\, a_g^2\, d\phi'\, dt\, d\phi\,. \tag{3.98}$$

Substituting Eqs. 3.84 and 3.85 into Eqs. 3.97 and 3.98 and solving the integrals with respect to ϕ' using Eq. 2.41, one obtains that V_i^T and V_i^P are different from zero only when $m = \pm 1$ and

$$V_i^T = \frac{-jk_\rho\, k_o^2}{2\Lambda \mathcal{Z}_{TE}}\, e^{-j\frac{\eta_o k_o}{\mathcal{Z}_{TE}} z_g} \int_t^{a_g} \int_0^{a_g} T_i(t) \left\{ \frac{J_1(k_\rho\, \rho')}{k_\rho\, \rho'} \left[\sin u \left(G_5(t, \rho') + \frac{jk_o \mathcal{Z}_{TE}}{\eta_o} (z_g - z) \right.\right.\right.$$
$$\left.\left.\left. \times\, G_2(t, \rho') \right) - \frac{jk_o \mathcal{Z}_{TE}}{\eta_o} \cos u \left(\rho'\, G_1(t, \rho') + (\rho' - \rho)\, G_2(t, \rho') \right) \right]$$
$$+\, m\, J_1'(k_\rho\, \rho') \left[\sin u \left(G_6(t, \rho') + \frac{jk_o \mathcal{Z}_{TE}}{\eta_o} (z_g - z)\, G_3(t, \rho') \right) \right.$$
$$\left. + \frac{jk_o \mathcal{Z}_{TE}}{\eta_o} \rho \cos u\, G_3(t, \rho') \right] \Bigg\} \rho'\, d\rho'\, dt$$
$$- \frac{jk_\rho\, k_o^2}{2\Lambda \mathcal{Z}_{TE}}\, e^{-j\frac{\eta_o k_o}{\mathcal{Z}_{TE}} z_g}\, a_g\, \frac{J_1(k_\rho\, a_g)}{k_\rho\, a_g} \int_t T_i(t) \left\{ \sin u \left[\rho\, G_1(t, a_g) - (a_g - \rho) \right.\right.$$
$$\left.\left. \times\, G_2(t, a_g) \right] - (z_g - z) \cos u \left[G_1(t, a_g) + G_2(t, a_g) \right] \right\} dt\,, \quad m = \pm 1\,, \tag{3.99}$$

$$V_i^P = \frac{k_\rho\, k_o^2}{2\Lambda \mathcal{Z}_{TE}}\, e^{-j\frac{\eta_o k_o}{\mathcal{Z}_{TE}} z_g} \int_t^{a_g} \int_0^{a_g} P_i(t)\, \frac{\rho}{\rho_i} \left\{ \frac{J_1(k_\rho\, \rho')}{k_\rho\, \rho'} \left[G_6(t, \rho') + \frac{jk_o \mathcal{Z}_{TE}}{\eta_o} (z_g - z) \right.\right.$$
$$\left.\left. \times\, G_3(t, \rho') \right] + m\, J_1'(k_\rho\, \rho') \left[G_5(t, \rho') + \frac{jk_o \mathcal{Z}_{TE}}{\eta_o} (z_g - z)\, G_2(t, \rho') \right] \right\} \rho'\, d\rho'\, dt$$
$$- \frac{k_\rho\, k_o^2}{2\Lambda \mathcal{Z}_{TE}}\, e^{-j\frac{\eta_o k_o}{\mathcal{Z}_{TE}} z_g}\, a_g^2\, \frac{J_1(k_\rho\, a_g)}{k_\rho\, a_g} \int_t P_i(t)\, \frac{\rho}{\rho_i}\, G_3(t, a_g)\, dt\,, \quad m = \pm 1\,, \tag{3.100}$$

where $G_1(t, \rho')$, $G_2(t, \rho')$, $G_3(t, \rho')$, $G_5(t, \rho')$, and $G_6(t, \rho')$ are respectively given by Eqs. 3.30–3.32, 2.46, and 2.47. The variable of integration t may be transformed into α applying the same procedure used to evaluate the integrals with respect to

t' in Sects. 2.3.3 and 3.2.2. From Eqs. 2.50–2.57 [for the weighting functions $T_i(t)$ and $P_i(t)$], Eqs. 3.99 and 3.100 may be rewritten as

$$
\begin{aligned}
V_i^T \;=\; & \frac{-jk_\rho\, k_o^2}{2\Lambda \mathcal{Z}_{TE}}\, e^{-j\frac{\eta_o k_o}{\mathcal{Z}_{TE}} z_g} \int_0^{a_g} \Bigg\{ \sum_{k=p-1}^{p} \frac{\Delta_k}{4} \Bigg[\frac{J_1(k_\rho\,\rho')}{k_\rho\,\rho'} \Bigg(\sin u_k \Big[G_{5a}(t_k,\rho') \\
& - (-1)^{p-k} G_{5b}(t_k,\rho') \Big] - \frac{jk_o \mathcal{Z}_{TE}}{\eta_o} \Bigg(\rho' \cos u_k \Big[G_{1a}(t_k,\rho') - (-1)^{p-k} G_{1b}(t_k,\rho') \Big] \\
& + \left[(\rho' - \rho_k) \cos u_k - (z_g - z_k) \sin u_k \right] \Big[G_{2a}(t_k,\rho') - (-1)^{p-k} G_{2b}(t_k,\rho') \Big] \Bigg) \Bigg) \\
& + m\, J_1'(k_\rho\,\rho') \Bigg(\sin u_k \Big[G_{6a}(t_k,\rho') - (-1)^{p-k} G_{6b}(t_k,\rho') \Big] + \frac{jk_o \mathcal{Z}_{TE}}{\eta_o} \left[\rho_k \cos u_k \right. \\
& \left. + \; (z_g - z_k) \sin u_k \right] \Big[G_{3a}(t_k,\rho') - (-1)^{p-k} G_{3b}(t_k,\rho') \Big] \Bigg) \Bigg] \Bigg\}\, \rho'\, d\rho' \\
& - \frac{jk_\rho\, k_o^2}{2\Lambda \mathcal{Z}_{TE}}\, e^{-j\frac{\eta_o k_o}{\mathcal{Z}_{TE}} z_g}\, a_g\, \frac{J_1(k_\rho\, a_g)}{k_\rho\, a_g} \sum_{k=p-1}^{p} \frac{\Delta_k}{4} \Bigg\{ \Big[\rho_k \sin u_k - (z_g - z_k) \cos u_k \Big] \\
& \times \Big[G_{1a}(t_k,a_g) + G_{2a}(t_k,a_g) - (-1)^{p-k} \left[G_{1b}(t_k,a_g) + G_{2b}(t_k,a_g) \right] \Big] \\
& + \frac{\Delta_k}{2} \Big[G_{1b}(t_k,a_g) + G_{2b}(t_k,a_g) - (-1)^{p-k} \left[G_{1c}(t_k,a_g) + G_{2c}(t_k,a_g) \right] \Big] \\
& - a_g \sin u_k \Big[G_{2a}(t_k,a_g) - (-1)^{p-k} G_{2b}(t_k,a_g) \Big] \Bigg\}, \qquad m = \pm 1\,, \qquad (3.101)
\end{aligned}
$$

$$
\begin{aligned}
V_i^P \;=\; & \frac{k_\rho\, k_o^2}{2\Lambda \mathcal{Z}_{TE}}\, e^{-j\frac{\eta_o k_o}{\mathcal{Z}_{TE}} z_g}\, \frac{\Delta_i}{2} \int_0^{a_g} \Bigg\{ \frac{J_1(k_\rho\,\rho')}{k_\rho\,\rho'} \Bigg[G_{6a}(t_i,\rho') + \frac{\Delta_i \sin u_i}{2\,\rho_i}\, G_{6b}(t_i,\rho') \\
& + \frac{jk_o \mathcal{Z}_{TE}}{\eta_o} \Bigg((z_g - z_i) \Big[G_{3a}(t_i,\rho') + \frac{\Delta_i \sin u_i}{2\,\rho_i}\, G_{3b}(t_i,\rho') \Big] - \frac{\Delta_i}{2} \cos u_i \\
& \times \Big[G_{3b}(t_i,\rho') + \frac{\Delta_i \sin u_i}{2\,\rho_i}\, G_{3c}(t_i,\rho') \Big] \Bigg) \Bigg] \;+\; m\, J_1'(k_\rho\,\rho') \Bigg[G_{5a}(t_i,\rho') \\
& + \frac{\Delta_i \sin u_i}{2\,\rho_i}\, G_{5b}(t_i,\rho') + \frac{jk_o \mathcal{Z}_{TE}}{\eta_o} \Bigg((z_g - z_i) \Big[G_{2a}(t_i,\rho') + \frac{\Delta_i \sin u_i}{2\,\rho_i}\, G_{2b}(t_i,\rho') \Big] \\
& - \frac{\Delta_i}{2} \cos u_i \Big[G_{2b}(t_i,\rho') + \frac{\Delta_i \sin u_i}{2\,\rho_i}\, G_{2c}(t_i,\rho') \Big] \Bigg) \Bigg] \Bigg\}\, \rho'\, d\rho' \\
& - \frac{k_\rho\, k_o^2}{2\Lambda \mathcal{Z}_{TE}}\, e^{-j\frac{\eta_o k_o}{\mathcal{Z}_{TE}} z_g}\, a_g^2\, \frac{J_1(k_\rho\, a_g)}{k_\rho\, a_g}\, \frac{\Delta_i}{2} \\
& \times \Big[G_{3a}(t_i,a_g) + \frac{\Delta_i \sin u_i}{2\,\rho_i}\, G_{3b}(t_i,a_g) \Big]\,, \qquad m = \pm 1\,, \qquad (3.102)
\end{aligned}
$$

where $G_{va}(t_k,\rho')$, $G_{vb}(t_k,\rho')$, and $G_{vc}(t_k,\rho')$ (with $v = 1,2,3,5,6$) are given by Eqs. 2.68, 2.69, and 3.44, respectively, and the subscript k represents the observation segments $p-1$, p, and i. Notice that here the distance R is given by

$$R = \left[\left(\rho' - \rho_k - \alpha\,\frac{\Delta_k}{2}\,\sin u_k\right)^2 + \left(z_g - z_k - \alpha\,\frac{\Delta_k}{2}\,\cos u_k\right)^2 + 4\,\rho'\left(\rho_k + \alpha\,\frac{\Delta_k}{2}\,\sin u_k\right)\sin^2\frac{\phi}{2}\right]^{\frac{1}{2}}, \tag{3.103}$$

where ρ' varies from 0 to a_g (being equal to a_g for the terms associated with the equivalent electric charge density). Finally, to evaluate the integrals with respect to ρ' in Eqs. 3.101 and 3.102 one may apply the following approximation:

$$\int_0^{a_g} F(\rho')\,d\rho' \approx \Delta_g \sum_{n_g=1}^{N_g} F(\rho_{n_g}), \tag{3.104}$$

where

$$\Delta_g = \frac{a_g}{N_g}, \tag{3.105}$$

$$\rho_{n_g} = \left(n_g - \frac{1}{2}\right)\Delta_g, \tag{3.106}$$

and $N_g = 50$ in this work.

The integrals $G_{va}(t_k,\rho')$, $G_{vb}(t_k,\rho')$, and $G_{vc}(t_k,\rho')$ (with $v = 1,2,3,5,6$) of Eqs. 3.101 and 3.102 are evaluated in the same way done in Sects. 2.3.4 and 3.2.3, where the present case does not require the application of Method 3. However, to avoid possible numerical difficulties whenever $\rho' = a_g$, the surface S_g is placed in between two adjacent generating-curve segments representing the waveguide internal wall (where $\rho = a_g$ and $z = z_g$), as illustrated in Fig. 3.3.

As a final comment, from Eqs. 3.101 and 3.102 one observes that Eqs. 2.159 and 2.160 are still valid for the TE_{11} modal excitation. Consequently, from Eqs. 2.23, 2.70–2.73, 3.7, and 3.45–3.48, Eqs. 2.161 and 2.162 are also valid in this case.

3.2.5 Resonance Problems

When the EFIE of Eq. 2.8 is applied over the BOR closed surface representing the horn feed, one may experience resonance problems. These problems are caused by the modes that can be excited inside the cavity described by the closed surface. These modes also satisfy the surface boundary conditions related to Eq. 2.8 at a particular frequency [15], and their currents do not radiate outside the cavity. The final consequence is that, when the resonant cavity modes are excited, the currents $\vec{J}(\vec{r}')$ and $\vec{M}(\vec{r}')$ induced over the BOR closed surface will have spurious components related to these internal modes. Since these cavity-mode currents can be substantially larger then the currents of interest, numerical instability may occur. One way to avoid this resonance problem is to apply a combination of the Electric and Magnetic Field Integral Equations [15]. However, this problem can be corrected without complicating the previously presented formulation, as explained below.

The resonance problems are eliminated by extending the weighting functions of Eq. 2.22 over dummy observation segments located inside the BOR closed surface (see Fig. 3.4) and enforcing the tangential electric field to be zero over these segments [48]. On doing so, for the efficient elimination of the resonances, the dummy

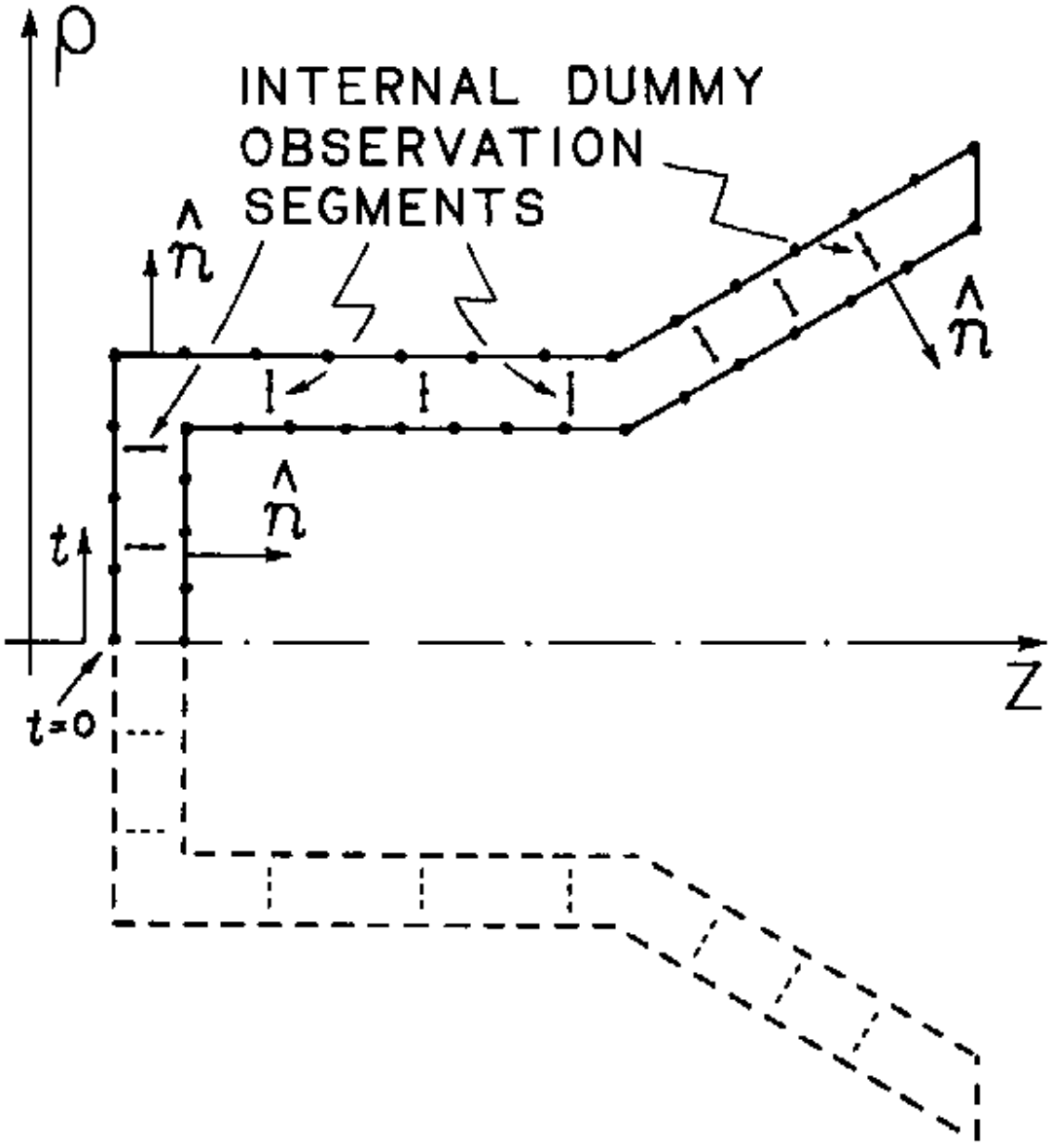

Figure 3.4: Geometry of a BOR Closed Surface Representing a Horn Feed with Internal Dummy Observation Segments.

segments must be judiciously placed. For example, in the geometry of Fig. 3.4 the dummy segments are placed perpendicular to the inner and outer surfaces of the feed, because this is the expected orientation of the electric field (if present) inside the cavity. The proper location and number of dummy segments will depend on the geometry being analyzed and this is the major disadvantage of the procedure. However, the resonance problem can be detected by inspecting the surface-current behavior after the MoM analysis. For example, assuming that the circular waveguide allows only the propagation of the fundamental TE_{11} mode and a matched load is placed over the waveguide end wall, at the waveguide surface between the planes $z = z_e$ and $z = z_g$ (see Fig. 3.3) the current amplitude must be constant. An oscillatory behavior of the current at this region is a clear indication that either resonances are present (and the number of internal dummy segments must be increased) or the number of basis functions representing the surface currents is insufficient. In all cases analyzed by the author to the present moment, the resonance detection and correction was successfully accomplished by this procedure.

In order to use the dummy segments, the weighting functions are now represented as

$$\vec{W}(\vec{r}) \;=\; \sum_i \vec{W}_i(\vec{r}) \;+\; \sum_\tau \vec{W}_\tau(\vec{r}) \;, \tag{3.107}$$

where $\vec{W}_i(\vec{r})$ represents the usual weighting functions over the BOR surfaces and $\vec{W}_\tau(\vec{r})$ represents the extended weighting functions over the internal dummy segments. $\vec{W}_\tau(\vec{r})$ is also given by Eq. 2.22 with the subscript i changed into τ. As no

field must be present inside the BOR closed surface, Eq. 2.8 may still be applied to enforce zero tangential electric field over the internal dummy surfaces (being assumed PEC). From the procedure adopted on Sects. 2.3.1 and 3.2.1, when the extended weighting functions $\vec{W}_\tau(\vec{r})$ are used, Eq. 2.23 (with the impedance matrix given by Eq. 3.7) is rewritten as

$$\begin{bmatrix} V^T \\ V^P \\ V^T_{ext} \\ V^P_{ext} \end{bmatrix} = \begin{bmatrix} Z^{TT}_{IBC} & Z^{TP}_{IBC} \\ Z^{PT}_{IBC} & Z^{PP}_{IBC} \\ Z^{TT}_{ext} & Z^{TP}_{ext} \\ Z^{PT}_{ext} & Z^{PP}_{ext} \end{bmatrix} \begin{bmatrix} I^T \\ I^P \end{bmatrix}. \tag{3.108}$$

In Eq. 3.108, the elements of the sub-matrices V^T_{ext} and V^P_{ext} are given by Eqs. 2.24 and 2.25, respectively, with the integration surface S representing the dummy observation segments, the subscript i replaced by τ, and N_T and N_P replaced by $N_{T_{ext}}$ (the total number of extended triangles) and $N_{P_{ext}}$ (the total number of extended pulses), respectively. The evaluation of V^T_{ext} and V^P_{ext} follows exactly the procedures of Sects. 2.3.5 (for a spherical-wave source) and 3.2.4 (for the TE_{11} excitation). Likewise, the elements of the sub-matrices Z^{TT}_{ext}, Z^{TP}_{ext}, Z^{PT}_{ext}, and Z^{PP}_{ext} are given by Eqs. 3.8–3.11, respectively, with the subscript i replaced by τ. The evaluation of these extended impedance-matrix elements follows the procedures of Sects. 2.3.3 and 3.2.2.

Finally, Eq. 3.108 turns out to be an overdetermined system of linear equations. In this work, the Moore-Penrose pseudo-inverse technique is applied to provide the

minimum-norm least squares solution [48]. This technique consists of multiplying both sides of Eq. 3.108 by the transpose-conjugate of the impedance matrix:

$$[Z^*]^T\,[V] \;=\; [Z^*]^T\,[Z]\,[I]\;, \tag{3.109}$$

where the symbol $*$ denotes the complex conjugate and the superscript T represents the transpose matrix. The new system represented by Eq. 3.109 has a square matrix and the electric-current coefficients of Eq. 2.21 may be finally obtained.

3.3 Radiated Near-Zone Fields

In the case where an IBC and, consequently, $\vec{M}(\vec{r}\,')$ are present, the total electric and magnetic near-zone fields radiated by the antenna system are given by

$$\vec{E}_{NF}(\vec{r}) \;=\; \vec{E}^J_{NF}(\vec{r}) \;+\; \vec{E}^M_{NF}(\vec{r}) \;+\; \vec{E}^{inc}_{NF}(\vec{r})\;, \tag{3.110}$$

$$\vec{H}_{NF}(\vec{r}) \;=\; \vec{H}^J_{NF}(\vec{r}) \;+\; \vec{H}^M_{NF}(\vec{r}) \;+\; \vec{H}^{inc}_{NF}(\vec{r})\;, \tag{3.111}$$

where $\vec{E}^{inc}_{NF}(\vec{r})$ and $\vec{H}^{inc}_{NF}(\vec{r})$ are the electric and magnetic fields produced by the external sources, respectively, $\vec{E}^J_{NF}(\vec{r})$ and $\vec{H}^J_{NF}(\vec{r})$ are the electric and magnetic fields radiated by the electric current $\vec{J}(\vec{r}\,')$ (given by Eqs. 2.185–2.198), respectively, and $\vec{E}^M_{NF}(\vec{r})$ and $\vec{H}^M_{NF}(\vec{r})$ are the electric and magnetic fields radiated by the magnetic current $\vec{M}(\vec{r}\,')$, respectively. The later are given from Eqs. 120 and 121 in Chap. 3 of Ref. [21] as

$$\vec{E}^M_{NF}(\vec{r}) \;=\; \frac{-1}{4\pi}\int\limits_{S'} \vec{M}(\vec{r}\,') \times \nabla'\Psi\; ds'\,, \tag{3.112}$$

$$\vec{H}^M_{NF}(\vec{r}) \;=\; \frac{-j}{4\pi\omega\mu_o}\int\limits_{S'}\Big\{\Big[\vec{M}(\vec{r}\,')\cdot\nabla'\Big]\,\nabla'\Psi \;+\; k_o^2\,\vec{M}(\vec{r}\,')\,\Psi\Big\}\;ds'\,, \quad (3.113)$$

where Ψ is given by Eq. 2.4. Applying Eqs. 2.167–2.173 [with $\vec{J}(\vec{r}\,')$ substituted by $\vec{M}(\vec{r}\,')$] and 3.5 into Eqs. 3.112 and 3.113, straightforward algebraic manipulations yield

$$\vec{E}^M_{NF}(\vec{r}) \;=\; E^M_{NF\rho}\,\hat{\rho} \;+\; E^M_{NF\phi}\,\hat{\phi} \;+\; E^M_{NFz}\,\hat{z}\,, \quad (3.114)$$

$$\vec{H}^M_{NF}(\vec{r}) \;=\; H^M_{NF\rho}\,\hat{\rho} \;+\; H^M_{NF\phi}\,\hat{\phi} \;+\; H^M_{NFz}\,\hat{z}\,, \quad (3.115)$$

where

$$\begin{aligned}
E^M_{NF\rho} \;&=\; \frac{-\eta_o k_o^3}{4\pi}\int\limits_{S'}\Bigg\{\frac{\mathcal{Z}^{IBC}_t}{\eta_o}\,J_t(\vec{r}\,')\;(z'-z)\;\cos(\phi'-\phi)\\
&\quad+\;\frac{\mathcal{Z}^{IBC}_\phi}{\eta_o}\,J_\phi(\vec{r}\,')\;\left[\rho'\cos u'-(z'-z)\,\sin u'\right]\,\sin(\phi'-\phi)\Bigg\}\,G_H\;ds'\,, \quad (3.116)\\
E^M_{NF\phi} \;&=\; \frac{-\eta_o k_o^3}{4\pi}\int\limits_{S'}\Bigg\{\frac{\mathcal{Z}^{IBC}_t}{\eta_o}\,J_t(\vec{r}\,')\;(z'-z)\;\sin(\phi'-\phi)\;\;-\;\;\frac{\mathcal{Z}^{IBC}_\phi}{\eta_o}\,J_\phi(\vec{r}\,')\\
&\quad\times\;\Big[\left[\rho'\cos u'-(z'-z)\,\sin u'\right]\cos(\phi'-\phi)-\rho\,\cos u'\Big]\Bigg\}\,G_H\;ds'\,, \quad (3.117)\\
E^M_{NFz} \;&=\; \frac{-\eta_o k_o^3}{4\pi}\int\limits_{S'}\Bigg\{\frac{\mathcal{Z}^{IBC}_t}{\eta_o}\,J_t(\vec{r}\,')\;\left[\rho\cos(\phi'-\phi)-\rho'\right]\\
&\quad-\;\frac{\mathcal{Z}^{IBC}_\phi}{\eta_o}\,J_\phi(\vec{r}\,')\;\rho\,\sin u'\,\sin(\phi'-\phi)\Bigg\}\,G_H\;ds'\,, \quad (3.118)\\
H^M_{NF\rho} \;&=\; \frac{-jk_o^2}{4\pi}\int\limits_{S'}\Bigg\{\frac{\mathcal{Z}^{IBC}_t}{\eta_o}\,J_t(\vec{r}\,')\Big[\sin(\phi'-\phi)\,(G_E-G_H)+k_o^2\rho\,\sin(\phi'-\phi)\\
&\quad\times\;\left[\rho-\rho'\cos(\phi'-\phi)\right]\,G_{EH}\Big]\\
&\quad+\;\frac{\mathcal{Z}^{IBC}_\phi}{\eta_o}\,J_\phi(\vec{r}\,')\Big[\sin u'\cos(\phi'-\phi)\;(G_E-G_H)+k_o^2\,[\rho-\rho'\cos(\phi'-\phi)]\\
&\quad\times\;\Big[\sin u'\Big(\rho\,\cos(\phi'-\phi)-\rho'\Big)-\cos u'\,(z'-z)\Big]\,G_{EH}\Big]\Bigg\}\;ds'\,, \quad (3.119)
\end{aligned}$$

$$H^M_{NF\phi} = \frac{jk_o^2}{4\pi}\int\limits_{S'}\Bigg\{\frac{\mathcal{Z}_t^{IBC}}{\eta_o}J_t(\vec{r}\,')\Big[\cos(\phi'-\phi)\,(G_E-G_H)+k_o^2\rho\,\rho'\sin^2(\phi'-\phi)\,G_{EH}\Big]$$
$$-\ \frac{\mathcal{Z}_\phi^{IBC}}{\eta_o}J_\phi(\vec{r}\,')\Big[\sin u'\sin(\phi'-\phi)\ (G_E-G_H)-k_o^2\rho'\sin(\phi'-\phi)$$
$$\times\ \Big[\sin u'\Big(\rho\,\cos(\phi'-\phi)-\rho'\Big)-\cos u'\,(z'-z)\Big]\,G_{EH}\Big]\Bigg\}\,ds'\,, \tag{3.120}$$

$$H^M_{NFz} = \frac{jk_o^2}{4\pi}\int\limits_{S'}\Bigg\{\frac{\mathcal{Z}_t^{IBC}}{\eta_o}J_t(\vec{r}\,')\,k_o^2\rho\,(z'-z)\,\sin(\phi'-\phi)\,G_{EH}$$
$$-\ \frac{\mathcal{Z}_\phi^{IBC}}{\eta_o}J_\phi(\vec{r}\,')\Big[\cos u'\ (G_E-G_H)-k_o^2(z'-z)$$
$$\times\ \Big[\sin u'\Big(\rho\,\cos(\phi'-\phi)-\rho'\Big)-\cos u'\,(z'-z)\Big]\,G_{EH}\Big]\Bigg\}\,ds'\,, \tag{3.121}$$

and G_E, G_H, and G_{EH} are given by Eqs. 2.182–2.184, respectively. Substituting Eq. 2.21 into Eqs. 3.114–3.121 (with the modal parameter n in Eq. 2.21 conveniently changed into m) and solving the two-dimension integrals following the procedure of Sects. 2.3.3 and 3.2.2:

$$\vec{E}^M_{NF}(\vec{r}) = \sum_{m=-\infty}^{\infty}\Bigg\{\sum_{j=1}^{N_T}I^T_{mj}\,\Big[\Big(E^M_{NF\rho}\Big)^T_{mj}\,\hat{\rho}\ +\ \Big(E^M_{NF\phi}\Big)^T_{mj}\,\hat{\phi}\ +\ \Big(E^M_{NFz}\Big)^T_{mj}\,\hat{z}\Big]$$
$$+\sum_{j=1}^{N_P}I^P_{mj}\,\Big[\Big(E^M_{NF\rho}\Big)^P_{mj}\,\hat{\rho}\ +\ \Big(E^M_{NF\phi}\Big)^P_{mj}\,\hat{\phi}\ +\ \Big(E^M_{NFz}\Big)^P_{mj}\,\hat{z}\Big]\Bigg\}, \tag{3.122}$$

$$\vec{H}^M_{NF}(\vec{r}) = \sum_{m=-\infty}^{\infty}\Bigg\{\sum_{j=1}^{N_T}I^T_{mj}\,\Big[\Big(H^M_{NF\rho}\Big)^T_{mj}\,\hat{\rho}\ +\ \Big(H^M_{NF\phi}\Big)^T_{mj}\,\hat{\phi}\ +\ \Big(H^M_{NFz}\Big)^T_{mj}\,\hat{z}\Big]$$
$$+\sum_{j=1}^{N_P}I^P_{mj}\,\Big[\Big(H^M_{NF\rho}\Big)^P_{mj}\,\hat{\rho}\ +\ \Big(H^M_{NF\phi}\Big)^P_{mj}\,\hat{\phi}\ +\ \Big(H^M_{NFz}\Big)^P_{mj}\,\hat{z}\Big]\Bigg\}, \tag{3.123}$$

where

$$\Big(E^M_{NF\rho}\Big)^T_{mj} = \frac{-\eta_o k_o^3}{8\pi}\,e^{jm\phi}\sum_{l=q-1}^{q}\frac{\mathcal{Z}^{IBC}_{t,l}}{\eta_o}\,\Delta_l\Bigg\{(z_l-z)\,\Big[G_{2a}(\vec{r},t_l)-(-1)^{q-l}G_{2b}(\vec{r},t_l)\Big]$$
$$+\ \frac{\Delta_l}{2}\cos u_l\,\Big[G_{2b}(\vec{r},t_l)-(-1)^{q-l}G_{2c}(\vec{r},t_l)\Big]\Bigg\}\,, \tag{3.124}$$

$$\left(E^M_{NF\phi}\right)^T_{mj} = \frac{-j\eta_o k_o^3}{8\pi}\, e^{jm\phi} \sum_{l=q-1}^{q} \frac{\mathcal{Z}^{IBC}_{t,l}}{\eta_o}\, \Delta_l \Bigg\{ (z_l - z)\, \Big[G_{3a}(\vec{r}, t_l) - (-1)^{q-l} G_{3b}(\vec{r}, t_l)\Big] + \frac{\Delta_l}{2}\, \cos u_l \Big[G_{3b}(\vec{r}, t_l) - (-1)^{q-l} G_{3c}(\vec{r}, t_l)\Big] \Bigg\}, \tag{3.125}$$

$$\left(E^M_{NFz}\right)^T_{mj} = \frac{\eta_o k_o^3}{8\pi}\, e^{jm\phi} \sum_{l=q-1}^{q} \frac{\mathcal{Z}^{IBC}_{t,l}}{\eta_o}\, \Delta_l \Bigg\{ (\rho_l - \rho)\, \Big[G_{2a}(\vec{r}, t_l) - (-1)^{q-l} G_{2b}(\vec{r}, t_l)\Big] + \rho_l\, \Big[G_{1a}(\vec{r}, t_l) - (-1)^{q-l} G_{1b}(\vec{r}, t_l)\Big] + \frac{\Delta_l}{2}\, \sin u_l \Big[G_{1b}(\vec{r}, t_l) + G_{2b}(\vec{r}, t_l) - (-1)^{q-l}\, [G_{1c}(\vec{r}, t_l) + G_{2c}(\vec{r}, t_l)]\Big] \Bigg\}, \tag{3.126}$$

$$\left(E^M_{NF\rho}\right)^P_{mj} = \frac{-j\eta_o k_o^3}{4\pi}\, e^{jm\phi}\, \frac{\mathcal{Z}^{IBC}_{\phi,j}}{\eta_o}\, \Delta_j\, [\rho_j\, \cos u_j - (z_j - z)\, \sin u_j] \times \left[G_{3a}(\vec{r}, t_j) + \frac{\Delta_j\, \sin u_j}{2\, \rho_j}\, G_{3b}(\vec{r}, t_j)\right], \tag{3.127}$$

$$\left(E^M_{NF\phi}\right)^P_{mj} = \frac{\eta_o k_o^3}{4\pi}\, e^{jm\phi}\, \frac{\mathcal{Z}^{IBC}_{\phi,j}}{\eta_o}\, \Delta_j \Bigg\{ [(\rho_j - \rho)\, \cos u_j - (z_j - z)\, \sin u_j] \times \left[G_{2a}(\vec{r}, t_j) + \frac{\Delta_j\, \sin u_j}{2\, \rho_j}\, G_{2b}(\vec{r}, t_j)\right] - \rho\, \cos u_j \left[G_{1a}(\vec{r}, t_j) + \frac{\Delta_j\, \sin u_j}{2\, \rho_j}\, G_{1b}(\vec{r}, t_j)\right] \Bigg\}, \tag{3.128}$$

$$\left(E^M_{NFz}\right)^P_{mj} = \frac{j\eta_o k_o^3}{4\pi}\, e^{jm\phi}\, \frac{\mathcal{Z}^{IBC}_{\phi,j}}{\eta_o}\, \Delta_j\, \rho\, \sin u_j \left[G_{3a}(\vec{r}, t_j) + \frac{\Delta_j\, \sin u_j}{2\, \rho_j}\, G_{3b}(\vec{r}, t_j)\right], \tag{3.129}$$

$$\left(H^M_{NF\rho}\right)^T_{mj} = \frac{k_o^2}{8\pi}\, e^{jm\phi} \sum_{l=q-1}^{q} \frac{\mathcal{Z}^{IBC}_{t,l}}{\eta_o}\, \Delta_l \Bigg\{ G_{6a}(\vec{r}, t_l) - G_{3a}(\vec{r}, t_l) - (-1)^{q-l}\, [G_{6b}(\vec{r}, t_l) - G_{3b}(\vec{r}, t_l)] + (k_o\rho)^2 \Big[G_{9a}(\vec{r}, t_l) - (-1)^{q-l} G_{9b}(\vec{r}, t_l)\Big] - k_o^2\, \frac{\rho\, \rho_l}{2} \Bigg[G_{11a}(\vec{r}, t_l) - (-1)^{q-l} G_{11b}(\vec{r}, t_l) + \frac{\Delta_l\, \sin u_l}{2\, \rho_l} \Big[G_{11b}(\vec{r}, t_l) - (-1)^{q-l} G_{11c}(\vec{r}, t_l)\Big]\Bigg] \Bigg\}, \tag{3.130}$$

$$\left(H^M_{NF\phi}\right)^T_{mj} = \frac{-jk_o^2}{8\pi}\, e^{jm\phi} \sum_{l=q-1}^{q} \frac{\mathcal{Z}^{IBC}_{t,l}}{\eta_o}\, \Delta_l \Bigg\{ G_{2a}(\vec{r},t_l) - G_{5a}(\vec{r},t_l) - (-1)^{q-l}\left[G_{2b}(\vec{r},t_l)\right.$$
$$\left. -\ G_{5b}(\vec{r},t_l)\right] - k_o^2\, \frac{\rho\,\rho_l}{2} \Bigg[G_{8a}(\vec{r},t_l) - G_{10a}(\vec{r},t_l) + G_{12a}(\vec{r},t_l)$$
$$+ \left(\frac{\Delta_l\, \sin u_l}{2\,\rho_l} - (-1)^{q-l} \right) \left[G_{8b}(\vec{r},t_l) - G_{10b}(\vec{r},t_l) + G_{12b}(\vec{r},t_l) \right]$$
$$- (-1)^{q-l}\, \frac{\Delta_l\, \sin u_l}{2\,\rho_l} \left[G_{8c}(\vec{r},t_l) - G_{10c}(\vec{r},t_l) + G_{12c}(\vec{r},t_l) \right] \Bigg] \Bigg\}, \qquad (3.131)$$

$$\left(H^M_{NFz}\right)^T_{mj} = \frac{-k_o^2}{8\pi}\, e^{jm\phi} \sum_{l=q-1}^{q} \frac{\mathcal{Z}^{IBC}_{t,l}}{\eta_o}\, \Delta_l\, k_o^2\, \rho \Bigg\{ (z_l - z) \left[G_{9a}(\vec{r},t_l) - (-1)^{q-l} G_{9b}(\vec{r},t_l) \right]$$
$$+ \frac{\Delta_l}{2}\, \cos u_l \left[G_{9b}(\vec{r},t_l) - (-1)^{q-l} G_{9c}(\vec{r},t_l) \right] \Bigg\}, \qquad (3.132)$$

$$\left(H^M_{NF\rho}\right)^P_{mj} = \frac{-jk_o^2}{4\pi}\, e^{jm\phi}\, \frac{\mathcal{Z}^{IBC}_{\phi,j}}{\eta_o}\, \Delta_j \Bigg\{ \sin u_j \Bigg[G_{5a}(\vec{r},t_j) - G_{2a}(\vec{r},t_j) + \frac{\Delta_j\, \sin u_j}{2\,\rho_j}$$
$$\times \left[G_{5b}(\vec{r},t_j) - G_{2b}(\vec{r},t_j) \right] \Bigg] + k_o^2 \Bigg[\frac{\rho\,\rho_j}{2}\, \sin u_j + (\rho_j - \rho)\left[(\rho_j - \rho) \sin u_j \right.$$
$$\left. +\ (z_j - z) \cos u_j \right] \Bigg] \left[G_{8a}(\vec{r},t_j) + \frac{\Delta_j\, \sin u_j}{2\,\rho_j}\, G_{8b}(\vec{r},t_j) \right]$$
$$+ k_o^2\, \frac{\Delta_j}{2} \Bigg[\rho_j - \rho + \sin u_j \left[\left(\rho_j - \frac{\rho}{2} \right) \sin u_j + (z_j - z) \cos u_j \right] \Bigg]$$
$$\times \left[G_{8b}(\vec{r},t_j) + \frac{\Delta_j\, \sin u_j}{2\,\rho_j}\, G_{8c}(\vec{r},t_j) \right] + \left(\frac{k_o \Delta_j}{2} \right)^2 \sin u_j$$
$$\times \left[G_{8c}(\vec{r},t_j) + \frac{\Delta_j\, \sin u_j}{2\,\rho_j}\, G_{8d}(\vec{r},t_j) \right] - k_o^2\, \frac{\rho\,\rho_j}{2}\, \sin u_j$$
$$\times \left[G_{10a}(\vec{r},t_j) + 2\, \frac{\Delta_j\, \sin u_j}{2\,\rho_j}\, G_{10b}(\vec{r},t_j) + \left(\frac{\Delta_j\, \sin u_j}{2\,\rho_j} \right)^2 G_{10c}(\vec{r},t_j) \right]$$
$$- k_o^2\, \rho \left[\frac{3\rho_j}{2}\, \sin u_j + (z_j - z) \cos u_j \right] \Bigg[G_{12a}(\vec{r},t_j)$$
$$+ \frac{\Delta_j\, \sin u_j}{2\,\rho_j}\, G_{12b}(\vec{r},t_j) \Bigg] - k_o^2\, \frac{\rho \Delta_j}{2} \left(1 + \frac{\sin^2 u_j}{2} \right)$$
$$\times \left[G_{12b}(\vec{r},t_j) + \frac{\Delta_j\, \sin u_j}{2\,\rho_j}\, G_{12c}(\vec{r},t_j) \right] \Bigg\}, \qquad (3.133)$$

$$\left(H^M_{NF\phi}\right)^P_{mj} = \frac{k_o^2}{4\pi}\, e^{jm\phi}\, \frac{\mathcal{Z}^{IBC}_{\phi,j}}{\eta_o}\, \Delta_j \left\{ \sin u_j \left[G_{6a}(\vec{r}, t_j) - G_{3a}(\vec{r}, t_j) + \frac{\Delta_j \sin u_j}{2\,\rho_j} \right.\right.$$
$$\times \left.\left[G_{6b}(\vec{r}, t_j) - G_{3b}(\vec{r}, t_j) \right] \right] + k_o^2\, \rho_j \left[\rho_j \sin u_j + (z_j - z) \cos u_j \right]$$
$$\times \left[G_{9a}(\vec{r}, t_j) + \frac{\Delta_j \sin u_j}{2\,\rho_j}\, G_{9b}(\vec{r}, t_j) \right] + k_o^2\, \frac{\Delta_j}{2} \left[\rho_j + \sin u_j \left[\rho_j \sin u_j \right.\right.$$
$$\left.\left. + (z_j - z) \cos u_j \right] \right] \left[G_{9b}(\vec{r}, t_j) + \frac{\Delta_j \sin u_j}{2\,\rho_j}\, G_{9c}(\vec{r}, t_j) \right] + \left(\frac{k_o \Delta_j}{2} \right)^2 \sin u_j$$
$$\times \left[G_{9c}(\vec{r}, t_j) + \frac{\Delta_j \sin u_j}{2\,\rho_j}\, G_{9d}(\vec{r}, t_j) \right] - k_o^2\, \frac{\rho\, \rho_j}{2} \sin u_j \left[G_{11a}(\vec{r}, t_j) \right.$$
$$\left. + 2\, \frac{\Delta_j \sin u_j}{2\,\rho_j}\, G_{11b}(\vec{r}, t_j) + \left(\frac{\Delta_j \sin u_j}{2\,\rho_j} \right)^2 G_{11c}(\vec{r}, t_j) \right] \Bigg\}, \tag{3.134}$$

$$\left(H^M_{NFz}\right)^P_{mj} = \frac{-jk_o^2}{4\pi}\, e^{jm\phi}\, \frac{\mathcal{Z}^{IBC}_{\phi,j}}{\eta_o}\, \Delta_j \left\{ \cos u_j \left[G_{7a}(\vec{r}, t_j) - G_{1a}(\vec{r}, t_j) - G_{2a}(\vec{r}, t_j) \right.\right.$$
$$\left. + \frac{\Delta_j \sin u_j}{2\,\rho_j} \left[G_{7b}(\vec{r}, t_j) - G_{1b}(\vec{r}, t_j) - G_{2b}(\vec{r}, t_j) \right] \right] + k_o^2 (z_j - z)$$
$$\times \left[(\rho_j - \rho) \sin u_j + (z_j - z) \cos u_j \right] \left[G_{8a}(\vec{r}, t_j) + \frac{\Delta_j \sin u_j}{2\,\rho_j}\, G_{8b}(\vec{r}, t_j) \right]$$
$$+ k_o^2\, \frac{\Delta_j}{2} \left[z_j - z + \cos u_j \left[(\rho_j - \rho) \sin u_j + (z_j - z) \cos u_j \right] \right] \left[G_{8b}(\vec{r}, t_j) \right.$$
$$\left. + \frac{\Delta_j \sin u_j}{2\,\rho_j}\, G_{8c}(\vec{r}, t_j) \right] + \left(\frac{k_o \Delta_j}{2} \right)^2 \cos u_j \left[G_{8c}(\vec{r}, t_j) + \frac{\Delta_j \sin u_j}{2\,\rho_j} \right.$$
$$\left. \times\, G_{8d}(\vec{r}, t_j) \right] + k_o^2\, (z_j - z) \left[\rho_j \sin u_j + (z_j - z) \cos u_j \right] \left[G_{12a}(\vec{r}, t_j) \right.$$
$$\left. + \frac{\Delta_j \sin u_j}{2\,\rho_j}\, G_{12b}(\vec{r}, t_j) \right] + k_o^2\, \frac{\Delta_j}{2} \left[z_j - z + \cos u_j \left[\rho_j \sin u_j \right.\right.$$
$$\left.\left. + (z_j - z) \cos u_j \right] \right] \left[G_{12b}(\vec{r}, t_j) + \frac{\Delta_j \sin u_j}{2\,\rho_j}\, G_{12c}(\vec{r}, t_j) \right]$$
$$+ \left(\frac{k_o \Delta_j}{2} \right)^2 \cos u_j \left[G_{12c}(\vec{r}, t_j) + \frac{\Delta_j \sin u_j}{2\,\rho_j}\, G_{12d}(\vec{r}, t_j) \right] \Bigg\}, \tag{3.135}$$

the integrals $G_{va}(\vec{r}, t_l)$, $G_{vb}(\vec{r}, t_l)$, and $G_{vc}(\vec{r}, t_l)$ are given by Eqs. 2.199–2.215, $\mathcal{Z}^{IBC}_{t,l}$ and $\mathcal{Z}^{IBC}_{\phi,l}$ are associated with the source segment l, and the subscript l represents the source segments $q-1$, q, and j. The double integrals of Eqs. 3.124–3.135 can

be numerically evaluated with a n_α- and n_ϕ-point Gaussian quadratures for the integrals with respect to α and ϕ, respectively, accordingly to the procedures of Sects. 2.3.4 and 3.2.3. As far as the observation point $\vec{r}$ is sufficiently distant from the source point $\vec{r}\,'$, no singularity problems will occur in these integrals.

To take care of the situations with negative indices m, Eqs. 2.199–2.215 and 3.124–3.135 yield

$$\left(E^M_{NF\rho}\right)^T_{mj}\ e^{-jm\phi} = \left(E^M_{NF\rho}\right)^T_{-mj}\ e^{jm\phi}\,, \tag{3.136}$$

$$\left(E^M_{NF\phi}\right)^T_{mj}\ e^{-jm\phi} = -\left(E^M_{NF\phi}\right)^T_{-mj}\ e^{jm\phi}\,, \tag{3.137}$$

$$\left(E^M_{NFz}\right)^T_{mj}\ e^{-jm\phi} = \left(E^M_{NFz}\right)^T_{-mj}\ e^{jm\phi}\,, \tag{3.138}$$

$$\left(E^M_{NF\rho}\right)^P_{mj}\ e^{-jm\phi} = -\left(E^M_{NF\rho}\right)^P_{-mj}\ e^{jm\phi}\,, \tag{3.139}$$

$$\left(E^M_{NF\phi}\right)^P_{mj}\ e^{-jm\phi} = \left(E^M_{NF\phi}\right)^P_{-mj}\ e^{jm\phi}\,, \tag{3.140}$$

$$\left(E^M_{NFz}\right)^P_{mj}\ e^{-jm\phi} = -\left(E^M_{NFz}\right)^P_{-mj}\ e^{jm\phi}\,, \tag{3.141}$$

$$\left(H^M_{NF\rho}\right)^T_{mj}\ e^{-jm\phi} = -\left(H^M_{NF\rho}\right)^T_{-mj}\ e^{jm\phi}\,, \tag{3.142}$$

$$\left(H^M_{NF\phi}\right)^T_{mj}\ e^{-jm\phi} = \left(H^M_{NF\phi}\right)^T_{-mj}\ e^{jm\phi}\,, \tag{3.143}$$

$$\left(H^M_{NFz}\right)^T_{mj}\ e^{-jm\phi} = -\left(H^M_{NFz}\right)^T_{-mj}\ e^{jm\phi}\,, \tag{3.144}$$

$$\left(H^M_{NF\rho}\right)^P_{mj}\ e^{-jm\phi} = \left(H^M_{NF\rho}\right)^P_{-mj}\ e^{jm\phi}\,, \tag{3.145}$$

$$\left(H^M_{NF\phi}\right)^P_{mj}\ e^{-jm\phi} = -\left(H^M_{NF\phi}\right)^P_{-mj}\ e^{jm\phi}\,, \tag{3.146}$$

$$\left(H^M_{NFz}\right)^P_{mj}\ e^{-jm\phi} = \left(H^M_{NFz}\right)^P_{-mj}\ e^{jm\phi}\,, \tag{3.147}$$

which allow the results for a positive mode m to be used to obtain the terms corresponding to a negative mode $-m$. Notice that for the external excitations presented in Sects. 2.3.5 and 3.2.4 only the modes $m = \pm 1$ are present.

The near-zone fields $\vec{E}_{NF}^{inc}(\vec{r})$ and $\vec{H}_{NF}^{inc}(\vec{r})$ produced by an external spherical-wave source were discussed in Sect. 2.4. For the modal currents $\vec{J}_g(\vec{r}\,')$ and $\vec{M}_g(\vec{r}\,')$ that excite the fundamental TE_{11} mode of the circular waveguide (as discussed in Sect. 3.2.4), $\vec{E}_{NF}^{inc}(\vec{r})$ and $\vec{H}_{NF}^{inc}(\vec{r})$ are given by Eqs. 3.95 and 3.96, respectively. Aiming their numerical calculation, the substitution of Eqs. 3.84 and 3.85 into Eqs. 3.95 and 3.96 yields

$$
\begin{aligned}
\vec{E}_{NF}^{inc}(\vec{r}) \;=\; & \frac{-j\eta_o k_\rho\, k_o^2}{2\pi\Lambda\mathcal{Z}_{TE}}\, e^{-j\frac{\eta_o k_o}{\mathcal{Z}_{TE}} z_g} \int_0^{a_g} \left\{ \left[G_5(\vec{r},\rho') + \frac{jk_o\mathcal{Z}_{TE}}{\eta_o}\,(z_g - z)\, G_2(\vec{r},\rho') \right] \right. \\
& \times \left[\frac{J_1(k_\rho\,\rho')}{k_\rho\,\rho'}\,\cos\phi\;\hat{\rho} \;-\; J_1'(k_\rho\,\rho')\,\sin\phi\;\hat{\phi} \right] + \left[G_6(\vec{r},\rho') \right. \\
& + \left. \frac{jk_o\mathcal{Z}_{TE}}{\eta_o}\,(z_g - z)\, G_3(\vec{r},\rho') \right] \left[J_1'(k_\rho\,\rho')\,\cos\phi\;\hat{\rho} \;-\; \frac{J_1(k_\rho\,\rho')}{k_\rho\,\rho'}\,\sin\phi\;\hat{\phi} \right] \\
& - \frac{jk_o\mathcal{Z}_{TE}}{\eta_o} \left[\frac{J_1(k_\rho\,\rho')}{k_\rho\,\rho'} \left(\rho'\, G_1(\vec{r},\rho') + (\rho' - \rho)\, G_2(\vec{r},\rho') \right) - J_1'(k_\rho\,\rho')\,\rho \right. \\
& \times \left. G_3(\vec{r},\rho') \right] \cos\phi\;\hat{z} \Bigg\}\, \rho'\, d\rho' \;+\; \frac{j\eta_o k_\rho\, k_o^2}{2\pi\Lambda\mathcal{Z}_{TE}}\, e^{-j\frac{\eta_o k_o}{\mathcal{Z}_{TE}} z_g}\, a_g\, \frac{J_1(k_\rho\, a_g)}{k_\rho\, a_g} \\
& \times \left\{ \left[\rho\, G_1(\vec{r}, a_g) - (a_g - \rho)\, G_2(\vec{r}, a_g) \right] \cos\phi\;\hat{\rho} \;+\; a_g\, G_3(\vec{r}, a_g) \right. \\
& \times \left. \sin\phi\;\hat{\phi} \;-\; (z_g - z) \left[G_1(\vec{r}, a_g) + G_2(\vec{r}, a_g) \right] \cos\phi\;\hat{z} \right\}, \qquad (3.148)
\end{aligned}
$$

$$\vec{H}_{NF}^{inc}(\vec{r}) = \frac{-k_\rho\, k_o^2}{2\pi\Lambda\mathcal{Z}_{TE}}\, e^{-j\frac{\eta_o k_o}{\mathcal{Z}_{TE}}z_g} \int_0^{a_g} \Bigg\{ \left[\frac{j\mathcal{Z}_{TE}}{\eta_o} G_5(\vec{r},\rho') - k_o\,(z_g - z)\, G_2(\vec{r},\rho')\right] \times \left[J_1'(k_\rho\,\rho')\,\sin\phi\;\hat{\rho} + \frac{J_1(k_\rho\,\rho')}{k_\rho\,\rho'}\cos\phi\;\hat{\phi}\right] + \left[\frac{j\mathcal{Z}_{TE}}{\eta_o} G_6(\vec{r},\rho') - k_o\,(z_g - z)\, G_3(\vec{r},\rho')\right]\left[\frac{J_1(k_\rho\,\rho')}{k_\rho\,\rho'}\sin\phi\;\hat{\rho} + J_1'(k_\rho\,\rho')\cos\phi\;\hat{\phi}\right] + \frac{jk_\rho\,\mathcal{Z}_{TE}}{\eta_o} J_1(k_\rho\,\rho')\Big[\Big[\rho\, G_1(\vec{r},\rho') - (\rho' - \rho)\, G_2(\vec{r},\rho')\Big]\sin\phi\;\hat{\rho} - \rho'\, G_3(\vec{r},\rho')\,\cos\phi\;\hat{\phi}\Big] - \left[\frac{J_1(k_\rho\,\rho')}{k_\rho\,\rho'}\left(k_o\rho\, G_3(\vec{r},\rho') + \frac{j(k_\rho)^2\mathcal{Z}_{TE}}{\eta_o} \times \rho'\,(z_g - z)\,\Big[G_1(\vec{r},\rho') + G_2(\vec{r},\rho')\Big]\right) - J_1'(k_\rho\,\rho')\,k_o\,\Big[\rho'\, G_1(\vec{r},\rho') + (\rho' - \rho)\, G_2(\vec{r},\rho')\Big]\right]\sin\phi\;\hat{z}\Bigg\}\,\rho'\,d\rho'\,, \tag{3.149}$$

where the integrals $G_v(\vec{r},\rho')$ (with $v = 1,2,3,5,6$) are given by Eqs. 3.50–3.52, 2.81, and 2.82, respectively, and R is directly given by Eq. 2.49 with $z' = z_g$ and ρ' varying from 0 to a_g (being equal to a_g for the terms corresponding to the ring electric charge in Eq. 3.148). The integrals with respect to ρ' in Eqs. 3.148 and 3.149 can be numerically evaluated using Eqs. 3.104–3.106, with $N_g = 50$ in the present work.

3.4 Radiated Far-Zone Fields

When the radiated field is calculated in the far-zone region of the antenna, the expressions obtained are somewhat simpler than in Sect. 3.3. In the case where an IBC is present over the BOR surface, Eq. 2.230 is expanded into

$$\vec{E}_{FF}(\vec{r}) = \vec{E}_{FF}^{J}(\vec{r}) + \vec{E}_{FF}^{M}(\vec{r}) + \vec{E}_{FF}^{inc}(\vec{r})\,, \tag{3.150}$$

where $\vec{E}_{FF}^{inc}(\vec{r})$ is the electric far-zone field radiated by the external sources, $\vec{E}_{FF}^{J}(\vec{r})$ is given by Eqs. 2.239–2.245, and $\vec{E}_{FF}^{M}(\vec{r})$ is the electric far-zone field radiated by the equivalent magnetic current $\vec{M}(\vec{r}\,')$ and obtained from Eq. 128 in Chap. 3 of Ref. [21] as

$$\vec{E}_{FF}^{M}(\vec{r}) \;=\; \frac{-jk_o}{4\pi}\,\frac{e^{-jk_o r}}{r}\int\limits_{S'}\left[\vec{M}(\vec{r}\,')\times\hat{r}\right]\,e^{jk_o\,\vec{r}\,'\cdot\hat{r}}\;\,ds'\,. \tag{3.151}$$

The total magnetic far-zone field $\vec{H}_{FF}(\vec{r})$ is directly given by Eq. 2.231.

Using Eqs. 2.169, 2.233–2.235, and 3.5, one may rewrite Eq. 3.151 as

$$\vec{E}_{FF}^{M}(\vec{r}) \;=\; E_{FF\theta}^{M}\,\hat{\theta} \;+\; E_{FF\phi}^{M}\,\hat{\phi}\,, \tag{3.152}$$

where

$$\begin{aligned} E_{FF\theta}^{M} \;&=\; \frac{j\eta_o k_o}{4\pi}\,\frac{e^{-jk_o r}}{r}\int\limits_{S'}\left[\frac{\mathcal{Z}_t^{IBC}}{\eta_o}\,J_t(\vec{r}\,')\,\cos(\phi'-\phi)\right. \\ &\quad\left. -\;\frac{\mathcal{Z}_\phi^{IBC}}{\eta_o}\,J_\phi(\vec{r}\,')\,\sin u'\,\sin(\phi'-\phi)\right]\,e^{jk_o[\rho'\,\sin\theta\,\cos(\phi'-\phi)\,+\,z'\,\cos\theta]}\;ds'\,, \end{aligned} \tag{3.153}$$

$$\begin{aligned} E_{FF\phi}^{M} \;&=\; \frac{j\eta_o k_o}{4\pi}\,\frac{e^{-jk_o r}}{r}\int\limits_{S'}\left\{\frac{\mathcal{Z}_t^{IBC}}{\eta_o}\,J_t(\vec{r}\,')\,\cos\theta\,\sin(\phi'-\phi)-\frac{\mathcal{Z}_\phi^{IBC}}{\eta_o}\,J_\phi(\vec{r}\,')\left[\cos u'\,\sin\theta\right.\right. \\ &\quad\left.\left. -\;\sin u'\,\cos\theta\,\cos(\phi'-\phi)\right]\right\}\,e^{jk_o[\rho'\,\sin\theta\,\cos(\phi'-\phi)\,+\,z'\,\cos\theta]}\;ds'\,. \end{aligned} \tag{3.154}$$

Substituting Eq. 2.21 into Eqs. 3.152–3.154 (with the modal parameter n in Eq. 2.21 conveniently changed into m), following the procedures of Sects. 2.3.3 and 3.2.2, and solving the integrals with respect to ϕ' in closed form, straightforward algebraic

manipulations yield

$$\vec{E}^M_{FF}(\vec{r}) = \sum_{m=-\infty}^{\infty} \left\{ \sum_{j=1}^{N_T} I^T_{mj} \left[\left(E^M_{FF\theta}\right)^T_{mj} \hat{\theta} + \left(E^M_{FF\phi}\right)^T_{mj} \hat{\phi} \right] + \sum_{j=1}^{N_P} I^P_{mj} \left[\left(E^M_{FF\theta}\right)^P_{mj} \hat{\theta} + \left(E^M_{FF\phi}\right)^P_{mj} \hat{\phi} \right] \right\}, \tag{3.155}$$

where

$$\left(E^M_{FF\theta}\right)^T_{mj} = \frac{-\eta_o k_o}{16} \left(je^{j\phi}\right)^m \frac{e^{-jk_o r}}{r} \sum_{l=q-1}^{q} \frac{\mathcal{Z}^{IBC}_{t,l}}{\eta_o} \Delta_l \left\{ F_{m+1,a}(t_l) - F_{m-1,a}(t_l) - (-1)^{q-l} \left[F_{m+1,b}(t_l) - F_{m-1,b}(t_l) \right] \right\}, \tag{3.156}$$

$$\left(E^M_{FF\phi}\right)^T_{mj} = \frac{j\eta_o k_o}{16} \left(je^{j\phi}\right)^m \frac{e^{-jk_o r}}{r} \cos\theta \sum_{l=q-1}^{q} \frac{\mathcal{Z}^{IBC}_{t,l}}{\eta_o} \Delta_l \left\{ F_{m+1,a}(t_l) + F_{m-1,a}(t_l) - (-1)^{q-l} \left[F_{m+1,b}(t_l) + F_{m-1,b}(t_l) \right] \right\}, \tag{3.157}$$

$$\left(E^M_{FF\theta}\right)^P_{mj} = \frac{-j\eta_o k_o}{8} \left(je^{j\phi}\right)^m \frac{e^{-jk_o r}}{r} \frac{\mathcal{Z}^{IBC}_{\phi,j}}{\eta_o} \Delta_j \sin u_j \left\{ F_{m+1,a}(t_j) + F_{m-1,a}(t_j) + \frac{\Delta_j \sin u_j}{2\,\rho_j} \left[F_{m+1,b}(t_j) + F_{m-1,b}(t_j) \right] \right\}, \tag{3.158}$$

$$\left(E^M_{FF\phi}\right)^P_{mj} = \frac{-j\eta_o k_o}{8} \left(je^{j\phi}\right)^m \frac{e^{-jk_o r}}{r} \frac{\mathcal{Z}^{IBC}_{\phi,j}}{\eta_o} \Delta_j \left\{ 2 \sin\theta \cos u_j \left[F_{m,a}(t_j) + \frac{\Delta_j \sin u_j}{2\,\rho_j} F_{m,b}(t_j) \right] - j \cos\theta \sin u_j \left[F_{m+1,a}(t_j) - F_{m-1,a}(t_j) + \frac{\Delta_j \sin u_j}{2\,\rho_j} \left[F_{m+1,b}(t_j) - F_{m-1,b}(t_j) \right] \right] \right\}, \tag{3.159}$$

the integrals $F_{n,a}(t_l)$ and $F_{n,b}(t_l)$ (with $n = m-1, m, m+1$) are given by Eqs. 2.244 and 2.245, respectively, and $\mathcal{Z}^{IBC}_{t,l}$ and $\mathcal{Z}^{IBC}_{\phi,l}$ are associated with the source segment l (where $l = q-1, q, j$). The integrals $F_{n,a}(t_l)$ and $F_{n,b}(t_l)$ can be numerically evaluated with a n_α-point Gaussian quadrature accordingly to Sects. 2.3.4 and 3.2.3 (with $n_\alpha = 2$ in this work).

From Eqs. 2.244, 2.245, and 3.156–3.159 one obtains the following relations:

$$\left(E^M_{FF\theta}\right)^T_{mj}\ \left(je^{j\phi}\right)^{-m} = (-1)^m \left(E^M_{FF\theta}\right)^T_{-mj}\ \left(je^{j\phi}\right)^{m}\ , \tag{3.160}$$

$$\left(E^M_{FF\phi}\right)^T_{mj}\ \left(je^{j\phi}\right)^{-m} = (-1)^{m+1} \left(E^M_{FF\phi}\right)^T_{-mj}\ \left(je^{j\phi}\right)^{m}\ , \tag{3.161}$$

$$\left(E^M_{FF\theta}\right)^P_{mj}\ \left(je^{j\phi}\right)^{-m} = (-1)^{m+1} \left(E^M_{FF\theta}\right)^P_{-mj}\ \left(je^{j\phi}\right)^{m}\ , \tag{3.162}$$

$$\left(E^M_{FF\phi}\right)^P_{mj}\ \left(je^{j\phi}\right)^{-m} = (-1)^{m} \left(E^M_{FF\phi}\right)^P_{-mj}\ \left(je^{j\phi}\right)^{m}\ , \tag{3.163}$$

from where the results for a positive mode m can be used to obtain the terms corresponding to a negative mode $-m$ (recalling that for the external excitations presented in Sects. 2.3.5 and 3.2.4 only the modes $m = \pm 1$ are present).

The electric far-zone field $\vec{E}^{inc}_{FF}(\vec{r})$ produced by an external spherical-wave source was previously discussed in Sect. 2.5. For the TE_{11} mode excitation of Sect. 3.2.4, the substitution of Eqs. 3.84–3.91 into Eq. 128 in Chap. 3 of Ref. [21] yields

$$\begin{aligned}
\vec{E}^{inc}_{FF}(\vec{r}) &= \frac{-jk_\rho\, k_o}{2\Lambda}\,\frac{e^{-jk_o r}}{r}\, e^{jk_o\left(\cos\theta - \frac{\eta_o}{\mathcal{Z}_{TE}}\right)z_g}\ a_g^2\ \frac{J_1(k_\rho\, a_g)}{k_\rho\, a_g} \\
&\times \left\{ \frac{J_1(k_\rho\, a_g\, \sin\theta)}{k_\rho\, a_g\, \sin\theta}\ \left(1 + \frac{\eta_o}{\mathcal{Z}_{TE}}\,\cos\theta\right)\ \cos\phi\ \hat{\theta} \right. \\
&- \left. k_\rho^2\ \frac{J_1'(k_\rho\, a_g\, \sin\theta)}{k_\rho^2 - (k_o \sin\theta)^2}\ \left(\cos\theta + \frac{\eta_o}{\mathcal{Z}_{TE}}\right)\ \sin\phi\ \hat{\phi} \right\}\ ,
\end{aligned} \tag{3.164}$$

where the contribution due to the equivalent electric charge distribution is already being taken into account [21].

3.5 Horn-Feed Return Loss

For the TE_{11} mode excitation discussed in Sect. 3.2.4 (see Fig. 3.3), part of the energy exciting the horn is radiated by the antenna system towards the surrounding environment (radiated energy) while the remaining part is reflected back into the circular waveguide connected to the horn (returned energy). Assuming that the waveguide is specified to allow only the fundamental TE_{11} mode propagation, well inside the circular waveguide this returned energy is completely transfered to the TE_{11} mode propagating towards the negative $\hat{z}$-direction. In order to simulate a matched load for the feed structure while accomplishing a small (and numerically tractable) dimension for the geometry, the waveguide is truncated at $z = z_e$ (see Fig. 3.3) and an IBC is specified over its end wall. This procedure also allows the direct determination of the feed return loss.

Since only the fundamental mode is allowed to propagate (this is controlled by the waveguide radius a_g) and assuming no discontinuities present for the waveguide geometry (i.e., the horn throat is sufficiently away from the waveguide end wall), at the plane $z = z_e$ the total waveguide field is represented by a linear combination between the TE_{11} modes propagating towards the positive and negative $\hat{z}$-directions. So, the matched load is obtained by specifying the necessary boundary condition (in terms of the IBC) that is completely satisfied by the returned mode and, thus, avoids its reflection. From Eqs. 3.1, 3.2, 3.84, and 3.85 (and observing the orientation of

$\hat{t}$ in Fig. 3.3) the IBC simulating the matched load is

$$\mathcal{Z}_t^{IBC} = \frac{E_\rho^-}{H_\phi^-} = -\mathcal{Z}_{TE}\,, \tag{3.165}$$

$$\mathcal{Z}_\phi^{IBC} = \frac{E_\phi^-}{-H_\rho^-} = -\mathcal{Z}_{TE}\,, \tag{3.166}$$

where the field components are those associated with the returned TE_{11} mode and $\mathcal{Z}_{TE}$ is given by Eq. 3.87. Consequently, the electric current $\vec{J}(\vec{r}\,')$ induced over the waveguide end wall is related to the returned TE_{11} mode by

$$\vec{J}(\vec{r}\,') = J_t(\vec{r}\,')\,\hat{t}' + J_\phi(\vec{r}\,')\,\hat{\phi}' = \hat{z}\times\vec{H}^-_{TE_{11}} = H_\phi^-\,\hat{t}' + H_\rho^-\,\hat{\phi}'\,. \tag{3.167}$$

From Ref. [47] and Eqs. 3.84, 3.85, and 3.167 (recalling from Sect. 3.2.4 that the excited TE_{11} mode has unit power), the power associated with the returned TE_{11} mode (return loss) is given by:

$$\begin{aligned} P_{RL} &= \frac{1}{2}\,\Re\mathrm{e}\left\{\int_0^{2\pi}\int_0^{a_g}\left(\vec{E}^-_{TE_{11}}\times\vec{H}^{-*}_{TE_{11}}\right)\cdot\hat{z}\;\;\rho'\,d\rho'\,d\phi'\right\} \\ &= \frac{\mathcal{Z}_{TE}}{2}\int_0^{2\pi}\int_0^{a_g}\left(|H_\rho^-|^2 + |H_\phi^-|^2\right)\,\rho'\,d\rho'\,d\phi' \\ &= \frac{\mathcal{Z}_{TE}}{2}\int_0^{2\pi}\int_0^{a_g}\left(|J_t(\vec{r}\,')|^2 + |J_\phi(\vec{r}\,')|^2\right)\,\rho'\,d\rho'\,d\phi'\,, \quad \text{at } z=z_e\,, \end{aligned} \tag{3.168}$$

where the symbol $*$ denotes the complex conjugate. As explained at the end of Sect. 3.2.4, for the excitation provided by the equivalent modal currents $\vec{J}_g(\vec{r}\,')$ and $\vec{M}_g(\vec{r}\,')$, only the modes $m=\pm1$ are excited and Eqs. 2.161 and 2.162 can be used together with Eq. 2.21 to yield

$$J_t(\vec{r}\,') = 2\cos\phi'\sum_j I^T_{1j}\,\frac{T_j(t')}{\rho'}\,, \tag{3.169}$$

$$J_\phi(\vec{r}\,') \;=\; j\,2\,\sin\phi' \sum_j I_{1j}^P \,\frac{P_j(t')}{\rho_j}\;, \tag{3.170}$$

where here the subscript j represents only the basis functions located at the inner surface of the waveguide end wall ($z = z_e$). Substituting Eqs. 3.169 and 3.170 into Eq. 3.168 and evaluating the integrals with respect to ϕ' in closed form, one obtains

$$\begin{aligned} P_{RL} \;&=\; 2\pi\,\mathcal{Z}_{TE} \sum_j \sum_i \left\{ \int_0^{a_g} \left[I_{1j}^T\, I_{1i}^{T*}\,\frac{1}{\rho'}\, T_j(t')\, T_i(t') \right.\right. \\ &+\; \left.\left. I_{1j}^P\, I_{1i}^{P*}\,\frac{\rho'}{\rho_j\,\rho_i}\, P_j(t')\, P_i(t') \right] d\rho' \right\}, \end{aligned} \tag{3.171}$$

where here the subscript i represents only the basis functions located over the waveguide end wall. From Eqs. 2.50–2.57, the integrals of Eq. 3.171 can be evaluated in closed form with the same approach used to evaluate Eqs. 3.28 and 3.29, yielding

$$P_{RL} \;=\; 2\pi\,\mathcal{Z}_{TE} \left[\sum_j \sum_i \left(I_{1j}^T\, I_{1i}^{T*}\, F_{ij}^T \right) \;+\; \sum_i \left(|I_{1i}^P|^2\, F_{ij}^P \right) \right], \tag{3.172}$$

where F_{ij}^T is given by Eqs. 3.33–3.38 (depending on the situations illustrated in Fig. 3.2) and F_{ij}^P is given by Eq. 3.39. Notice from Fig. 3.3 that $\sin u = -1$ for all the generating-curve segments representing the inner surface of the waveguide end wall, as $\hat{t} = -\hat{\rho}$ at this surface.

3.6 Numerical Examples with the Impedance Boundary Condition

The computer code developed in Chapter 2 was augmented to include the formulation of the present chapter. To demonstrate this code, two test cases are discussed

below: the propagation of the fundamental TE_{11} mode inside a circular waveguide and the radiation characteristics of a corrugated-horn feed. This examples (together with several others successfully accomplished and compared against the results available in the open literature) demonstrate the correctness and accuracy of the code and, consequently, the present formulation.

3.6.1 Fundamental-Mode Propagation in a Circular Waveguide

The geometry of a circular waveguide is depicted in Fig. 3.5. The operation frequency is such that the free-space wavelength $\lambda = 1$ meter. The waveguide cross-section radius $a_g = 0.37\lambda$ enables only the propagation of the fundamental TE_{11} mode [47]. The equivalent modal currents $\vec{J}_g(\vec{r}')$ and $\vec{M}_g(\vec{r}')$ previously explained in Sect. 3.2.4 are located at $z = 0$. The waveguide is truncated at $z = -2\lambda$ and $z = 2\lambda$. As the unit surface normal $\hat{n}$ must point towards the region where the excitation sources are present, the generating curve of the present geometry is described in the counterclockwise sense, from $z = 2\lambda$ to $z = -2\lambda$. A total of 60 segments are used to describe the generating curve (5 on each end wall and 50 on the remaining region corresponding to $\rho = a_g$), such that approximately 20 segments per λ_g are used (where $\lambda_g = 1.637878\lambda$ is the guided wavelength of the TE_{11} mode).

The portion of the waveguide surface where $\rho = a_g$ is assumed a PEC. An IBC is placed over the end-wall surface at $z = 2\lambda$ in order to match the TE_{11} mode excited by $\vec{J}_g(\vec{r}')$ and $\vec{M}_g(\vec{r}')$ towards the positive $\hat{z}$-direction. In this situation, the

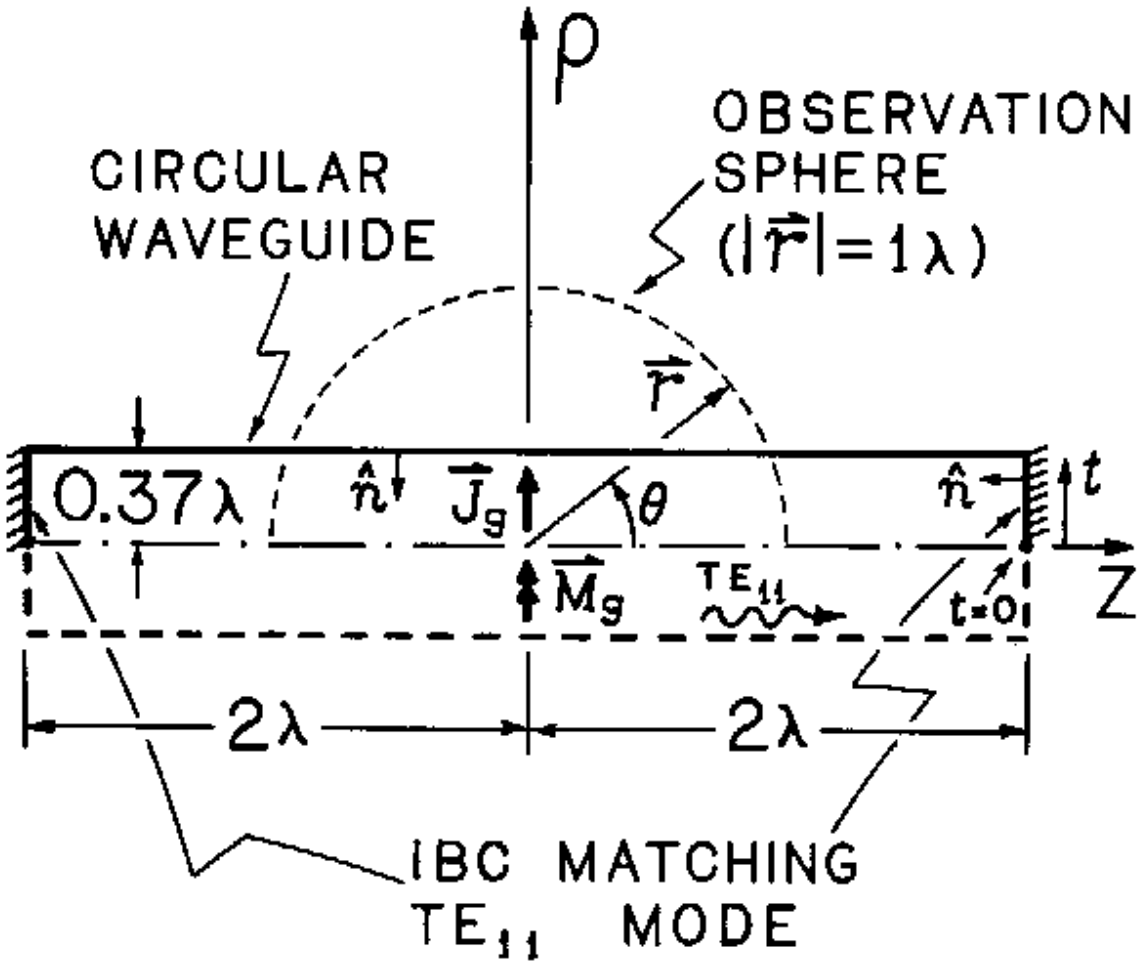

Figure 3.5: Geometry of the Circular Waveguide Excited by the TE_{11} Equivalent Modal Currents $\vec{J}_g(\vec{r}')$ and $\vec{M}_g(\vec{r}')$.

present example is simulating the propagation of the TE_{11} mode inside an infinite waveguide at the region $z > 0$ and no fields should be present at the region where $z < 0$. However, due to numerical limitations, this is not exactly true. In order to measure the accuracy of the numerical procedure, another IBC is placed over the end-wall surface at $z = -2\lambda$ to match any possible returned TE_{11} mode and permit the calculation of its associated power using Eq. 3.172. On both end walls, the IBC components are given by Eqs. 3.165 and 3.166. Although $\hat{\rho} = \hat{t}$ at $z = 2\lambda$, over this surface the IBC is matching a TE_{11} mode propagating along the positive $\hat{z}$-direction and Eqs. 3.165 and 3.166 still apply (see Eqs. 3.1, 3.2, 3.84, and 3.85).

For this geometry, the total electric and magnetic fields (calculated from the results of Sect. 3.3) are shown in Fig. 3.6. In these plots, the observation point $\vec{r}$ is located over the plane $\phi = 45°$ with $|\vec{r}| = 1\lambda$ (see Fig. 3.5). From Fig. 3.6, it is observed that the fields outside the waveguide ($21.716° < \theta < 158.284°$) and inside the waveguide at $z < 0$ ($\theta > 158.284°$) are negligible, as expected. At the regions where the observation point is close to the waveguide PEC surface ($\theta = 21.716°$ and $158.284°$), one observes the electric-field singularities of Eqs. 2.199–2.214, as previously discussed in Sect. 2.6.1. At the observation point located over the z-axis ($z = 1\lambda$) the electric and magnetic fields can be analytically determined using Eqs. 3.84–3.89 as

$$\vec{E}^{+}_{TE_{11}} = 77.528 \angle -39.80° \; \hat{x} \quad \text{V/m} \,, \tag{3.173}$$

$$\vec{H}^{+}_{TE_{11}} = 0.12565 \angle -39.80° \; \hat{y} \quad \text{A/m} \,. \tag{3.174}$$

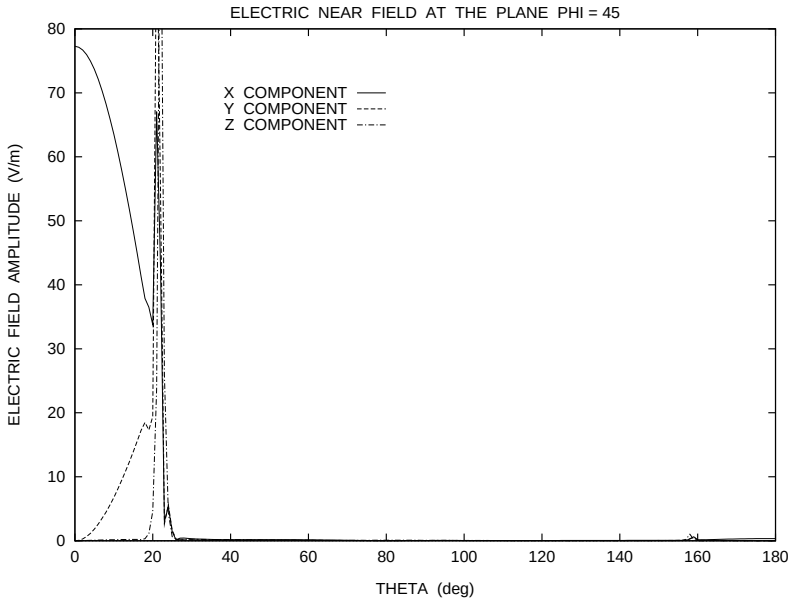

a) Electric Field Components (Plane $\phi = 45°$)

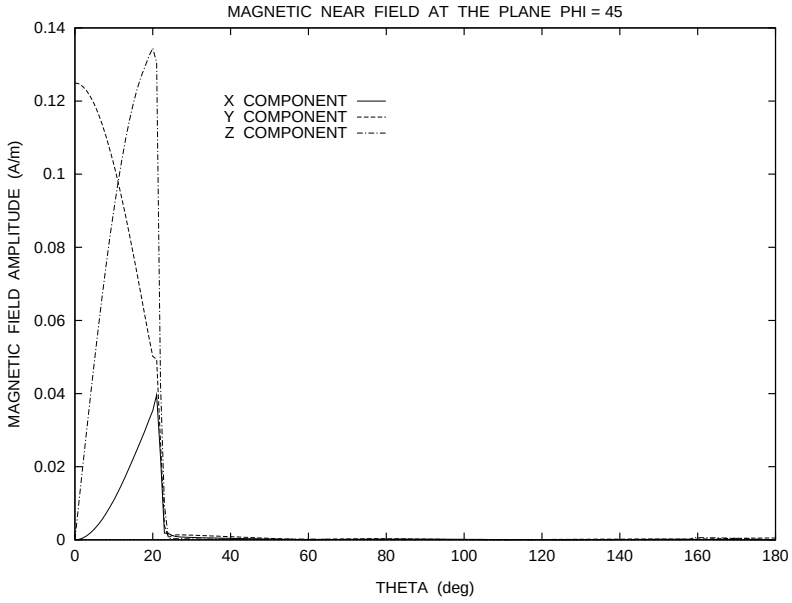

b) Magnetic Field Components (Plane $\phi = 45°$)

Figure 3.6: Field Inside the Circular Waveguide Excited by the TE_{11} Mode.

At the same location, the numerical results give:

$$\vec{E}^{+}_{TE_{11}} = 77.279 \angle -39.40^{\circ}\ \hat{x} \quad \text{V/m}\,, \tag{3.175}$$

$$\vec{H}^{+}_{TE_{11}} = 0.12495 \angle -40.00^{\circ}\ \hat{y} \quad \text{A/m}\,, \tag{3.176}$$

corresponding to an error of about -45 dB in the power associated with the excited TE_{11} mode, which is equal to 1 Watt. The application of Eq. 3.172 at the waveguide end wall at $z = -2\lambda$ gives

$$P_{RL} = 2.123 \times 10^{-5} \ \text{Watts} \tag{3.177}$$

instead of the expected $P_{RL} = 0$, which corresponds, once more, to an error of about -45 dB.

3.6.2 Far-Zone Pattern of a Corrugated Horn

The presented formulation may be used to analyze a corrugated horn by either describing its PEC corrugations on the generating curve or by applying an IBC to simulate these corrugations. Both cases are discussed in this section and the corresponding feed geometries are illustrated in Fig. 3.7. Again, the operation frequency is set such that the free-space wavelength $\lambda = 1$ meter. Both geometries have the same basic dimensions. The cross-section radius of the internal circular waveguide is $a_g = 0.37\lambda$, ensuring that only the fundamental TE_{11} mode is able to propagate. The internal length of the waveguide is equal to 1.5λ and the equivalent modal currents $\vec{J}_g(\vec{r}\,')$ and $\vec{M}_g(\vec{r}\,')$ are placed exactly at its center. The thickness

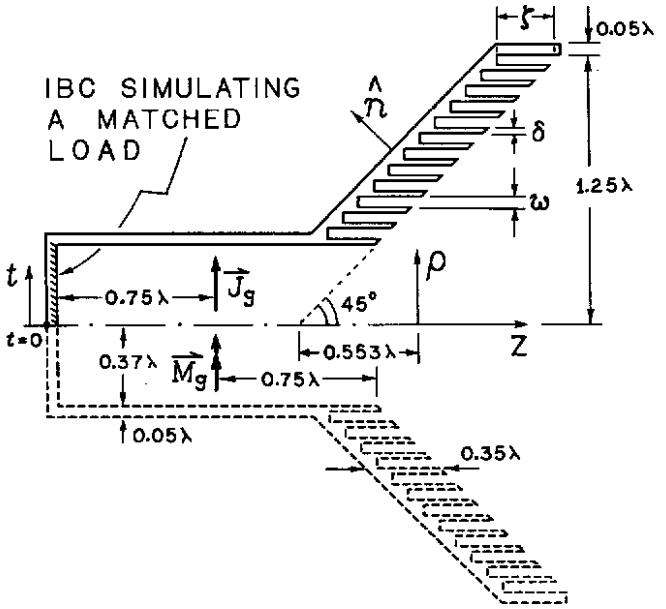

a) Horn with the PEC Corrugations

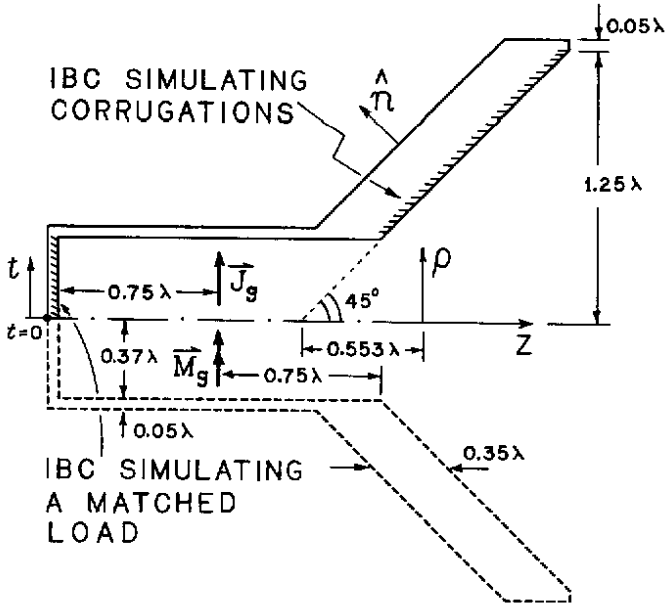

b) Horn with the IBC Approximation

Figure 3.7: Geometries of the Corrugated Horn.

of the waveguide wall is 0.05λ. The IBC given by Eqs. 3.165 and 3.166 is placed over the inner surface of the waveguide end wall to simulate a matched load. The horn has an aperture radius of 1.25λ and a flare angle of 45°. The flare width along the $\hat{z}$-direction is 0.35λ. The origin of the coordinate system is placed at the horn phase center, which is located over the z-axis at a distance of 0.553λ to the right of the conical-horn vertex (see Fig. 3.7).

In the case where the PEC corrugations are present, 12 corrugations are placed over the horn-flare surface (see Fig. 3.7). The dimension of each corrugation aperture is $w = 0.0489\lambda$ along the radial direction. The tooth-thickness of each corrugation is $\delta = 0.0244\lambda$. The depth of each corrugation along the $\hat{z}$-direction, measured from their aperture center, is $\zeta = 0.2720\lambda$. In the case where an IBC is used to simulate the PEC corrugations over the internal surface of the horn flare, the IBC components of Eq. 3.4 are given by [35]

$$\mathcal{Z}_t^{IBC} = -j \frac{w}{w+\delta} \tan k_o \zeta \,, \tag{3.178}$$

$$\mathcal{Z}_\phi^{IBC} = 0 \,, \tag{3.179}$$

where w, δ, and ζ are the parameters associated with the corrugation geometry previously described. Equations 3.178 and 3.179 are derived by averaging the fundamental TEM-mode impedances associated with the several shorted coaxial waveguides formed by the corrugations [37]. About 30 segments per λ are used to represent both generating curves, which are covered clockwise (marching from

the outer surface to the inner surface of the horn) with the unit normal vector $\hat{n}$ pointing towards the region where $\vec{J}_g(\vec{r}')$ and $\vec{M}_g(\vec{r}')$ are present (see Fig. 3.7).

The far-zone radiation patterns, obtained from Eq. 3.150, are shown in Fig. 3.8. The co- and cross-polarizations are defined accordingly to Ludwig Third definition [45]. From this figure, one may observe the excellent agreement obtained when the IBC is applied to simulate the radiation of a corrugated horn. The boresight gain obtained for the horn with PEC corrugations is 14.22 dBi, while the one obtained for the horn with the IBC is 14.24 dBi. However, from Eq. 3.172, the calculated return loss for the horn with PEC corrugations is -14.55 dB, while for the other one the return loss is -17.03 dB. This indicates that, although the IBC can be successfully used to simulate the radiation of a corrugated horn, it can not be used to obtain the return loss with a high accuracy.

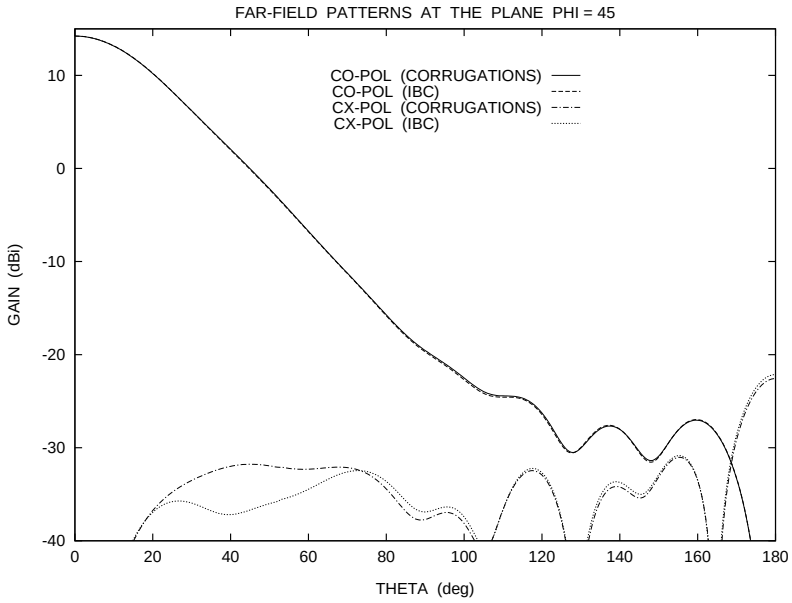

a) CO- and CX-POL Gains (Plane $\phi = 45°$)

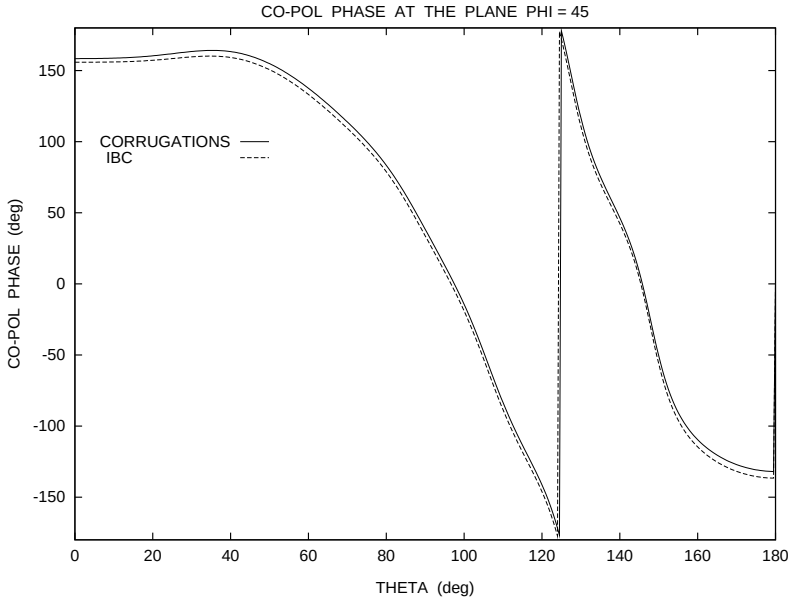

b) CO-POL Phase (Plane $\phi = 45°$)

Figure 3.8: Far-Zone Patterns of the Horns with PEC Corrugations and IBC.

Chapter 4

GENERALIZED CLASSICAL AXIALLY-SYMMETRIC DUAL-REFLECTOR ANTENNAS

Chapters 2 and 3 presented the necessary tools to rigorously analyze an axially-symmetric dual-reflector antenna system based on the EFIE formulation and the MoM technique. Although accurate, the inherent complexity of the formulation does not allow simple physical insights for the antenna design. However, for antenna systems with electrically large reflectors, a simpler analysis based on the Geometrical Optics (GO) approximation may be adopted. Although the GO approximation does not provide the desired accuracy, its simplicity enables the necessary insights to establish the basic parameters for the design procedure. In this chapter, the GO approximation is used to obtain closed-form design equations for generalized classical axially-symmetric dual-reflector antennas. Although a rigorous analysis is not conducted in this particular chapter, due to the axial symmetry these antenna configurations can be treated as bodies of revolution (BOR) and analyzed with the numerical tools presented in the last two chapters.

Classical axially-symmetric Cassegrain and Gregorian reflectors are widely used in high-gain antenna applications [25],[26]. The main disadvantage of these configurations is the subreflector blockage, which causes a number of deleterious effects such as the decrease of the antenna aperture efficiency. However, this problem can be minimized by reducing the main-reflector radiation towards the subreflector. This may be accomplished by either shaping both reflectors [27] or using alternative classical configurations [28]–[31]. In this chapter, the second option is considered by presenting, in a unified way, generalized classical axially-symmetric dual-reflector configurations that prevent, from a GO stand point, the main-reflector scattered energy from striking the subreflector surface. The formulation presented in this chapter can be applied to determine the optimum classical geometry or even to establish an initial configuration for a shaping procedure, which is discussed in Chapter 5.

The basic characteristics of the generalized classical axially-symmetric dual-reflector configurations are introduced in Sect. 4.1. Then, starting from initial design variables, closed-form expressions are derived for the relevant reflector parameters in Sect. 4.2. The blockage effects associated with the different configurations are briefly discussed in Sect. 4.3. Closed-form expressions for the GO aperture field distribution are obtained in Sect. 4.4. From these expressions, the gain, efficiency, and radiation pattern of the generalized classical configurations are established in

Sect. 4.5. Finally, Sect. 4.6 presents a parametric comparison among the different classical configurations to investigate their particular tradeoffs.

4.1 Generalized Classical Axially-Symmetric Dual-Reflector Geometries

There are four distinct types of classical axially-symmetric dual-reflector configurations that avoid the main-reflector scattering towards the subreflector. Their generating curves and relevant parameters are depicted in Figs. 4.1–4.4. They are obtained from GO concepts by imposing a uniform-phase field distribution over the antenna aperture (herein assumed at the plane $z = 0$), starting from a spherical-wave feed source at the antenna primary focus (located at the coordinate-system origin). The three-dimensional reflector surfaces are yield by spinning the generating curves about the z-axis (the symmetry axis of the BOR). At the $y = 0$ plane of Figs. 4.1–4.4, the basic geometric parameters of the four configurations are defined as follows. D_M and D_S are the main- and subreflector diameters, respectively. The edge of the subreflector generating curve is located at $x = X_S$ and, consequently, $D_S = 2|X_S|$. D_B is the blockage diameter, which locates the main-reflector generating-curve lower point at $x = D_B/2$. D_B is not necessarily equal to D_S and its value can be set to reduce the main-reflector illumination over the subreflector surface. V_M and V_S are, respectively, the z-coordinates of the main-

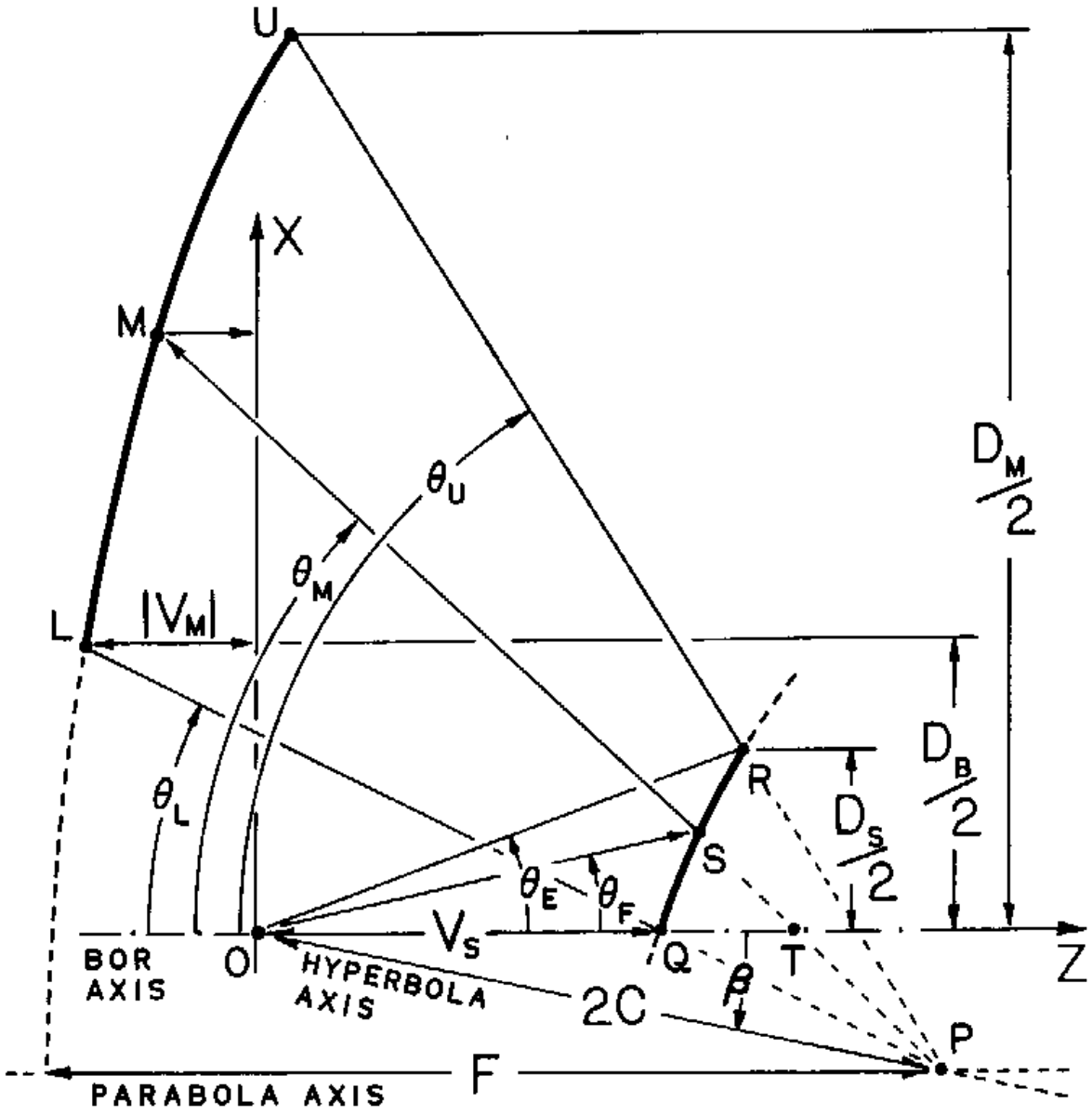

Figure 4.1: Basic Parameters of Classical Geometry I.

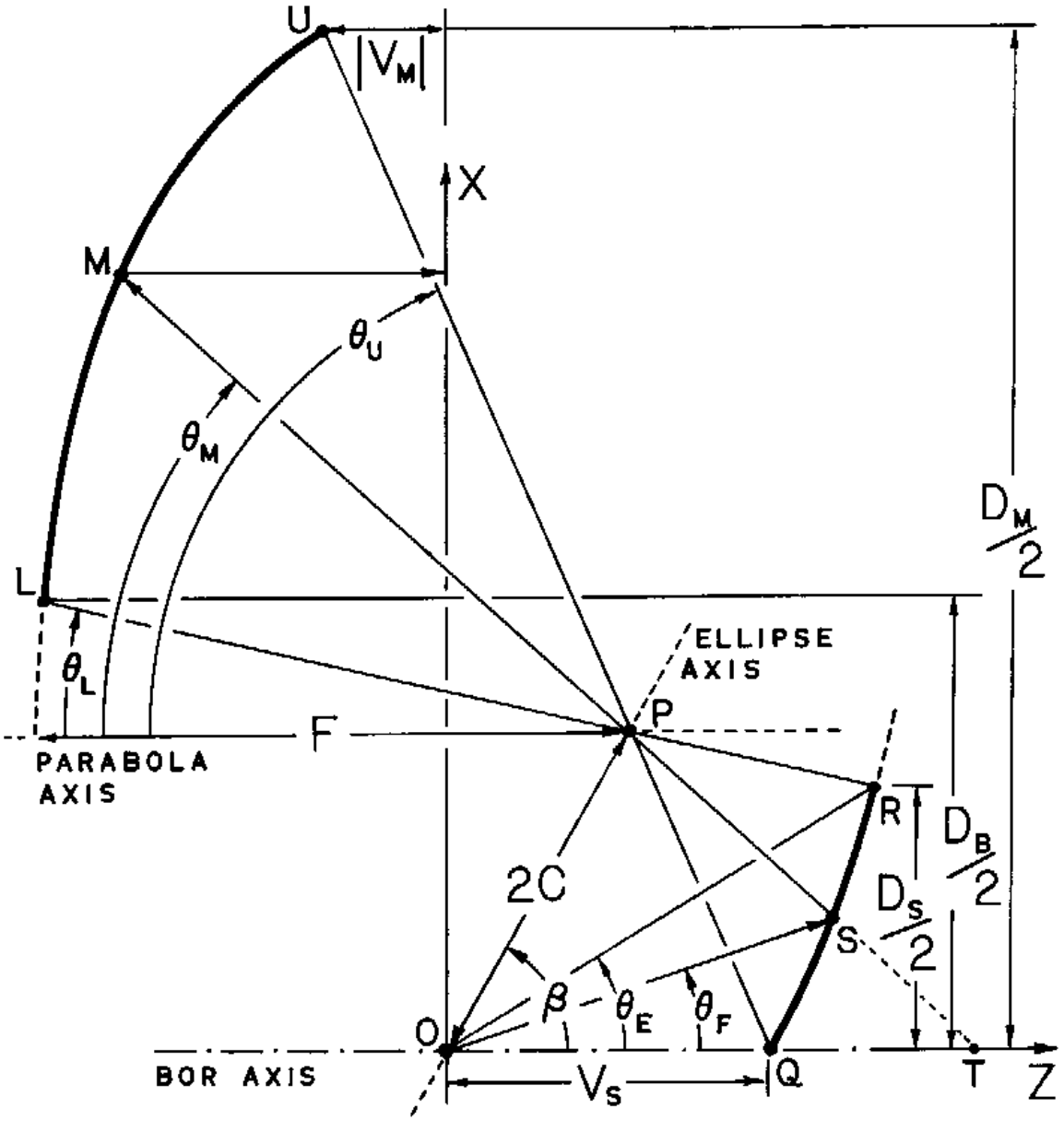

Figure 4.2: Basic Parameters of Classical Geometry II.

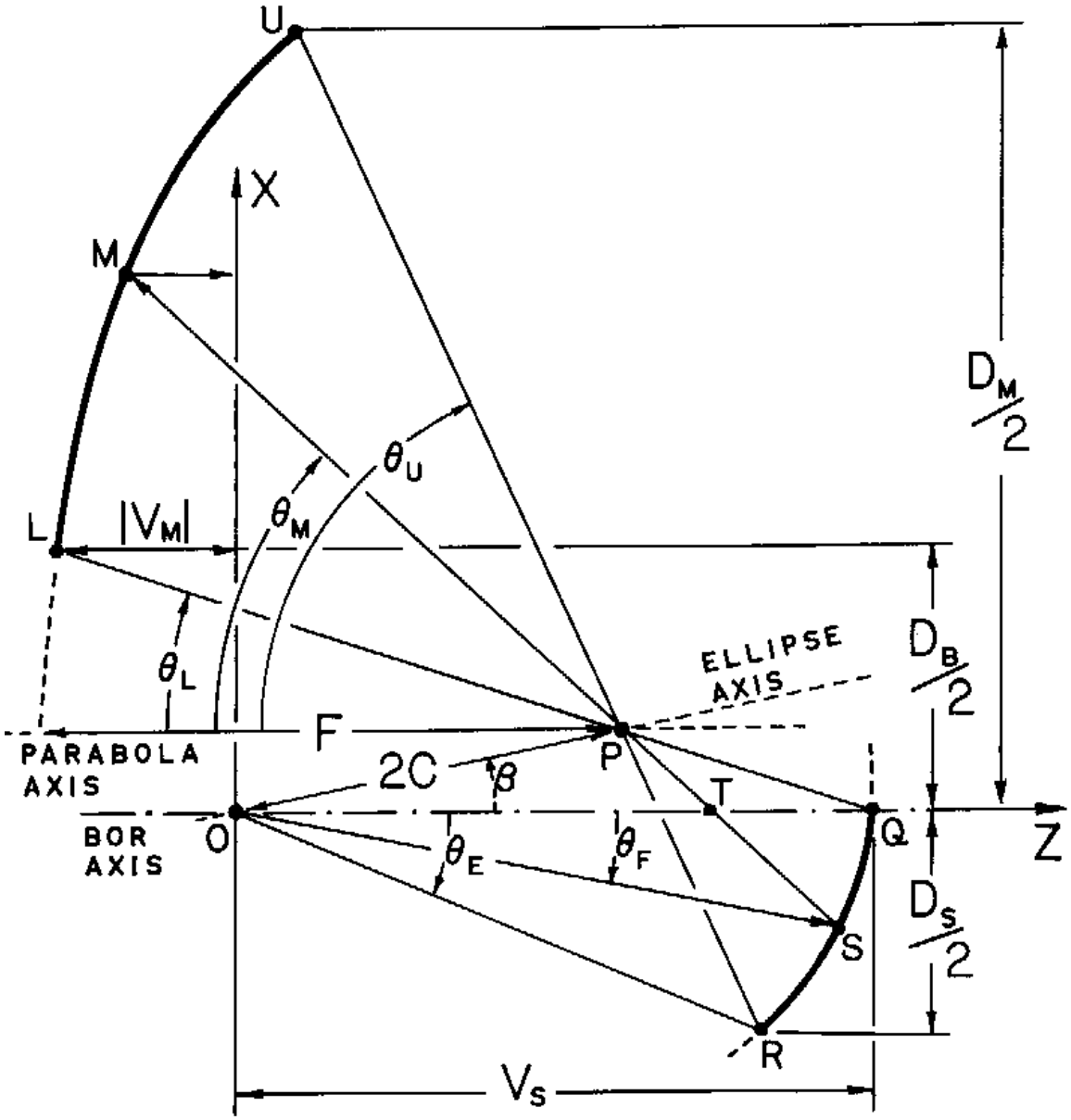

Figure 4.3: Basic Parameters of Classical Geometry III.

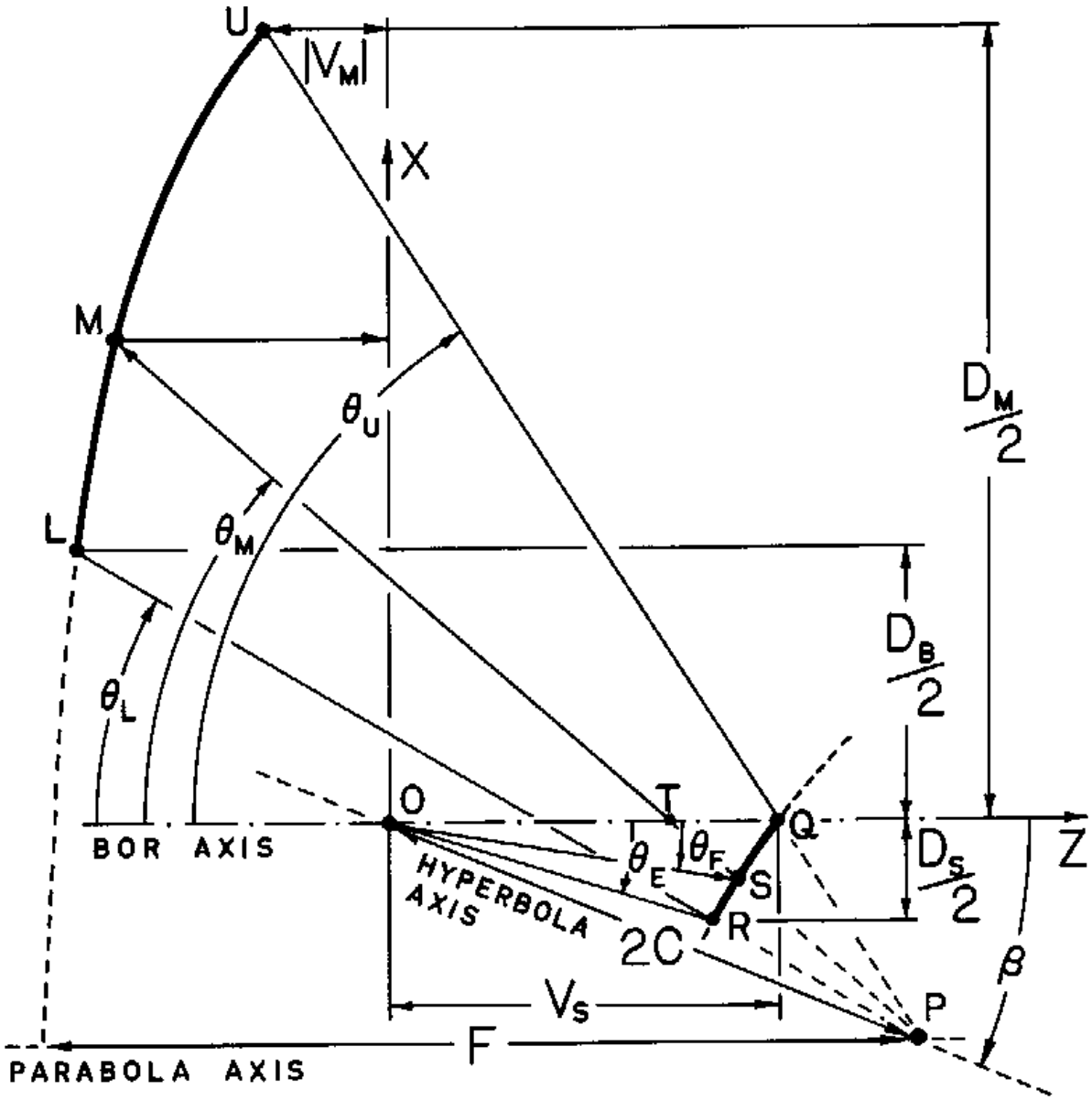

Figure 4.4: Basic Parameters of Classical Geometry IV.

and subreflector points corresponding to the principal ray (leaving the feed along the z-axis). F is the focal length of the parabola generating the main reflector and $2c$ and e are the inter-focal distance and eccentricity of the hyperbola or ellipse generating the subreflector, respectively. θ_E is the subreflector edge angle and β is the tilt angle between the z-axis and the axis of the subreflector generating conic section. θ_L and θ_U are the lower and upper angles of the main reflector. Finally, the angle θ_F defines an arbitrary feed-ray direction in the $y = 0$ plane. It is important to note that, in this work, positive (negative) angular values correspond to counterclockwise (clockwise) angles in the $y = 0$ plane shown in Figs. 4.1–4.4.

The four classical configurations are basically characterized by the location of the two subreflector caustic regions. One caustic (a ring caustic) is located by the rotation of the parabola focal point about the symmetry axis (z-axis). The second caustic (a line caustic) is located by the intersection of the subreflector reflected ray with the symmetry axis. The Classical Geometry I (CG I) illustrated in Fig. 4.1 is defined such that the feed-rays with $\theta_F > 0$ are reflected towards the aperture region with $x > 0$. The subreflector edge ray ($\theta_F = \theta_E > 0$) is reflected to $x = D_M/2$. Consequently, this configuration has virtual ring and line caustics. CG I was previously studied in Ref. [28] and named Axially Tilted Hyperbola (ATH). The Classical Geometry II (CG II) illustrated in Fig. 4.2 is defined such that the feed-rays with $\theta_F > 0$ are reflected towards the aperture region with $x > 0$. The subreflector edge ray ($\theta_F = \theta_E > 0$) is reflected to $x = D_B/2$. This configuration has a real

ring caustic and a virtual line caustic. CG II was previously studied in Ref. [28] under the denomination Axially Tilted Ellipse (ATE) and is also referred in the literature as the Axially Displaced Ellipse (ADE) configuration [30]. The Classical Geometry III (CG III) illustrated in Fig. 4.3 is defined such that the feed-rays with $\theta_F < 0$ are reflected towards the aperture region with $x > 0$. The subreflector edge ray ($\theta_F = \theta_E < 0$) is reflected to $x = D_M/2$. This configuration has real ring and line caustics. Finally, the Classical Geometry IV (CG IV) illustrated in Fig. 4.4 is defined such that the feed-rays with $\theta_F < 0$ are reflected towards the aperture region with $x > 0$. The subreflector edge ray ($\theta_F = \theta_E < 0$) is reflected to $x = D_B/2$. This configuration has a virtual ring caustic and a real line caustic. To the best knowledge of this author, CG III and IV were never presented in the open literature before Ref. [31]. In all these configurations the main-reflector generating curve is a parabola, while the subreflector generating curve is a hyperbola for CG I and IV and an ellipse for CG II and III. The feed is located at one of the hyperbola/ellipse foci and the parabola focus coincides with the other hyperbola/ellipse focus. In CG I and IV the hyperbola can be convex ($e > 1$) or concave ($e < -1$), and $|e| \to \infty$ yields a straight line. In all geometries V_S is a positive quantity and V_M can be either positive or negative. The basic parameters of the four antenna configurations are summarized in Table 4.1.

Geometry	I	II	III	IV
Main Reflector	Parabola	Parabola	Parabola	Parabola
Subreflector	Hyperbola	Ellipse	Ellipse	Hyperbola
e	$\|e\| > 1$	$0 < e < 1$	$0 < e < 1$	$\|e\| > 1$
β	$-\pi < \beta < 0$	$0 < \beta < \pi$	$0 < \beta < \pi$	$-\pi < \beta < 0$
θ_F	$\theta_F > 0$	$\theta_F > 0$	$\theta_F < 0$	$\theta_F < 0$
θ_E	$\theta_E > 0$	$\theta_E > 0$	$\theta_E < 0$	$\theta_E < 0$
θ_M	$\theta_M < 0$	$\theta_M < 0$	$\theta_M < 0$	$\theta_M < 0$
X_S	$X_S > 0$	$X_S > 0$	$X_S < 0$	$X_S < 0$
D_1	$D_1 = D_B$	$D_1 = D_M$	$D_1 = D_B$	$D_1 = D_M$
D_2	$D_2 = D_M$	$D_2 = D_B$	$D_2 = D_M$	$D_2 = D_B$
θ_1	$\theta_1 = \theta_L < 0$	$\theta_1 = \theta_U < 0$	$\theta_1 = \theta_L < 0$	$\theta_1 = \theta_U < 0$
θ_2	$\theta_2 = \theta_U < 0$	$\theta_2 = \theta_L < 0$	$\theta_2 = \theta_U < 0$	$\theta_2 = \theta_L < 0$

Table 4.1: Parameters of the Generalized Classical Geometries.

4.2 Design Equations

For design purposes, the reflector generating curves of Figs. 4.1–4.4 can be conveniently established from the starting parameters D_M, $D_S = 2|X_S|$, D_B, θ_E, and ℓ_o, where ℓ_o is the total path length from the feed to the antenna aperture (plane $z = 0$). Note from Figs. 4.1–4.4 that $\ell_o/2$ is approximately equal to the distance between the main- and subreflector surfaces. All expressions to be derived in this section are valid for the four different antenna configurations. For this reason it is imperative to observe the sign convention adopted in Sect. 4.1 for the several antenna parameters, which is summarized in Table 4.1.

To obtain the generating-curve parameters, the equations describing the conic sections are defined as follows. The parabola generating the main reflector in Figs. 4.1–4.4 is described by the equation

$$\overline{PM} = \frac{2F}{1 + \cos\theta_M}, \tag{4.1}$$

where $\overline{PM}$ is the distance from the parabola focal point P to the main-reflector point M (associated with the feed-ray θ_F) and the negative angle θ_M is illustrated in Figs. 4.1–4.4. The conic section generating the subreflector is described by

$$\overline{OS} \pm \overline{SP} = \frac{2c}{e}, \tag{4.2}$$

where $\overline{OS}$ is the distance from the feed located at the origin (point O) to the subreflector point S, $\overline{SP}$ is the distance from point S to P, and the positive (negative) sign corresponds to the ellipse (hyperbola) conic section.

Starting from the five input parameters, the design process first establishes the values of θ_1 and θ_2 (see Table 4.1), then the values of β, V_S, and V_M, and finally the conic sections parameters $2c$, e, and F. From Figs. 4.1–4.4 one directly obtains

$$\tan\theta_1 \;=\; -\,\frac{D_1}{2\,(V_S\,-\,V_M)}\,, \tag{4.3}$$

where, accordingly to Table 4.1, the negative angle θ_1 is either θ_L or θ_U and D_1 is either D_B or D_M. From the same figures, the constant path length ℓ_o (from the feed to the aperture plane $z = 0$) associated with the principal-ray ($\theta_F = 0$) and the subreflector-edge-ray ($\theta_F = \theta_E$) directions are respectively given by

$$\ell_o \;=\; V_S + \frac{V_S\,-\,V_M}{\cos\theta_1} - V_M \;=\; (V_S\,-\,V_M)\left(1 + \frac{1}{\cos\theta_1}\right)\,, \tag{4.4}$$

$$\begin{aligned}\ell_o \;&=\; \frac{X_S}{\sin\theta_E} - \frac{D_2\,-\,2\,X_S}{2\,\sin\theta_2} - \frac{X_S}{\tan\theta_E} - \frac{D_2\,-\,2\,X_S}{2\,\tan\theta_2} \\ &=\; X_S\,\tan\left(\frac{\theta_E}{2}\right) - \frac{D_2\,-\,2\,X_S}{2}\,\cot\left(\frac{\theta_2}{2}\right)\,,\end{aligned} \tag{4.5}$$

where the negative angle θ_2 is either θ_U or θ_L and D_2 is either D_M or D_B (accordingly to Table 4.1). Combining Eqs. 4.3 and 4.4, θ_1 is obtained from

$$\tan\left(\frac{\theta_1}{2}\right) \;=\; -\,\frac{D_1}{2\,\ell_o}\,. \tag{4.6}$$

Similarly, Eq. 4.5 yields θ_2 as

$$\tan\left(\frac{\theta_2}{2}\right) \;=\; -\,\frac{D_2\,-\,2\,X_S}{2\,\ell_o\,-\,2\,X_S\,\tan(\theta_E/2)}\,. \tag{4.7}$$

To derive the remaining antenna parameters, one applies Eq. 4.2 and the law of sines to the triangle OPQ in Figs. 4.1–4.4 to obtain

$$-\,\frac{2c}{\sin\theta_1} \;=\; \frac{V_S}{\sin(\beta\,-\,\theta_1)} \;=\; \frac{2c/e\,-\,V_S}{\sin\beta}\,, \tag{4.8}$$

and also to the triangle OPR in the same figures to obtain

$$\frac{2c}{\sin(\theta_E - \theta_2)} = \frac{X_S/\sin\theta_E}{\sin(\beta - \theta_2)} = \frac{2c/e - X_S/\sin\theta_E}{\sin(\beta - \theta_E)} . \tag{4.9}$$

From Eqs. 4.8 and 4.9 one obtains that

$$2c = -\frac{V_S \sin\theta_1}{\sin(\beta - \theta_1)} = \frac{X_S \sin(\theta_E - \theta_2)}{\sin\theta_E \sin(\beta - \theta_2)} , \tag{4.10}$$

$$\frac{2c}{e} = V_S \left[1 + \frac{\sin\beta}{\sin(\beta - \theta_1)}\right] = \frac{X_S}{\sin\theta_E} \left[1 + \frac{\sin(\beta - \theta_E)}{\sin(\beta - \theta_2)}\right] . \tag{4.11}$$

The division of Eq. 4.10 by Eq. 4.11 yields

$$\frac{\sin\theta_1}{\sin\beta + \sin(\beta - \theta_1)} = -\frac{\sin(\theta_E - \theta_2)}{\sin(\beta - \theta_2) + \sin(\beta - \theta_E)} , \tag{4.12}$$

which can be trigonometrically manipulated to establish the value of β:

$$\tan\beta = \frac{\sin\theta_E + \sin\theta_2 + \sin(\theta_E - \theta_2)}{\cos\theta_E + \cos\theta_2 + \sin(\theta_E - \theta_2)/\tan(\theta_1/2)} , \tag{4.13}$$

where the quadrant ambiguity of β is removed using Table 4.1. From Eq. 4.10, V_S is given by

$$V_S = -\frac{X_S \sin(\theta_E - \theta_2) \sin(\beta - \theta_1)}{\sin\theta_E \sin\theta_1 \sin(\beta - \theta_2)} , \tag{4.14}$$

and from Eq. 4.3, V_M is then given by

$$V_M = V_S + \frac{D_1}{2\tan\theta_1} . \tag{4.15}$$

Note that, although V_S is always a positive quantity, V_M may assume either positive or negative values.

With the values of θ_1, θ_2, β, V_S, and V_M established from Eqs. 4.6, 4.7, and 4.13–4.15, respectively, the conic-section parameters are finally obtained. From Eqs. 4.10 and 4.11, the inter-focal distance $2c$ and the eccentricity e of the conic section generating the subreflector are given by

$$2c = -\frac{V_S \sin\theta_1}{\sin(\beta - \theta_1)}, \tag{4.16}$$

$$e = -\frac{\sin\theta_1}{\sin\beta + \sin(\beta - \theta_1)}. \tag{4.17}$$

From Figs. 4.1–4.4 and Eq. 4.1 (with $\theta_M = \theta_1$), the focal length F of the parabola generating the main reflector is then given by

$$F = -\frac{D_1 - 4c \sin\beta}{4 \tan(\theta_1/2)}. \tag{4.18}$$

The commonly encountered classical Cassegrain and Gregorian configurations can be directly derived from CG I and III, respectively, by taking the limit $D_B \to 0$ in Eqs. 4.3–4.18. Note that, from Table 4.1 and for CG I and III, $D_1 = D_B$, $D_2 = D_M$, $\theta_1 = \theta_L$, and $\theta_2 = \theta_U$. Under these circumstances, the antenna parameters of the classical Cassegrain and Gregorian configurations are given by

$$\theta_L = \beta = 0, \tag{4.19}$$

$$\tan\left(\frac{\theta_U}{2}\right) = -\frac{D_M - 2X_S}{2\ell_o - 2X_S \tan(\theta_E/2)}, \tag{4.20}$$

$$V_S = \frac{X_S}{2}\left[\cot\left(\frac{\theta_E}{2}\right) + \tan\left(\frac{\theta_U}{2}\right)\right], \tag{4.21}$$

$$V_M = V_S - \frac{\ell_o}{2}, \tag{4.22}$$

$$2c = -\frac{2\,V_S\,\sin(\theta_E - \theta_U)}{\sin\theta_U + \sin\theta_E - \sin(\theta_E - \theta_U)}\,, \tag{4.23}$$

$$e = \frac{2c}{2V_S - 2c}\,, \tag{4.24}$$

$$F = 2c - V_M\,, \tag{4.25}$$

where Eqs. 4.19–4.25 are valid for both Cassegrain and Gregorian configurations as far as one observes the sign convention defined in Sect. 4.1 for the antenna parameters associated with CG I and III, respectively.

4.3 Blockage Considerations

For the generalized classical axially-symmetric dual-reflector antennas presented in this chapter, three blockage mechanisms may be present (not considering the blockage provided by the subreflector supporting structure): the rays reflected by the subreflector may intersect the subreflector surface (self blockage); the rays reflected by the subreflector may intersect the feed structure (feed blockage); and the rays reflected by the main reflector may intersect the subreflector surface (subreflector blockage).

The GO concepts used to derive the formulation of Sect. 4.2 do not take into account that the spinning of the subreflector generating curve about the z-axis may result in a ray leaving the subreflector lower half and striking the subreflector upper half, which characterizes the self blockage. By inspection of Figs. 4.1–4.4 one observes that the self blockage can only occur for CG III and IV. The necessary

conditions to avoid this blockage mechanism are obtained by imposing allowable ranges for the angles θ_L and θ_U. Here, following the notation of Table 4.1, these conditions are obtained in terms of the angles θ_1 and θ_2, in order to handle CG III and IV in a general way. The condition for θ_2 is directly obtained by spinning the geometry of Fig. 4.3 about the z-axis and observing that the self blockage corresponding to this angle occurs whenever the z-coordinate of the main-reflector point U is greater than the z-coordinate of the subreflector point R. So, the self blockage corresponding to θ_2 is avoided whenever

$$|\theta_2| \leq \frac{\pi}{2} . \tag{4.26}$$

Note from Fig. 4.4 that this condition is not relevant for CG IV as $|\theta_2| < |\theta_1|$ for this geometry. The two necessary conditions for θ_1 are obtained with the help of Fig. 4.5. The first condition is obtained from (see Fig. 4.5a)

$$|\theta_1| \leq \theta_{ST} , \tag{4.27}$$

$$|\theta_1| = 2\,\theta_{SI} , \tag{4.28}$$

$$\theta_{ST} + \theta_{SI} = \frac{\pi}{2} , \tag{4.29}$$

where θ_{ST} is the positive angle between the z-axis and the surface tangent (in the plane of the figure) at the subreflector vertex and θ_{SI} is the positive angle between the principal feed ray and the surface normal. The combination of Eqs. 4.27–4.29 yields

$$|\theta_1| \leq \frac{\pi}{3} . \tag{4.30}$$

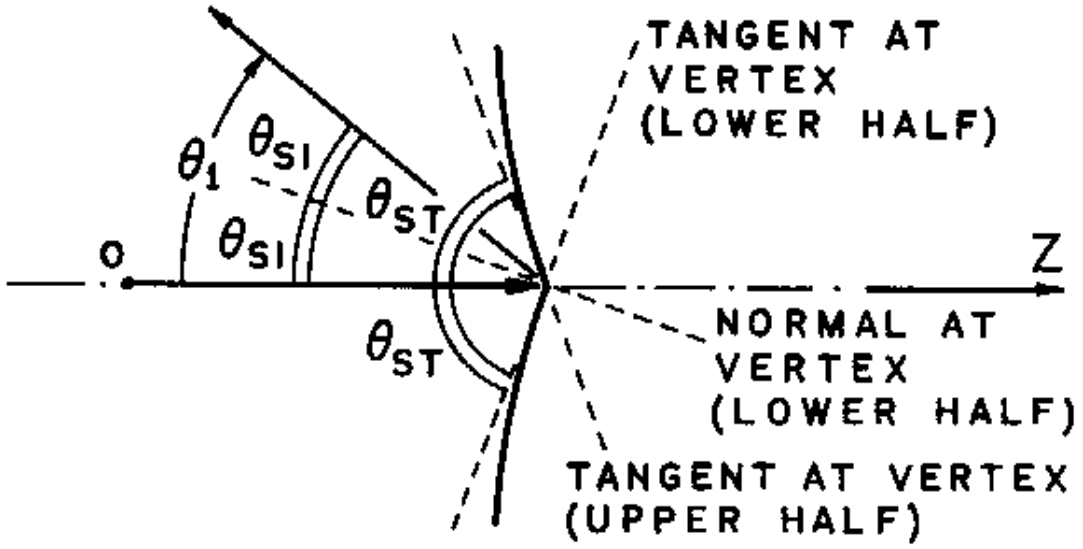

a) First Condition

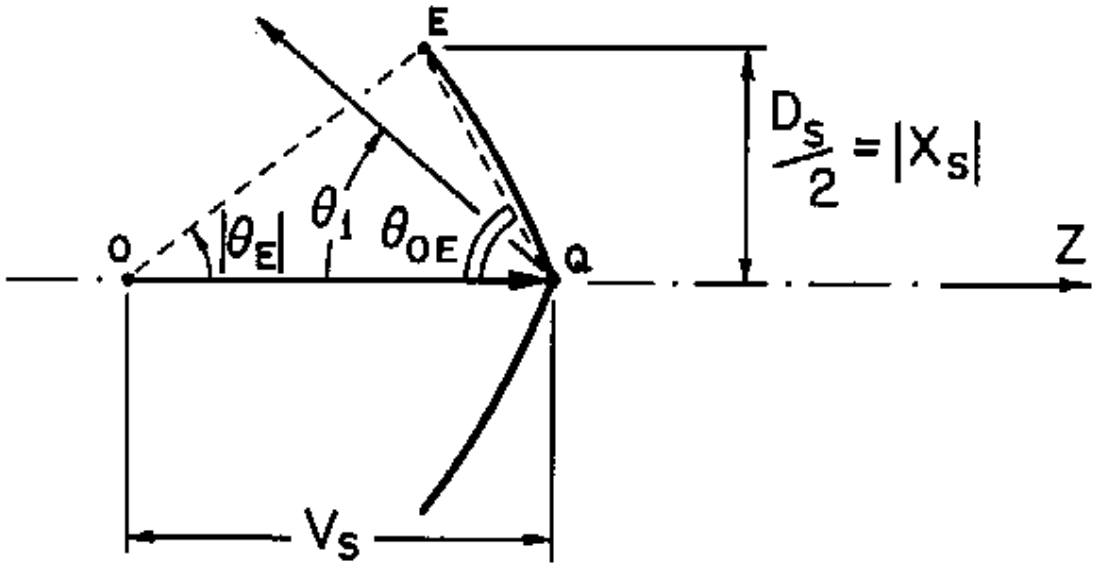

b) Second Condition

Figure 4.5: θ_1 Conditions to Avoid the Self Blockage in CG III and IV.

The second condition is given by

$$|\theta_1| \leq \theta_{OE} , \tag{4.31}$$

where, from the triangle OQE in Fig. 4.5b,

$$\tan\theta_{OE} = \frac{X_S \sin\theta_E}{X_S \cos\theta_E - V_S \sin\theta_E} , \tag{4.32}$$

noticing that $\theta_{OE} > 0$ and, accordingly to the sign convention of Sect. 4.1, both X_S and θ_E are negative. Observe that, depending on the geometry, Eq. 4.30 or Eq. 4.31 will be the limiting condition for θ_1.

The feed blockage depends on the physical dimensions of the feed. For this reason, it is impossible to obtain specific conditions to avoid this blockage mechanism without specific feed details. The GO formulation adopted in Sect. 4.2 always assume the feed illumination to be produced by a point source. Under this condition, the subreflector of CG I and II will never scatter towards the feed (see Figs. 4.1 and 4.2). For CG III and IV the scattering towards the feed point source can be avoided, provided that the real line caustic is located between the point source and the subreflector vertex. From Figs. 4.3 and 4.4, this is provided by the condition

$$|\theta_E| \leq |\theta_2| , \tag{4.33}$$

where, accordingly to Table 4.1, θ_2 is θ_U and θ_L for CG III and IV, respectively, and $\theta_E < 0$.

From Figs. 4.1–4.4, the subreflector blockage is directly avoided by specifying

$$D_B \geq D_S . \tag{4.34}$$

This condition will also prevent the main-reflector scattering towards the feed structure as long as the feed maximum diameter does not exceed D_S.

4.4 Aperture Field Distribution

The basic antenna radiation characteristics (e.g., gain, efficiency, radiation pattern, etc.) can be calculated from the GO aperture field distribution. However, diffraction effects are ignored by GO and this might be a significant source of inaccuracy in all but reflector systems with very large electric dimensions (when GO is the dominant effect). Besides the diffraction effects, the GO aperture field distribution also neglects the direct feed contribution to the antenna radiation pattern, multiple bounces over the reflector structure, etc.. In any event, for antenna-design purposes the information contained in the GO aperture distribution is very useful, and hence this section will concentrate on it.

The GO field distribution over the aperture plane is obtained from the geometries described in Figs. 4.1–4.4 and from the corresponding conic-section equations (given by Eqs. 4.1 and 4.2). On doing so one must recall that Figs. 4.1–4.4 represent the generating-curve geometries in the $y = 0$ plane—the three-dimensional configurations are obtained by spinning these generating curves about the symmetry axis (z-axis). However, assuming that an aperture point is described by the usual cylindrical coordinates ρ_A and ϕ_A (with $z_A = 0$), due to the axial symmetry

the aperture field over an arbitrary ϕ_A-constant plane can still be obtained using Figs. 4.1–4.4.

The spherical-wave feed source illuminating the antennas will be assumed to be given by

$$\vec{E}_F(\vec{r}_F) = [E_\theta(\theta_F, \phi_F)\ \hat{\theta}_F + E_\phi(\theta_F, \phi_F)\ \hat{\phi}_F]\ \frac{e^{-jk_o r_F}}{r_F}\,, \tag{4.35}$$

$$\vec{H}_F(\vec{r}_F) = \frac{1}{\eta_o}\,\hat{r}_F \times \vec{E}_F(\vec{r}_F)\,, \tag{4.36}$$

where $\vec{E}_F(\vec{r}_F)$ and $\vec{H}_F(\vec{r}_F)$ are the electric and magnetic fields of the feed TEM radiation and r_F, θ_F, and ϕ_F are the usual spherical coordinates associated with the feed system. The TEM representation of the feed radiation assumes that the feed is sufficiently away from the subreflector, which generally occurs. Equations 4.35 and 4.36 allows the representation of most practical feeds, including the RCF model given by Eqs. 2.126–2.129. Using GO concepts and Figs. 4.1–4.4 one observes that, after the reflection by the two surfaces, the feed electric field polarized in the positive (negative) $\hat{\theta}_F$-direction is mapped at the aperture in the positive $\hat{\rho}_A$-direction and the feed electric field polarized in the positive (negative) $\hat{\phi}_F$-direction is mapped at the aperture in the positive $\hat{\phi}_A$-direction for CG I and II (CG III and IV). Also, noticing that the path length ℓ_o is constant for all the feed rays propagating towards the aperture (uniform phase distribution), the GO electric-field Cartesian

components E_X^{GO} and E_Y^{GO} at the aperture plane can be written as

$$\begin{bmatrix} E_X^{GO}(\rho_A, \phi_A) \\ E_Y^{GO}(\rho_A, \phi_A) \end{bmatrix} = \begin{bmatrix} \cos\phi_A & -\sin\phi_A \\ \sin\phi_A & \cos\phi_A \end{bmatrix} \begin{bmatrix} \cos(\phi_F - \phi_A)\ E_\theta(\theta_F, \phi_F) \\ \cos(\phi_F - \phi_A)\ E_\phi(\theta_F, \phi_F) \end{bmatrix}$$

$$\times \quad A_{GO}(\theta_F)\ e^{j(\Phi_G - k_o \ell_o)}\ , \tag{4.37}$$

where Φ_G is the Gouy phase shift [49] and $A_{GO}(\theta_F)$ is the amplitude of the GO aperture fields. The value of ϕ_F is obtained from:

$$\phi_F = \begin{cases} \phi_A & \text{for Geometries I and II ,} \\ \phi_A + \pi & \text{for Geometries III and IV .} \end{cases} \tag{4.38}$$

The Gouy phase shift Φ_G is obtained by adding a $\pi/2$ phase shift each time a ray leaving the feed crosses a real caustic [49]. From Figs. 4.1–4.4 one then has

$$\Phi_G = \begin{cases} 0\ , & \text{for Geometry I ,} \\ \pi/2\ , & \text{for Geometry II ,} \\ \pi\ , & \text{for Geometry III ,} \\ \pi/2\ , & \text{for Geometry IV .} \end{cases} \tag{4.39}$$

The amplitude $A_{GO}(\theta_F)$ is obtained using GO concepts, with the help of Eqs. 4.1 and 4.2 and Figs. 4.1–4.4. The expressions to be derived are valid for all the different classical configurations, as long as one observes the sign convention defined in Sect. 4.1 for the antenna parameters. $A_{GO}(\theta_F)$ is represented as [9]

$$A_{GO}(\theta_F) = \frac{1}{r_F} \sqrt{\left| \frac{\rho_{1r}^S\ \rho_{2r}^S}{(R_{SM} + \rho_{1r}^S)\,(R_{SM} + \rho_{2r}^S)} \right|}\ , \tag{4.40}$$

where r_F is the distance between the primary focus and the subreflector surface along the feed-ray θ_F (segment $\overline{OS}$), R_{SM} is the distance between the sub- and main-reflector surfaces along the reflected feed-ray θ_F (segment $\overline{SM}$), and ρ_{1r}^S and ρ_{2r}^S are the subreflector-reflected wavefront principal radii of curvature at point S (associated with the ring and line caustics, respectively). ρ_{1r}^S and ρ_{2r}^S are positive (divergent wave) or negative (convergent wave) if the corresponding caustics are virtual or real, respectively. The absolute values of ρ_{1r}^S and ρ_{2r}^S are given by the lengths of $\overline{SP}$ and $\overline{TS}$, respectively. From Figs. 4.1–4.4 and Eq. 4.2, the distance r_F is given by

$$r_F \;=\; \frac{c\,(e\,-\,1/e)}{e\,\cos(\beta\,-\,\theta_F)\,-\,1}\,, \tag{4.41}$$

and the principal radius of curvature ρ_{1r}^S is given by

$$\rho_{1r}^S \;=\; r_F\,-\,\frac{2c}{e}\,. \tag{4.42}$$

Note that Eq. 4.42 already takes into account the correct sign of ρ_{1r}^S for the different classical geometries. The distance $R_{SM}\,+\,\rho_{1r}^S$ corresponds to the length of $\overline{PM}$, which is given by Eq. 4.1 as

$$R_{SM}\,+\,\rho_{1r}^S \;=\; \frac{2\,F}{1\,+\,\cos\theta_M}\,. \tag{4.43}$$

Applying the law of sines to the triangle OTS in Figs. 4.1–4.4, the principal radius of curvature ρ_{2r}^S is given by

$$\rho_{2r}^S \;=\; -\,\frac{r_F\,\sin\theta_F}{\sin\theta_M}\,, \tag{4.44}$$

noticing that θ_M is a negative angle, accordingly to Table 4.1. Similarly to ρ_{1r}^S in Eq. 4.42, this equation already accounts for the sign of ρ_{2r}^S. The distance $R_{SM}+\rho_{2r}^S$ corresponds to the length of $\overline{TM}$ and is obtained from Eq. 4.1 and by applying the law of sines to the triangle OPT:

$$R_{SM} + \rho_{2r}^S = \frac{2\,F}{1 + \cos\theta_M} - \frac{2c\,\sin\beta}{\sin\theta_M} . \tag{4.45}$$

Substituting Eqs. 4.41–4.45 into Eq. 4.40 one obtains

$$A_{GO}(\theta_F) = \sqrt{\left| \frac{\sin\theta_F\,[1 - (2c)/(e\,r_F)]\,(1 + \cos\theta_M)}{4\,F\,[c\,\sin\beta - (F\,\sin\theta_M)/(1 + \cos\theta_M)]} \right|} . \tag{4.46}$$

In order to eliminate θ_M from Eq. 4.46, from Figs. 4.1–4.4 and Eq. 4.2 one obtains the following relation:

$$\tan\left(\frac{\beta - \theta_F}{2}\right) = \left(\frac{1 - e}{1 + e}\right) \tan\left(\frac{\beta - \theta_M}{2}\right) , \tag{4.47}$$

which yields, after some trigonometric manipulations,

$$\frac{\sin\theta_M}{1 + \cos\theta_M} = \tan\left(\frac{\theta_M}{2}\right) = -\frac{e\,\sin\beta\,(1 + \cos\theta_F) - (1 + e\,\cos\beta)\,\sin\theta_F}{(1 - e\,\cos\beta)\,(1 + \cos\theta_F) - e\,\sin\beta\,\sin\theta_F} , \tag{4.48}$$

$$1 + \cos\theta_M = \frac{2}{1 + \tan^2(\theta_M/2)} = \frac{[(1 - e\,\cos\beta)\,(1 + \cos\theta_F) - e\,\sin\beta\,\sin\theta_F]^2}{[e^2 - 2\,e\,\cos(\beta - \theta_F) + 1]\,(1 + \cos\theta_F)} . \tag{4.49}$$

From Eq. 4.41 one obtains

$$1 - \frac{2c}{e\,r_F} = \frac{e^2 - 2\,e\,\cos(\beta - \theta_F) + 1}{e^2 - 1} \tag{4.50}$$

which can be substituted, together with Eqs. 4.48 and 4.49, into Eq. 4.46 to yield

$$A_{GO}(\theta_F) = \sqrt{\left| \frac{\tan(\theta_F/2)}{4\,F\,(e^2 - 1)} \frac{[A_1\,(1 + \cos\theta_F) - A_2\,\sin\theta_F]^3}{[A_3\,(1 + \cos\theta_F) - A_4\,\sin\theta_F]} \right|} , \tag{4.51}$$

where

$$A_1 = 1 - e\cos\beta\,, \tag{4.52}$$

$$A_2 = e\sin\beta\,, \tag{4.53}$$

$$A_3 = (c\,A_1 + e\,F)\sin\beta\,, \tag{4.54}$$

$$A_4 = F\,(1 + e\cos\beta) + c\,A_2\sin\beta\,. \tag{4.55}$$

To conclude the derivation of the aperture electric-field components $E_X^{GO}(\rho_A, \phi_A)$ and $E_Y^{GO}(\rho_A, \phi_A)$, one substitutes Eq. 4.51 into 4.37 to obtain

$$\begin{aligned}\begin{bmatrix} E_X^{GO}(\rho_A,\phi_A) \\ E_Y^{GO}(\rho_A,\phi_A) \end{bmatrix} &= \begin{bmatrix} \cos\phi_A & -\sin\phi_A \\ \sin\phi_A & \cos\phi_A \end{bmatrix} \begin{bmatrix} \cos(\phi_F-\phi_A)\,E_\theta(\theta_F,\phi_F) \\ \cos(\phi_F-\phi_A)\,E_\phi(\theta_F,\phi_F) \end{bmatrix} \\ &\times \sqrt{\left|\frac{\tan(\theta_F/2)}{4\,F\,(e^2-1)}\,\frac{[A_1\,(1+\cos\theta_F) - A_2\,\sin\theta_F]^3}{[A_3\,(1+\cos\theta_F) - A_4\,\sin\theta_F]}\right|} \\ &\times e^{j\,(\Phi_G - k_o\ell_o)}\,, \end{aligned} \tag{4.56}$$

where ϕ_F and Φ_G are given by Eqs. 4.38 and 4.39, respectively, and A_1, A_2, A_3, and A_4 are given by Eqs. 4.52–4.55, respectively. Finally, the angle θ_F, corresponding to the feed-ray direction in the plane of Figs. 4.1–4.4, can be obtained from Eqs. 4.1 and 4.48 as

$$\tan\left(\frac{\theta_F}{2}\right) = \frac{e\,(\sin\beta + \Delta\,\cos\beta) - \Delta}{e\,(\cos\beta - \Delta\,\sin\beta) + 1}\,, \tag{4.57}$$

where

$$\Delta = \frac{\rho_A - 2c\,\sin\beta}{2\,F} = -\tan\left(\frac{\theta_M}{2}\right)\,. \tag{4.58}$$

Note that the correct sign of the angle θ_F is already taken into account by Eqs. 4.57 and 4.58, as long as one observes the sign convention defined in Sect. 4.1 for the antenna parameters.

The analysis to be performed in the following sections is based on the $\hat{x}$-polarized RCF model given by Eqs.2.126–2.129 with the parameter $e = h$ in order to provide a circularly-symmetric radiation pattern, which characterizes most of the practical feeds used in antenna applications. In this case, Eq. 4.35 is rewritten as

$$\vec{E}_F(\vec{r}_F) = \begin{cases} \cos^h\theta_F \ (\cos\phi_F \ \hat{\theta}_F - \sin\phi_F \ \hat{\phi}_F) \ \frac{e^{-jk_o r_F}}{r_F} \ , & \text{for } |\theta_F| \leq \pi/2 \ , \\ 0 \ , & \text{for } |\theta_F| > \pi/2 \ , \end{cases} \tag{4.59}$$

where the parameter h controls the circularly-symmetric pattern of the RCF model. Substituting Eqs. 4.38 and 4.59 into Eq. 4.58 one obtains that the GO aperture electric field for the above RCF illumination is given by (assuming $|\theta_F| \leq \pi/2$)

$$\vec{E}_A^{GO}(\rho_A) = \cos^h\theta_F \ A_{GO}(\theta_F) \ e^{j(\Phi_G - k_o\ell_o)} \ \hat{x} \ , \tag{4.60}$$

which indicates that the GO aperture electric field has the same polarization of the RCF model and does not depend on ϕ_A.

4.5 Radiation Characteristics of the Aperture Field Distribution

Useful estimates for the antenna radiation characteristics (i.e., radiation pattern, gain, and efficiency) can be obtained from the GO aperture field distribution de-

rived in Sect. 4.4 for the generalized classical axially-symmetric dual-reflector configurations. As already mentioned in the beginning of Sect. 4.4, although the GO approximation ignores diffraction effects, the results still carry sufficient accuracy to assume their usefulness for design purposes.

In this section, the reflector illumination is provided by the RCF model described in Eq. 4.59 and, consequently, the GO aperture electric field is given by Eq. 4.60. The electric far-zone field radiated by the aperture distribution of Eq. 4.60 is obtained from [21]

$$\begin{aligned}\vec{E}_{FF}(\vec{r}) &= \frac{jk_o}{4\pi}\,\frac{e^{-jk_o r}}{r}\,(1+\cos\theta)\,(\cos\phi\,\hat{\theta}\,-\,\sin\phi\,\hat{\phi}) \\ &\times \int_0^{2\pi}\int_{D_B/2}^{D_M/2} \vec{E}_A^{GO}(\rho_A)\cdot\hat{x}\;\; e^{jk_o\,\rho_A\,\sin\theta\,\cos(\phi_A-\phi)}\;\; \rho_A\;\; d\rho_A\;\; d\phi_A\;, \qquad (4.61)\end{aligned}$$

where r, θ, and ϕ are the usual spherical coordinates of the far-zone observation point. Note that the integration with respect to ρ_A is evaluated from $D_B/2$ to $D_M/2$ because the GO aperture illumination is zero outside this range. $D_B/2$ is the lower limit for the ρ_A-integration in Eq. 4.61 assuming that Eq. 4.34 is satisfied (i.e., the subreflector does not block the aperture illumination). Due to the fact that $\vec{E}_A^{GO}(\rho_A)$ does not depend on ϕ_A, the integration with respect to ϕ_A can be evaluated in closed form, yielding

$$\begin{aligned}\vec{E}_{FF}(\vec{r}) &= \frac{jk_o}{2}\,\frac{e^{-jk_o r}}{r}\,(1+\cos\theta)\,(\cos\phi\,\hat{\theta}\,-\,\sin\phi\,\hat{\phi}) \\ &\times \int_{D_B/2}^{D_M/2} \vec{E}_A^{GO}(\rho_A)\cdot\hat{x}\;\; J_0(k_o\,\rho_A\,\sin\theta)\;\; \rho_A\;\; d\rho_A\;, \qquad (4.62)\end{aligned}$$

where $J_0(k_o\,\rho_A\,\sin\theta)$ is the Bessel function of order zero and argument $k_o\,\rho_A\,\sin\theta$. This equation provides the far-zone pattern radiated by the GO aperture distribution and, consequently, does not take into account any kind of spillover contributions.

The antenna gain G is defined as the ratio between the peak power density (in the present case occurring at the boresight direction $\theta = 0$) radiated by the antenna and the one of an isotropic source radiating the same total feed power P_{in} [50]:

$$G \;=\; \frac{2\pi}{\eta_o}\,\frac{r^2\,|\vec{E}_{FF}(\theta=0)|^2}{P_{in}}\,, \tag{4.63}$$

where $\vec{E}_{FF}(\theta = 0)$ is obtained from Eq. 4.62 (noticing that the feed direct contribution is blocked by the subreflector at $\theta = 0$) as

$$\vec{E}_{FF}(\theta=0) \;=\; jk_o\,\frac{e^{-jk_or}}{r}\int\limits_{D_B/2}^{D_M/2}\vec{E}_A^{GO}(\rho_A)\;\;\rho_A\;\;d\rho_A\;. \tag{4.64}$$

For the RCF model of Eq. 4.59, the power radiated inside a spherical sector with half-angle $|\theta_F|$ and radius r_F is obtained from

$$\begin{aligned} P_{feed}(\theta_F) \;&=\; \frac{1}{2\,\eta_o}\int\limits_0^{|\theta_F|}\int\limits_0^{2\pi}|\vec{E}_F(\vec{r}_F)|^2\;r_F^2\;\sin\theta'\;d\phi'\;d\theta' \\ &=\; \frac{\pi}{\eta_o}\,\frac{1\;-\;\cos^{2h+1}\theta_F}{2\,h\;+\;1}\,, \end{aligned} \tag{4.65}$$

and, consequently,

$$P_{in} \;=\; P_{feed}(\theta_F = \pm\pi/2) \;=\; \frac{\pi}{\eta_o\,(2\,h\;+\;1)}\,. \tag{4.66}$$

The antenna efficiency η is defined in order to take into account the several losses associated with the antenna system (e.g., poor aperture illumination, spillover,

feed return loss, polarization mismatch, ohmic losses, etc.). In the present study, only the efficiencies associated with the aperture illumination and feed spillover are considered and η is then defined as

$$\eta \;=\; \eta_A \, \eta_S \;, \tag{4.67}$$

where η_A and η_S represent the aperture and feed-spillover efficiencies, respectively. The aperture efficiency η_A is defined as the ratio between the gain of the actual aperture and the one of an unblocked aperture with a uniform illumination and diameter D_M (which provides the maximum possible gain), both radiating the same power P_{ape} [21]:

$$\eta_A \;=\; \frac{2\pi}{\eta_o} \, \frac{r^2 \, |\vec{E}_{FF}(\theta = 0)|^2}{P_{ape}} \, \left(\pi \, \frac{D_M}{\lambda} \right)^{-2} \;. \tag{4.68}$$

From the GO concepts used to obtain the aperture illumination, the power P_{ape} radiated by the aperture is the one that the feed radiates towards the subreflector. From Eq. 4.65 one obtains

$$P_{ape} \;=\; P_{feed}(\theta_F = \theta_E) \;=\; \frac{\pi}{\eta_o} \, \frac{1 \,-\, \cos^{2h+1} \theta_E}{2\,h \,+\, 1} \;. \tag{4.69}$$

The feed-spillover efficiency η_S is then defined as the ratio between the power P_{ape} radiated by the aperture and the total power P_{in} radiated by the feed. From Eqs. 4.66 and 4.69:

$$\eta_S \;=\; \frac{P_{ape}}{P_{in}} \;=\; 1 \,-\, \cos^{2h+1} \theta_E \;. \tag{4.70}$$

Finally, from Eqs. 4.63, 4.68, and 4.70 one obtains

$$G = \left(\pi \frac{D_M}{\lambda}\right)^2 \eta_A \eta_S . \tag{4.71}$$

4.6 Efficiencies of the Generalized Classical Geometries

In this section, a numerical study based on the results of Sects. 4.4 and 4.5 is conducted in order to determine the optimum generalized classical geometries capable of yielding the highest possible gain. Due to the GO concepts used throughout this chapter, the aperture and feed-spillover efficiencies given by Eqs. 4.68 and 4.70 are identical for similar antennas when the same feed illumination is applied. An antenna is considered similar to another if they only differ by a scale factor and, consequently, all the angular dimensions remain unchanged. Due to this property and under a GO perspective, it is then possible to study the efficiencies of different antenna geometries using any one of the antenna linear dimensions as a normalization factor (consequently reducing the number of possible variables by one).

From Sect. 4.2, the geometries of the four possible generalized classical configurations are obtained by specifying the values of D_M, D_S, D_B, ℓ_o, and θ_E. From Sects. 4.4 and 4.5, the aperture illumination and, consequently, the antenna efficiency are further obtained by also specifying the feed radiation. In the present study, the feed is modeled by the raised-cosine pattern of Eq. 4.59, in which case the feed radiation is completely determined by the parameter h. However, it is

desirable to instead specify the feed radiation by its taper towards the subreflector-edge direction. The relation between this feed taper F_{tap} (in dB) and the parameter h is obtained from Eq. 4.59 as

$$F_{tap} \;=\; 20\,\log_{10}\left[\frac{\left|\vec{E}_F(\theta_F=\theta_E)\right|}{\left|\vec{E}_F(\theta_F=0)\right|}\right] \;=\; 20\,h\,\log_{10}(\cos\theta_E)\;. \qquad (4.72)$$

Due to the fact that the antenna gain can not be obtained in closed-form (see Eqs. 4.60 and 4.64), its parametric study is performed by normalizing all linear dimensions to D_M. Also, in order to provide the maximum illuminated aperture area, D_B is always assumed equal to D_S. On doing so, a convenient set of antenna parameters to consider is formed by D_S/D_M, ℓ_o/D_M, θ_E, and F_{tap}. Also, since the antenna gain (which is the primary concern of this section) is directly obtained from Eq. 4.71, the present study needs to be concerned only with the aperture and feed-spillover efficiencies given by Eqs. 4.68 and 4.70, respectively. Furthermore, it was observed that CG I and III have the same efficiency characteristics, and the same being true between CG II and IV. For this reason, the following study is conducted in two separate subsections.

4.6.1 Efficiencies of Classical Geometries I and III

A parametric study of the CG I and III (see Figs. 4.1 and 4.3, respectively) efficiencies was performed for specific values of ℓ_o/D_M and θ_E. For CG I, the parameter ℓ_o/D_M was varied from 0.5 up to 2, corresponding to representative distances between reflectors of about $D_M/4$ to D_M, respectively. However, it was found for

CG III that the condition given by Eq. 4.26 to prevent the subreflector self blockage was never satisfied when $\ell_o/D_M = 0.5$. Due to this, ℓ_o/D_M started at 0.6 for CG III. For both geometries, the subreflector edge angle $|\theta_E|$ (recalling that θ_E is negative for CG III, see Table 4.1) was varied from 10° to 60°. For each pair of parameters ℓ_o/D_M and θ_E, the values of D_S/D_M and F_{tap} were numerically obtained from the results of Sect. 4.5 in order to provide the maximum possible antenna efficiency η. The results obtained are shown in Tables 4.2 and 4.3 for CG I and III, respectively. Furthermore, in Table 4.3, the symbol † in the column associated with η depicts the CG III configurations where the condition given by Eq. 4.33 (to prevent the subreflector rays from striking the feed point source) is not satisfied.

Besides the values of ℓ_o/D_M, θ_E, D_S/D_M, F_{tap}, β, η_S, η_A, and η, Tables 4.2 and 4.3 also show the results for F/D_p, V_S/D_M, and V_M/D_M. The parameter F/D_p is provided since it impacts the main-reflector manufacturing cost (the main reflector is the largest and usually the most expensive surface to manufacture in the dual-reflector system). F is the generating-parabola focal length and D_p is the main-reflector diameter assuming that the symmetry axis coincides with the parabola axis ($D_p \neq D_M$). From Figs. 4.1–4.4 and Eq. 4.1 (with $\theta_M = \theta_U$), F/D_p is given for all geometries by

$$\frac{F}{D_p} = \frac{F}{D_M - 4\,c\,\sin\beta} = -\frac{1}{4\,\tan(\theta_U/2)}\,. \tag{4.73}$$

$\frac{\ell_o}{D_M}$	θ_E	$\frac{D_S}{D_M}$	F_{tap}	β	$\frac{F}{D_p}$	$\frac{V_S}{D_M}$	$\frac{V_M}{D_M}$	η_S	η_A	η
0.5	10°	0.100	−11 db	−1.1°	0.275	0.261	0.013	0.92	0.90	0.83
0.5	20°	0.095	−11 db	−1.9°	0.272	0.111	−0.137	0.93	0.90	0.83
0.5	30°	0.095	−11 db	−2.7°	0.269	0.065	−0.183	0.93	0.89	0.83
0.5	40°	0.085	−10 db	−3.0°	0.265	0.037	−0.211	0.92	0.90	0.83
0.5	50°	0.075	−9 db	−3.0°	0.261	0.021	−0.227	0.92	0.90	0.83
0.5	60°	0.065	−8 db	−3.0°	0.257	0.012	−0.237	0.92	0.90	0.83
1.0	10°	0.100	−11 db	−1.0°	0.553	0.273	−0.225	0.92	0.90	0.83
1.0	20°	0.100	−11 db	−1.8°	0.551	0.129	−0.369	0.93	0.90	0.83
1.0	30°	0.100	−11 db	−2.3°	0.548	0.081	−0.418	0.93	0.89	0.83
1.0	40°	0.095	−10 db	−2.6°	0.543	0.053	−0.445	0.92	0.90	0.83
1.0	50°	0.095	−10 db	−2.9°	0.540	0.039	−0.460	0.94	0.89	0.83
1.0	60°	0.090	−9 db	−3.0°	0.535	0.028	−0.471	0.94	0.89	0.83
1.5	10°	0.100	−11 db	−0.9°	0.831	0.277	−0.472	0.92	0.90	0.83
1.5	20°	0.100	−11 db	−1.5°	0.828	0.133	−0.616	0.93	0.90	0.83
1.5	30°	0.105	−11 db	−2.0°	0.830	0.089	−0.660	0.93	0.89	0.83
1.5	40°	0.095	−10 db	−2.1°	0.819	0.057	−0.692	0.92	0.90	0.83
1.5	50°	0.100	−10 db	−2.4°	0.820	0.045	−0.704	0.94	0.89	0.83
1.5	60°	0.095	−9 db	−2.9°	0.814	0.033	−0.716	0.94	0.89	0.84
2.0	10°	0.100	−11 db	−0.9°	1.109	0.280	−0.720	0.92	0.90	0.83
2.0	20°	0.105	−11 db	−1.4°	1.112	0.142	−0.857	0.93	0.90	0.83
2.0	30°	0.105	−11 db	−1.7°	1.109	0.091	−0.908	0.93	0.89	0.83
2.0	40°	0.100	−10 db	−1.8°	1.101	0.062	−0.937	0.92	0.90	0.83
2.0	50°	0.105	−10 db	−2.1°	1.104	0.050	−0.950	0.94	0.89	0.83
2.0	60°	0.100	−9 db	−2.1°	1.095	0.037	−0.962	0.94	0.89	0.84

Table 4.2: Maximum-Efficiency Configurations of CG I for Prescribed Values of ℓ_o/D_M and θ_E, with $D_B = D_S$.

$\frac{\ell_o}{D_M}$	$\lvert\theta_E\rvert$	$\frac{D_S}{D_M}$	F_{tap}	β	$\frac{F}{D_p}$	$\frac{V_S}{D_M}$	$\frac{V_M}{D_M}$	η_S	η_A	η
0.6	10°	0.115	−12 dB	1°	0.267	0.359	0.061	0.94	0.89	0.83
0.6	20°	0.110	−11 dB	2°	0.266	0.185	−0.113	0.93	0.90	0.83
0.6	30°	0.115	−11 dB	4°	0.262	0.138	−0.159	0.93	0.90	0.84
0.6	40°	0.125	−11 dB	8°	0.257	0.121	−0.176	0.94	0.89	0.84
0.6	50°	0.120	−10 dB	11°	0.255	0.098	−0.199	0.94	0.90	0.84
0.6	60°	0.120	−9 dB	17°	0.252	0.086	−0.211	0.94	0.91	0.85
1.0	10°	0.115	−12 dB	1°	0.446	0.346	−0.152	0.94	0.89	0.83
1.0	20°	0.110	−11 dB	3°	0.446	0.173	−0.325	0.93	0.90	0.83
1.0	30°	0.115	−11 dB	7°	0.442	0.125	−0.373	0.93	0.90	0.83
1.0	40°	0.120	−11 dB	15°	0.437	0.102	−0.396	0.94	0.89	0.84
1.0	50°	0.120	−10 dB	40°	0.434	0.084	−0.414	0.94	0.90	0.84
1.0	60°	0.115	−9 dB	120°	0.434	0.069	−0.430	0.94	0.90	$0.84_\dagger$
1.5	10°	0.115	−12 dB	1°	0.670	0.340	−0.408	0.94	0.89	0.83
1.5	20°	0.105	−11 dB	4°	0.675	0.160	−0.590	0.93	0.90	0.83
1.5	30°	0.110	−11 dB	15°	0.669	0.114	−0.635	0.93	0.90	0.83
1.5	40°	0.115	−11 dB	125°	0.663	0.091	−0.658	0.94	0.89	0.83
1.5	50°	0.115	−10 dB	163°	0.661	0.074	−0.675	0.94	0.90	$0.84_\dagger$
1.5	60°	0.115	−9 dB	169°	0.658	0.062	−0.687	0.94	0.90	$0.84_\dagger$
2.0	10°	0.115	−12 dB	1°	0.895	0.337	−0.662	0.94	0.89	0.83
2.0	20°	0.105	−11 dB	7°	0.901	0.157	−0.842	0.93	0.90	0.83
2.0	30°	0.110	−11 dB	133°	0.894	0.111	−0.888	0.93	0.89	0.83
2.0	40°	0.115	−11 dB	169°	0.887	0.088	−0.911	0.94	0.89	$0.83_\dagger$
2.0	50°	0.115	−10 dB	172°	0.885	0.071	−0.928	0.94	0.89	$0.84_\dagger$
2.0	60°	0.110	−9 dB	174°	0.887	0.056	−0.943	0.94	0.90	$0.84_\dagger$

Table 4.3: Maximum-Efficiency Configurations of CG III for Prescribed Values of ℓ_o/D_M and θ_E, with $D_B = D_S$.

The parameter V_S/D_M (V_M/D_M) is proportional to the distance between the feed location and the subreflector vertex (main-reflector lower point L), as illustrated in Figs. 4.1 and 4.3. A positive value of V_M/D_M indicates that the feed point source is located behind the main reflector, and hence an appropriate access hole must be carved on the main-reflector surface.

The results of Tables 4.2 and 4.3 indicate that the maximum η possible for both CG I and III is about 83%, obtained when $D_S \approx 0.1\, D_M$ and $F_{tap} \approx -11$ dB for the wide range of the parameters ℓ_o/D_M and θ_E used. These results come with no surprise. As $D_S \ll D_M$, CG I and III approximate the classical Cassegrain and Gregorian configurations, respectively. It is known that the GO aperture fields of the classical Cassegrain and Gregorian can be determined using an equivalent paraboloid of focal length [25]

$$F_{eq} = F\,\frac{|e^2 - 1|}{e^2 + 1}\,, \tag{4.74}$$

with the same aperture diameter and feed illumination (where in Eq. 4.74 F and e are the main-reflector focal length and the subreflector eccentricity of the classical Cassegrain or Gregorian configuration, respectively). So, the present CG I and III approximately behave (under the GO perspective) as axially-symmetric paraboloidal reflectors, for which the maximum efficiency and corresponding feed taper are known to be $\eta \approx 83\%$ and $F_{tap} \approx -11$ dB, respectively [21].

From Tables 4.2 and 4.3 it can also be observed that the main-reflector curvature (which is proportional to D_p/F) decreases as the distance between both reflectors increases, as expected. The distance $|V_M|$ increases with $|\theta_E|$, while V_M remains negative for practically all cases. Consequently, V_S decreases as $|\theta_E|$ increases, which may result in a prohibitively small distance between the feed aperture and the subreflector for large values of $|\theta_E|$. On the other hand, to provide the desired illumination for small values of $|\theta_E|$ the feed is required to have a higher gain (larger aperture), which may result in the feed structure blocking the subreflector radiation. These observations indicate that great care must be exercised to avoid the undesirable feed blockage for both CG I and III.

In Figs. 4.6 and 4.7 some representative configurations providing maximum efficiency η are shown for CG I (with $D_S = D_B = 0.1\,D_M$) and CG III (with $D_S = D_B = 0.115\,D_M$), respectively. These figures demonstrate that the feed blockage will be of less concern for small values of ℓ_o/D_M and $|\theta_E|$. Furthermore, in Figs. 4.8 and 4.9 the characteristics of the aperture illumination for the configurations depicted in Figs. 4.6d and 4.7d, respectively, are illustrated, where $F_{tap} = -11$ dB on both cases. Although presented for particular configurations, these figures show the general trend of the aperture illumination provided by CG I and III. The total aperture field illumination is given by Eq. 4.60, where the GO and feed contributions are associated with the terms $A_{GO}(\theta_F)$ and $\cos^h \theta_F$, respectively (each curve is independently normalized). Figures 4.8 and 4.9 show that the GO

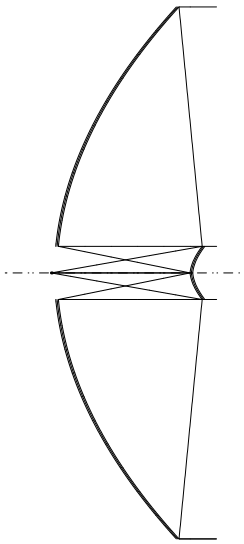

a) $\frac{\ell_o}{D_M} = 0.5$ and $\theta_E = 10°$

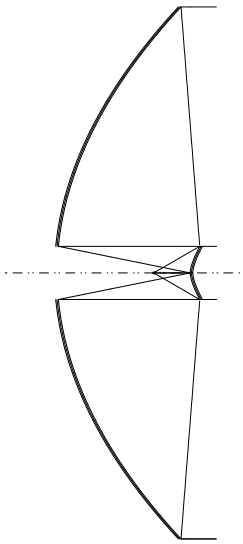

b) $\frac{\ell_o}{D_M} = 0.5$ and $\theta_E = 30°$

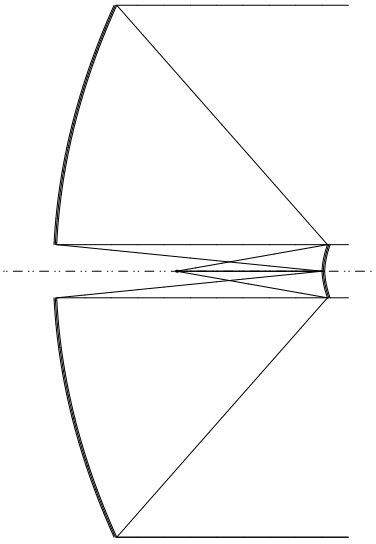

c) $\frac{\ell_o}{D_M} = 1$ and $\theta_E = 10°$

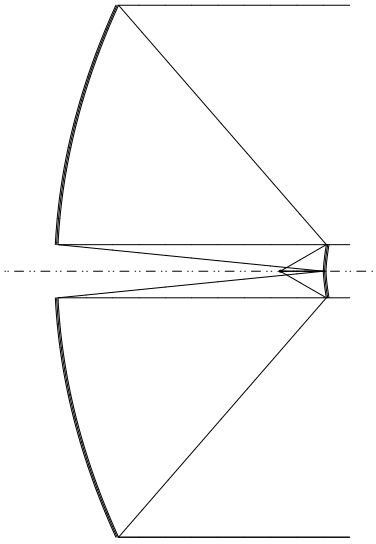

d) $\frac{\ell_o}{D_M} = 1$ and $\theta_E = 30°$

Figure 4.6: Representative Configurations of CG I ($D_S = D_B = 0.1\, D_M$).

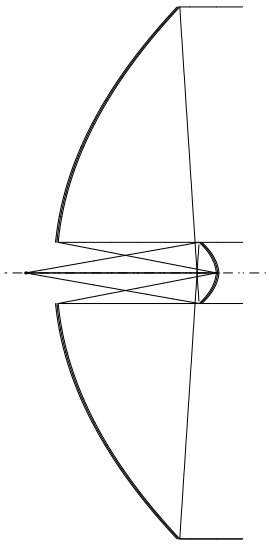

a) $\frac{\ell_o}{D_M} = 0.6$ and $|\theta_E| = 10°$

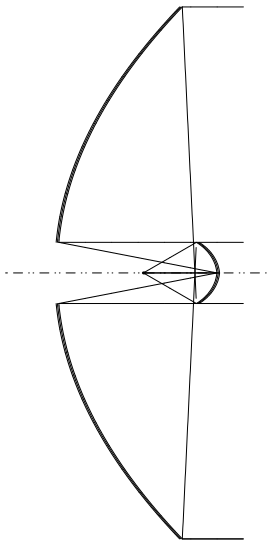

b) $\frac{\ell_o}{D_M} = 0.6$ and $|\theta_E| = 30°$

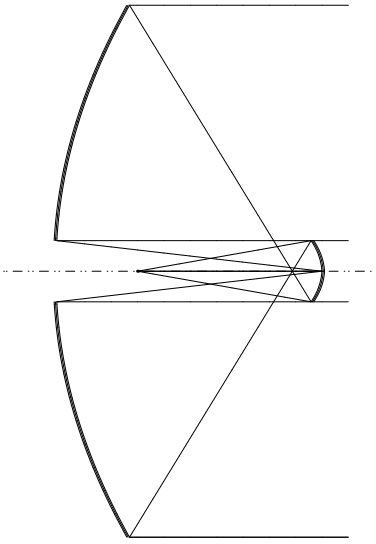

c) $\frac{\ell_o}{D_M} = 1$ and $|\theta_E| = 10°$

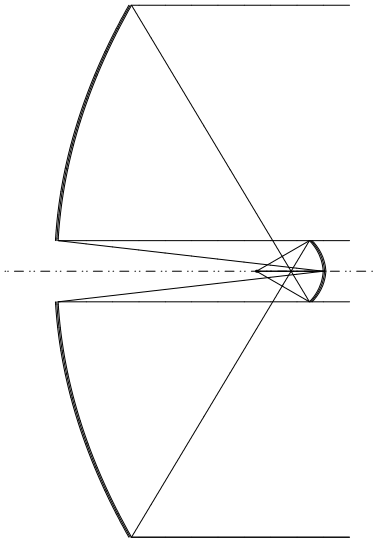

d) $\frac{\ell_o}{D_M} = 1$ and $|\theta_E| = 30°$

Figure 4.7: Representative Configurations of CG III ($D_S = D_B = 0.115\, D_M$).

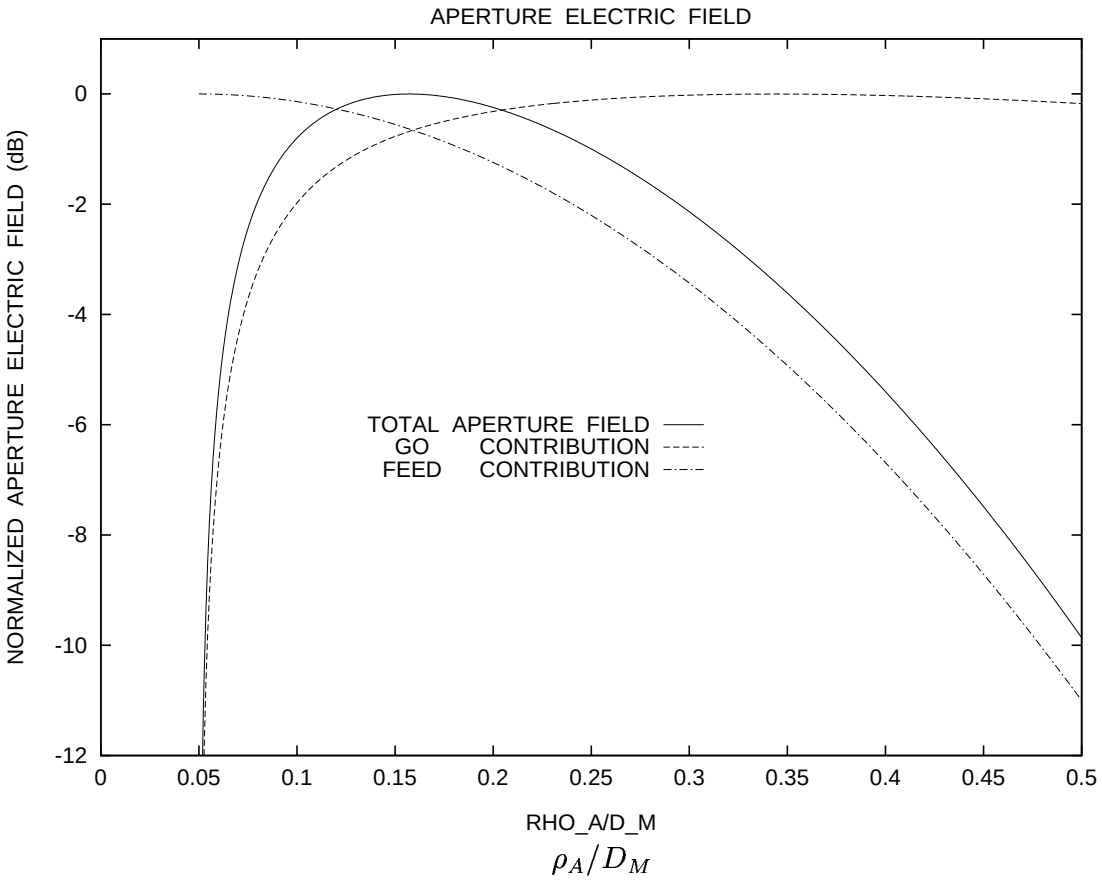

Figure 4.8: Characteristics of the Aperture Illumination for CG I, with Parameters $D_S = D_B = 0.1\,D_M$, $\ell_o = D_M$, $\theta_E = 30°$, and $F_{tap} = -11$ dB ($\eta = 83\%$).

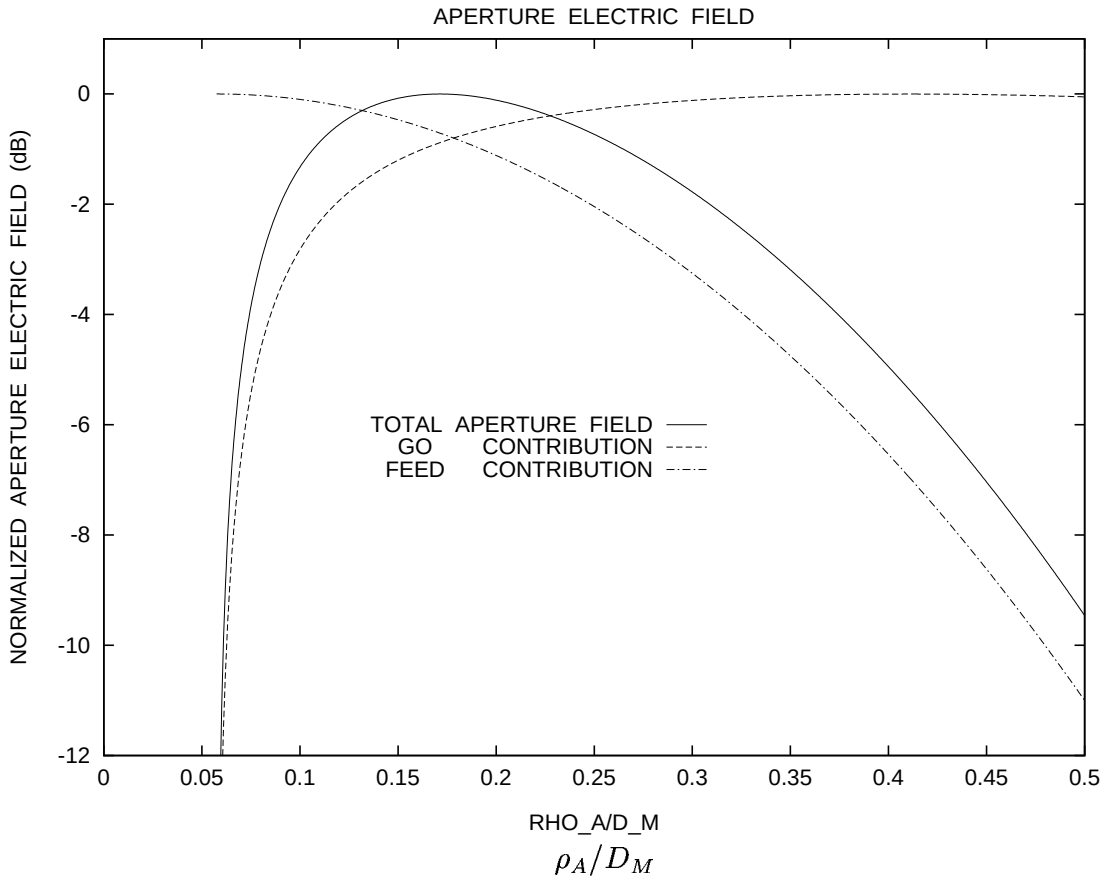

Figure 4.9: Characteristics of the Aperture Illumination for CG III, with Parameters $D_S = D_B = 0.115\, D_M$, $\ell_o = D_M$, $|\theta_E| = 30°$, and $F_{tap} = -11$ dB ($\eta = 84\%$).

contribution provides, outside the blocked region, an almost uniform illumination. However, the feed tapering precludes the total aperture illumination from being almost uniform. The ultimate consequence is that the maximum possible value of the antenna efficiencies for CG I and III (under a GO perspective) is $\eta \approx 83\%$.

4.6.2 Efficiencies of Classical Geometries II and IV

The parametric study of the efficiencies of CG II and IV (see Fig. 4.2 and 4.4, respectively) was conducted in the same manner as in Sect. 4.6.1. For CG II, the specific values of ℓ_o/D_M and θ_E used were exactly the same ones adopted for CG I. However, it was observed for CG IV that the conditions given by Eqs. 4.30 (to prevent the subreflector self blockage) and 4.33 (to prevent the feed blockage) were not satisfied for small values of ℓ_o/D_M and large values of $|\theta_E|$, respectively. Due to these facts, the results of CG IV were obtained for $1 \leq \ell_o/D_M \leq 2$ and $5^\circ \leq |\theta_E| \leq 20^\circ$, recalling that $\theta_E < 0$ for CG IV (accordingly to Table 4.1). Furthermore, it was found for both CG II and IV that the maximum efficiency ($\eta \approx 94\%$) was always obtained in the limit when $D_S \rightarrow 0$ and for large $|F_{tap}|$ values, which is obviously not practical. So, for both geometries, the efficiency results are presented for D_S/D_M values fixed at 0.1 and 0.2. Tables 4.4 and 4.5 show the results of CG II with $D_S/D_M = 0.1$ and 0.2, respectively, while Table 4.6 presents the results obtained for CG IV. In Table 4.6, the symbol † in the column associated with η depicts the CG IV configurations where Eq. 4.33 was not satisfied.

$\frac{\ell_o}{D_M}$	θ_E	$\frac{D_S}{D_M}$	F_{tap}	β	$\frac{F}{D_p}$	$\frac{V_S}{D_M}$	$\frac{V'_M}{D_M}$	η_S	η_A	η
0.5	10°	0.100	−21 dB	11°	0.250	0.261	0.036	0.99	0.92	0.91
0.5	20°	0.100	−20 dB	23°	0.250	0.117	−0.108	0.99	0.93	0.92
0.5	30°	0.100	−18 dB	36°	0.250	0.068	−0.157	0.99	0.93	0.92
0.5	40°	0.100	−16 dB	49°	0.250	0.044	−0.181	0.98	0.94	0.92
0.5	50°	0.100	−14 dB	60°	0.250	0.029	−0.196	0.97	0.94	0.92
0.5	60°	0.100	−12 dB	70°	0.250	0.018	−0.207	0.97	0.94	0.91
1.0	10°	0.100	−21 dB	12°	0.500	0.273	−0.214	0.99	0.92	0.91
1.0	20°	0.100	−21 dB	28°	0.500	0.129	−0.358	0.99	0.92	0.91
1.0	30°	0.100	−20 dB	49°	0.500	0.081	−0.407	0.99	0.92	0.92
1.0	40°	0.100	−19 dB	69°	0.500	0.056	−0.431	0.99	0.93	0.92
1.0	50°	0.100	−17 dB	86°	0.500	0.041	−0.446	0.99	0.93	0.92
1.0	60°	0.100	−16 dB	97°	0.500	0.031	−0.457	0.99	0.93	0.92
1.5	10°	0.100	−22 dB	13°	0.750	0.277	−0.464	0.99	0.92	0.91
1.5	20°	0.100	−21 dB	37°	0.750	0.133	−0.608	0.99	0.92	0.91
1.5	30°	0.100	−20 dB	70°	0.750	0.085	−0.657	0.99	0.92	0.91
1.5	40°	0.100	−19 dB	97°	0.750	0.060	−0.681	0.99	0.92	0.92
1.5	50°	0.100	−18 dB	113°	0.750	0.045	−0.696	0.99	0.93	0.92
1.5	60°	0.100	−16 dB	122°	0.750	0.035	−0.707	0.99	0.93	0.92
2.0	10°	0.100	−22 dB	15°	1.000	0.280	−0.714	0.99	0.92	0.91
2.0	20°	0.100	−21 dB	50°	1.000	0.136	−0.858	0.99	0.92	0.91
2.0	30°	0.100	−21 dB	97°	1.000	0.087	−0.907	0.99	0.92	0.91
2.0	40°	0.100	−20 dB	122°	1.000	0.062	−0.931	0.99	0.92	0.91
2.0	50°	0.100	−18 dB	133°	1.000	0.047	−0.946	0.99	0.92	0.92
2.0	60°	0.100	−18 dB	138°	1.000	0.037	−0.957	0.99	0.92	0.92

Table 4.4: Maximum-Efficiency Configurations of CG II for Prescribed Values of ℓ_o/D_M and θ_E, with $D_B = D_S$ and $D_S/D_M = 0.1$.

$\frac{\ell_o}{D_M}$	θ_E	$\frac{D_S}{D_M}$	F_{tap}	β	$\frac{F}{D_p}$	$\frac{V_S}{D_M}$	$\frac{V'_M}{D_M}$	η_S	η_A	η
0.5	10°	0.200	−19 dB	11°	0.250	0.522	0.322	0.99	0.89	0.88
0.5	20°	0.200	−18 dB	23°	0.250	0.234	0.034	0.99	0.90	0.88
0.5	30°	0.200	−17 dB	36°	0.250	0.137	−0.063	0.98	0.90	0.88
0.5	40°	0.200	−15 dB	49°	0.250	0.087	−0.113	0.98	0.91	0.88
0.5	50°	0.200	−13 dB	60°	0.250	0.057	−0.143	0.97	0.91	0.88
0.5	60°	0.200	−11 dB	70°	0.250	0.037	−0.163	0.96	0.90	0.87
1.0	10°	0.200	−20 dB	12°	0.500	0.547	0.072	0.99	0.89	0.88
1.0	20°	0.200	−19 dB	28°	0.500	0.259	−0.216	0.99	0.89	0.88
1.0	30°	0.200	−18 dB	49°	0.500	0.162	−0.313	0.99	0.90	0.88
1.0	40°	0.200	−17 dB	69°	0.500	0.112	−0.363	0.98	0.90	0.88
1.0	50°	0.200	−16 dB	86°	0.500	0.082	−0.393	0.98	0.90	0.89
1.0	60°	0.200	−13 dB	97°	0.500	0.062	−0.413	0.98	0.90	0.89
1.5	10°	0.200	−20 dB	13°	0.750	0.555	−0.178	0.99	0.89	0.88
1.5	20°	0.200	−19 dB	37°	0.750	0.267	−0.466	0.99	0.89	0.88
1.5	30°	0.200	−18 dB	70°	0.750	0.170	−0.563	0.99	0.89	0.88
1.5	40°	0.200	−18 dB	97°	0.750	0.121	−0.613	0.99	0.89	0.88
1.5	50°	0.200	−17 dB	113°	0.750	0.091	−0.643	0.99	0.90	0.88
1.5	60°	0.200	−15 dB	122°	0.750	0.070	−0.663	0.98	0.90	0.89
2.0	10°	0.200	−20 dB	15°	1.000	0.559	−0.428	0.99	0.89	0.88
2.0	20°	0.200	−19 dB	50°	1.000	0.271	−0.716	0.99	0.89	0.88
2.0	30°	0.200	−18 dB	97°	1.000	0.174	−0.813	0.99	0.89	0.88
2.0	40°	0.200	−18 dB	122°	1.000	0.125	−0.863	0.99	0.89	0.88
2.0	50°	0.200	−17 dB	133°	1.000	0.095	−0.893	0.99	0.89	0.88
2.0	60°	0.200	−16 dB	138°	1.000	0.074	−0.913	0.99	0.90	0.88

Table 4.5: Maximum-Efficiency Configurations of CG II for Prescribed Values of ℓ_o/D_M and θ_E, with $D_B = D_S$ and $D_S/D_M = 0.2$.

$\frac{\ell_o}{D_M}$	$\lvert\theta_E\rvert$	$\frac{D_S}{D_M}$	F_{tap}	β	$\frac{F}{D_p}$	$\frac{V_S}{D_M}$	$\frac{V'_M}{D_M}$	η_S	η_A	η
1.0	5°	0.100	−22 dB	−5°	0.500	0.588	0.078	0.99	0.91	0.91
1.0	10°	0.100	−23 dB	−10°	0.500	0.301	−0.209	1.00	0.91	0.91
1.0	15°	0.100	−22 dB	−13°	0.500	0.205	−0.305	1.00	0.91	$0.91_\dagger$
1.0	20°	0.100	−23 dB	−17°	0.500	0.157	−0.353	1.00	0.91	$0.90_\dagger$
1.5	5°	0.100	−22 dB	−5°	0.750	0.583	−0.174	0.99	0.91	0.91
1.5	10°	0.100	−22 dB	−9°	0.750	0.296	−0.461	0.99	0.91	$0.91_\dagger$
1.5	15°	0.100	−22 dB	−12°	0.750	0.200	−0.557	1.00	0.91	$0.91_\dagger$
1.5	20°	0.100	−23 dB	−14°	0.750	0.152	−0.605	1.00	0.91	$0.91_\dagger$
2.0	5°	0.100	−22 dB	−4°	1.000	0.580	−0.425	0.99	0.91	0.91
2.0	10°	0.100	−22 dB	−8°	1.000	0.293	−0.712	0.99	0.91	$0.91_\dagger$
2.0	15°	0.100	−22 dB	−11°	1.000	0.197	−0.808	0.99	0.91	$0.91_\dagger$
2.0	20°	0.100	−22 dB	−13°	1.000	0.149	−0.856	0.99	0.91	$0.91_\dagger$
1.0	5°	0.200	−20 dB	−7°	0.500	1.180	0.665	0.99	0.89	0.88
1.0	10°	0.200	−21 dB	−12°	0.500	0.607	0.092	0.99	0.88	0.88
1.0	15°	0.200	−21 dB	−17°	0.500	0.416	−0.100	0.99	0.88	0.88
1.0	20°	0.200	−21 dB	−20°	0.500	0.320	−0.196	0.99	0.88	0.87
1.5	5°	0.200	−20 dB	−6°	0.750	1.169	0.409	0.99	0.89	0.88
1.5	10°	0.200	−20 dB	−11°	0.750	0.595	−0.165	0.99	0.89	0.88
1.5	15°	0.200	−19 dB	−14°	0.750	0.403	−0.357	0.99	0.88	0.88
1.5	20°	0.200	−20 dB	−17°	0.750	0.307	−0.453	0.99	0.88	$0.88_\dagger$
2.0	5°	0.200	−20 dB	−6°	1.000	1.163	0.155	0.99	0.89	0.88
2.0	10°	0.200	−20 dB	−10°	1.000	0.589	−0.418	0.99	0.89	0.88
2.0	15°	0.200	−19 dB	−13°	1.000	0.397	−0.610	0.99	0.89	$0.88_\dagger$
2.0	20°	0.200	−20 dB	−15°	1.000	0.301	−0.706	0.99	0.88	$0.88_\dagger$

Table 4.6: Maximum-Efficiency Configurations of CG IV for Prescribed Values of ℓ_o/D_M and θ_E, with $D_B = D_S$ and $D_S/D_M = 0.1$ and 0.2.

In Tables 4.4–4.6, the results are presented for the same parameters illustrated in Tables 4.2 and 4.3 of Sect. 4.6.1, with the exception that here the distance between the feed and the main-reflector lower point L is now proportional to the parameter V'_M/D_M (for CG II and IV, V'_M is the z-coordinate of the main-reflector point L). From Figs. 4.2 and 4.4, V'_M is directly given by

$$V'_M = V_S + \frac{D_B}{2\tan\theta_L}, \tag{4.75}$$

and a positive value of V'_M corresponds to a feed point source located behind the main reflector. For both CG II and IV, the results show that the maximum η values are about 92% and 88% for $D_S/D_M = 0.1$ and 0.2, respectively, indicating that η is not strongly dependent on the subreflector diameter. However, for CG II, F_{tap} is considerably dependent on θ_E, decreasing in magnitude (i.e., less taper) as θ_E increases. For both CG II and IV and for small values of $|\theta_E|$, $|F_{tap}|$ achieves very large values, indicating that a high-gain feed (larger feed aperture) must be employed in this situation. As the subreflector inverts the feed illumination (i.e., the feed-boresight radiation is reflected towards the main-reflector outer rim as illustrated in Figs. 4.2 and 4.4), the equivalent-paraboloid concept can not be applied to CG II and IV, even for small values of D_S.

It can also be observed from Tables 4.4–4.6 that the main-reflector curvature (proportional to D_p/F) decreases as ℓ_o/D_M increases, as expected. The distance $|V'_M|$ increases with $|\theta_E|$, while V'_M remains negative for practically all cases. Con-

sequently, V_S decreases as $|\theta_E|$ increases, which arouses some concerns about the distance between the feed aperture and the subreflector surface for large values of $|\theta_E|$. In Figs. 4.10 and 4.11 some representative configurations of CG II and IV, respectively, are illustrated. Comparing Figs. 4.6, 4.7, 4.10, and 4.11, it is observed that among the generalized classical geometries the feed blockage is of less concern in CG II and a great problem in CG IV. Actually, CG II allows the feed structure to be closer to the subreflector, in which case the subreflector may be supported by a radome directly attached to the feed, avoiding the supporting struts and the associated blockage effects. In Figs. 4.12 and 4.13 the aperture-illumination characteristics for the configurations of Figs. 4.10d (with $F_{tap} = -20$ dB) and 4.11a (with $F_{tap} = -22$ dB), respectively, are illustrated, where the several plots are independently normalized. These figures show that, as the feed boresight radiation is reflected towards the aperture outer rim in CG II and IV, the feed contribution to the aperture illumination is inverted (being maximum at $\rho_A = D_M/2$). The combination of the GO and feed contributions then provides a more uniform aperture illumination (when compared with the results of Figs. 4.8 and 4.9 for CG I and III, respectively), enabling the achievement of an antenna efficiency η higher than 90%.

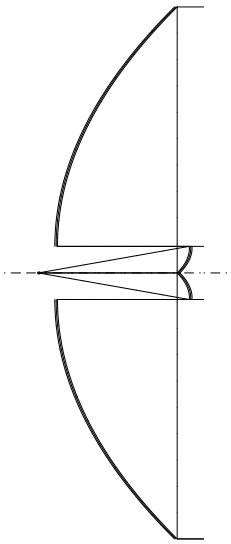

a) $\frac{\ell_o}{D_M} = 0.5$ and $\theta_E = 10°$

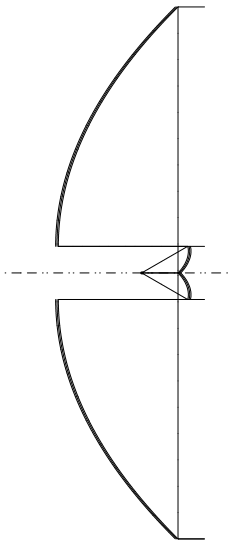

b) $\frac{\ell_o}{D_M} = 0.5$ and $\theta_E = 30°$

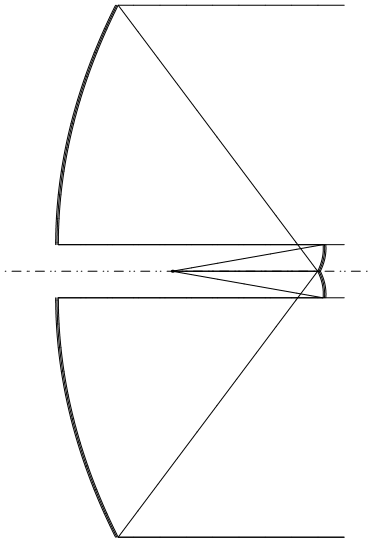

c) $\frac{\ell_o}{D_M} = 1$ and $\theta_E = 10°$

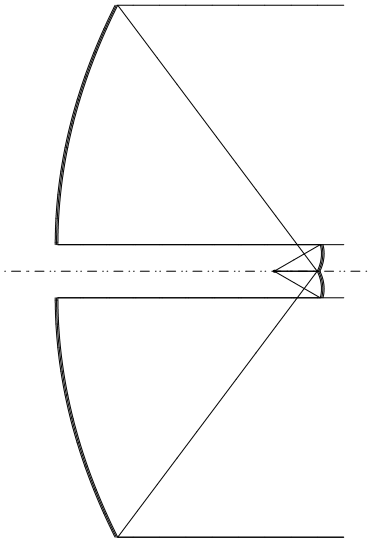

d) $\frac{\ell_o}{D_M} = 1$ and $\theta_E = 30°$

Figure 4.10: Representative Configurations of CG II ($D_S = D_B = 0.1\, D_M$).

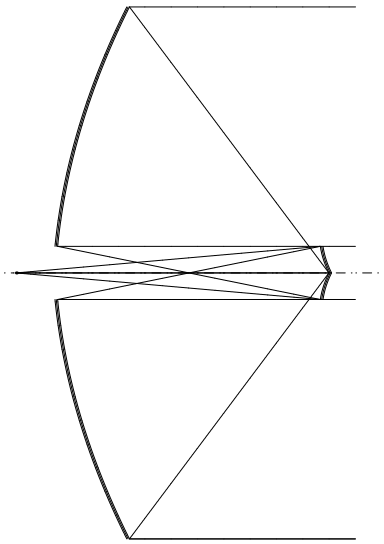

a) $\frac{\ell_o}{D_M} = 1$, $|\theta_E| = 5°$, $D_S = 0.1\, D_M$

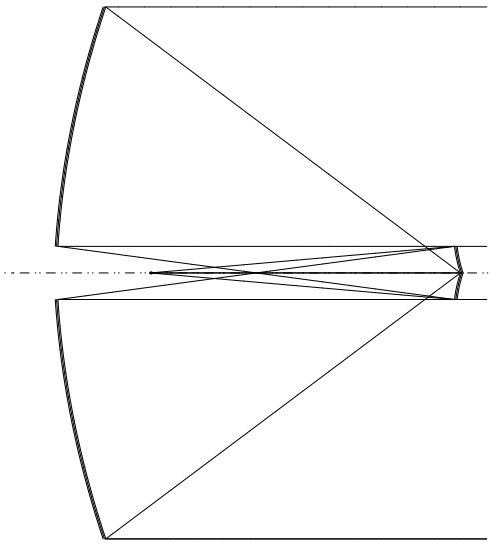

b) $\frac{\ell_o}{D_M} = 1.5$, $|\theta_E| = 5°$, $D_S = 0.1\, D_M$

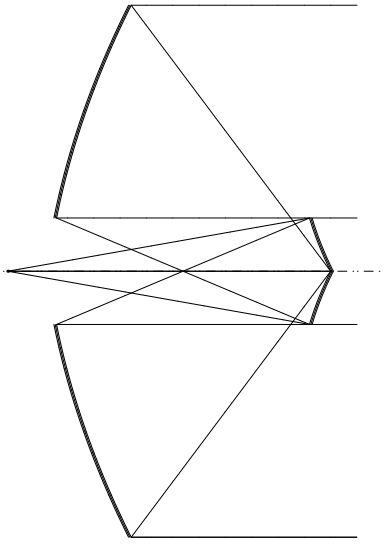

c) $\frac{\ell_o}{D_M} = 1$, $|\theta_E| = 10°$, $D_S = 0.2\, D_M$

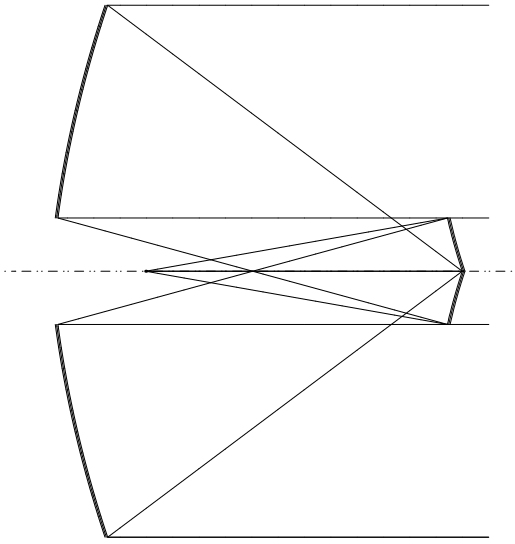

d) $\frac{\ell_o}{D_M} = 1.5$, $|\theta_E| = 10°$, $D_S = 0.2\, D_M$

Figure 4.11: Representative Configurations of CG IV ($D_S = D_B$).

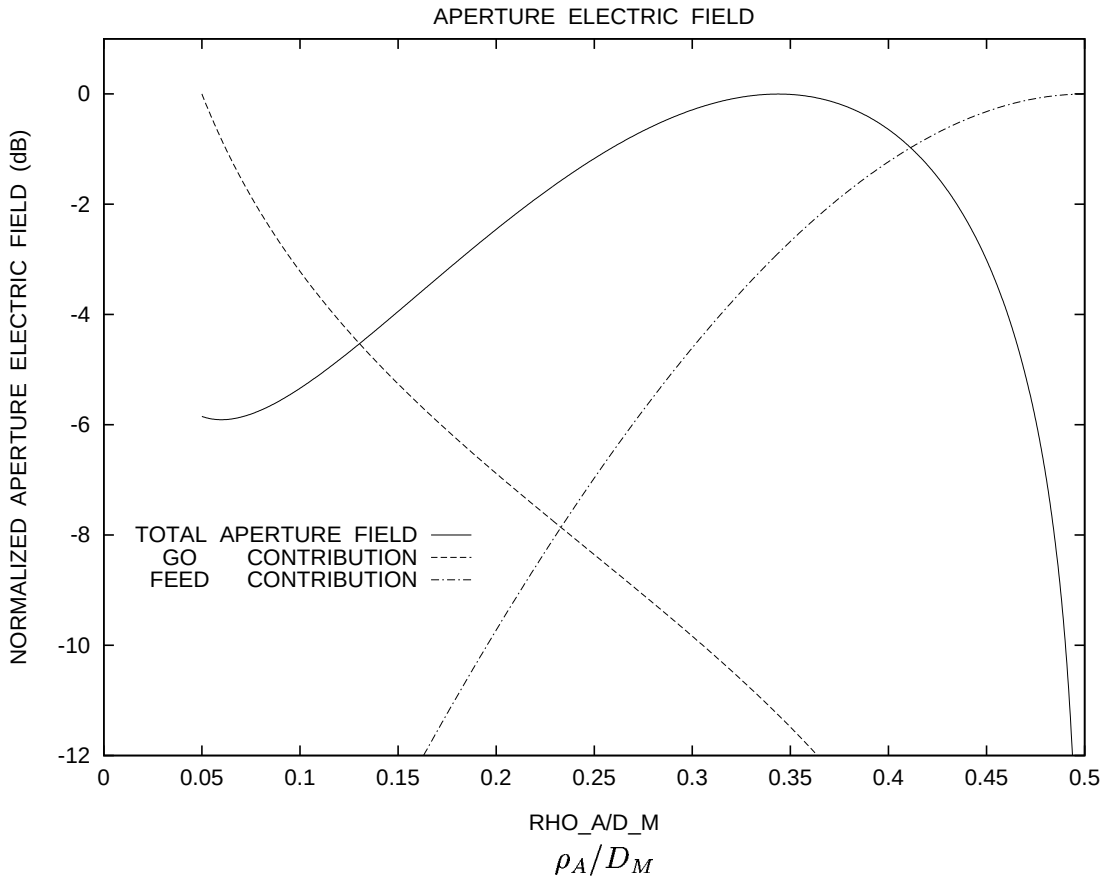

Figure 4.12: Characteristics of the Aperture Illumination for CG II, with Parameters $D_S = D_B = 0.1\,D_M$, $\ell_o = D_M$, $\theta_E = 30°$, and $F_{tap} = -20$ dB ($\eta = 92\%$).

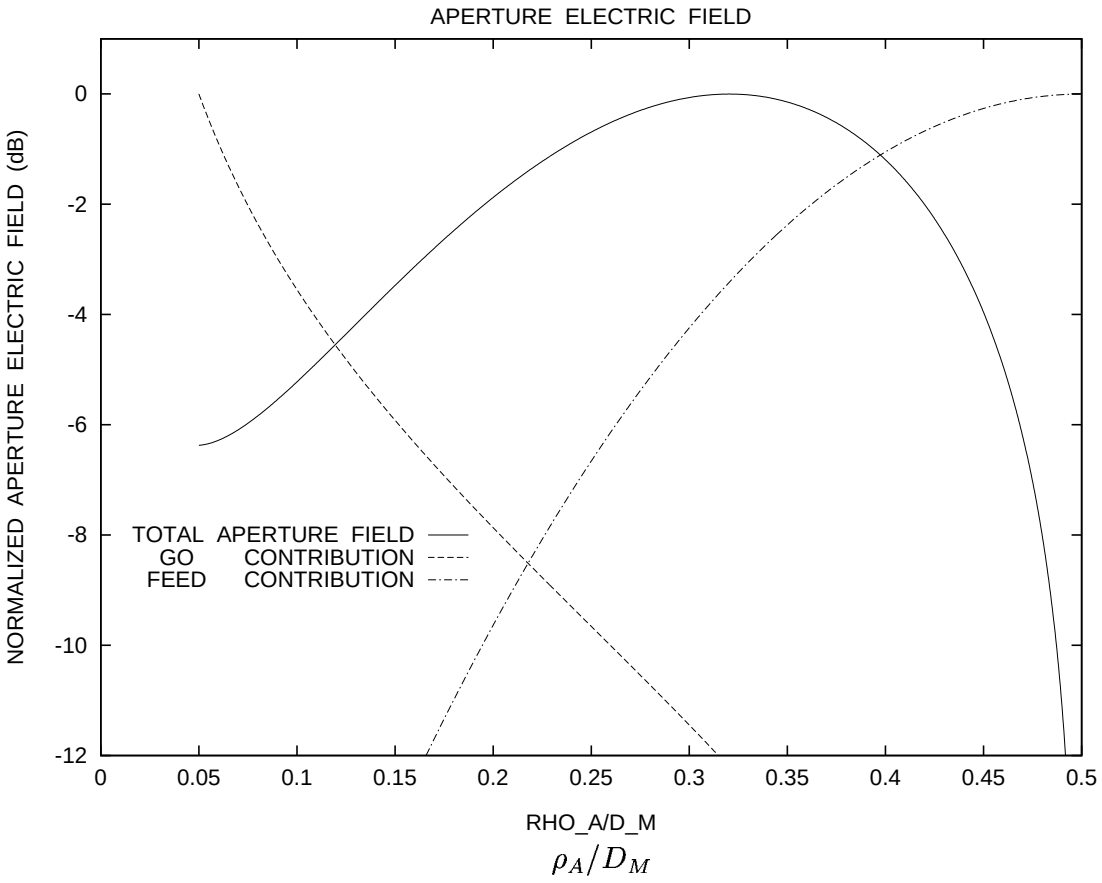

Figure 4.13: Characteristics of the Aperture Illumination for CG IV, with Parameters $D_S = D_B = 0.1\,D_M$, $\ell_o = D_M$, $|\theta_E| = 5°$, and $F_{tap} = -22$ dB ($\eta = 91\%$).

Chapter 5

DESIGN OF GENERALIZED AXIALLY-SYMMETRIC DUAL-REFLECTOR ANTENNAS WITH HIGH GAIN AND A PRESCRIBED SIDELOBE ENVELOPE

Chapter 4 introduced generalized classical axially-symmetric dual-reflector antennas that prevent (under a GO perspective) the main-reflector radiation to strike the subreflector. The configurations have improved aperture efficiencies. However, in practical antenna designs it is also desired to obtain radiation patterns with low sidelobe levels to minimize the interference on other communication systems and/or to reduce the antenna noise temperature. It will be shown in this chapter that (besides the spillover and diffraction effects) the major contribution to the antenna sidelobe levels comes from the field distribution at the blocked aperture rims ($\rho_A = D_B/2$ and $D_M/2$), which must be highly tapered to accomplish the desired sidelobe pattern. However, from the results of Chapter 4 it was observed that the classical geometries can provide a reduced illumination (while maintaining a high efficiency) only at one of the aperture rims (region illuminated by the feed

boresight). An alternative solution to this difficulty is to obtain the desired aperture illumination through a shaped-reflector configuration [27], in which case the classical geometries presented in Chapter 4 can be successfully applied to establish the initial design parameters.

In Sect. 5.1, a closed-form asymptotic expression for the wide-angle sidelobe envelope is derived to provide the necessary insights to determine the desired aperture illumination. This expression indicates that the aperture-radiation sidelobe levels can be entirely controlled from the field distribution at the aperture rims. Then, Sect. 5.2 proposes an aperture field distribution that yields a high efficiency while controlling the aperture-rim illumination. The proposed distribution can be accomplished through reflector shaping (using GO principles), which is explained in Sect. 5.3. However, the spillover and diffraction mechanisms (not considered by the GO approximations) also contribute to the antenna radiation pattern and, consequently, their effects must be taken into account. So, in Sect. 5.4 the feed and subreflector spillovers are analyzed by an asymptotic theory, which provides some useful insights for controlling their impacts on the antenna radiation pattern. Then, in Sect. 5.5 the effects of the subreflector-edge diffraction on the aperture illumination are investigated. Finally, as a case study, Sect. 5.6 presents the synthesis and analysis of a shaped axially-symmetric Cassegrain antenna, where the complete formulation derived throughout this work is applied.

5.1 Control of the Sidelobes Radiated by a Blocked Circular Aperture

For both the classical and shaped axially-symmetric dual-reflector configurations discussed in this work, the uniform-phase aperture illumination is present at the annular region with $D_B/2 \leq \rho_A \leq D_M/2$, where D_B and D_M are the blockage and aperture diameters, respectively. Furthermore, it was shown at the end of Sect. 4.4 that for a classical geometry excited by a circularly-symmetric RCF model (which can be applied to characterize most of the feeds used in practical antenna applications) the aperture illumination varies only with ρ_A. Under a GO perspective, this ρ_A dependence remains valid for any axially-symmetric configuration (classical or shaped), in which case the aperture electric field can be represented as

$$\vec{E}_A^{GO}(\rho_A) \;=\; E_o\, f(\rho_A)\, \hat{e}_A \;, \tag{5.1}$$

where E_o is an arbitrary complex amplitude, $f(\rho_A)$ defines the aperture-illumination distribution, and $\hat{e}_A$ describes the linear polarization of the aperture electric field. As an example, for the classical geometries illuminated by the $\hat{x}$-polarized RCF model given by Eq. 4.59, Eq. 5.1 describes the aperture electric field given by Eq. 4.60 (with $\hat{e}_A = \hat{x}$). If the feed radiation is not linearly polarized, then Eq. 5.1 may represent each component describing the actual aperture electric field.

Without losing generality, it is assumed that $\hat{e}_A = \hat{x}$ and the far-zone radiation provided by the aperture illumination of Eq. 5.1 is evaluated from Eq. 4.62, which

can be integrated in closed form to obtain the wide-angle radiation characteristics. This is done by assuming the aperture dimensions D_B and D_M much larger than the operation wavelength and applying the asymptotic formula for the Bessel function given by Eq. 9.2.1 of Ref. [51]:

$$\lim_{x\to\infty} J_0(x) \;=\; \sqrt{\frac{2}{\pi\, x}}\,\cos(x\,-\,\pi/4)\;. \tag{5.2}$$

Substituting Eqs. 5.1 (with $\hat{e}_A = \hat{x}$) and 5.2 into Eq. 4.62 one obtains for $\theta \neq 0$ that

$$\begin{aligned}\vec{E}_{FF}(\vec{r}) \;&\approx\; \frac{jk_o}{\sqrt{2\pi}}\,\frac{e^{-jk_o r}}{r}\,E_o\,(1+\cos\theta)\,(\cos\phi\,\hat{\theta}\,-\,\sin\phi\,\hat{\phi}) \\ &\times\; \int_{D_B/2}^{D_M/2} f(\rho_A)\;\frac{\cos(k_o\,\rho_A\,\sin\theta\,-\,\pi/4)}{\sqrt{k_o\,\rho_A\,\sin\theta}}\;\rho_A\;\,d\rho_A\;.\end{aligned} \tag{5.3}$$

The above integral can be successively integrated by parts, yielding

$$\int f(\rho_A)\;\frac{\cos(k_o\,\rho_A\,\sin\theta\,-\,\pi/4)}{\sqrt{k_o\,\rho_A\,\sin\theta}}\;\rho_A\;\,d\rho_A \;=\; F_{rim}(\rho_A) + O\left[(k_o\sin\theta)^{-\frac{7}{2}}\right]\;, \tag{5.4}$$

where

$$\begin{aligned}F_{rim}(\rho_A) \;&=\; \frac{\rho_A^2}{(k_o\,\rho_A\,\sin\theta)^{\frac{3}{2}}}\left\{f(\rho_A)\;\sin(k_o\,\rho_A\,\sin\theta\,-\,\pi/4)\right. \\ &+\;\left.\left[\frac{f(\rho_A)}{2}\;+\;\frac{d\,f(\rho_A)}{d\rho_A}\,\rho_A\right]\frac{\cos(k_o\,\rho_A\,\sin\theta\,-\,\pi/4)}{k_o\,\rho_A\,\sin\theta}\right\}.\end{aligned} \tag{5.5}$$

Substituting Eq. 5.4 into Eq. 5.3 one obtains

$$\begin{aligned}\vec{E}_{FF}(\vec{r}) \;&\approx\; \frac{jk_o}{\sqrt{2\pi}}\,\frac{e^{-jk_o r}}{r}\,E_o\,(1+\cos\theta)\,(\cos\phi\,\hat{\theta}\,-\,\sin\phi\,\hat{\phi}) \\ &\times\; \left[F_{rim}(\rho_A = D_M/2)\;-\;F_{rim}(\rho_A = D_B/2)\right],\end{aligned} \tag{5.6}$$

from which (and Eq. 5.5) the expression for the sidelobe envelope is obtained as

$$E_{FF}^{env}(\vec{r}) \approx \pm \frac{k_o\,(1+\cos\theta)}{2\sqrt{\pi}\,r}\,|E_o|\left[\frac{D_B^2}{(k_o\,D_B\,\sin\theta)^{\frac{3}{2}}}\sqrt{f_B^2+\left(\frac{f_B+D_B\,f_B'}{k_o\,D_B\,\sin\theta}\right)^2}\right.$$
$$\left. + \frac{D_M^2}{(k_o\,D_M\,\sin\theta)^{\frac{3}{2}}}\sqrt{f_M^2+\left(\frac{f_M+D_M\,f_M'}{k_o\,D_M\,\sin\theta}\right)^2}\right], \tag{5.7}$$

where

$$f_B = f(\rho_A = D_B/2)\,, \tag{5.8}$$

$$f_M = f(\rho_A = D_M/2)\,, \tag{5.9}$$

$$f_B' = \frac{d}{d\rho_A}f(\rho_A = D_B/2)\,, \tag{5.10}$$

$$f_M' = \frac{d}{d\rho_A}f(\rho_A = D_M/2)\,. \tag{5.11}$$

Note that Eq. 5.7 does not depend on the polarization-direction $\hat{e}_A$ and was derived assuming both $f(\rho_A)$ and its first derivative continuous at $D_B/2 \leq \rho_A \leq D_M/2$. Also, Eqs. 5.6 and 5.7 show that the sidelobe levels of the aperture radiation can be entirely controlled by D_B, D_M, f_B, f_M, f_B', and f_M'. As previously mentioned in Sect. 4.5, the radiation characteristics obtained from the aperture illumination does not take into account neither diffraction effects associated with multiple bounces nor spillover.

5.2 Proposed Aperture Illumination for High Efficiency and Low Sidelobe Levels

Aperture distributions capable of successfully reducing the wide-angle sidelobe levels in blocked circular apertures have been proposed by Ludwig in terms of a generalization of Taylor's aperture synthesis [32]. However, these distributions do not provide an almost-uniform aperture illumination and, consequently, it was observed that $\eta_A < 80\%$ [32]. In order to provide an almost-uniform illumination over the aperture (required to obtain a high aperture efficiency η_A) while controlling the illumination characteristics at the aperture rims (to obtain low sidelobe levels), the following representation for $f(\rho_A)$ of Eq. 5.1 is proposed here (see Fig. 5.1):

$$f(\rho_A) = \begin{cases} 0\ , & 0 \le \rho_A < D_B/2\ , \\ \exp[-\alpha_B\,(\rho_A - \rho_{int})^2]\ , & D_B/2 \le \rho_A \le \rho_{int}\ , \\ 1\ , & \rho_{int} \le \rho_A \le \rho_{ext}\ , \\ \exp[-\alpha_M\,(\rho_A - \rho_{ext})^2]\ , & \rho_{ext} \le \rho_A \le D_M/2\ , \\ 0\ , & \rho_A > D_M/2\ , \end{cases} \tag{5.12}$$

where the parameters α_B, ρ_{int} and α_M, ρ_{ext} control the illumination at $\rho_A = D_B/2$ and $D_M/2$, respectively. For the distribution of Eq. 5.12, Eqs. 5.8–5.11 become

$$f_B = e^{-\alpha_B\,(D_B/2-\rho_{int})^2}\ , \tag{5.13}$$

$$f_M = e^{-\alpha_M\,(D_M/2-\rho_{ext})^2}\ , \tag{5.14}$$

$$f'_B = -2\,\alpha_B\,(D_B/2 - \rho_{int})\,f_B\ , \tag{5.15}$$

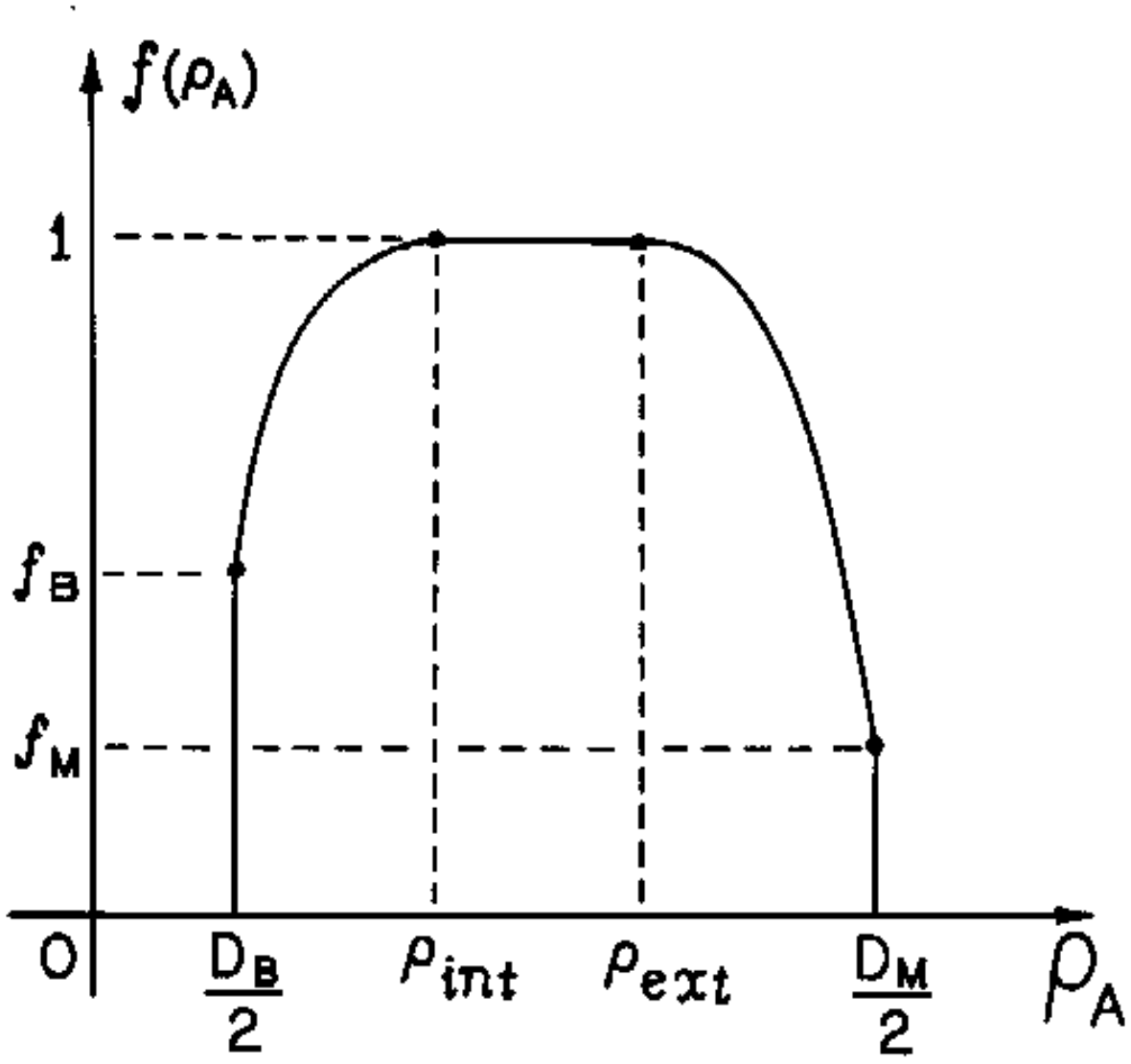

Figure 5.1: Proposed High-Efficiency Aperture-Illumination Distribution.

$$f'_M \;=\; -2\,\alpha_M\,(D_M/2-\rho_{ext})\,f_M\;, \tag{5.16}$$

respectively. Hence, once the values of f_B, f_M, f'_B, and f'_M are established from the desired sidelobe-envelope characteristics given by Eq. 5.7, then the required α_B, α_M, ρ_{int}, and ρ_{ext} can be obtained from Eqs. 5.13–5.16. Furthermore, note that the proposed distribution (illustrated in Fig. 5.1) assumes $\alpha_B > 0$, $\alpha_M > 0$, and $D_B/2 < \rho_{int} < \rho_{ext} < D_M/2$.

The aperture efficiency η_A associated with the above distribution can be evaluated in closed form from the results of Sect. 4.5. From Eqs. 4.64, 5.1, 5.12, and Eq. 7.1.1 of Ref. [51], the electric far-zone field in the antenna boresight direction is given by

$$\begin{aligned}\vec{E}_{FF}(\theta=0) \;&=\; \frac{jk_o}{2}\,\frac{e^{-jk_or}}{r}\,E_o\,\hat{e}_A\left\{\rho_{ext}^2-\rho_{int}^2+\frac{1-f_M}{\alpha_M}-\frac{1-f_B}{\alpha_B}\right.\\ &+\;\sqrt{\pi}\left[\frac{\rho_{ext}}{\sqrt{\alpha_M}}\;\mathrm{erf}[\sqrt{\alpha_M}(D_M/2-\rho_{ext})]\right.\\ &-\;\left.\left.\frac{\rho_{int}}{\sqrt{\alpha_B}}\;\mathrm{erf}[\sqrt{\alpha_B}(D_B/2-\rho_{int})]\right]\right\},\end{aligned} \tag{5.17}$$

and the power radiated by the aperture is given by

$$\begin{aligned}P_{ape} \;&=\; \frac{\pi}{\eta_o}\int_{D_B/2}^{D_M/2}\left|\vec{E}_A^{GO}(\rho_A)\right|^2\,\rho_A\,d\rho_A\\ &=\; \frac{\pi\,|E_o|^2}{2\,\eta_o}\left\{\rho_{ext}^2-\rho_{int}^2+\sqrt{\frac{\pi}{2}}\left[\frac{\rho_{ext}}{\sqrt{\alpha_M}}\;\mathrm{erf}[\sqrt{2\,\alpha_M}(D_M/2-\rho_{ext})]\right.\right.\\ &-\;\left.\left.\frac{\rho_{int}}{\sqrt{\alpha_B}}\;\mathrm{erf}[\sqrt{2\,\alpha_B}(D_B/2-\rho_{int})]\right]+\frac{1-f_M^2}{2\,\alpha_M}-\frac{1-f_B^2}{2\,\alpha_B}\right\},\end{aligned} \tag{5.18}$$

where $\mathrm{erf}(x)$ is the Error function [51]:

$$\mathrm{erf}(x) \;=\; \frac{2}{\sqrt{\pi}} \int_0^x e^{-t^2}\, dt\,. \tag{5.19}$$

Finally, substituting Eqs. 5.17 and 5.18 into Eq. 4.68 one obtains the aperture efficiency η_A.

To illustrate the application of the proposed aperture distribution, $f(\rho_A)$ of Eq. 5.12 will be now specified in order to provide a far-zone radiation satisfying the envelope requirements of the ITU Recommendations 465-5 and 580-5 for earth stations operating in satellite communications [41]. These recommendations require the gain (relative to an isotropic radiator) of at least 90% of the sidelobe peaks to not exceed the envelope given by

$$G_{ITU}(\theta) \;=\; \begin{cases} 29 \;-\; 25\log_{10}\theta \;\; \mathrm{dBi}\,, & \text{for } \theta_{min} < \theta < 20^\circ\,, \\ -3.526 \;\; \mathrm{dBi}\,, & \text{for } 20^\circ < \theta < 26.4^\circ\,, \\ 32 \;-\; 25\log_{10}\theta \;\; \mathrm{dBi}\,, & \text{for } 26.4^\circ < \theta < 47.9^\circ\,, \\ -10 \;\; \mathrm{dBi}\,, & \text{for } 47.9^\circ < \theta < 180^\circ\,, \end{cases} \tag{5.20}$$

where θ_{min} is 1° or $100\lambda/D_M$ whichever is the greater. The diameters $D_B = 20\lambda$ and $D_M = 100\lambda$ are chosen together with $f_B = 0.1$, $f_M = 0.1778$, $f'_B = 0.03/\lambda$, and $f'_M = -0.041/\lambda$ in order to obtain tapers of 20 dB ($20\log_{10} f_B = -20$) and 15 dB ($20\log_{10} f_M = -15$) for the aperture distribution at $\rho_A = 10\lambda$ and 50λ, respectively, and derivatives of 2.6 dB/λ and -3 dB/λ, respectively. In this case, the normalized aperture distribution given by Eqs. 5.12–5.16 is shown in Fig. 5.2a.

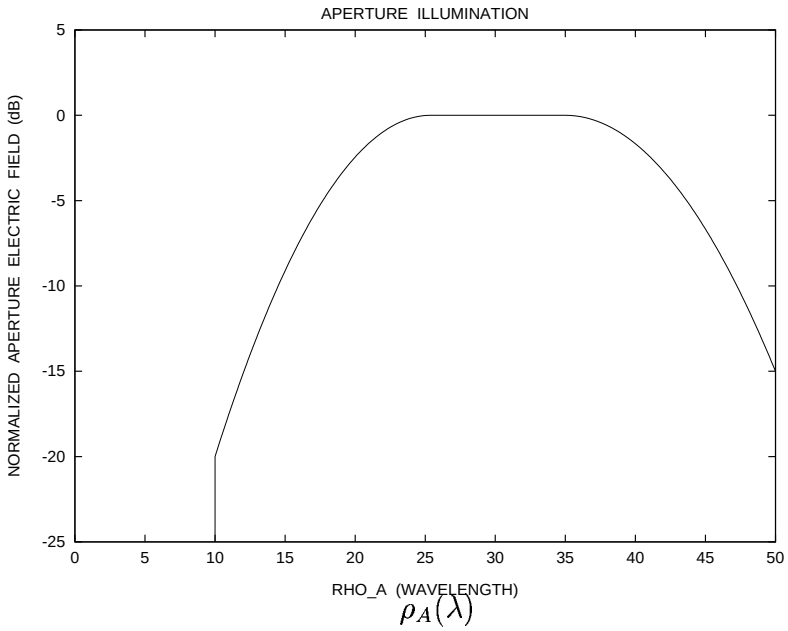

a) Normalized Aperture Illumination

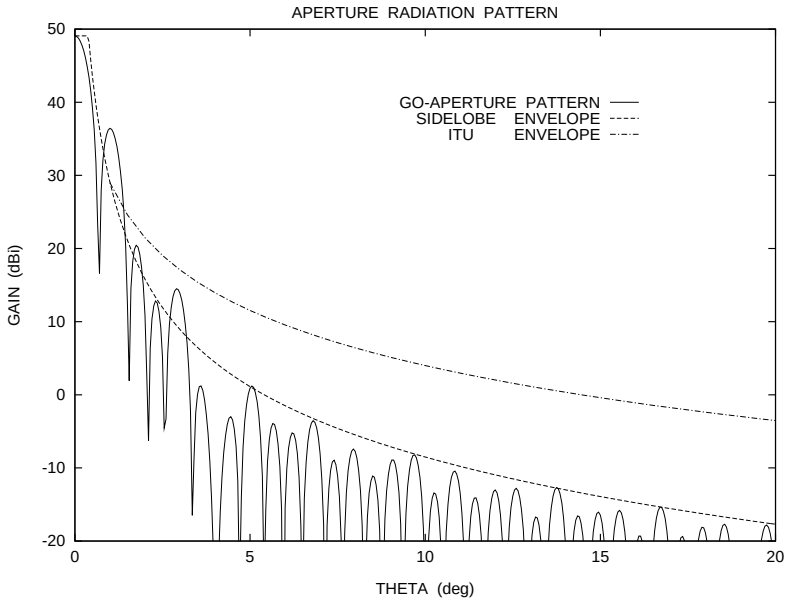

b) Aperture Radiation Pattern

Figure 5.2: Characteristics of the Aperture Illumination and Radiation.

In the present case, $\eta_A = 82\%$ from Eqs. 4.68, 5.17, and 5.18. Figure 5.2b shows the GO-aperture radiation pattern obtained from the numerical evaluation of Eq. 4.62, together with the sidelobe and the ITU envelopes given by Eqs. 5.7 and 5.20, respectively. Note from this figure that the sidelobe envelope agrees very with the radiation pattern only for $\theta > 5°$, due to the asymptotic approximation adopted (Eq. 5.2). However, even for $\theta < 5°$ Eq. 5.7 provides useful design information. The specified illumination is capable of placing all but the first sidelobe below the ITU envelope. To reduce the first sidelobe level a higher illumination taper should be set at $\rho_A = D_M/2$, which would dramatically decrease the aperture efficiency. The tradeoff to obtain a high efficiency in this case is then to allow the first sidelobe to violate the requirements.

It must be recalled that the radiation characteristics obtained from the GO aperture illumination do not take into account several spillover and diffraction mechanisms, which are specially relevant at directions away from the antenna boresight. At these directions, the spillover and diffraction effects must be added to the results of Sects. 5.1 and 5.2 for a practical design.

5.3 GO Shaping of Axially-Symmetric Dual-Reflector Antennas

The proposed aperture illumination given by Eqs. 5.1 and 5.12 can only be accomplished through a shaped-reflector antenna. The shaping of axially-symmetric dual-reflector antennas for a prescribed aperture illumination was considered by Galindo [27]. However, in the present work an elegant and more efficient formulation [40] will be adopted. In this procedure, Fermat's principle and the law of the optical path are applied to obtain the sub- and main-reflector surfaces, respectively, while the conservation of power is applied to establish the desired aperture illumination.

Four different shaped configurations can in principle (i.e., from a GO stand point) provide the same desired aperture illumination, apart from phase differences associated with the Gouy phase shift [49]. Their generating curves (assumed in the $y = 0$ plane) are illustrated in Figs. 5.3–5.6. Observe that these shaped geometries are similar to the classical ones presented in Chapter 4 (see Figs. 4.1–4.4). Their three-dimensional surfaces are obtained by spinning their generating curves about the z-axis (axis of symmetry). In Figs. 5.3–5.6 the feed is assumed a spherical-wave point source located at the coordinate-system origin and the aperture plane is located at $z = 0$. The point S of the subreflector generating curve is located by the spherical coordinates r_F and θ_F, where r_F is the distance from the feed to point S

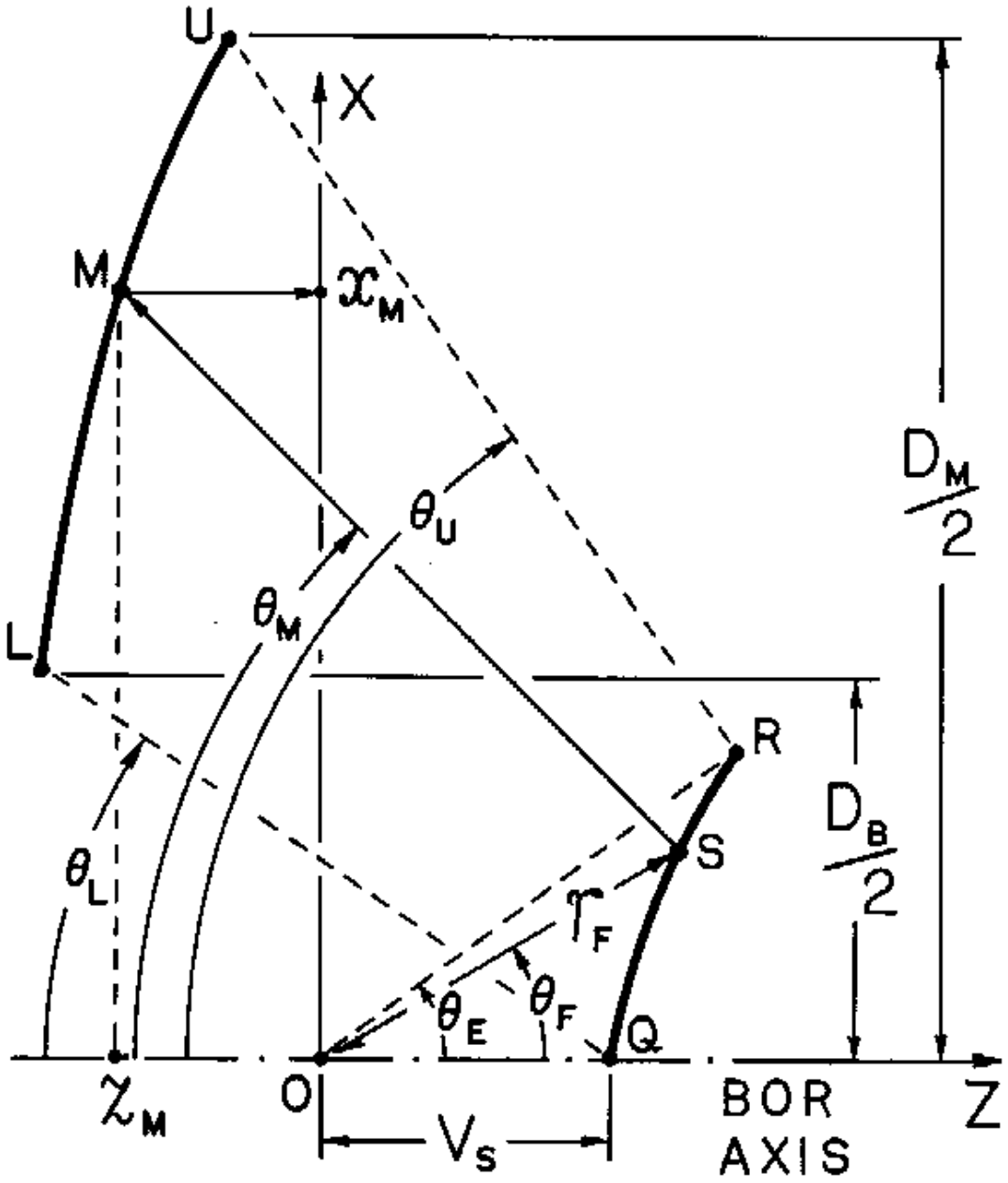

Figure 5.3: Basic Parameters of Shaped Geometry I.

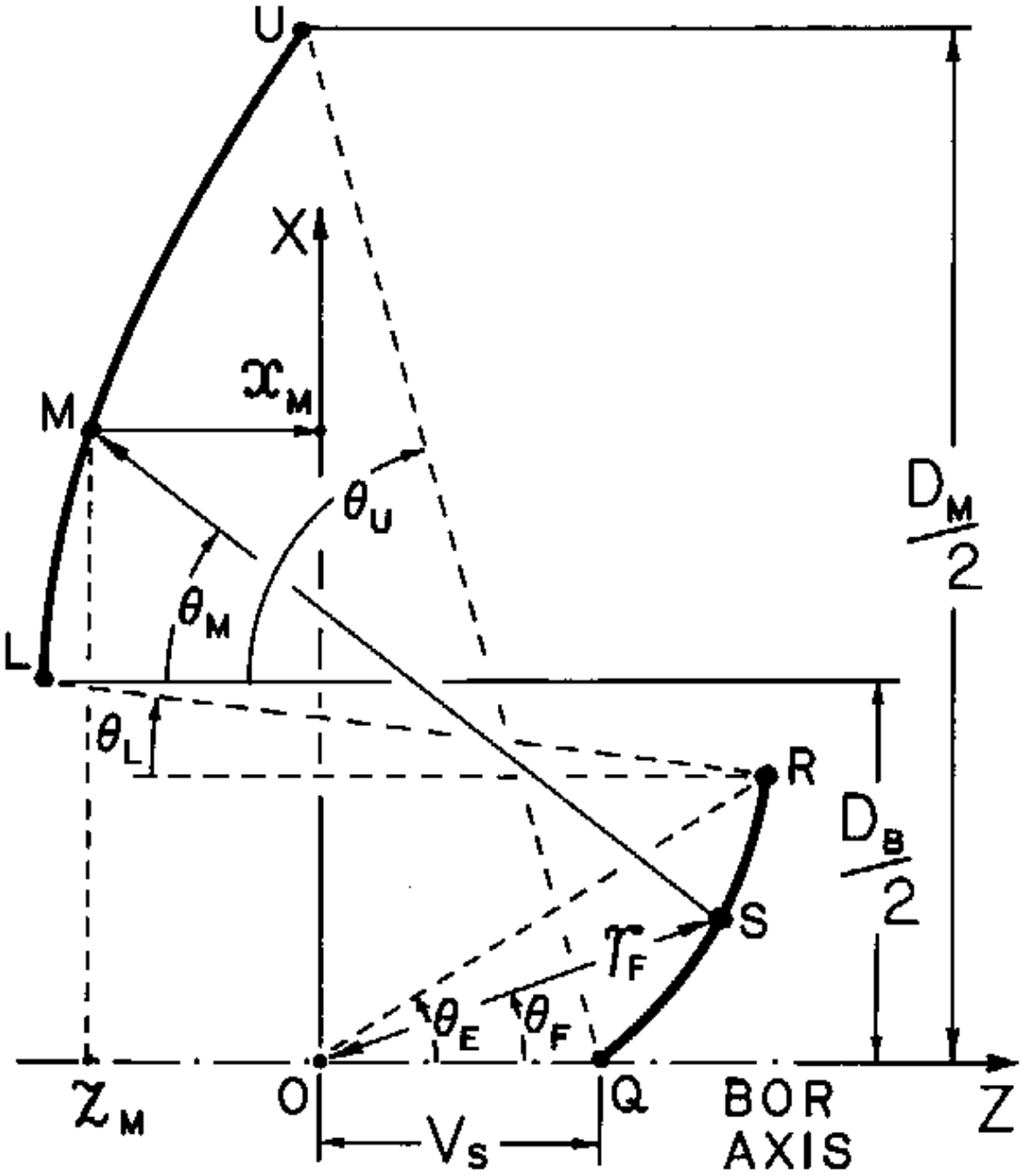

Figure 5.4: Basic Parameters of Shaped Geometry II.

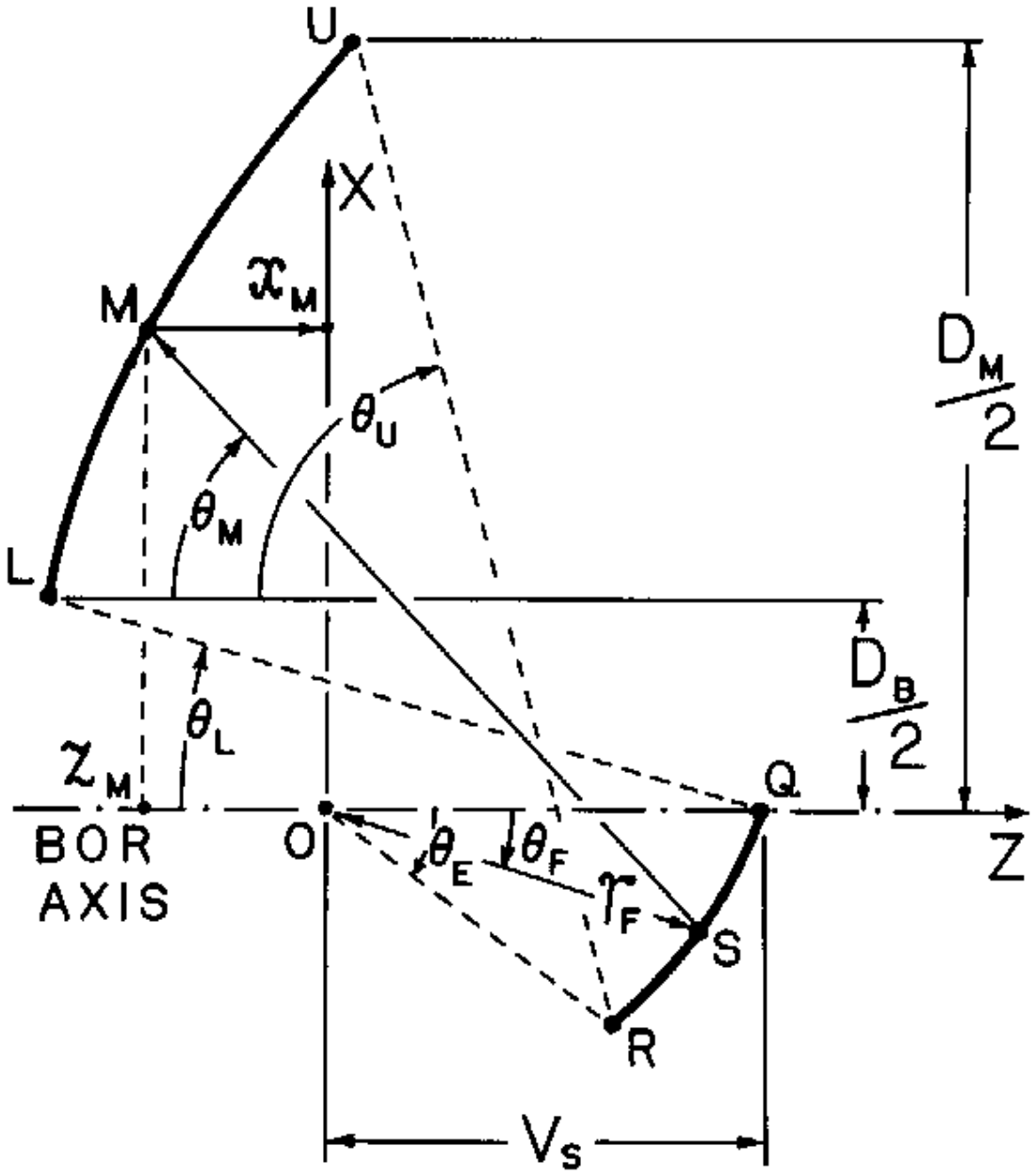

Figure 5.5: Basic Parameters of Shaped Geometry III.

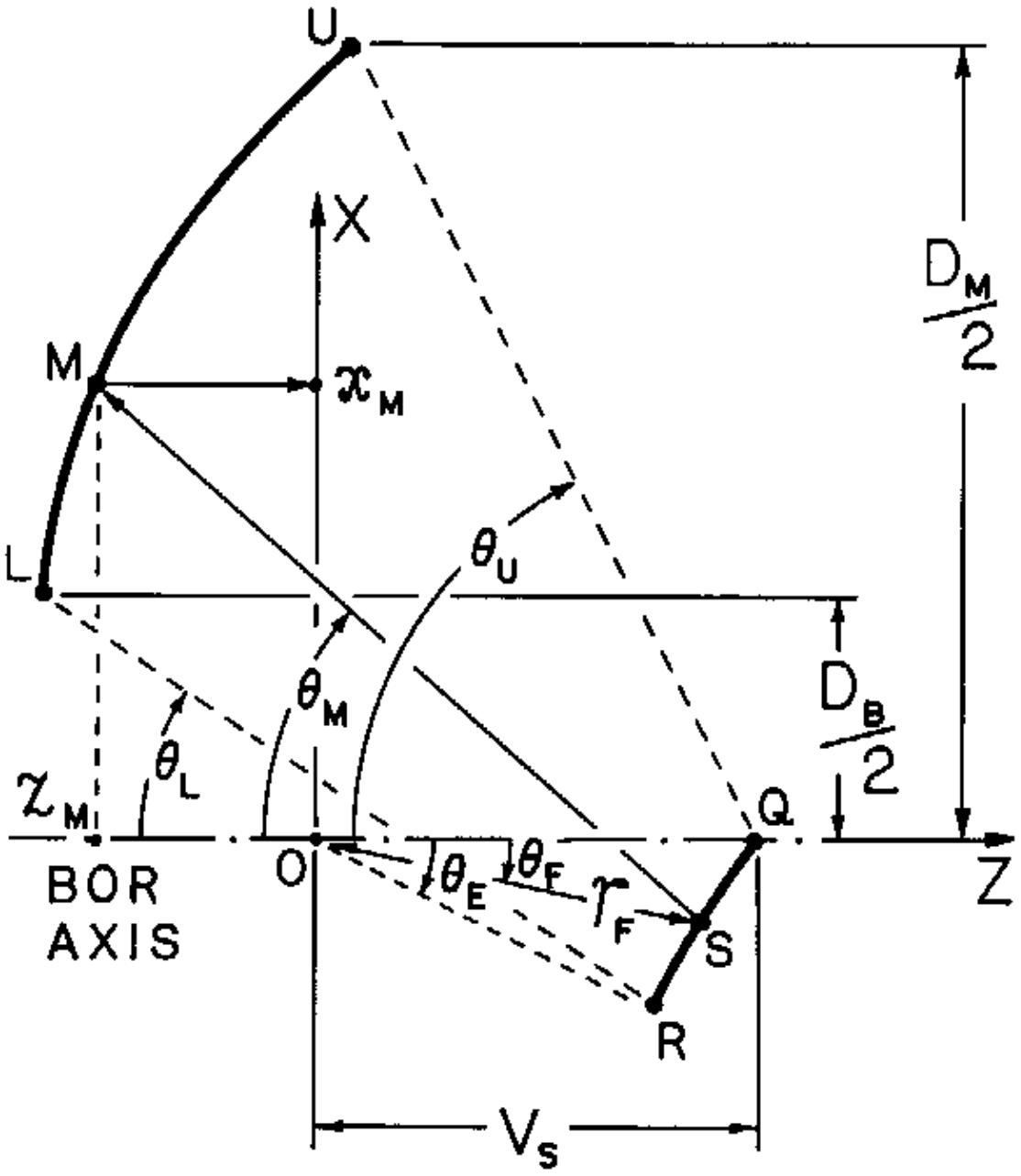

Figure 5.6: Basic Parameters of Shaped Geometry IV.

and the angle θ_F is positive (counterclockwise) or negative (clockwise) depending on its orientation with respect to the z-axis. The subreflector vertex is located at $z = V_S$ and its rim defined by the edge angle θ_E, such that $|\theta_F| \leq |\theta_E|$ and its sign convention follows the one adopted for θ_F (see Figs. 5.3–5.6). The point M of the main-reflector generating curve (associated with the feed-ray θ_F) is located by the Cartesian coordinates x_M and z_M, where $D_B/2 \leq x_M \leq D_M/2$ and D_B and D_M are blockage and aperture diameters, respectively. The negative angles θ_L, θ_M, and θ_U are associated with main-reflector points L, M, and U, respectively (see Figs. 5.3–5.6). Finally, the constant path length ℓ_o from the feed to the aperture plane enforces a uniform-phase aperture illumination.

The basic differences among the shaped geometries of Figs. 5.3–5.6 are similar to those explained in Sect. 4.1 for the generalized classical geometries, with the exception that now the caustic region associated with both sub- and main-reflectors is not necessarily a ring anymore. The other subreflector caustic region remains over the z-axis (line caustic) due to the axial symmetry. The Shaped Geometry I (SG I), illustrated in Fig. 5.3, is similar to CG I of Fig. 4.1, with a positive x_M associated with a positive θ_F and $\theta_F = \theta_E > 0$ being reflected to $x_M = D_M/2$. The subreflector line caustic is virtual. The other caustic region may be present behind the subreflector (virtual) or behind the main reflector (real, but the subreflector-reflected rays never intercept it). The Shaped Geometry II (SG II), represented by Fig. 5.4, is similar to CG II of Fig. 4.2, with a positive x_M associated with a positive

θ_F and $\theta_F = \theta_E > 0$ being reflected to $x_M = D_B/2$. In this case, the line caustic is virtual and the other caustic is present between both reflectors (real caustic). The Shaped Geometry III (SG III), illustrated in Fig. 5.5, is similar to CG III of Fig. 4.3, with a positive x_M associated with a negative θ_F and $\theta_F = \theta_E < 0$ being reflected to $x_M = D_M/2$. In this geometry, the line caustic is real and the other caustic behaves like in SG II. Finally, the Shaped Geometry IV (SG IV), shown in Fig. 5.6, is similar to the CG IV of Fig. 4.4, with a positive x_M associated with a negative θ_F and $\theta_F = \theta_E < 0$ being reflected to $x_M = D_B/2$. The line caustic is real and the other caustic behaves like in SG I.

The shaping equations to be derived next are applicable to all the above four different geometries, as long as the angular sign convention previously defined in this section is observed. Following Ref. [40], the subreflector equation is obtained using Fermat's principle. With the help of Figs. 5.3–5.6, the path length $\overline{OSM}$ from the feed to the subreflector and to the main reflector is given by

$$\overline{OSM} \;=\; r_F \;+\; \sqrt{(x_M \;-\; r_F \sin\theta_F)^2 \;+\; (z_M \;-\; r_F \cos\theta_F)^2}\,. \qquad (5.21)$$

Since S corresponds to a reflection point at the subreflector, Fermat's principle ensures that

$$\frac{d\overline{OSM}}{d\theta_F} \;=\; 0\,. \qquad (5.22)$$

From Eqs. 5.21 and 5.22 and noticing that r_F is a function of θ_F, after some algebraic manipulations the subreflector equation is obtained as

$$\frac{dr_F}{d\theta_F} = \frac{r_F\,(x_M\cos\theta_F - z_M\sin\theta_F)}{\overline{OSM} - (x_M\sin\theta_F + z_M\cos\theta_F)}\,. \tag{5.23}$$

Note that if the subreflector satisfies Eq. 5.23 then Snell's law is automatically satisfied at an arbitrary point S.

Since high gain is desired from the antenna, its aperture illumination is specified with a uniform phase [21]. Hence, the main-reflector equation is obtained by enforcing that the total path length associated with an arbitrary feed-ray θ_F must be equal to ℓ_o. From Figs. 5.3–5.6, ℓ_o is given by

$$\ell_o = \overline{OSM} - z_M\,. \tag{5.24}$$

After some algebraic manipulations, Eqs. 5.21 and 5.24 yield

$$z_M = \frac{(x_M - r_F\sin\theta_F)^2 - (\ell_o - r_F)^2 + (r_F\cos\theta_F)^2}{2\,[\ell_o - r_F(1-\cos\theta_F)]}\,. \tag{5.25}$$

Note that if the main reflector satisfies Eq. 5.25 then Snell's law is automatically satisfied at an arbitrary point M.

In order to obtain the desired aperture-field distribution of Eq. 5.1, the conservation of power is applied. Assuming a circularly-symmetric spherical-wave feed, its electric field is given by

$$E_F(\vec{r}_F) = g(\theta_F)\,\frac{e^{-jk_o r_F}}{r_F}\,, \tag{5.26}$$

where $g(\theta_F)$ defines the circularly-symmetric feed pattern. The power $P_{feed}(\theta_F)$, radiated by this feed inside a spherical sector with half-angle $|\theta_F|$ and radius r_F, is

$$\begin{aligned} P_{feed}(\theta_F) &= \int_0^{|\theta_F|} \int_0^{2\pi} \frac{|E_F(\vec{r}_F)|^2}{2\,\eta_o}\; r_F^2\; \sin\theta'\; d\phi'\; d\theta' \\ &= \frac{\pi}{\eta_o} \int_0^{|\theta_F|} g^2(\theta')\; \sin\theta'\; d\theta' \; . \end{aligned} \tag{5.27}$$

For the RCF model of Eq. 4.59, $g(\theta_F) = \cos^h \theta_F$ (assuming $\theta_F \leq \pi/2$) and Eq. 5.27 reduces to Eq. 4.65. Furthermore, GO principles ensure that the total power P_{ape} radiated by the aperture must be equal to the feed power illuminating the subreflector, in which case

$$P_{ape} = P_{feed}(\theta_F = \theta_E) \; . \tag{5.28}$$

From Eq. 5.1, the power flowing through the aperture annular region with inner and outer radii $D_B/2$ and ρ_A (where $D_B/2 \leq \rho_A \leq D_M/2$), respectively, is given by

$$\begin{aligned} P_{ap}(\rho_A) &= \int_{D_B/2}^{\rho_A} \int_0^{2\pi} \frac{|\vec{E}_A^{GO}(\rho')|^2}{2\,\eta_o}\; \rho'\; d\phi'\; d\rho' \\ &= \frac{\pi}{\eta_o}\, |E_o|^2 \int_{D_B/2}^{\rho_A} f^2(\rho')\; \rho'\; d\rho' \; , \end{aligned} \tag{5.29}$$

and, consequently,

$$P_{ape} = P_{ap}(\rho_A = D_M/2) \; . \tag{5.30}$$

The amplitude of E_o is then established by equating Eqs. 5.28 and 5.30 to ensure power conservation. Its phase (with respect to the feed radiation) is obtained by

recalling the uniform-phase aperture illumination and any possible contribution from the Gouy phase shift Φ_G [49]. On doing so:

$$E_o \;=\; \left[\frac{\int_0^{|\theta_E|} g^2(\theta')\,\sin\theta'\,d\theta'}{\int_{D_B/2}^{D_M/2} f^2(\rho')\,\rho'\,d\rho'} \right]^{\frac{1}{2}} e^{j(\Phi_G - k_o \ell_o)}\,, \tag{5.31}$$

where Φ_G is still given by Eq. 4.39. Finally, the power inside the feed cone with half-angle $|\theta_F|$ must be equal to the power inside the aperture annular region defined by this feed cone after the reflections on both reflector surfaces. From Figs. 5.3–5.6 it is clear that this aperture annular region is located at $D_B/2 \leq \rho_A \leq x_M$ for SG I and III and at $x_M \leq \rho_A \leq D_M/2$ for SG II and IV. So, from Eqs. 5.27 and 5.29, conservation of power requires that

$$P_{feed}(\theta_F) \;=\; \begin{cases} P_{ap}(\rho_A = x_M)\,, & \text{for SG I and III}\,, \\ P_{ap}(\rho_A = D_M/2) \;-\; P_{ap}(\rho_A = x_M)\,, & \text{for SG II and IV}\,, \end{cases} \tag{5.32}$$

with E_o given by Eq. 5.31.

Equations 5.23, 5.25 and 5.32 form a system of three equations with three unknowns (namely r_F, x_M, and z_M, assuming θ_F as the variable), which can be solved to yield the reflector surfaces. The coordinates of the reflector generating curves are obtained by solving the first-order non-linear differential equation given by Eq. 5.23, with x_M and z_M given by Eqs. 5.32 and 5.25, respectively. An initial condition is required for this task, and a convenient one is established by the location of the subreflector vertex

$$r_F(\theta_F = 0) \;=\; V_S\,. \tag{5.33}$$

Finally, the non-linear differential equation may be numerically integrated using any widely available method. In this work, a fourth-order Runge-Kutta method was adopted [43].

From Eqs. 5.23, 5.25, 5.32, and 5.33 it is clear that the surfaces of axially-symmetric dual-reflector antennas are obtained once the desired aperture illumination [given by $f(\rho_A)$], feed pattern [given by $g(\theta_F)$], and geometric parameters D_M, D_B, θ_E, ℓ_o, and V_S are established, together with the desired basic geometry (i.e., SG I, II, III, or IV). Although the surfaces of the shaped geometries are not conic sections, the classical geometries studied in Chapter 4 (for which closed-form design equations were derived) are still very useful to establish the basic initial parameters of a particular design. Also, note that the shaping equations presented in this section do not directly consider the subreflector diameter D_S. Hence, after the shaping procedure is carried out one may end up with $D_S > D_B$ (indicating that the subreflector blocks part of the aperture illumination) or even that the clearance between D_S and D_B is over specified (indicating that an even higher aperture efficiency could be obtained). In either case the problem is overcome by starting the shaping procedure from a highly efficient classical configuration where both D_S and D_B are specified. Most probably, the shaping procedure given above will then provide a value of D_S very close to the desired one, and if necessary this value can be further adjusted by small increments on the initial antenna parameters.

The formulation presented in Chapter 4 can also be used to test the accuracy of the shaping code. Starting with prescribed values of D_M, D_S, D_B, θ_E, and ℓ_o (V_S is then given by Eq. 4.14), and specifying the feed and aperture illuminations from Eqs. 4.59 and 4.60, respectively, the shaping procedure must yield the associated classical reflector surfaces.

5.4 Impact of the Feed and Subreflector Spillovers on the Antenna Pattern

The formulations presented for the classical (Chapter 4) and shaped (beginning of this chapter) geometries were obtained in terms of GO concepts and, consequently, do not consider the diffraction effects caused by the multiple interactions among the various antenna elements (e.g., main reflector, subreflector, feed, etc.) or the spillover radiation of the feed (past the subreflector rim) and subreflector (past the main-reflector rim). These combined effects preclude the determination of the antenna pattern using only the aperture-field radiation, and hence must be considered in the antenna design if a desired sidelobe envelope is to be achieved. The present section concentrates only on two spillover mechanisms and their effects to the antenna radiation pattern: the forward feed spillover (associated with the feed radiation that does not illuminate the subreflector) and the backward subreflector spillover (associated with the subreflector radiation that does not illuminate the

main reflector). Their analysis will be carried out using the Geometrical Theory of Diffraction (GTD) [9], which provides closed-form results that yield design insights. Note that the GTD approximation has the necessary accuracy for reflector surfaces with an overall electrical dimension of about 10λ or higher.

The main-reflector surfaces of the classical and shaped geometries (Figs. 4.1–4.4 and Figs. 5.3–5.6, respectively) may have an aperture at their center, corresponding to the region not illuminated by the subreflector radiation (accordingly to GO concepts). However, in order to enhance the front-to-back ratio of the antenna pattern and also to avoid the corresponding edge diffraction, this aperture is usually closed by a continuous extrapolation of the main-reflector surface (with only a small opening to allow passage for the feed structure). Thus, the spillover through this main-reflector central hole is not considered in here.

5.4.1 Feed Spillover Near the Subreflector Shadow Boundary (Forward Spillover)

The forward feed spillover may preclude the achievement of a desired sidelobe envelope and hence must be kept as small as possible. A low forward feed spillover is achieved by imposing a highly tapered feed illumination towards the subreflector rim. However, this degrades the subreflector and, consequently, aperture illuminations, reducing the overall antenna efficiency (which can be compensated by the antenna shaping, as long as the feed taper is not extremely high). The tradeoff

between high efficiency and low forward spillover can be understood by investigating the diffraction mechanisms around the subreflector shadow boundary. This allows the specification of the smallest feed taper required to satisfy any restrictions imposed on the sidelobe levels at this region.

The present study is based on the geometry shown in Fig. 5.7. The subreflector shadow region is defined as the region behind the subreflector where no direct contribution from the feed radiation is present (from a GO stand point). This region is then determined by the subreflector surface and the associated shadow boundary. Similarly, the reflection region is characterized by the presence of subreflector-reflected rays and determined by the subreflector and its associated reflection boundary (see Fig. 5.7). According to the GTD principles [9], near the shadow boundary the total field of the feed/subreflector combination is provided by the GO contribution from the feed direct radiation plus the field diffracted at the subreflector rim. For the present case of a BOR, the diffraction contribution comes from the two subreflector-rim points R and R' located in the plane of Fig. 5.7 (plane of incidence). However, near the shadow boundary corresponding to the subreflector point R, the contribution associated with R' is negligible [9] and, thus, will be ignored here. The GO field is discontinuous across the shadow boundary associated with R. However, this discontinuity is compensated by the field diffracted at point R, and GTD ultimately ensures the continuity of the total radiated field [9].

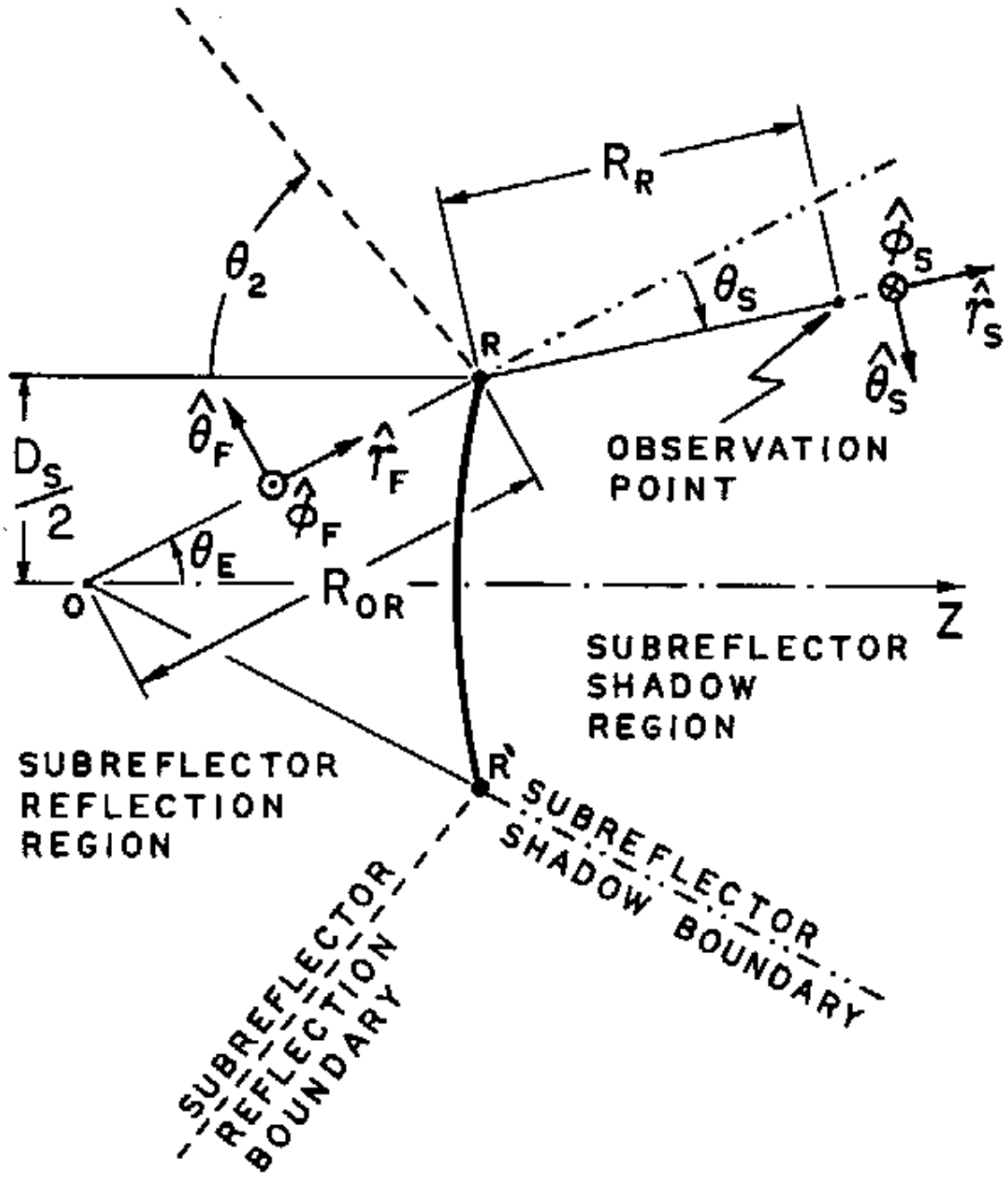

Figure 5.7: GTD Analysis of the Forward Feed Spillover.

The feed radiation illuminating point R in Fig. 5.7 can be described using the usual spherical coordinates r_F, θ_F, and ϕ_F, with the associated base vectors

$$\hat{r}_F = \sin\theta_E\,\hat{\rho} + \cos\theta_E\,\hat{z}\,, \tag{5.34}$$

$$\hat{\theta}_F = \cos\theta_E\,\hat{\rho} - \sin\theta_E\,\hat{z}\,, \tag{5.35}$$

$$\hat{\phi}_F = \hat{\phi}\,, \tag{5.36}$$

where θ_E is the subreflector edge angle and assumed positive in the present section without loss of generality. The electromagnetic field of the rays diffracted at point R can be described using the base vectors

$$\hat{r}_S = \sin(\theta_E - \theta_S)\,\hat{\rho} + \cos(\theta_E - \theta_S)\,\hat{z}\,, \tag{5.37}$$

$$\hat{\theta}_S = -\cos(\theta_E - \theta_S)\,\hat{\rho} + \sin(\theta_E - \theta_S)\,\hat{z}\,, \tag{5.38}$$

$$\hat{\phi}_S = -\hat{\phi}\,, \tag{5.39}$$

where the angle θ_S is measured with respect to the shadow boundary, being *positive* for diffracted rays *inside* the shadow region (see Fig. 5.7). In the limit when $\theta_S \to 0$ (region very close to the shadow boundary, which is the region of interest here) one may describe both the GO and diffracted fields using the same base vectors given by Eqs. 5.37–5.39. On doing so, the electric field around the shadow boundary is [9]

$$\vec{E}_{GTD}(R_R,\theta_S)\Big|_{\theta_S\approx 0} = \vec{E}_{GO}(R_R,\theta_S)\Big|_{\theta_S\approx 0} + \vec{E}_{DIFF}(R_R,\theta_S)\Big|_{\theta_S\approx 0}\,, \tag{5.40}$$

where $\vec{E}_{GO}(R_R,\theta_S)$ and $\vec{E}_{DIFF}(R_R,\theta_S)$ are the GO and diffracted electric fields, respectively, and R_R is the distance from point R to the observation point.

The GO contribution from the feed direct radiation is given by [9]

$$\vec{E}_{GO}(R_R,\theta_S)\Big|_{\theta_S\approx 0} = \vec{E}_F(R^-)\,\frac{R_{OR}}{R_R+R_{OR}}\;e^{-jk_oR_R}\left[\frac{1-Sign(\theta_S)}{2}\right], \qquad (5.41)$$

where $\vec{E}_F(R^-)$ is the feed electric field immediately before the incidence at point R and conveniently expressed in the diffracted-ray base vectors as

$$\vec{E}_F(R^-) = -\left[\vec{E}_F(R^-)\cdot\hat{\theta}_F\right]\hat{\theta}_S - \left[\vec{E}_F(R^-)\cdot\hat{\phi}_F\right]\hat{\phi}_S\,. \qquad (5.42)$$

In the above expressions, R_{OR} is the distance between the feed (point O) and point R, and

$$Sign(\theta) = \begin{cases} +1\,, & \text{for } \theta > 0\,, \\ -1\,, & \text{for } \theta \le 0\,. \end{cases} \qquad (5.43)$$

The diffracted electric field is given by [9]

$$\vec{E}_{DIFF}(R_R,\theta_S)\Big|_{\theta_S\approx 0} = \sqrt{k_o}\,\overline{\overline{\mathcal{D}}}\cdot\vec{E}_F(R^-)\sqrt{\frac{R_D}{R_R+R_D}}\sqrt{\frac{1}{k_o\,R_R}}\;e^{-jk_oR_R}\,, \qquad (5.44)$$

where the diffraction dyadic $\sqrt{k_o}\,\overline{\overline{\mathcal{D}}}$ is given by [9]

$$\begin{aligned}\sqrt{k_o}\,\overline{\overline{\mathcal{D}}} &= -\left[\mathcal{D}_i(\pi+\theta_S) + \mathcal{D}_r(\theta_2-\theta_E+\theta_S)\right]\hat{\theta}_S\,\hat{\theta}_S \\ &\quad -\left[\mathcal{D}_i(\pi+\theta_S) - \mathcal{D}_r(\theta_2-\theta_E+\theta_S)\right]\hat{\phi}_S\,\hat{\phi}_S\,, \end{aligned} \qquad (5.45)$$

with

$$\mathcal{D}_l(\theta) = \frac{|\cos(\theta/2)|}{\cos(\theta/2)}\sqrt{k_o\,L_l}\;K_-\left[\sqrt{2\,k_o\,L_l\,\cos^2(\theta/2)}\right],\quad l=i \text{ or } r\,, \qquad (5.46)$$

$$K_-(x) = \sqrt{\frac{1}{\pi}}\;e^{j(x^2+\pi/4)}\int_x^\infty e^{-jt^2}\,dt\,, \qquad (5.47)$$

and, for a BOR subreflector,

$$L_i = \frac{R_R\, R_{OR}}{R_R + R_{OR}}\,, \tag{5.48}$$

$$L_r = \frac{R_R\, \rho_{1r}^R}{R_R + \rho_{1r}^R}\,. \tag{5.49}$$

In the above expressions, θ_2 is the negative angle (accordingly to the notation of Chapter 4) between the reflection boundary and the z-axis (see Fig. 5.7), ρ_{1r}^R is the subreflector-reflected-wavefront principal radius of curvature in the plane of incidence (immediately after the reflection at point R), R_D is the distance between the caustic at the edge and the second caustic of the diffracted ray, given by (from Eq. 12 of Ref. [9])

$$\frac{1}{R_D} = \frac{1}{R_{OR}} - \frac{\hat{\rho}\cdot(\hat{r}_F - \hat{r}_S)}{D_S/2}\,, \tag{5.50}$$

and D_S is the subreflector diameter. From Eqs. 5.34, 5.37, and 5.50 one obtains

$$\lim_{\theta_S \to 0} R_D = R_{OR}\,. \tag{5.51}$$

Also, using the results presented in Ref. [52] on Eqs. 5.45–5.47 one obtains

$$\lim_{\theta_S \to 0} \mathcal{D}_i(\pi + \theta_S) = -\frac{\sqrt{k_o\, L_i}}{2}\, Sign(\theta_S)\,, \tag{5.52}$$

$$\lim_{\theta_S \to 0} \mathcal{D}_r(\theta_2 - \theta_E + \theta_S) = -\frac{e^{-j\pi/4}}{2\sqrt{2\pi}}\, \sec\left(\frac{\theta_E - \theta_2}{2}\right)\,, \tag{5.53}$$

and, as $\mathcal{D}_i(\pi + \theta_S) \gg \mathcal{D}_r(\theta_2 - \theta_E + \theta_S)$ in Eqs. 5.52 and 5.53,

$$\lim_{\theta_S \to 0} \sqrt{k_o}\,\overline{\overline{\mathcal{D}}} \approx \frac{\sqrt{k_o\, L_i}}{2}\, Sign(\theta_S)\, \left(\hat{\theta}_S\, \hat{\theta}_S + \hat{\phi}_S\, \hat{\phi}_S\right)\,, \tag{5.54}$$

where in Eqs. 5.53 and 5.54 it is being assumed that the incident feed ray does not have a grazing incidence at point R (i.e., $\theta_E - \theta_2 < \pi$).

Substituting Eqs. 5.41–5.54 into Eq. 5.40, in the limit when $\theta_S \to 0$ one obtains

$$\vec{E}_{GTD}(R_R, \theta_S = 0) \approx \frac{1}{2}\vec{E}_{GO}(R_R, \theta_S = 0) , \tag{5.55}$$

which shows that the field at the shadow boundary is about 6 dB below the field that would be provided by the feed without the presence of the subreflector.

To illustrate the application of Eq. 5.55 in the design process of an antenna system, Fig. 5.8 shows the radiation pattern (with respect to an isotropic radiator, boresight along the z-axis) of the RCF model given by Eq. 4.59 with $h = 16$, together with the ITU specifications given by Eq. 5.20. From this figure one observes that the RCF pattern intersects the required envelope at $\theta \approx 33°$, being 6 dB above the envelope at $\theta \approx 28°$. As the subreflector-edge diffraction reduces the feed radiation by 6 dB around the shadow boundary (see Eq. 5.55), to prevent the forward feed spillover from increasing the antenna sidelobe levels beyond the specified envelope, while still providing the best possible subreflector illumination, the edge angle $|\theta_E|$ should be specified around 30° for the present example (with a safety margin included on this $|\theta_E|$ value).

5.4.2 Subreflector Spillover Near the Reflection Boundary (Backward Spillover)

Similarly to the analysis performed in Sect. 5.4.1, the backward subreflector spillover produced near its reflection boundary can be analyzed in closed form using GTD [9]. Considering the classical and shaped geometries previously studied one observes

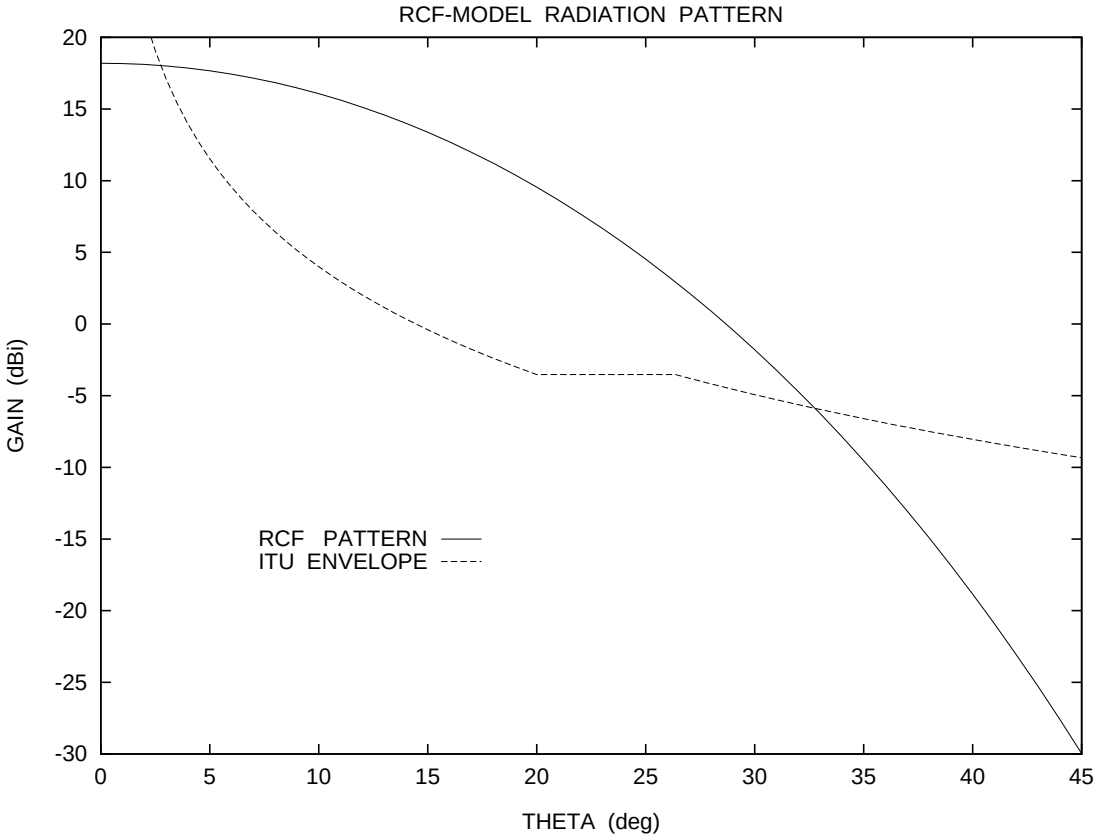

Figure 5.8: Pattern of a Circularly-Symmetric RCF Model with $h = 16$.

that they generally present a curvature discontinuity at the subreflector vertex, which leads to the presence of two subreflector reflection boundaries, as illustrated in Figs. 5.9–5.12. For Geometries I and III (classical and shaped), the backward spillover occurs around the reflection boundary associated with the subreflector-edge point R (Figs. 5.9 and 5.11). Near this region and using GTD principles, the subreflector scattering is mainly caused by the reflected field plus the diffraction contribution from point R [9]. On the other hand, Geometries II and IV (classical and shaped) have their backward spillover around the reflection boundary corresponding to the subreflector-vertex point Q (Figs. 5.10 and 5.12). Although the subreflector-edge diffraction does not have its highest impact occurring at this region, its effects can not be ignored since the vertex-tip diffraction is negligible when compared to the edge one [53]. The ultimate consequence is that no simple approximations can be obtained to describe the field behavior at the region corresponding to the backward spillover for Geometries II and IV (the complete analysis of the subreflector radiation should be conducted). So, in this work the subreflector spillover analysis will only cover Geometries I and III (Figs. 5.9 and 5.11, respectively).

Similarly to Sect. 5.4.1, near the reflection boundary associated with the subreflector edge the scattered field can be decomposed into a reflection and a diffraction contributions emanating from the subreflector-edge point R. Ultimately, GTD ensures the continuity of the total field across the boundary by compensating for the

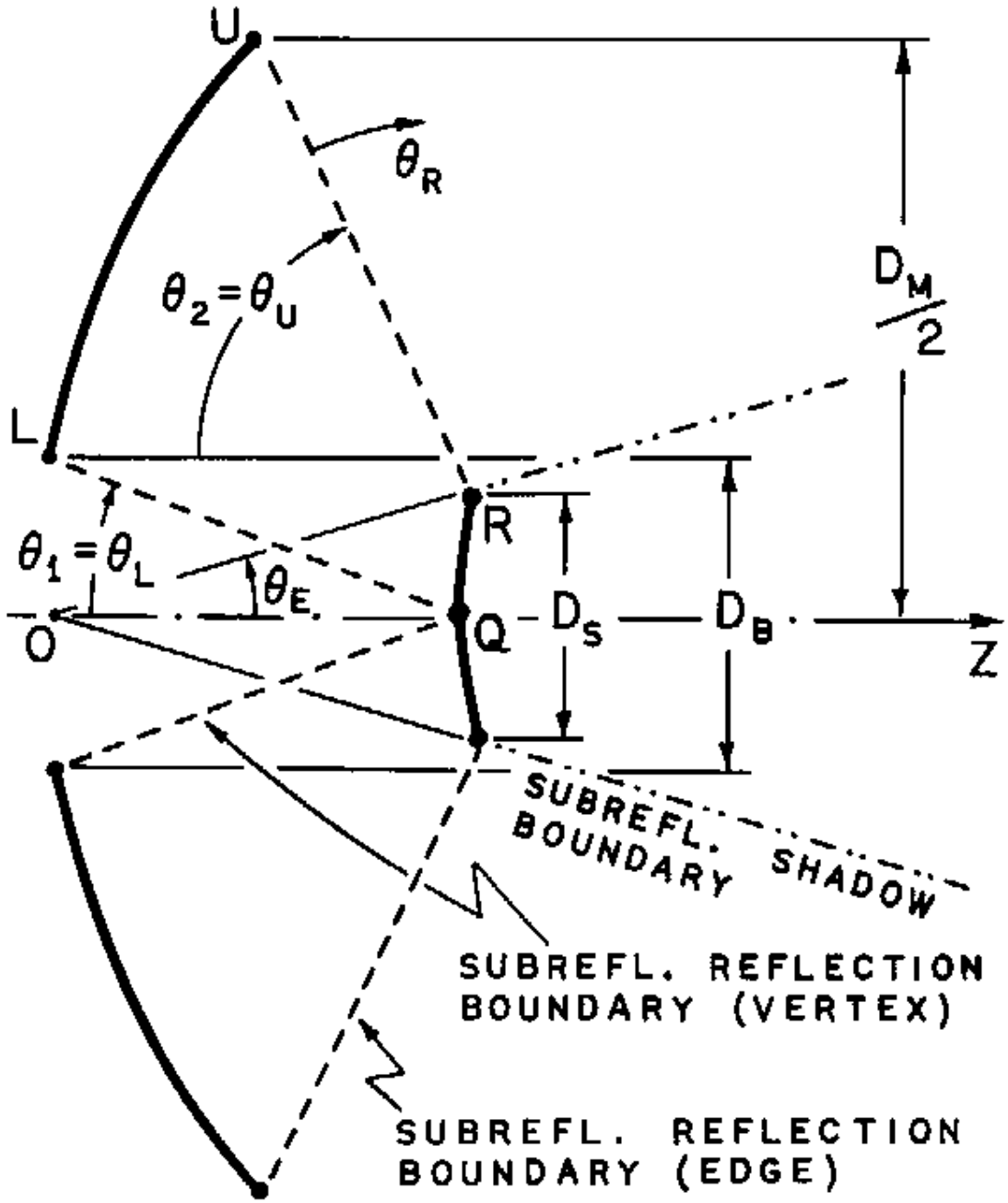

Figure 5.9: Subreflector Reflection Boundaries for CG I and SG I.

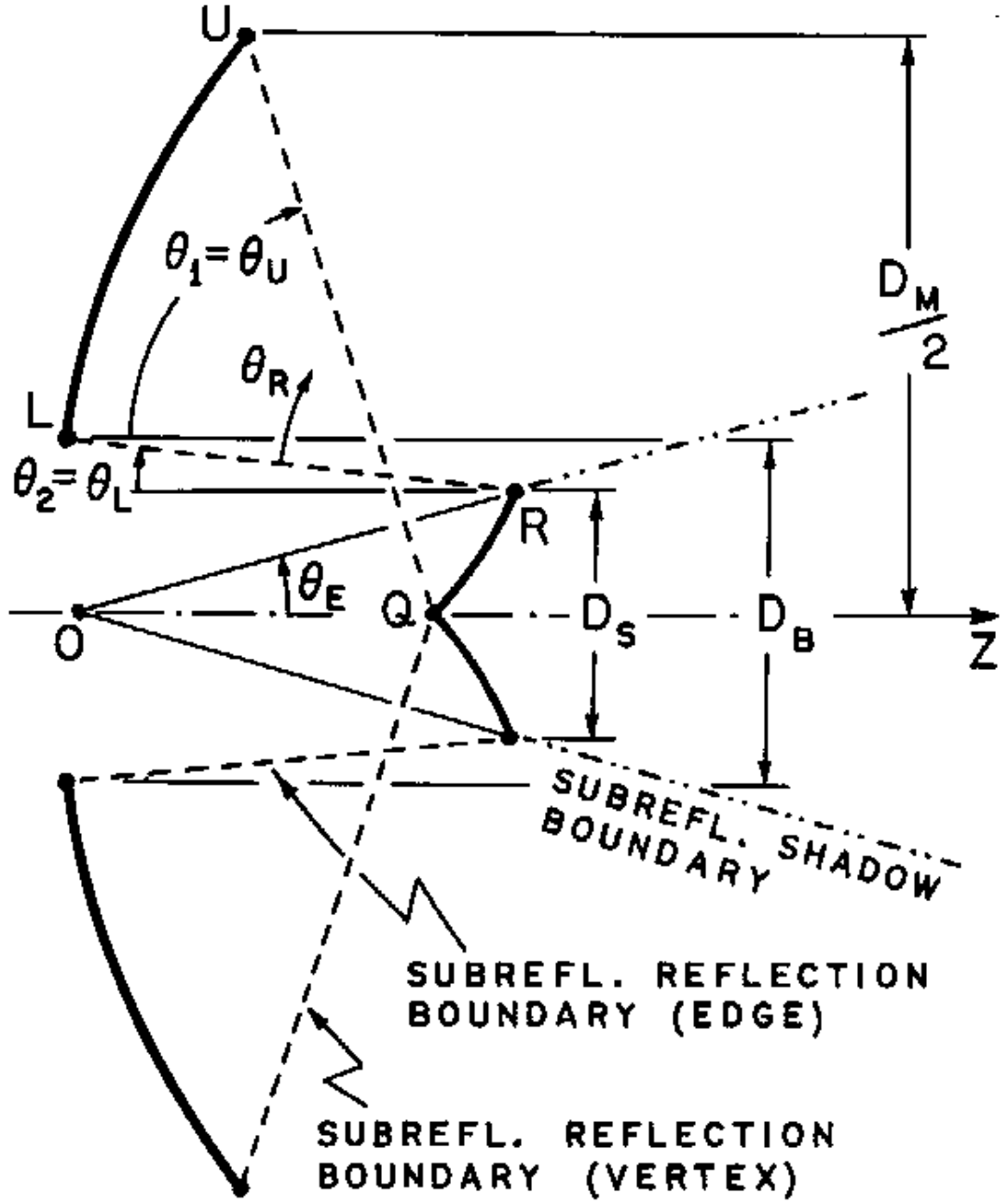

Figure 5.10: Subreflector Reflection Boundaries for CG II and SG II.

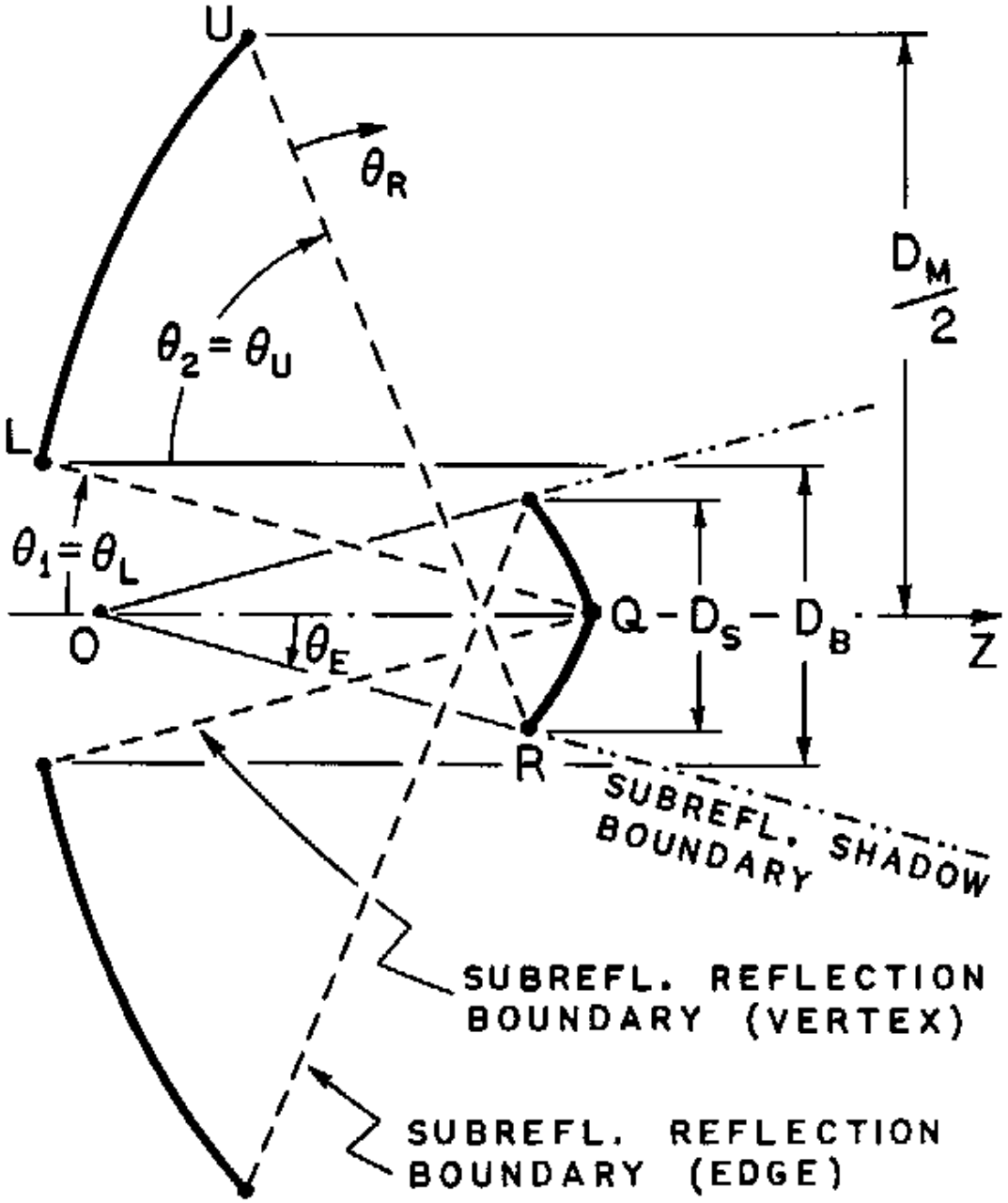

Figure 5.11: Subreflector Reflection Boundaries for CG III and SG III.

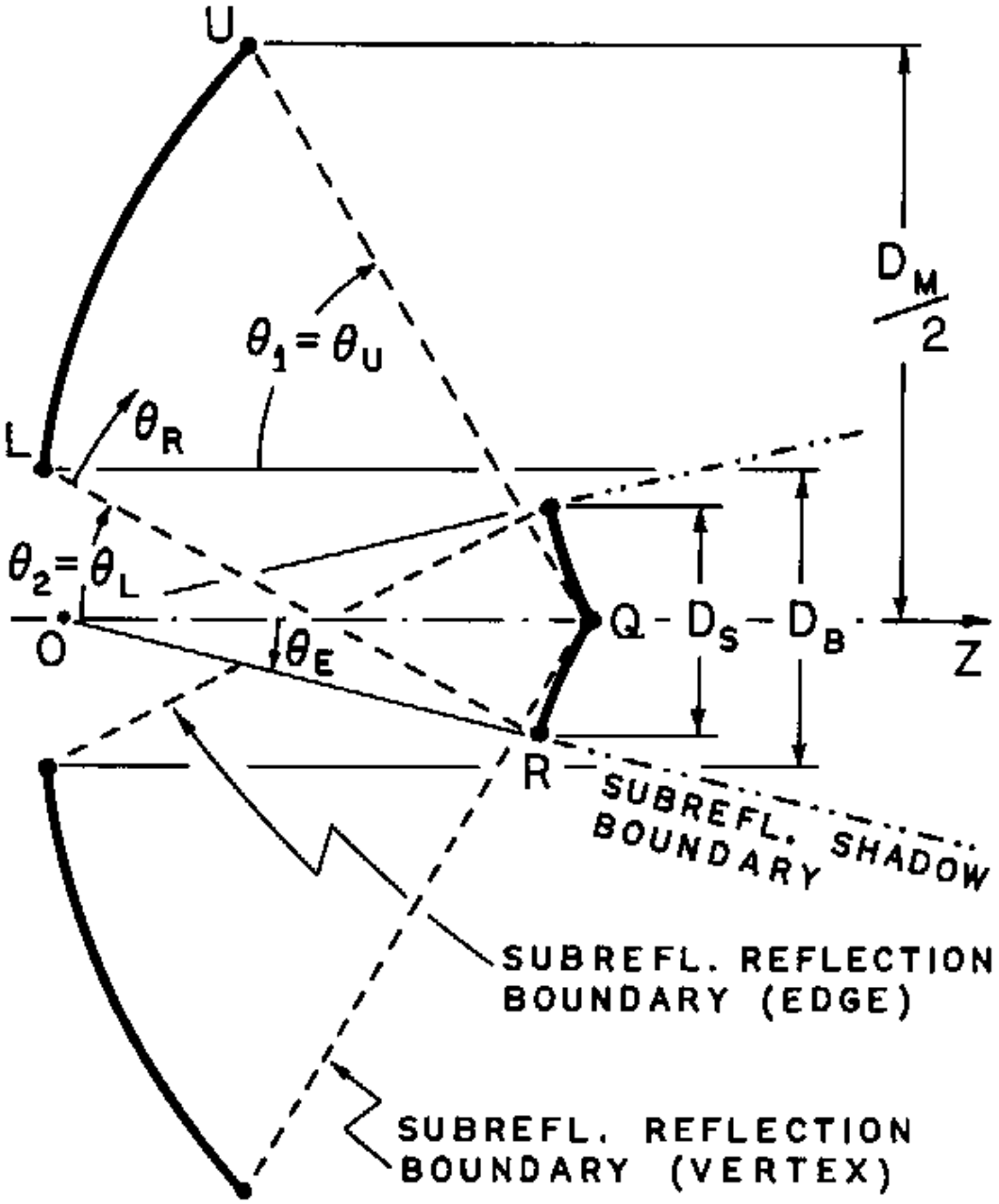

Figure 5.12: Subreflector Reflection Boundaries for CG IV and SG IV.

reflected field discontinuity [9]. For practical designs of the classical and shaped geometries previously described, the subreflector reflection region is almost always intercepted by the main reflector (see Figs. 5.9 and 5.11) and hence, according to GTD principles, the subreflector spillover is caused by the field diffracted at R (no reflected field contribution). To consider this diffraction, the feed radiation can still be represented by the spherical base vectors of Eqs. 5.34–5.36. However, for the diffracted rays it is more convenient to use the base vectors (see Fig. 5.13)

$$\hat{r}_R = \sin(\theta_R - \theta_2)\ \hat{\rho} - \cos(\theta_R - \theta_2)\ \hat{z}\,, \tag{5.56}$$

$$\hat{\theta}_R = \cos(\theta_R - \theta_2)\ \hat{\rho} + \sin(\theta_R - \theta_2)\ \hat{z}\,, \tag{5.57}$$

$$\hat{\phi}_R = -\hat{\phi}\,, \tag{5.58}$$

where the angle θ_R is measured with respect to the reflection boundary, being *positive* for diffracted rays *outside* the reflection region (i.e., in the region where no reflected rays are present), and θ_2 is the negative angle between the reflection boundary and the z-axis. The formulation presented in this section is based on the Geometry I illustrated in Fig. 5.13. However, the final results are valid for both Geometries I and III, as long as θ_R is defined accordingly to Fig. 5.11 for Geometry III.

Near the reflection boundary, $\theta_R \approx 0$ and hence one may represent both the GO and diffracted fields using the base vectors given by Eqs. 5.56–5.58. On doing so, the electric field radiated by the subreflector near the reflection boundary is

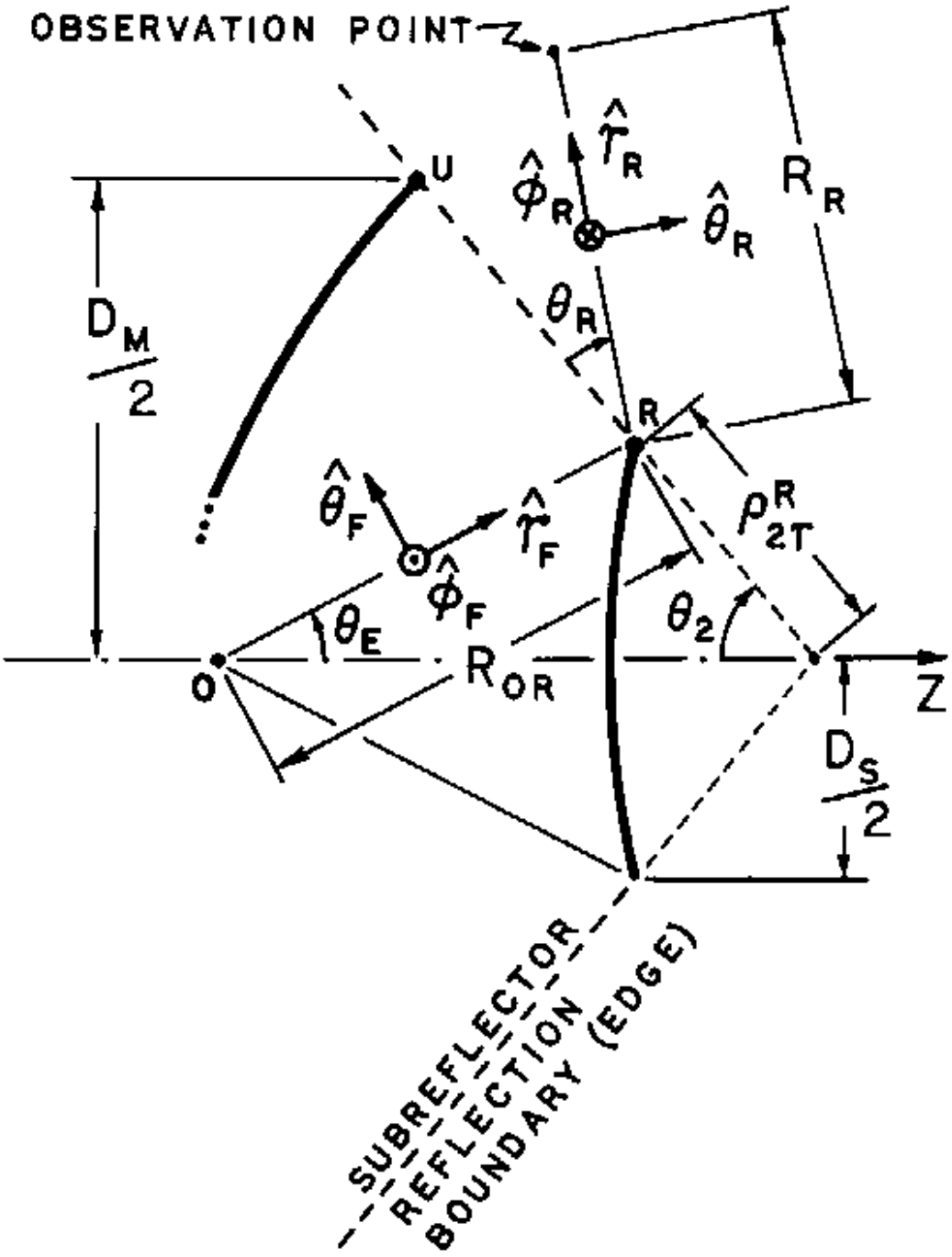

Figure 5.13: GTD Analysis of the Subreflector Spillover for Geometry I.

represented as

$$\vec{E}_{GTD}(R_R,\theta_R)\Big|_{\theta_R\approx 0} = \vec{E}_{GO}(R_R,\theta_R)\Big|_{\theta_R\approx 0} + \vec{E}_{DIFF}(R_R,\theta_R)\Big|_{\theta_R\approx 0}, \quad (5.59)$$

where $\vec{E}_{GO}(R_R,\theta_R)$ and $\vec{E}_{DIFF}(R_R,\theta_R)$ are the GO and diffracted electric fields, respectively. The GO contribution from the subreflector-reflected rays is given by [9]

$$\begin{aligned}\vec{E}_{GO}(R_R,\theta_R)\Big|_{\theta_R\approx 0} &= \vec{E}_F(R^+)\sqrt{\frac{\rho_{1r}^R}{R_R+\rho_{1r}^R}}\sqrt{\frac{\rho_{2r}^R}{R_R+\rho_{2r}^R}}\; e^{-jk_oR_R} \\ &\times \left[\frac{1-Sign(\theta_R)}{2}\right], \end{aligned} \quad (5.60)$$

where ρ_{2r}^R is the subreflector-reflected-wavefront principal radius of curvature in the plane perpendicular to the plane of incidence (immediately after the reflection at R) and $\vec{E}_F(R^+)$ is the feed electric field immediately after the reflection at the subreflector point R and conveniently expressed in terms of the diffracted-ray base vectors around the reflection boundary as

$$\vec{E}_F(R^+) = -\left[\vec{E}_F(R^-)\cdot\hat{\theta}_F\right]\hat{\theta}_R + \left[\vec{E}_F(R^-)\cdot\hat{\phi}_F\right]\hat{\phi}_R, \quad (5.61)$$

with $\vec{E}_F(R^-)$ being the feed electric field immediately before the reflection at R. The remaining parameters in the above expressions were previously defined in Sect. 5.4.1. Observe that by separating the square-root terms in Eq. 5.60, the Gouy phase shift [49] is being implicitly considered [40].

Similarly to Eq. 5.44, the diffracted electric field is given by [9]

$$\vec{E}_{DIFF}(R_R,\theta_R)\Big|_{\theta_R\approx 0} = \sqrt{k_o}\,\overline{\overline{\mathcal{D}}}\cdot\vec{E}_F(R^+)\sqrt{\frac{R_D}{R_R+R_D}}\sqrt{\frac{1}{k_o\,R_R}}\; e^{-jk_oR_R}, \quad (5.62)$$

where R_D is given by Eq. 5.50 (with $\hat{r}_S$ replaced by $\hat{r}_R$) and here the diffraction dyadic $\sqrt{k_o}\,\overline{\overline{\mathcal{D}}}$ is conveniently expressed as [9]

$$\begin{aligned}\sqrt{k_o}\,\overline{\overline{\mathcal{D}}} &= -\left[\mathcal{D}_i(\theta_E-\theta_2+\theta_R)+\mathcal{D}_r(\pi+\theta_R)\right]\hat{\theta}_R\,\hat{\theta}_R \\ &+ \left[\mathcal{D}_i(\theta_E-\theta_2+\theta_R)-\mathcal{D}_r(\pi+\theta_R)\right]\hat{\phi}_R\,\hat{\phi}_R\ ,\end{aligned} \tag{5.63}$$

with $\mathcal{D}_i(\theta)$ and $\mathcal{D}_r(\theta)$ given by Eqs. 5.46–5.49. From Eqs. 5.34, 5.50, and 5.56, and observing from Fig. 5.13 that $D_S/2 = R_{OR}\sin\theta_E = -\rho_{2r}^R\sin\theta_2$ (recalling that $\theta_2 < 0$), one obtains

$$\lim_{\theta_R\to 0} R_D = \rho_{2r}^R\,(1+\theta_R\cot\theta_2)\ . \tag{5.64}$$

Also, from Ref. [52] and Eqs. 5.46, 5.47, and 5.63:

$$\lim_{\theta_R\to 0}\mathcal{D}_i(\theta_E-\theta_2+\theta_R) = \frac{e^{-j\pi/4}}{2\sqrt{2\pi}}\sec\left(\frac{\theta_E-\theta_2}{2}\right)\ , \tag{5.65}$$

$$\lim_{\theta_R\to 0}\mathcal{D}_r(\pi+\theta_R) = -\frac{\sqrt{k_o\,L_r}}{2}\,Sign(\theta_R)\ , \tag{5.66}$$

and, as $\mathcal{D}_r(\pi+\theta_R) \gg \mathcal{D}_i(\theta_E-\theta_2+\theta_R)$ in Eqs. 5.65 and 5.66,

$$\lim_{\theta_R\to 0}\sqrt{k_o}\,\overline{\overline{\mathcal{D}}} \approx \frac{\sqrt{k_o\,L_r}}{2}\,Sign(\theta_R)\left(\hat{\theta}_R\,\hat{\theta}_R+\hat{\phi}_R\,\hat{\phi}_R\right)\ , \tag{5.67}$$

where in Eqs. 5.65 and 5.67 it is being assumed that the incident feed ray does not have a grazing incidence at point R (i.e., $\theta_E-\theta_2<\pi$). Finally, The substitution of Eqs. 5.60–5.67 into Eq. 5.59 yields

$$\vec{E}_{GTD}(R_R,\theta_R=0) \approx \frac{1}{2}\,\vec{E}_{GO}(R_R,\theta_R=0)\ . \tag{5.68}$$

This result (which is similar to Eq. 5.55 obtained at the shadow boundary) indicates that the electric field at the reflection boundary (associated with the subreflector edge) is 6 dB below the field obtained from the GO approximations. Note that Eq. 5.68 applies to all classical and shaped geometries around the respective subreflector reflection boundaries associated with point R (see Figs. 5.9–5.12). However, these regions correspond to the backward subreflector spillover only for Geometries I and III (Figs. 5.9 and 5.11, respectively).

To conclude the analysis of the backward spillover for Geometries I and III, the edge-diffraction effects to the subreflector-pattern roll-off are now investigated. The roll-off, which in some designs should be large enough to reduce the subreflector spillover, is analyzed trough the partial derivative of $|\vec{E}_{GTD}(R_R, \theta_R)|$ with respect to θ_R, in the neighborhood of the reflection boundary. In order to simplify this task a circularly-symmetric feed radiation is assumed, which characterizes the feed illumination used throughout this work. On doing so, one directly observes from Eq. 5.60 that the GO electric field is also circularly symmetric and hence can be treated as a scalar radiation (i.e., $|\vec{E}_{GO}(R_R, \theta_R)|$ does not depend on the plane of incidence). Similarly, from Eqs. 5.62–5.67 the same can be extended to the diffracted electric field, as $\mathcal{D}_i(\theta_E - \theta_2 + \theta_R)$ can be neglected when $\theta_R \to 0$. So, the derivative of the electric-field complex amplitude in the vicinity of the reflection

boundary can be expressed as

$$\frac{\partial}{\partial\theta_R}E_{GTD}(R_R,\theta_R)\,\Big|_{\theta_R\approx 0} = \frac{\partial}{\partial\theta_R}E_{GO}(R_R,\theta_R)\,\Big|_{\theta_R\approx 0} + \frac{\partial}{\partial\theta_R}E_{DIFF}(R_R,\theta_R)\,\Big|_{\theta_R\approx 0}, \tag{5.69}$$

where, from Eq. 5.60,

$$\begin{aligned} E_{GO}(R_R,\theta_R)\,\Big|_{\theta_R\approx 0} &= E_F(R^+)\,\sqrt{\frac{\rho_{1r}^R}{R_R+\rho_{1r}^R}}\,\sqrt{\frac{\rho_{2r}^R}{R_R+\rho_{2r}^R}}\;e^{-jk_oR_R} \\ &\times \left[\frac{1-Sign(\theta_R)}{2}\right], \end{aligned} \tag{5.70}$$

and, from Eqs. 5.62–5.67,

$$E_{DIFF}(R_R,\theta_R)\,\Big|_{\theta_R\approx 0} = -\mathcal{D}_r(\pi+\theta_R)\;E_F(R^+)\,\sqrt{\frac{R_D}{R_R+R_D}}\,\sqrt{\frac{1}{k_o\,R_R}}\;e^{-jk_oR_R}. \tag{5.71}$$

The derivative of $|\vec{E}_{GTD}(R_R,\theta_R)|$ is then obtained from the relation

$$\begin{aligned} \frac{\partial\,|E_{GTD}|}{\partial\theta_R} &= \frac{1}{2\,|E_{GTD}|}\left(E_{GTD}\,\frac{\partial E_{GTD}^*}{\partial\theta_R} + E_{GTD}^*\,\frac{\partial E_{GTD}}{\partial\theta_R}\right) \\ &= \frac{1}{|E_{GTD}|}\,\Re\mathrm{e}\left(E_{GTD}^*\,\frac{\partial E_{GTD}}{\partial\theta_R}\right), \end{aligned} \tag{5.72}$$

where $*$ denotes the complex conjugate.

In order to simultaneously handle the problem where θ_R approaches zero from both sides (i.e., $\theta_R \to 0^-$ and $\theta_R \to 0^+$), the step function defined by Eq. 5.43 is employed in the following formulation. However, on doing so one must bear in mind that the results to be shown are not valid exactly at $\theta_R = 0$, as the GO and diffracted electric fields are discontinuous across the reflection boundary. This is related to the fact that GTD ensures the continuity of the total field across the boundary, but not the continuity its derivatives [9].

The derivative of $E_{GO}(R_R, \theta_R)$ with respect to θ_R can not be obtained in closed form without the prior knowledge of the subreflector-reflected wavefront characteristics (see Eq. 5.70). So, for now it will be simply represented as

$$\frac{\partial}{\partial \theta_R} E_{GO}(R_R, \theta_R) \Big|_{\theta_R \approx 0} = E_{GO}(R_R, \theta_R) \Big|_{\theta_R \approx 0} \; D_{GO}(R_R, \theta_R) \left[\frac{1 - Sign(\theta_R)}{2} \right] , \tag{5.73}$$

where in this expression it is being assumed that the subreflector is continuously extrapolated beyond its original rim and, consequently, $D_{GO}(R_R, \theta_R)$ is assumed known and continuous across the reflection boundary. The abrupt discontinuity is then taken into account by the step function $Sign(\theta_R)$. The derivative of $E_{DIFF}(R_R, \theta_R)$ is obtained from Eq. 5.71, observing that R_R is orthogonal to θ_R and recalling the derivative violation at $\theta_R = 0$:

$$\begin{aligned} \frac{\partial}{\partial \theta_R} E_{DIFF}(R_R, \theta_R) \Big|_{\theta_R \approx 0} &= - E_F(R^+) \sqrt{\frac{1}{k_o R_R}} \left[\sqrt{\frac{R_D}{R_R + R_D}} \; \frac{\partial}{\partial \theta_R} \mathcal{D}_r(\pi + \theta_R) \right. \\ &\quad \left. + \frac{\partial}{\partial \theta_R} \left(\sqrt{\frac{R_D}{R_R + R_D}} \right) \mathcal{D}_r(\pi + \theta_R) \right] e^{-jk_o R_R} . \end{aligned} \tag{5.74}$$

From Eqs. 5.46 and 5.47 one obtains

$$\frac{\partial}{\partial \theta} \mathcal{D}_l(\theta) = j\, 2\, k_o\, L_l \, \sin(\theta/2) \left[\frac{e^{-j\pi/4}}{2\sqrt{2\pi}} - \cos(\theta/2)\, \mathcal{D}_l(\theta) \right] , \quad l = i \text{ or } r , \tag{5.75}$$

which, together with Eqs. 5.65 and 5.66, yields

$$\lim_{\theta_R \to 0} \frac{\partial}{\partial \theta_R} \mathcal{D}_i(\theta_E - \theta_2 + \theta_R) = 0 , \tag{5.76}$$

$$\begin{aligned} \lim_{\theta_R \to 0} \frac{\partial}{\partial \theta_R} \mathcal{D}_r(\pi + \theta_R) &= \frac{k_o\, L_r}{\sqrt{2\pi}} \, e^{j\pi/4} \\ &\approx - 2 \sqrt{\frac{L_r}{\lambda}} \, e^{j\pi/4} \; Sign(\theta_R) \; \mathcal{D}_r(\pi + \theta_R) . \end{aligned} \tag{5.77}$$

From Eq. 5.76 one observes that the derivative of $\mathcal{D}_i(\theta_E - \theta_2 + \theta_R)$ can be neglected, ratifying the approximation used to obtain Eq. 5.71. Furthermore, the derivative of the square-root term in Eq. 5.74 is given by

$$\frac{\partial}{\partial \theta_R}\sqrt{\frac{R_D}{R_R + R_D}} \;=\; \sqrt{\frac{R_D}{R_R + R_D}}\;\frac{R_R}{2\,R_D\,(R_R + R_D)}\;\frac{\partial\, R_D}{\partial \theta_R}\,, \tag{5.78}$$

which, using Eq. 5.64, can be approximated by

$$\lim_{\theta_R \to 0}\;\frac{\partial}{\partial \theta_R}\sqrt{\frac{R_D}{R_R + R_D}} \;\approx\; \sqrt{\frac{R_D}{R_R + R_D}}\;\frac{R_R \cot\theta_2}{2\,(R_R + \rho_{2r}^R)}\,. \tag{5.79}$$

Substituting Eqs. 5.77 and 5.79 into Eq. 5.74, and using Eq. 5.71, one obtains

$$\begin{aligned}\frac{\partial}{\partial \theta_R} E_{DIFF}(R_R, \theta_R)\,\Big|_{\theta_R \approx 0} \;\approx\; & -\,E_{DIFF}(R_R, \theta_R)\,\Big|_{\theta_R \approx 0}\,\left[2\sqrt{\frac{L_r}{\lambda}}\,e^{j\pi/4}\,Sign(\theta_R)\right. \\ & \left. -\;\frac{R_R \cot\theta_2}{2\,(R_R + \rho_{2r}^R)}\right]. \end{aligned} \tag{5.80}$$

However, since (see Eqs. 5.68–5.71)

$$E_{DIFF}(R_R, \theta_R)\,\Big|_{\theta_R \approx 0} \;\approx\; \frac{1}{2}\,E_{GO}(R_R, \theta_R)\,\Big|_{\theta_R \approx 0}\;Sign(\theta_R)\,, \tag{5.81}$$

Eq. 5.80 can be rewritten as

$$\begin{aligned}\frac{\partial}{\partial \theta_R} E_{DIFF}(R_R, \theta_R)\,\Big|_{\theta_R \approx 0} \;\approx\; & -\,E_{GO}(R_R, \theta_R)\,\Big|_{\theta_R \approx 0}\,\left[\sqrt{\frac{L_r}{\lambda}}\,e^{j\pi/4}\right. \\ & \left. -\;\frac{R_R \cot\theta_2}{4\,(R_R + \rho_{2r}^R)}\;Sign(\theta_R)\right]. \end{aligned} \tag{5.82}$$

Substituting Eqs. 5.73 and 5.82 into Eq. 5.69 one obtains (recalling that the above expressions are valid in the limit when $\theta_R \to 0$ from both sides, but not

when $\theta_R = 0$)

$$\frac{\partial}{\partial\theta_R} E_{GTD}(R_R,\theta_R)\Big|_{\theta_R\approx 0} \approx E_{GO}(R_R,\theta_R)\Big|_{\theta_R\approx 0} \left\{ D_{GO}(R_R,\theta_R) \left[\frac{1-Sign(\theta_R)}{2}\right] - \left[\sqrt{\frac{L_r}{\lambda}}\, e^{j\pi/4} - \frac{R_R \cot\theta_2}{4\,(R_R+\rho_{2r}^R)}\, Sign(\theta_R)\right]\right\}, \tag{5.83}$$

which presents an expected discontinuity when θ_R approaches zero from both sides, as the GTD asymptotic approximation only ensures the continuity of the field across the reflection boundary [9]. However, this derivative discontinuity is not physically possible, since the electromagnetic field must have continuous derivatives of all orders. To handle this difficulty, an knowing that the GTD results are extremely accurate when applied to large reflector antennas, the field first derivative is approximated by the average of the results obtained in Eq. 5.83. On doing so, one obtains

$$\frac{\partial}{\partial\theta_R} E_{GTD}(R_R,\theta_R)\Big|_{\theta_R\approx 0} \approx E_{GO}(R_R,\theta_R)\Big|_{\theta_R\approx 0} \left[\frac{D_{GO}(R_R,\theta_R)}{2} - \sqrt{\frac{R_R\,\rho_{1r}^R/\lambda}{R_R+\rho_{1r}^R}}\, e^{j\pi/4}\right]. \tag{5.84}$$

Finally, the substitution of Eq. 5.84 into Eq. 5.72 (and also applying Eq. 5.68) yields

$$\frac{\partial}{\partial\theta_R} |E_{GTD}(R_R,\theta_R)|\Big|_{\theta_R\approx 0} \approx |E_{GTD}(R_R,\theta_R)|\Big|_{\theta_R\approx 0} \left[D_{GO}(R_R,\theta_R) - \sqrt{\left|\frac{2\,R_R\,\rho_{1r}^R/\lambda}{R_R+\rho_{1r}^R}\right|}\right], \tag{5.85}$$

where the above result is valid for both Geometries I and III as long as the orientation of θ_R is defined accordingly to Figs. 5.9 and 5.11, respectively.

In order to evaluate Eq. 5.85, the value of $D_{GO}(R_R, \theta_R)$ must be obtained from the GO analysis of the subreflector radiation. However, the purpose of this formulation is to provide the necessary insights for the reduction of the backward subreflector spillover. The backward spillover is reduced by enforcing a large roll-off for the subreflector radiation (i.e., a large derivative of $|E_{GTD}(R_R, \theta_R)|$ near the reflection boundary), which can be accomplished by adjusting the values of R_R and ρ_{1r}^R inside the square-root term of Eq. 5.85. Hence, if this term is large, $D_{GO}(R_R, \theta_R)$ (which is generally bounded) can be neglected.

For both classical and shaped Geometries I and III, the value of R_R is obtained from the distance between the subreflector-edge point R to the observation point, and much can not be done about it. For the classical configurations studied in Chapter 4, ρ_{1r}^R can be obtained from Eqs. 4.41 and 4.42 by setting $\theta_F = \theta_E$, but no closed-form expression is available for it in a shaped geometry. In this case, however, ρ_{1r}^R can be estimated with a great precision. To do so, from Eq. 5.70, Figs. 5.9 and 5.11, noticing from Eq. 5.61 that $|E_F(R^+)| = |E_F(R^-)|$, and recalling that all geometries are specified with a uniform-phase aperture illumination, one obtains

$$\begin{aligned} \left|E_A^{GO}(\rho_A = D_M/2)\right| &= |E_{GO}(R_R = R_{RU}, \theta_R = 0)| \\ &= \left|E_F(R^-)\right| \left| \sqrt{\frac{\rho_{1r}^R}{R_{RU} + \rho_{1r}^R}} \sqrt{\frac{\rho_{2r}^R}{R_{RU} + \rho_{2r}^R}} \right| , \end{aligned} \tag{5.86}$$

where R_{RU} is the distance between the subreflector-edge point R and main-reflector-

edge point U (see Figs. 5.9 and 5.11). As the feed radiation towards the subreflector rim $[E_F(R^-)]$ and the aperture illumination at $\rho_A = D_M/2$ $[E_A^{GO}(\rho_A = D_M/2)]$ are both specified for the shaping procedure (see Sect. 5.3), then ρ_{1r}^R can be determined from Eq. 5.86 once R_{RU} and ρ_{2r}^R are known. The value of R_{RU} is obtained from Figs. 5.9, 5.11, and 5.13 as

$$R_{RU} = \frac{D_M \mp D_S}{2 \sin|\theta_2|}, \tag{5.87}$$

where the negative and positive signs correspond to Geometries I and III, respectively, and $\theta_2 < 0$ accordingly to the notation of Sect. 4.1. From the same figures, ρ_{2r}^R is directly given by

$$|\rho_{2r}^R| = \frac{D_S}{2 \sin|\theta_2|}, \tag{5.88}$$

where ρ_{2r}^R is positive and negative for Geometries I and III, respectively. In Eqs. 5.87 and 5.88, the value of θ_2 must be estimated (as its correct value is only determined after the antenna shaping is completed), which can be accomplished with the help of a similar classical geometry (used to start the shaping procedure) and Eq. 4.7. So, Eqs. 5.85–5.88 can be used to determine the required feed and aperture illumination to yield a small backward subreflector spillover (this will be demonstrated in Sect. 5.6).

To illustrate the accuracy of the formulation presented in this section, the classical feed/subreflector combination of Fig. 4.7b (CG III) is used as a case study, where $D_M = 100\lambda$. The subreflector illumination is provided by the RCF model

of Eq. 4.59 with $h = 8.8043$ ($F_{tap} = -11$ dB). In Fig. 5.14 the far-zone patterns (analyzed using the MoM technique developed in Chapter 2) at both E- ($\phi = 0°$) and H- ($\phi = 90°$) planes are depicted together with the associated GO field and the ITU specification given by Eq. 5.20. The ITU requirements are used once more as a reference for the antenna performance. From this figure (where $\theta = 0°$ corresponds to the feed boresight), it can be observed that at the shadow ($\theta \approx 30°$) and reflection ($\theta \approx 93°$) boundaries the respective fields are about 6 dB below the levels predicted by GO, according with Eqs. 5.55 and 5.68, respectively. It can also be observed that the feed spillover will cause the final antenna pattern to exceed the required envelope near $\theta \approx 30°$. However, the subreflector spillover does not present the same concerns, as the diffraction effects at the main-reflector rim will further reduce the subreflector radiation by an extra 6 dB near $\theta \approx 93°$ (the associated mechanisms are similar to those discussed in the present section).

The dB per radian value of the far-zone pattern roll-off near $\theta \approx 93°$ is obtained using

$$\frac{d}{d\theta}\left(20\ \log_{10}|E|\right) \;=\; -\,\frac{20\ \log_{10} e}{|E|}\ \frac{d|E|}{d\theta_R} \tag{5.89}$$

and Eq. 5.85, where $\log_{10} e \approx 0.434294$. Notice that a negative sign was incorporated in Eq. 5.89 as $d|E|/d\theta = -d|E|/d\theta_R$ (see Fig. 5.11). For the present classical configuration the value of $\rho_{1r}^{R} = -6.56\lambda$ is obtained from Eqs. 4.41 and 4.42 (calculated at point R). The value of $D_{GO}(R_R, \theta_R) \approx 0.3$ dB/degree near $\theta \approx 93°$ is obtained from Fig. 5.14. Finally, in the limit when $R_R \to \infty$ (at the far-zone region)

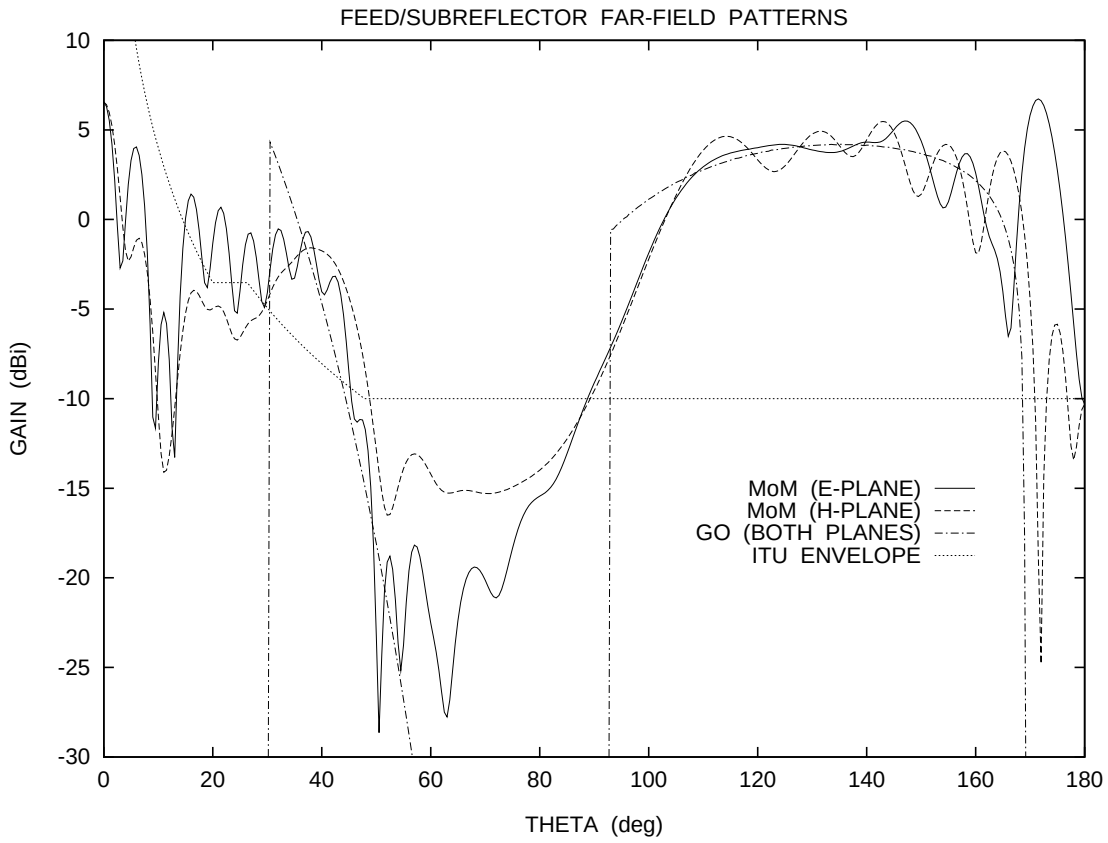

Figure 5.14: Far-Zone Patterns of the Feed/Subreflector Combination of Fig. 4.7b with $D_M = 100\lambda$, $D_S = D_B = 11.5\lambda$, $\ell_o = 60\lambda$, $|\theta_E| = 30°$, and Illuminated by a RCF Model with $F_{tap} = -11$ dB.

and from Eqs. 5.85 and 5.89 (transforming the values from radian to degree), the predicted value for the pattern roll-off is about 0.85 dB/degree, which is in excellent agreement with the results obtained in Fig. 5.14 at both E- and H-planes.

5.5 Impact of the Subreflector-Edge Diffraction on the Aperture Illumination

The diffraction effects in an axially-symmetric dual-reflector system preclude the accuracy of the GO results, specially when the reflector surfaces have small electrical dimensions. For large reflector surfaces, the diffraction effects related to the multiple bounces and subreflector blockage can be tremendously reduced through the use of the generalized classical (Figs. 4.1–4.4) or shaped (Figs. 5.3–5.6) geometries to decrease the sub- and main-reflector radiation towards the feed and subreflector, respectively. In Sect. 4.3, considerations about the blockage reduction for the different classical geometries were presented, and these results can also be applied to their shaped counterparts.

The blockage associated with the supporting struts is also an important effect in the antenna diffraction mechanism. However, it is not considered in this work. Nevertheless, it was verified in Sect. 4.6.2 that CG II (and, analogously, SG II) yields a highly efficient configuration with the feed located close to the subreflector, in which case the supporting struts may be replaced by a dielectric radome

attaching the subreflector directly to the feed. This section will concentrate only on the aperture-illumination degradation caused by the subreflector-edge diffraction (which is the most relevant factor for the antenna aperture illumination). The diffraction effects caused by the subreflector tip are ignored since they are generally negligible when compared to the ones produced by the subreflector edge [53].

The effects associated with the subreflector-edge diffraction were previously studied, for example, in Refs. [54]–[56]. It was observed that these effects produce a field tapering at the aperture region associated with the subreflector-edge illumination, precluding the achievement of a uniform field distribution and, consequently, decreasing the aperture efficiency. However, Eq. 5.7 indicates that this field tapering can be judiciously used to accomplish low sidelobe levels, which requires reduced aperture illumination at $\rho_A = D_B/2$ and $D_M/2$. The objective of the present section is then to study how the edge diffraction mechanism affects the aperture illumination (specially at the aperture rims), and how to establish an appropriate aperture distribution for the reflector-shaping procedure, in order to control the sidelobe envelope. This is done using the results of Sect. 5.4.2.

From the results of Sect. 5.4.2, the aperture electric field is represented as

$$\vec{E}_A(\rho_A) \;=\; \vec{E}_A^{GO}(\rho_A) \;+\; \vec{E}_A^{DIFF}(\rho_A)\;, \tag{5.90}$$

where $\vec{E}_A^{GO}(\rho_A)$ and $\vec{E}_A^{DIFF}(\rho_A)$ are the contributions from the GO aperture field and the subreflector-edge diffraction (after the reflection upon the main reflector),

respectively. Recalling that the classical and shaped geometries operate with a uniform phase distribution over the aperture, the subreflector-reflected wavefront amplitude is not changed after it reflects on the main-reflector surface. The same can be said about the rays diffracted by the subreflector edge striking the main reflector near the associated reflection boundary, as both reflected and diffracted rays propagate along the same direction (towards the main reflector) and generally the distance between the sub- and main-reflectors is considerably large (such that it can be assumed that both reflected and diffracted rays depart from the approximately same location). Under these circumstances (and near the subreflector-edge reflection boundary), the result of Eq. 5.68 can be applied to Eq. 5.90. For Geometries I and III (see Figs. 5.9 and 5.11, respectively) this results in:

$$|\vec{E}_A(\rho_A = D_M/2)| \approx \frac{1}{2}|\vec{E}_A^{GO}(\rho_A = D_M/2)| . \tag{5.91}$$

Likewise, for Geometries II and IV (see Figs. 5.10 and 5.12, respectively)

$$|\vec{E}_A(\rho_A = D_B/2)| \approx \frac{1}{2}|\vec{E}_A^{GO}(\rho_A = D_B/2)| , \tag{5.92}$$

One may observe at this point that a diffraction mechanism similar to the one studied in Sect. 5.4.2 also occurs at the main-reflector rim. However, the main-reflector-rim diffraction is implicitly included in the aperture-field integral that yields the far-zone radiation, and hence one does not need to account for it separately.

The sidelobe-envelope control through Eq. 5.7 depends also on the derivative of the electric field at the aperture rims. To handle this task (and recalling the results

of Sect. 5.4.2), one observes that if the axially-symmetric antenna is illuminated by a circularly-symmetric feed pattern then the GO aperture field will also be circularly symmetric and the following analysis can be reduced into a scalar problem (i.e., the amplitude of the GO aperture field does not depend on the plane of incidence). This is also true for the diffracted field, as long as its contribution is accounted for near the associated reflection boundary (see Sect. 5.4.2). So, following the same approach used to derive Eqs. 5.90–5.92, the derivative of the aperture-field complex amplitude with respect to ρ_A can be expressed (near the reflection boundary associated with the subreflector edge) as

$$\frac{d}{d\rho_A} E_A(\rho_A) \;=\; \frac{d}{d\rho_A} E_A^{GO}(\rho_A) \;+\; \frac{d}{d\rho_A} E_A^{DIFF}(\rho_A)\;. \tag{5.93}$$

The derivative of $E_A^{GO}(\rho_A)$ can be directly obtained from the GO aperture distribution. Here it is convenient to represent it in the form

$$\frac{d}{d\rho_A} E_A^{GO}(\rho_A) \;=\; E_A^{GO}(\rho_A)\;\; D_A^{GO}(\rho_A)\;. \tag{5.94}$$

For a classical configuration illuminated by the circularly-symmetric RCF model (Eq. 4.59) one obtains from Eq. 4.60 the closed-form $D_A^{GO}(\rho_A)$ expression

$$\begin{aligned} D_A^{GO}(\rho_A) \;=\; & \frac{[A_1\,(1+\cos\theta_F) \;-\; A_2\,\sin\theta_F]^2}{2\,F\,(e^2-1)\,(1+\cos\theta_F)} \left\{ -\,h\,\tan\theta_F \right. \\ & +\; \frac{1}{2}\left[\frac{1}{\sin\theta_F} \;-\; \frac{3\,(A_1\,\sin\theta_F \;+\; A_2\,\cos\theta_F)}{A_1\,(1+\cos\theta_F) \;-\; A_2\,\sin\theta_F} \right. \\ & \left. \left. +\; \frac{A_3\,\sin\theta_F \;+\; A_4\,\cos\theta_F}{A_3\,(1+\cos\theta_F) \;-\; A_4\,\sin\theta_F} \right] \right\}, \end{aligned} \tag{5.95}$$

where θ_F is given by Eqs. 4.57 and 4.58 and A_1, A_2, A_3, and A_4 are given by

Eqs. 4.52–4.55, respectively. For a shaped geometry with the proposed aperture illumination given by Eqs. 5.1 and 5.12 one obtains

$$D_A^{GO}(\rho_A) \;=\; \begin{cases} -\,2\,\alpha_B\,(\rho_A - \rho_{int})\;, & D_B/2 \le \rho_A \le \rho_{int}\;, \\ -\,2\,\alpha_M\,(\rho_A - \rho_{ext})\;, & \rho_{ext} \le \rho_A \le D_M/2\;, \\ 0\;, & \text{elsewhere}\;. \end{cases} \tag{5.96}$$

Furthermore, the derivative of $E_A^{DIFF}(\rho_A)$ in Eq. 5.93 can be rewritten as

$$\frac{d}{d\rho_A} E_A^{DIFF}(\rho_A) \;=\; \frac{d}{d\theta_R} E_A^{DIFF}(\rho_A)\;\frac{d\theta_R}{d\rho_A}\;, \tag{5.97}$$

where, using the same reasoning adopted to derive Eqs. 5.91 and 5.92,

$$\frac{d}{d\theta_R} E_A^{DIFF}(\rho_A) \;\approx\; \frac{\partial}{\partial\theta_R} E_{DIFF}(R_R,\theta_R)\,\Big|_{\theta_R\approx 0}\;, \tag{5.98}$$

the partial derivative of $E_{DIFF}(R_R,\theta_R)$ with respect to θ_R is given (after averaging the results at both sides of the reflection boundary) by the first term of Eq. 5.82, and R_R is the distance from point R to the main reflector, measured along the associated reflection boundary. Invoking differential-geometry concepts [57] and defining θ_R accordingly to Figs. 5.9–5.12, one can write

$$\lim_{\theta_R\to 0} \frac{d\theta_R}{d\rho_A} \;\approx\; \frac{1}{R_R}\;. \tag{5.99}$$

Hence, from Eqs. 5.72 (with E_{GTD} replaced by E_A), 5.82, 5.86, and 5.90–5.99 one finally obtains (in the limit when $\theta_R \to 0$)

$$\frac{d}{d\rho_A}\,|E_A(\rho_A)| \;\approx\; |E_A(\rho_A)|\,\left[D_A^{GO}(\rho_A) \;-\; \frac{2}{R_R}\,\Re\mathrm{e}\left(\sqrt{\frac{R_R\,\rho_{1r}^R/\lambda}{R_R+\rho_{1r}^R}}\;e^{j\pi/4}\right)\right]\;. \tag{5.100}$$

For Geometries I and III (Figs. 5.9 and 5.11, respectively) $R_R = R_{RU}$, the argument of the square-root term is always positive, and Eq. 5.100 can be rewritten as

$$\frac{d}{d\rho_A}|E_A(\rho_A = D_M/2)| \approx |E_A(\rho_A = D_M/2)| \left[D_A^{GO}(\rho_A = D_M/2) - \frac{1}{R_{RU}} \sqrt{\left| \frac{2\, R_{RU}\, \rho_{1r}^R/\lambda}{R_{RU} + \rho_{1r}^R} \right|} \right]. \quad (5.101)$$

For Geometries II and IV (see Figs. 5.10 and 5.12, respectively) $R_R = R_{RL}$ (where R_{RL} is the distance between points R and L), the argument of the square-root term is always negative, and Eq. 5.100 is rewritten as

$$\frac{d}{d\rho_A}|E_A(\rho_A = D_B/2)| \approx |E_A(\rho_A = D_B/2)| \left[D_A^{GO}(\rho_A = D_B/2) + \frac{1}{R_{RL}} \sqrt{\left| \frac{2\, R_{RL}\, \rho_{1r}^R/\lambda}{R_{RL} + \rho_{1r}^R} \right|} \right]. \quad (5.102)$$

As a case study, to confirm the validity of the formulation derived in this section, the results were applied to the CG III of Fig. 4.7b, originally with $D_M = 100\lambda$. Note that the feed/subreflector combination of this configuration was previously analyzed at the end of Sect. 5.4.2. The objective of the present example is to obtain the aperture electric field of this antenna (using the MoM formulation of Chapter 2) and verify how well the formulation of this section compares with the actual results. To only account for the contribution associated with the subreflector scattering to the aperture field, the aperture plane was placed close to the main reflector (see Fig. 5.15) and the main-reflector surface was continuously extended from $\rho_A = 0$ to 5.75λ and from $\rho_A = 50$ to 55λ (in order to reduce the effects associated with the

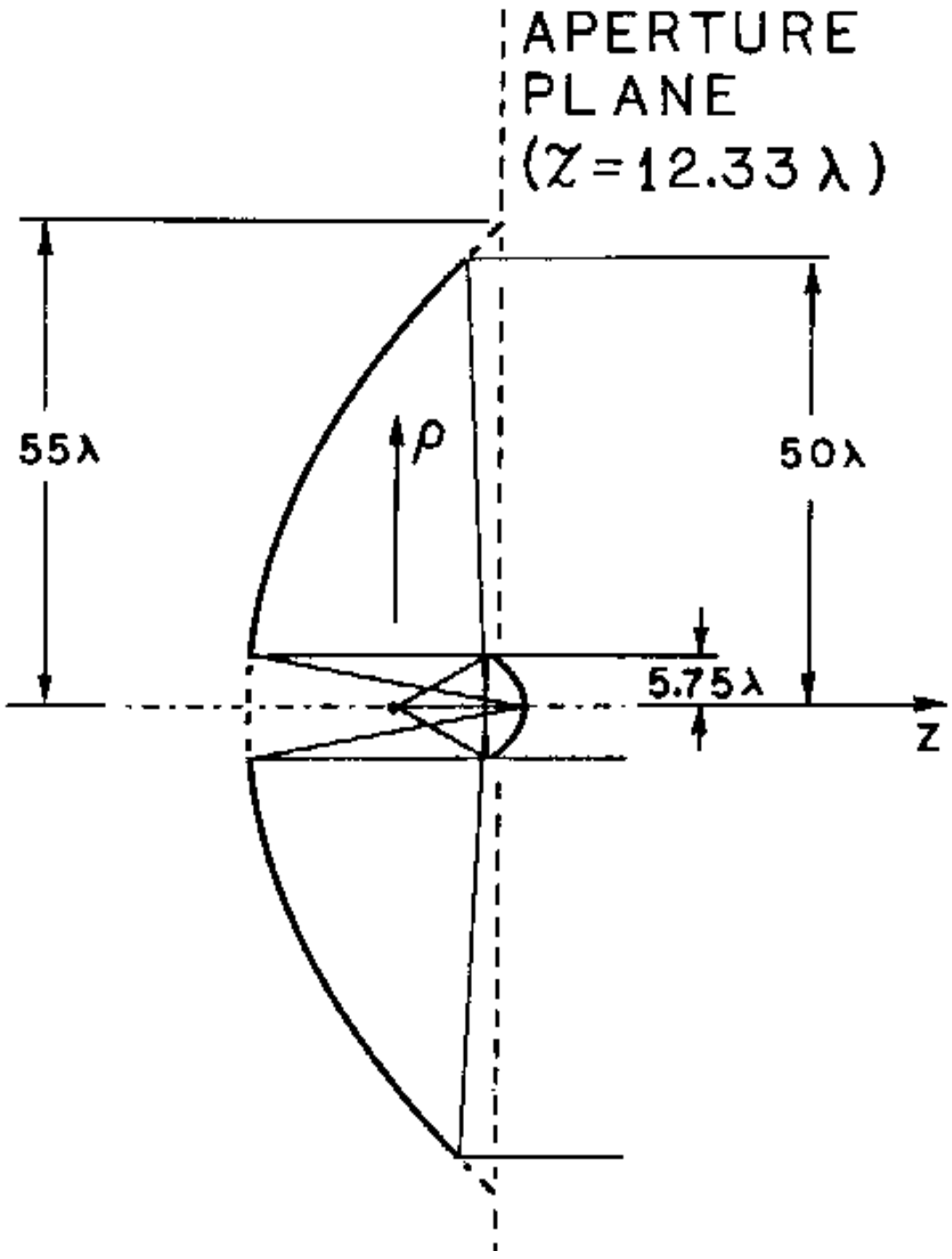

Figure 5.15: Geometry of the CG III with $D_S = D_B = 11.5\lambda$, $\ell_o = 60\lambda$, $|\theta_E| = 30°$, and Main Reflector Extended from $\rho_A = 0$ to 5.75λ and from $\rho_A = 50$ to 55λ.

main-reflector-edge diffraction). For similar reasons, the feed direct illumination towards the main reflector was removed. The antenna was excited by the the RCF model (Eq. 4.59) with $h = 8.8043$ ($F_{tap} = -11$ dB). Furthermore, only the main-reflector currents (obtained from the MoM analysis) were used to calculate the electric field at the aperture plane (located at $z = 12.33\lambda$, as illustrated in Fig. 5.15). As an $\hat{x}$-polarized RCF model is used, the aperture electric field is mainly linearly polarized in the $\hat{x}$-direction. In Fig. 5.16 the x-component of the aperture electric field is plotted for both E- ($\phi = 0°$) and H- ($\phi = 90°$) planes, together with the GO results (up to $\rho_A = 50\lambda$, the original main-reflector outer rim). The GO aperture phase is equal to 61.2° as $\ell_o = 60\lambda$, $\Phi_G = \pi$, and the present aperture plane is located at $z = 12.33\lambda$. From Fig. 5.16a one observes that the actual aperture illumination at $\rho_A = 50\lambda$ is about 6 dB below the GO one (for both E- and H-planes), as expected from Eq. 5.91. The oscillatory behavior of the aperture field is caused by the interference of the various diffraction contributions to the GO field (primarily the subreflector-edge diffraction). This interference is specially strong at the main-reflector center, where the whole subreflector-rim diffraction has a caustic.

The aperture-field amplitude slope at $\rho_A = 50\lambda$ is obtained from Eq. 5.101. For the present geometry, Eqs. 4.41–4.43 yield $\rho_{1r}^R = -6.56\lambda$ and $R_{RU} = 55.8\lambda$. From Eq. 5.95, $D_A^{GO}(\rho_A = 50\lambda) = -0.0598/\lambda$. Finally, from Eq. 5.101 the slope is predicted to be equal to -1.1 dB/λ, which is about the result observed in Fig. 5.16a.

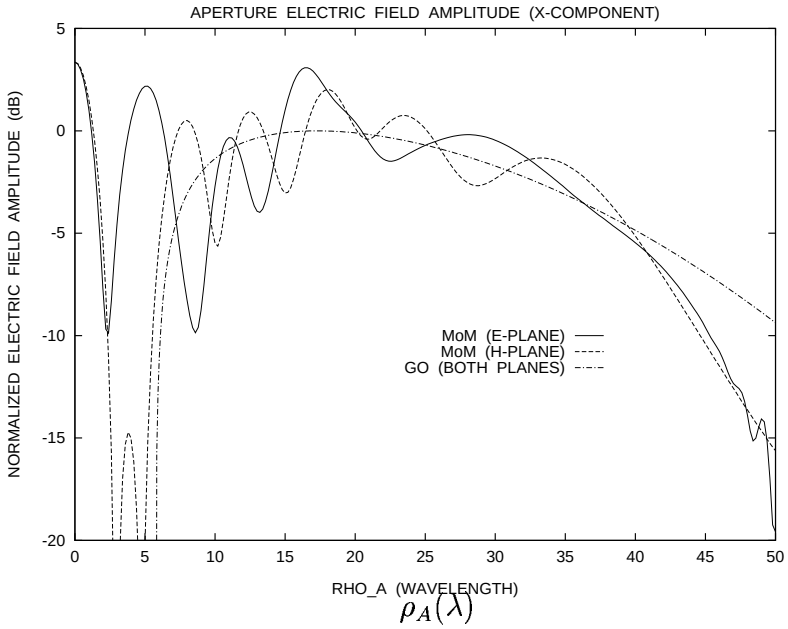

a) Aperture Electric Field Amplitude

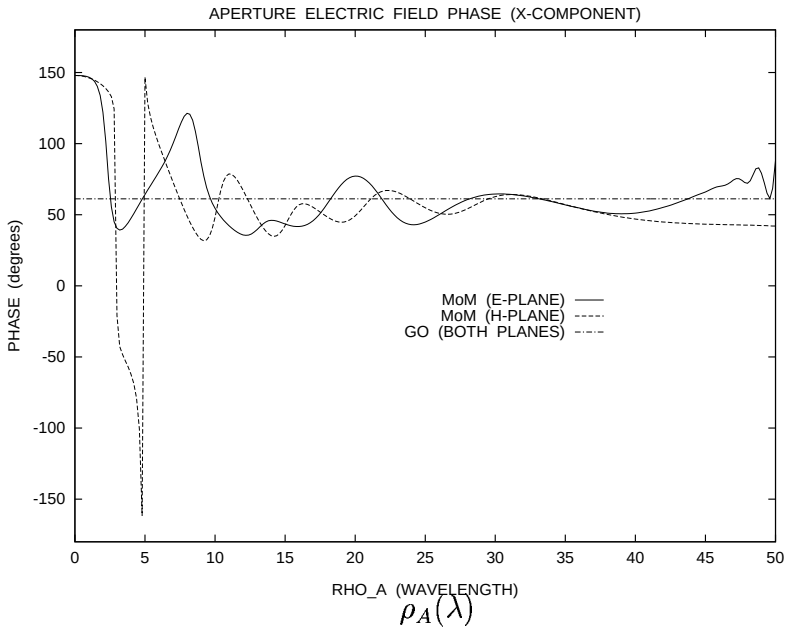

b) Aperture Electric Field Phase

Figure 5.16: Aperture Electric Field x-Component of the Antenna Depicted in Fig. 5.15, Illuminated by a RCF Model with $F_{tap} = -11$ dB.

5.6 Design of a Shaped Axially-Symmetric Cassegrain Configuration

In the present section the formulation described throughout this work is applied to the design of a representative axially-symmetric Cassegrain antenna (Geometry I). The main reflector is required to have $D_M = 100\lambda$ with an F/D ratio of about 0.3, in which case $\ell_o \approx 60\lambda$. In order to work in a realistic application, the design aims the satisfaction of the ITU requirements (Eq. 5.20) over at least 90% of the antenna radiation pattern, together with the maximum possible antenna efficiency.

5.6.1 Feed Structure

The design starts by determining the feed structure to be used. To provide a circularly-symmetric feed pattern, a corrugated horn is adopted [37]–[39]. Its dimensions are chosen such that the feed spillover must not increase the antenna pattern beyond the required envelope (as discussed in Sect. 5.4.1), while offering negligible blockage to the subreflector radiation. From Sect. 4.6.1, it was observed for the present Geometry-I configuration that the feed blockage is avoided by keeping the horn relatively far from the subreflector, in which case a relatively high-gain horn aperture must be used for proper subreflector illumination. The horn design (the details are beyond the scope of the present work) was accomplished with the help of Ref. [39] and the EFIE/MoM technique discussed in Chapter 3. The chosen

feed configuration is illustrated in Fig. 5.17, with a flare half-angle of 8° and an aperture diameter of 3λ. The flare corrugations are simulated by and anisotropic IBC (given by Eqs. 3.178 and 3.179 with $w = 0.05\lambda$, $\delta = 0.025\lambda$, and $\zeta = 0.27\lambda$), placed over the internal wall of the horn flare. The excitation is provided by the $\hat{x}$-polarized fundamental TE_{11} mode of the circular waveguide (diameter of 0.64λ), as discussed in Sect. 3.2.4 (the modal sources are located 2λ to the right of the waveguide end-wall). Another IBC (given by Eqs. 3.165 and 3.166) is placed over the waveguide end-wall to simulate a matched load for the feed. Although the IBC corrugation simulation precludes the accurate evaluation of the return loss (as observed in Sect. 3.6.2), in here the only concern regards to the radiation characteristics of the horn. The MoM analysis of the feed structure indicates that its phase center is located about 9.62λ away from the horn-flare vertex, as indicated in Fig. 5.17. For all following results to be shown, the coordinate-system origin is assumed at this location, with the z-axis aligned with the feed boresight direction ($\theta = 0$).

The feed far-zone pattern obtained from the MoM analysis (carried out with several dummy observation segments to avoid any resonance problem, as discussed in Sect. 3.2.5) is illustrated in Fig. 5.18. This figure also shows the ITU envelope (Eq. 5.20) and the pattern of the RCF model (Eq. 4.59) that better simulates the actual feed radiation ($h = 16$). This RCF model was the one discussed at the end of Sect. 5.4.1, where it was determined that $\theta_E \approx 30°$ in oder to provide the best

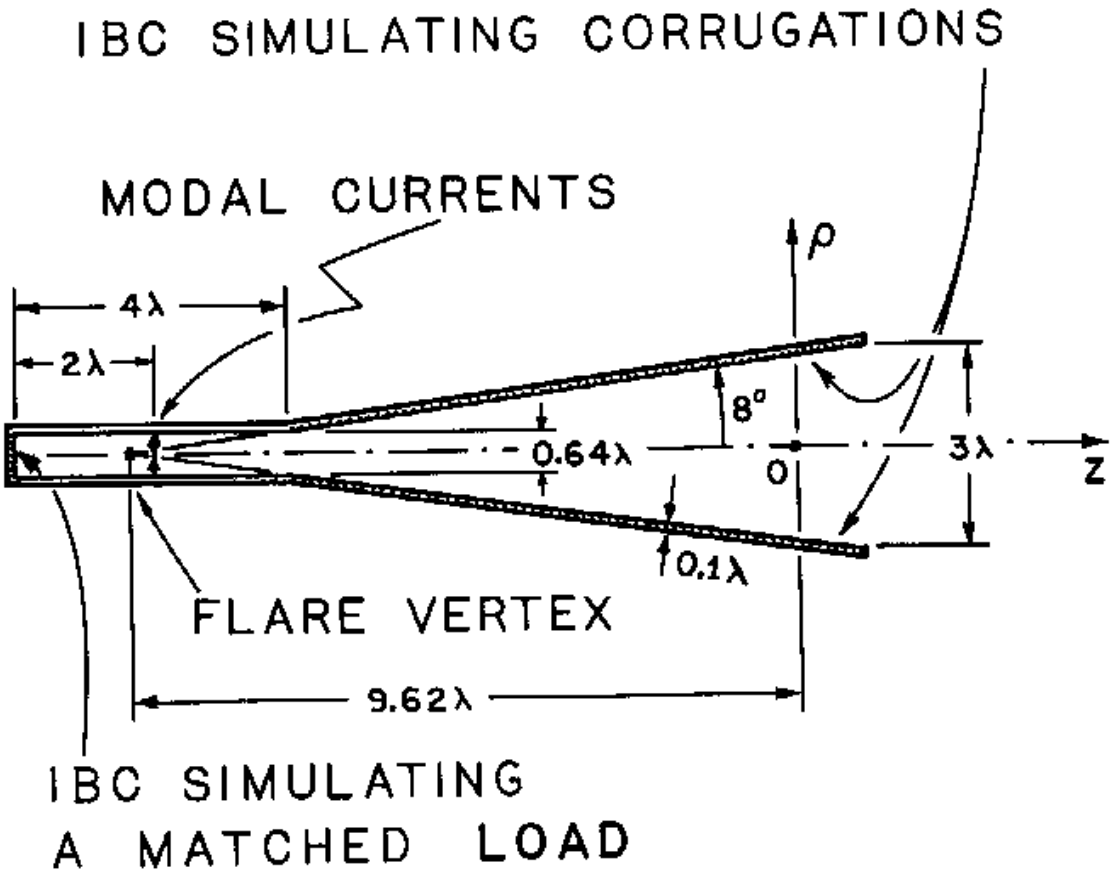

Figure 5.17: Geometry of the Cassegrain Horn Feed with Corrugations Simulated by an IBC.

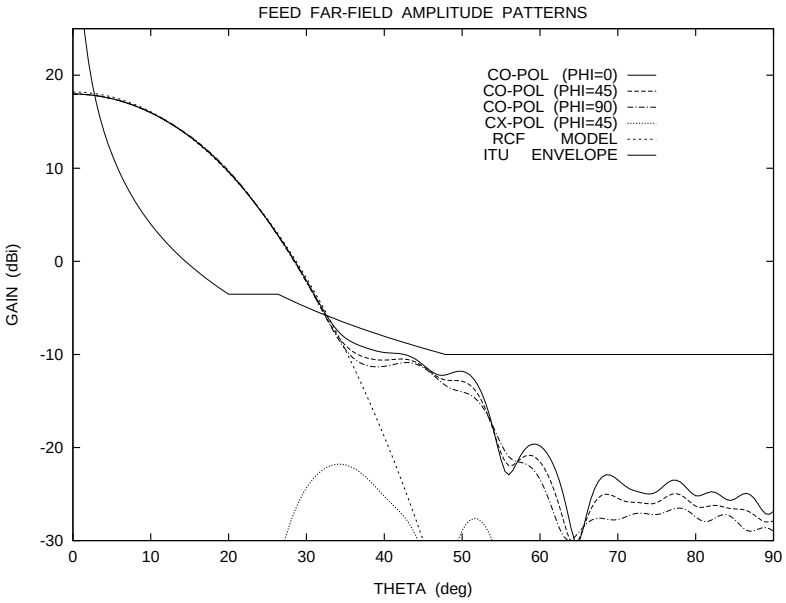

a) Amplitude

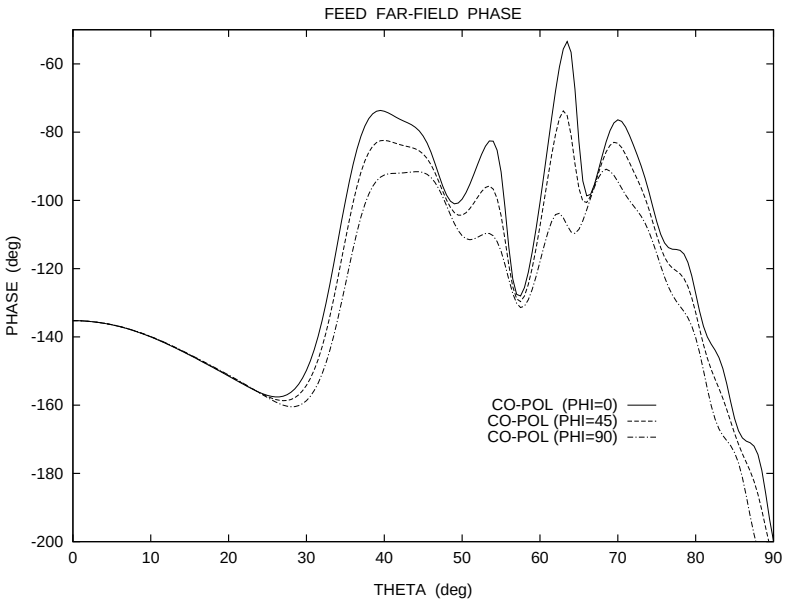

b) Phase

Figure 5.18: Far-Zone Patterns of the Horn Feed.

subreflector illumination with reduced feed spillover. However, from Fig. 5.18 one notices that the actual feed radiation is uncomfortably close to the ITU envelope in the region $30° < \theta < 50°$, which may create envelope-violation difficulties when the feed spillover is combined with the dual-reflector scattering. To provide some margin against these difficulties, the subreflector edge is then specified at $\theta_E = 35°$ ($F_{tap} = -27.7$ dB). Also, notice that Eq. 5.55 indicates that the subreflector-edge diffraction will provide a 6 dB drop on the feed spillover at $\theta = 35°$.

5.6.2 Classical Dual-Reflector Geometry

The best starting point for the reflector design process is from a generalized classical geometry, for which closed-form design equations are available in Chapter 4. At the present stage, the subreflector and blockage diameters (D_S and D_B, respectively) are still undetermined. Similarly as done in Sect. 4.6.1, with $D_M = 100\lambda$, $\ell_o = 60\lambda$, $\theta_E = 35°$, $F_{tap} = -27.7$ dB, and assuming $D_S = D_B$, the best efficiency η (around 61%) was obtained for $10\lambda < D_S < 30\lambda$. This efficiency is unnecessarily small and will be increased later by shaping the reflector surfaces. Bearing this in mind, one notices that the present feed offers a highly tapered illumination towards the subreflector edge, which reduces the subreflector effective area. Although it is desirable to use the smallest possible subreflector (to reduce the aperture blockage), in this case a $D_S = 15\lambda$ will be selected in order to increase the subreflector effective area and hence allow more control of its scattering. Furthermore, to accomplish

the largest possible area for the illuminated aperture, $D_B = D_S$. The generalized classical geometry corresponding to the above dimensions is obtained from Sect. 4.2 and illustrated (in scale) in Fig. 5.19 together with the horn feed. To enhance the front-to-back ratio of the antenna pattern, the central portion of the main reflector (represented by a dashed line in Fig. 5.19) is closed by extending the corresponding surface. To reduce the numerical burden of the MoM analysis, the circular waveguide of the feed structure was not extended through the main-reflector surface and its geometry remains the one illustrated in Fig. 5.17. Accordingly to GO, it can be observed from Fig. 5.19 that the feed aperture does not block the subreflector-reflected rays. However, the several diffraction mechanisms will ultimately produce electromagnetic radiation towards the feed.

To better understand the radiation characteristics of the antenna, its analysis (always applying the MoM technique) is conducted below on an incremental basis in order to identify the origin of each diffraction mechanism. The feed far-zone radiation was already covered in Sect. 5.6.1. The next step is to analyze the feed/subreflector combination. Two analysis are performed: one with the actual horn feed and another using the RCF model (RCF/subreflector), in order to determine the diffraction effects associated with the subreflector illumination upon the feed structure. The results are shown in Fig. 5.20. The discrepancies observed at the subreflector shadow region ($\theta < 35°$) between Figs. 5.20a and 5.20b are due to the fact that the RCF model does not satisfy Maxwell's equations [58] (as previously

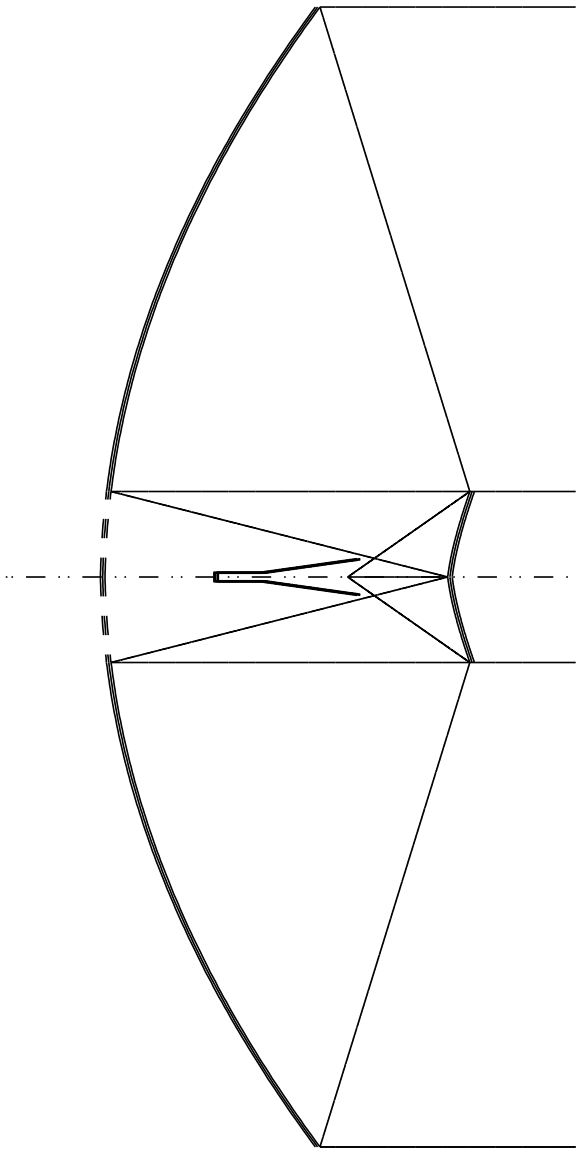

Figure 5.19: Classical Configuration (CG I) with $D_M = 100\lambda$, $D_S = D_B = 15\lambda$, $\ell_o = 60\lambda$, and $\theta_E = 35°$.

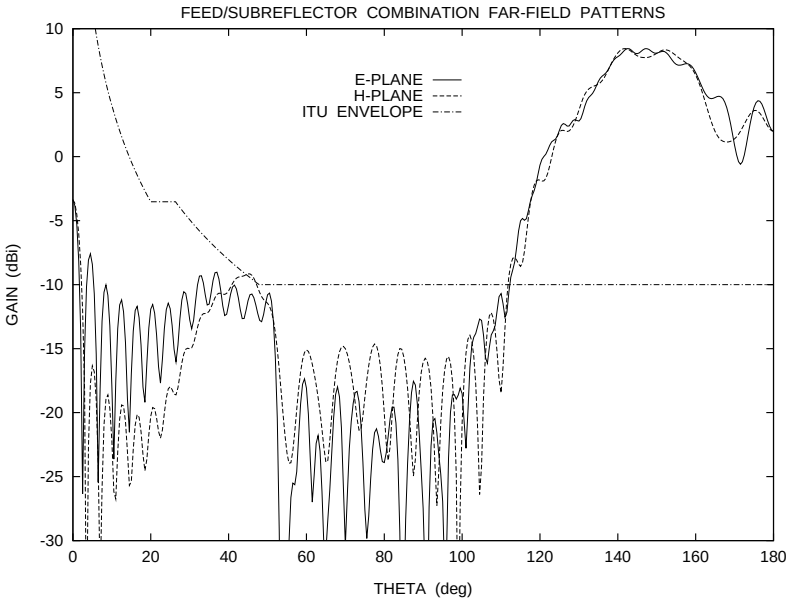

a) With the Horn Feed

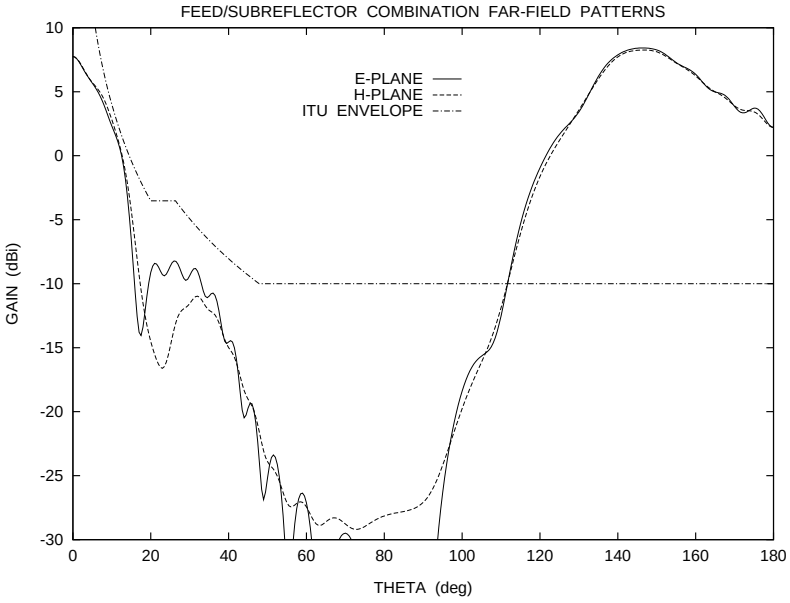

b) With the RCF Model

Figure 5.20: Far-Zone Patterns of the Classical Feed/Subreflector Combination at the E- ($\phi = 0°$) and H- ($\phi = 90°$) Planes.

mentioned in Sect. 2.4). Consequently, when its field is added to the one radiated by the induced subreflector currents, the result is grossly incorrect behind the subreflector. Nevertheless, the RCF/subreflector combination has enough accuracy at regions where the feed illumination is negligible or not present, as noticed from the results at the subreflector reflection region ($107° \leq \theta \leq 180°$). The discrepancies around $\theta = 180°$ between Figs. 5.20a and 5.20b are associated with the feed blockage, which is not considered when the RCF model is used. It can also be observed that the feed ($\theta = 35°$) and subreflector ($\theta = 107°$) spillovers do not present great concerns to the envelope requirements for this configuration. A significant observation from the present results is the approximately -15 dBi radiation envelope over $60° < \theta < 100°$ in Fig. 5.20a. Since the feed pattern over this region is below -22 dBi (see Fig. 5.18a), the level increase on going from Fig. 5.20b to Fig. 5.20a is primarily caused by the subreflector scattering towards the feed external wall (specially for the H-plane, as expected, since the electric field is tangent to the feed external surface at this plane).

Similarly to what as done at the end of Sect. 5.5, Fig. 5.21 shows the $\hat{x}$-polarized aperture electric field of the present configuration at both E- and H-planes, where the amplitude results are normalized with respect to the peak of the GO aperture electric-field amplitude (9.69×10^{-3} V/λ in the present case). The analysis was performed with the RCF model (to remove the feed blockage) and only the main-reflector induced currents (calculated from the MoM analysis) were used to obtain

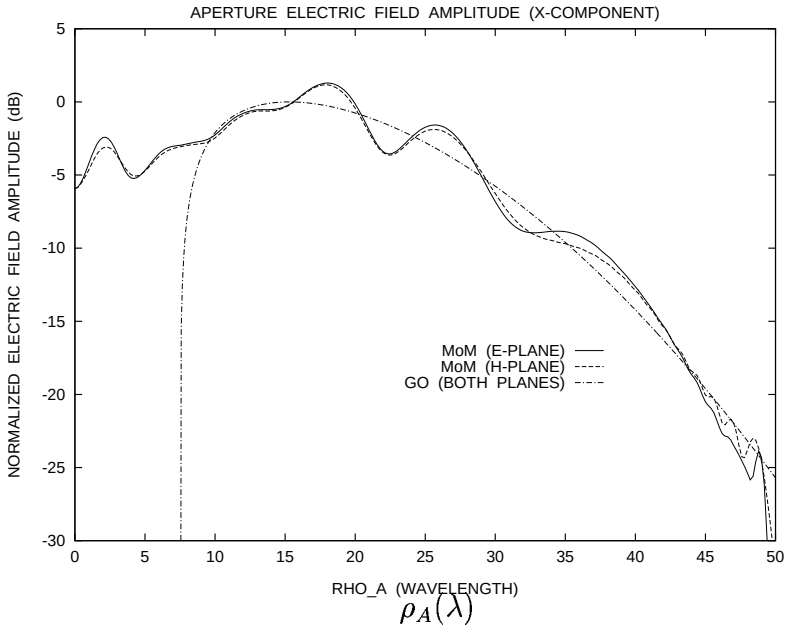

a) Aperture Electric Field Amplitude

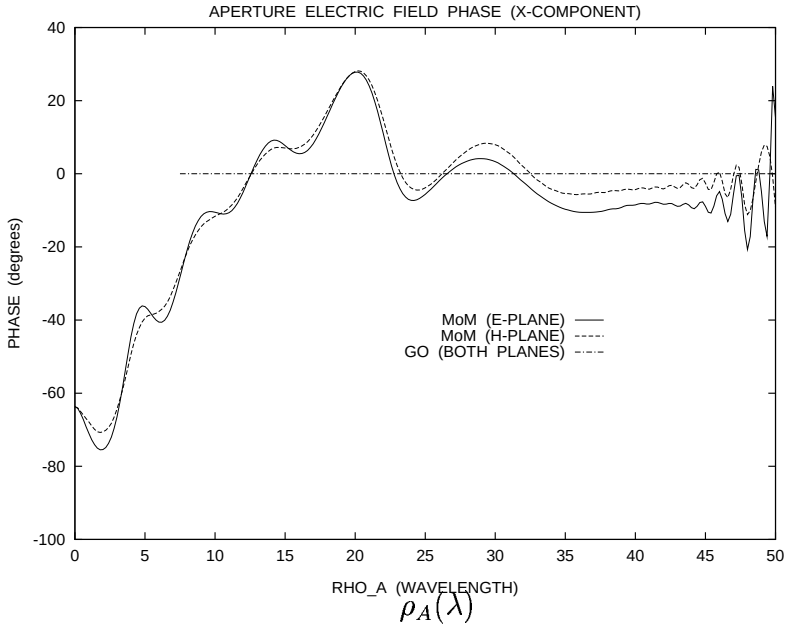

b) Aperture Electric Field Phase

Figure 5.21: Aperture Electric Field x-Component of the Classical Geometry in the E- ($\phi = 0°$) and H- ($\phi = 90°$) Planes.

the aperture field (located at $z = 0$). In this example, as the main reflector was not extended beyond $\rho_A = 50\lambda$, oscillations caused by the main-reflector-edge diffraction are present near $\rho_A = 50\lambda$. The GO aperture phase is equal to 0°, as $\ell_o = 60\lambda$ and $\Phi_G = 0$. The results show the poor aperture illumination provided by the classical geometry, which causes the low antenna efficiency ($\eta \approx 61\%$, from GO). From Eq. 5.101 [where $\rho_{1r}^R = 9.08\lambda$, $R_{RU} = 44.49\lambda$, and $D_A^{GO}(\rho_A = 50\lambda) = -0.149/\lambda$ for this geometry] the roll-off of the aperture illumination at $\rho_A = 50\lambda$ is predicted around -2 dB/λ, which is about the result obtained from Fig. 5.21a (averaging the oscillations).

The next step is the analysis of the complete geometry (see Fig. 5.19). The antenna far-zone patterns are shown in Figs. 5.22 and 5.23, where the co- and cross-polarizations are defined accordingly to Ludwig Third definition [45]. In Fig. 5.22 the radiation patterns are plotted for $\theta < 20°$, together with the GO aperture pattern (obtained from Eq. 4.62) and the ITU envelope. As previously mentioned in this section, the discrepancies observed between Figs. 5.22a and 5.22b are primarily caused by the fact that the RCF model violates Maxwell's equations. From Fig. 5.22a, the antenna gain is 47.64 dBi ($\eta = 59\%$), which is approximately equal to the gain obtained from the GO aperture radiation (47.83 dBi, $\eta = 61\%$). Actually, Fig. 5.22a shows that the GO results are almost identical to the MoM ones up to the second sidelobe region ($\theta < 4°$). As previously discussed at the end of Sect. 5.2, the low aperture illumination at $\rho_A = 50\lambda$ (see Fig. 5.21) reduces the first

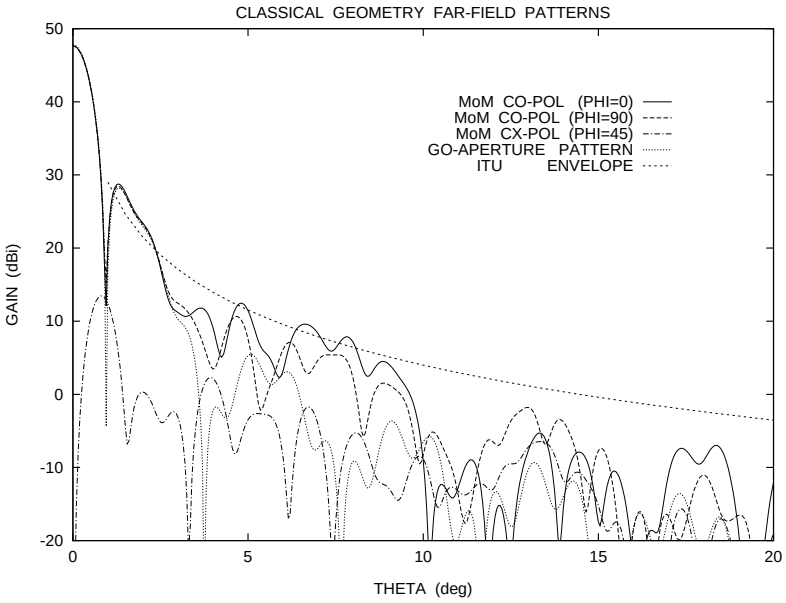

a) With the Horn Feed

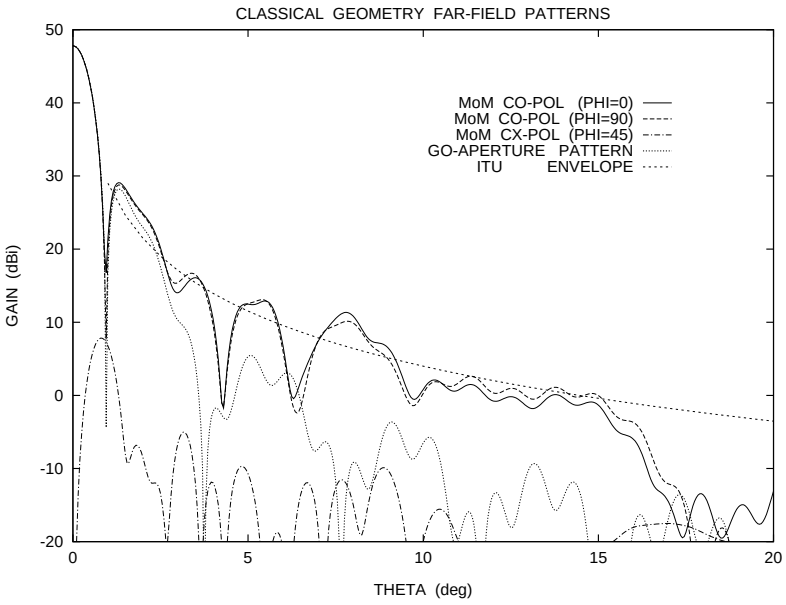

b) With the RCF Model

Figure 5.22: Far-Zone Patterns of the Classical Geometry at $0° \leq \theta \leq 20°$.

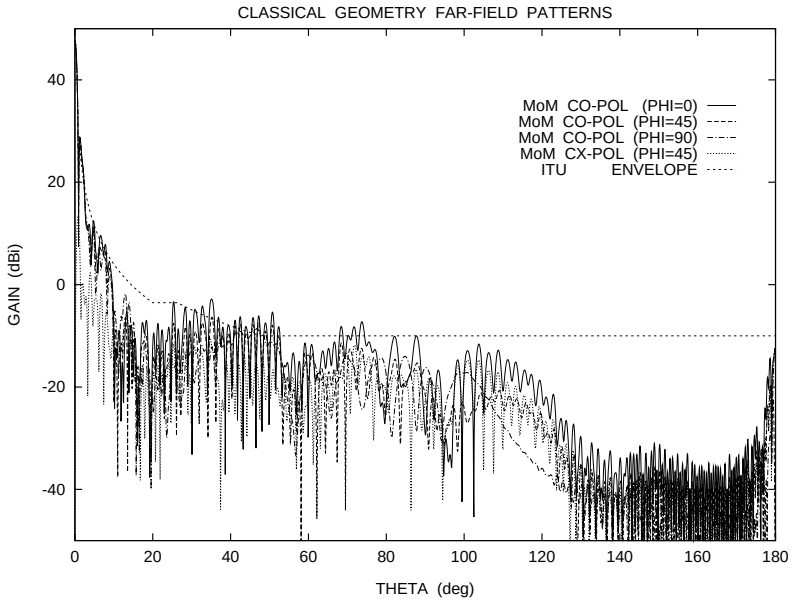

a) With the Horn Feed

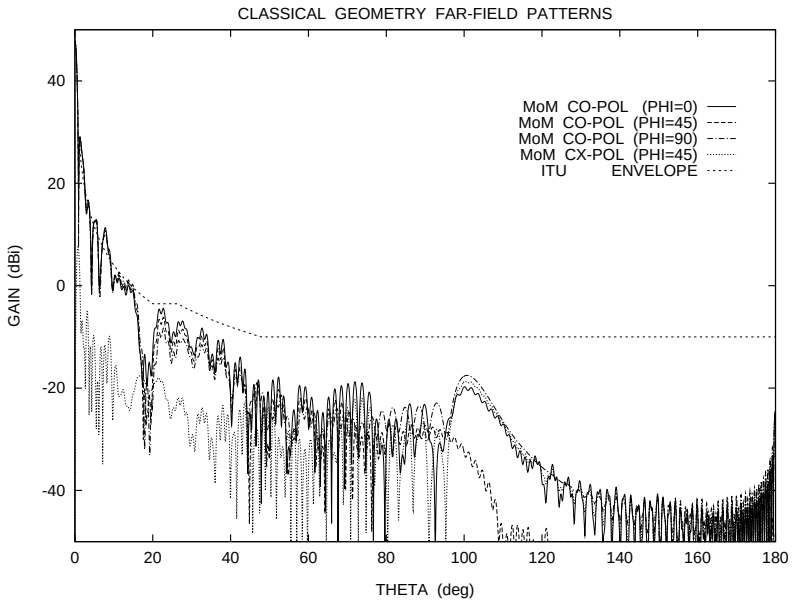

b) With the RCF Model

Figure 5.23: Far-Zone Patterns of the Classical Geometry at $0° \leq \theta \leq 180°$.

sidelobe level (about 19 dB below the main-beam level) almost down to the ITU envelope. However, this is accomplished in association with an extremely reduced aperture efficiency, which is not tolerable. Furthermore, Fig. 5.22a shows that the cross-polarization peak is about 34 dB below the main beam, which is approximately the polarization isolation provided by the corrugated horn (see Fig. 5.18a). In Fig. 5.23 the radiation patterns over the complete θ-range are plotted together with the ITU envelope. It can be observed from this figure that, as expected from Fig. 5.20a, the feed and subreflector spillovers do not significantly violate the envelope requirements. Furthermore, the results of Figs. 5.20b and 5.23b (where the RCF model is used) indicate that the subreflector edge diffracts the main-reflector radiation (with a stronger effect at the E-plane, as expected), which increases the antenna radiation levels up to -20 dBi over $60° < \theta < 100°$. This subreflector diffraction and the scattering by the feed structure (previously determined around -15 dBi) add to about -11 dBi over the corresponding region, as observed from Fig. 5.23a.

5.6.3 Shaped Dual-Reflector Geometry with a Uniform Aperture Illumination

The classical geometry analyzed in the previous section has low efficiency as its major drawback. This is caused by its poorly illuminated aperture. The aperture illumination must then be improved, which is accomplished by shaping both reflec-

tor surfaces to provide an almost uniform illumination over the unblocked aperture region ($D_B/2 \leq \rho_A \leq D_M/2$). However, this arouses some concerns about the required envelope specifications as the higher illumination of the aperture edges will consequently increase the subreflector spillover and the wide-angle radiation levels. To better understand these effects, the present section concentrates on the analysis of a shaped configuration with a prescribed uniform field distribution over its unblocked aperture area, to provide the maximum possible efficiency. The analysis is carried out in a step-by-step basis, similarly to Sect. 5.6.2.

The aperture illumination is specified by Eqs. 5.1 and 5.12 with $f_B = f_M = 1$ and $f'_B = f'_M = 0$. Consequently, $\alpha_B = \alpha_M = 0$, $\rho_{int} = D_B/2$, and $\rho_{ext} = D_M/2$ from Eqs. 5.13–5.16. The shaped configuration is obtained from the formulation of Sect. 5.3 with $f(\rho_A)$ given by Eq. 5.12 (under the above circumstances), $g(\theta_F)$ given by the circularly-symmetric RCF model (Eq. 4.59) with $h = 16$, $D_M = 100\lambda$, $\theta_E = 35°$, and $D_B = 15\lambda$. The desired value of $D_S = 15\lambda$ is accomplished by setting $\ell_o = 57.54\lambda$ and $V_S = 7.52\lambda$ (starting from the classical geometry adopted in Sect. 5.6.2). Similarly to what as done in Sect. 5.6.2, the central main-reflector region is generated by quadratic interpolation over the last three main-reflector points (located near $\rho_A = 7.5\lambda$). The resulting configuration is illustrated (in scale) in Fig. 5.24. The predicted GO efficiency of the present geometry is $\eta = 98\%$.

The results of the MoM analysis of the feed/subreflector combination are shown in Fig. 5.25 for both E- and H-planes. The general characteristics of these results

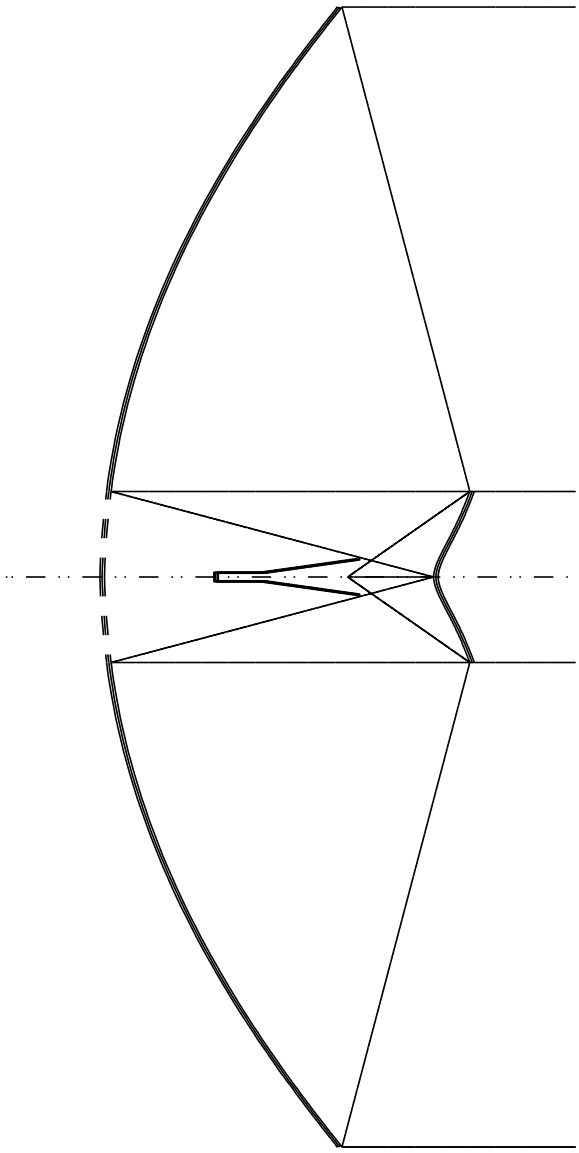

Figure 5.24: Shaped Configuration (SG I) for a Blocked Aperture Uniformly Illuminated with $D_M = 100\lambda$, $D_S = D_B = 15\lambda$, $\ell_o = 57.54\lambda$, $\theta_E = 35°$, and $V_S = 7.52\lambda$.

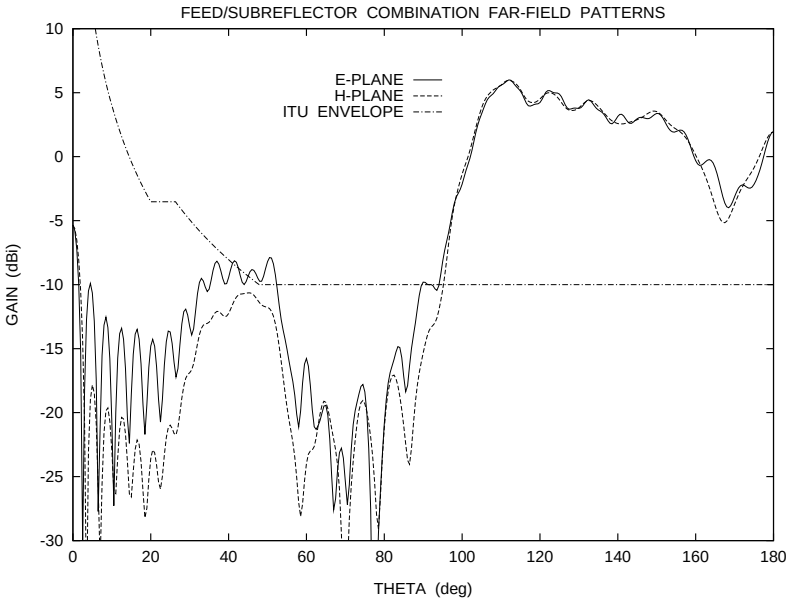

a) With the Horn Feed

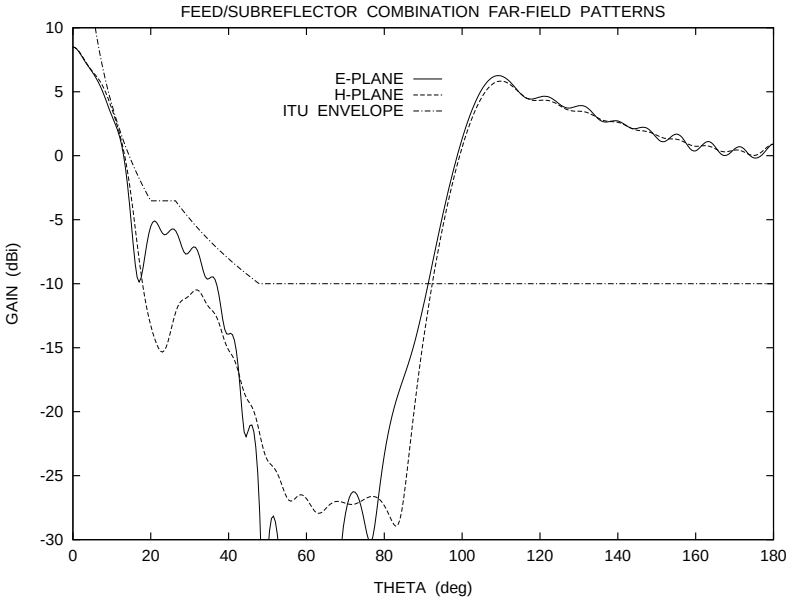

b) With the RCF Model

Figure 5.25: Far-Zone Patterns of the Shaped (Uniform Illumination) Feed/Subreflector Combination at the E- ($\phi = 0°$) and H- ($\phi = 90°$) Planes.

are as discussed in Sect. 5.6.2 for Fig. 5.20, except for what follows. Now one observes from Fig. 5.25 that the subreflector spillover around the associated reflection boundary ($\theta = 105°$) will increase the antenna pattern beyond the required envelope at this region. Although the main-reflector-edge will provide an extra 6 dB taper to the subreflector radiation (the associated mechanisms are similar to those discussed for the subreflector-edge diffraction throughout Sect. 5.4), since the feed/subreflector radiation levels at $\theta = 105°$ are about 6 dBi (see Fig. 5.25) the subreflector-spillover contribution is still expected to violate by approximately 10 dB the required envelope (which enforces a maximum of -10 dBi at this region). Also, as the feed radiation is uniformly distributed over the unblocked aperture region, the subreflector scattering towards the feed external wall is slightly reduced (compare Figs. 5.20a and 5.25a at $60° < \theta < 90°$).

Figure 5.26 shows the $\hat{x}$-polarized aperture electric field of the present configuration on both E- and H-planes, where the results are normalized with respect to the peak of the GO aperture electric-field amplitude (4.98×10^{-3} V/λ for this configuration). The MoM analysis of the aperture fields was conducted in the same way explained in Sect. 5.6.2 (the aperture plane is at $z = 0$ and the RCF model is employed). Again, oscillations are observed for the aperture electric field near $\rho_A = 50\lambda$, which are caused by the main-reflector-edge diffraction. The GO aperture phase is equal to 166°, as $\ell_o = 57.54\lambda$ and $\Phi_G = 0$. For the present configuration, it is determined that $\rho_{1r}^R = -44.38\lambda$ and $R_{RU} = 43.95\lambda$, indicating that

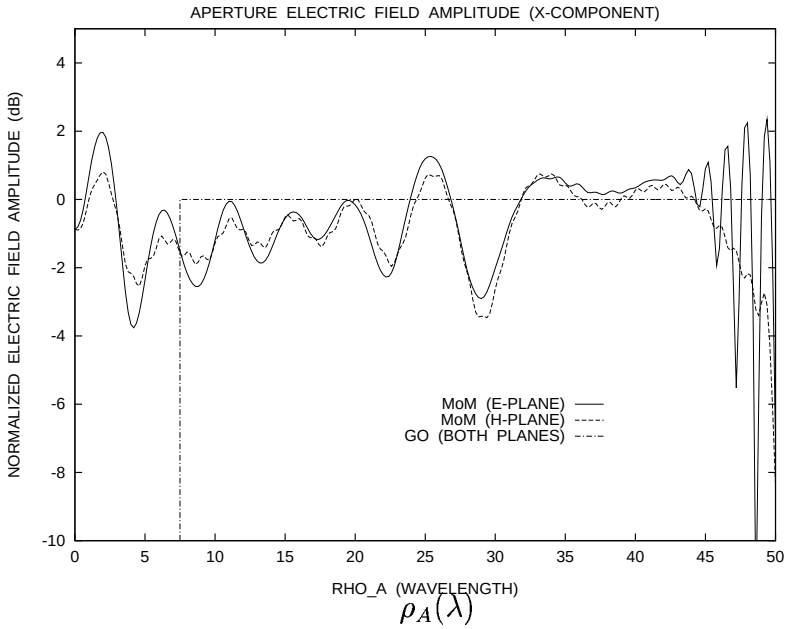

a) Aperture Electric Field Amplitude

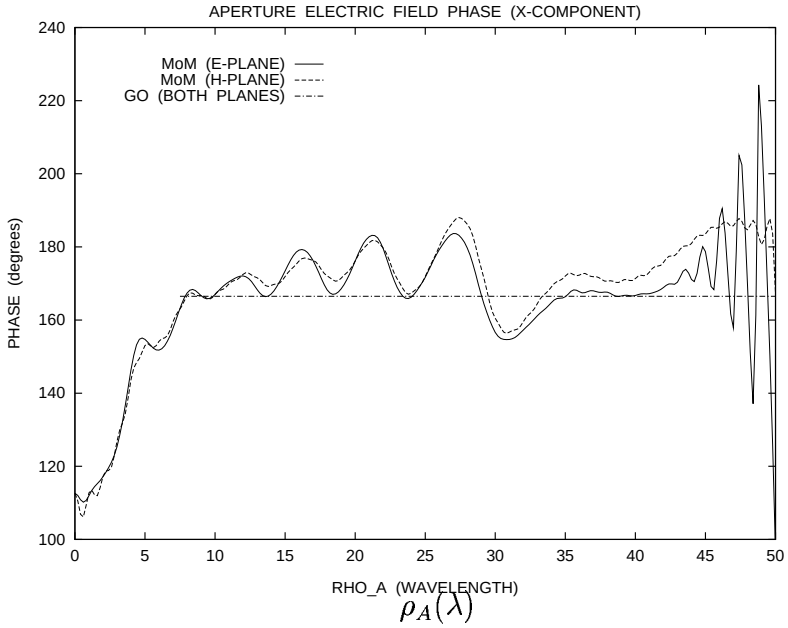

b) Aperture Electric Field Phase

Figure 5.26: Aperture Electric Field x-Component of the Shaped Geometry (Uniform Illumination) in the E- ($\phi = 0°$) and H- ($\phi = 90°$) Planes.

the subreflector caustic in the plane of incidence is extremely close to the back of the main reflector. As the GO and GTD approximations are violated close to a caustic, Eq. 5.101 can not be used to predict the aperture-illumination roll-off. The presence of this caustic close to the main reflector surface can be understood from Eq. 5.86. As the feed illumination towards the subreflector edge is extremely low and the GO shaping requires a uniform aperture illumination, the term $R_{RU} + \rho_{1r}^{R}$ must tend to zero in Eq. 5.86.

The analysis of the complete geometry illustrated in Fig. 5.24 is now conducted. The far-zone patterns of the antenna are shown in Figs. 5.27 and 5.28. In Fig. 5.27 the radiation patterns are plotted over $\theta < 20°$, together with the GO aperture pattern (obtained from Eq. 4.62) and the ITU envelope. Once more, the RCF results in Fig. 5.27b violate Maxwell's equations. From Fig. 5.27a, the antenna gain is 49.44 dBi ($\eta = 89\%$), corresponding to an efficiency 9% below the one obtained from the GO analysis. Most of this difference in efficiency is caused by the backward subreflector-spillover losses, which are not present in the GO analysis. Nevertheless, one observes from the same figure that the GO aperture pattern is capable of predicting extremely well the initial sidelobes of the antenna radiation. Comparing Figs. 5.22a and 5.27a, it is also noticed that the uniform aperture illumination provides a narrower half-power beam width ($\theta_{HPBW} \approx 0.3°$) and a higher first-sidelobe level (32.97 dBi, about 16.5 dB down the main-beam level) with respect to the classical geometry. However, the ITU requirements are still met over 90%

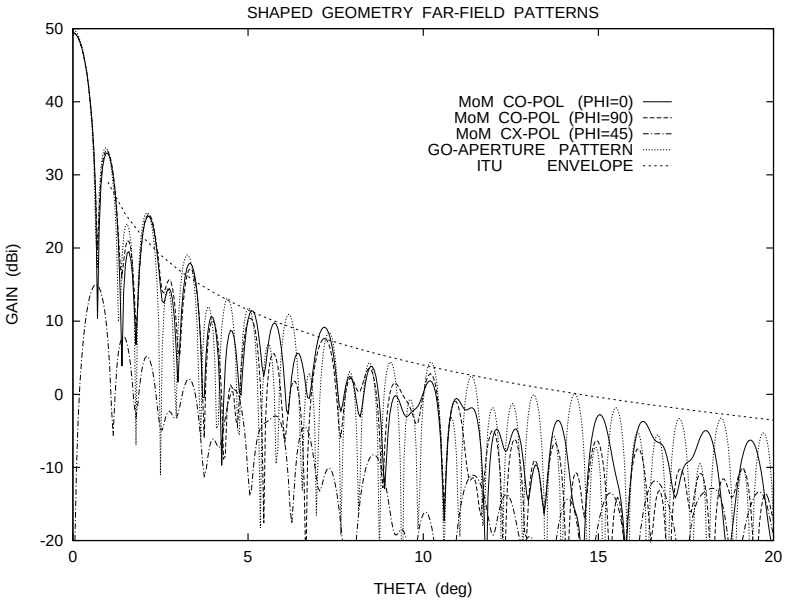

a) With the Horn Feed

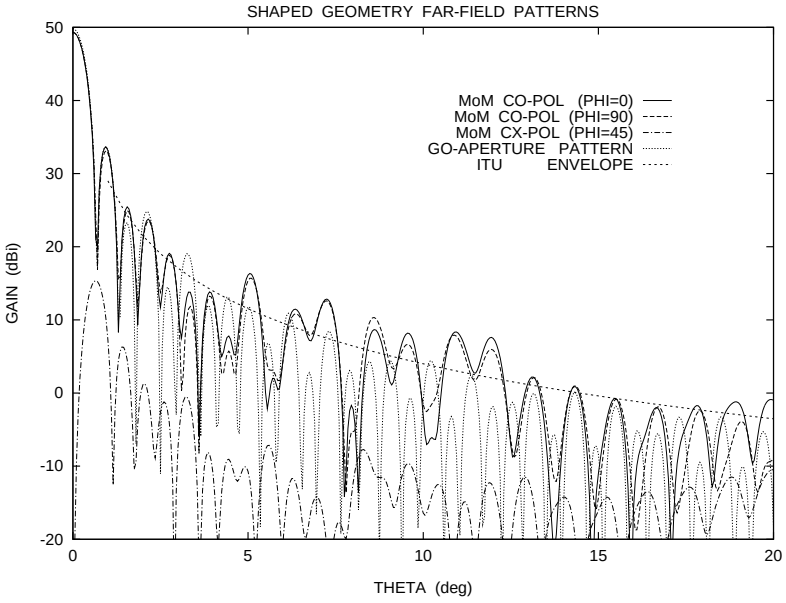

b) With the RCF Model

Figure 5.27: Far-Zone Patterns of the Shaped Geometry (Uniform Illumination) at $0° \leq \theta \leq 20°$.

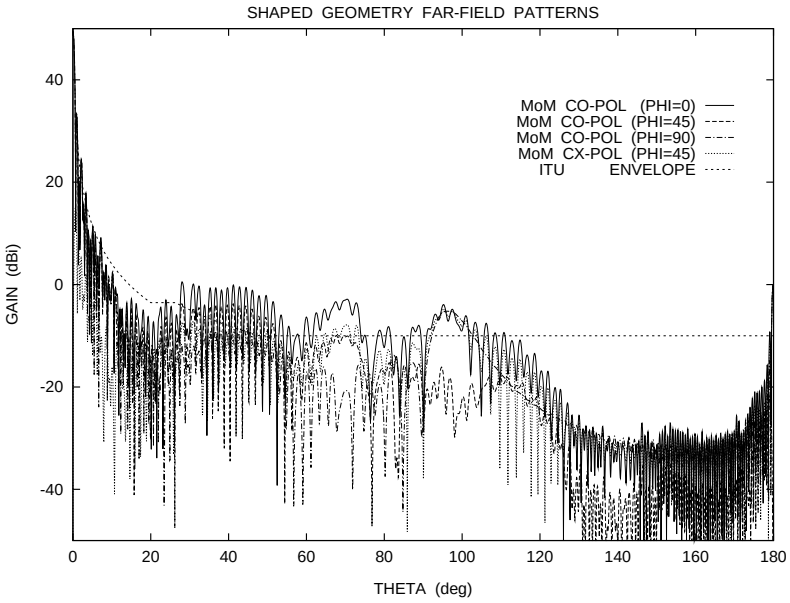

a) With the Horn Feed

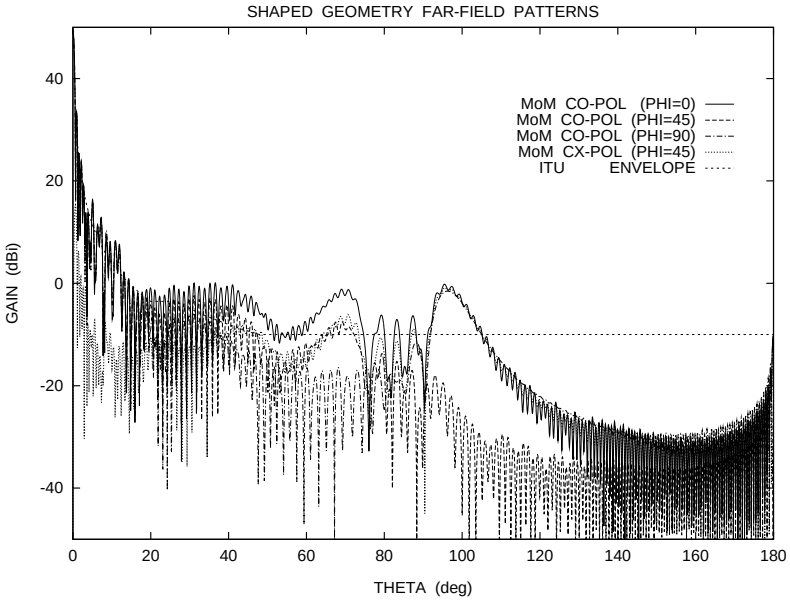

b) With the RCF Model

Figure 5.28: Far-Zone Patterns of the Shaped Geometry (Uniform Illumination) at $0° \leq \theta \leq 180°$.

of the radiation pattern shown in Fig. 5.27a. The cross-polarization peak is still 34 dB below the main beam. The pattern over the complete θ-range is shown in Fig. 5.28. As expected from the previous discussion of Fig. 5.25, it is observed from Fig. 5.28 that the feed spillover causes an approximate 10 dB violation of the required envelope around $\theta = 95°$. Furthermore, Figs. 5.25b and 5.28b (where the RCF model is used) indicate that the subreflector edge diffracts the main-reflector radiation (with a stronger effect at the E-plane, as expected), increasing the pattern levels up to about 0 dBi over $50° < \theta < 80°$. As this effect is much stronger than the one associated with the subreflector scattering towards the feed external wall (see Fig. 5.25), the results of Figs. 5.28a and 5.28b are practically identical over the corresponding region.

5.6.4 Final Shaped Dual-Reflector Geometry Design

The results of the previous section indicate that, although the uniform aperture illumination provides a higher efficiency, the subreflector spillover and the main-reflector radiation towards the subreflector edge preclude the accomplishment of the required sidelobe envelope. A new shaped-reflector configuration must then be obtained by specifying its aperture illumination in order to reduce the above mentioned effects while providing a satisfactory antenna efficiency. In this section, the formulation presented throughout this work is adopted to this task. On doing so, some estimates need to be performed and their results are then compared to the

actual values, which are obtained *after* the final design and analysis of the present configuration.

The subreflector spillover is reduced by implementing a higher roll-off of the subreflector radiation directed towards the main-reflector rim. From Eq. 5.85, one observes that this could be accomplished by allowing $R_{RU} + \rho_{1r}^R \to 0$. However, this condition places the subreflector caustic near the main-reflector surface (as discussed in Sect. 5.6.3), and the GTD approximation used to derive Eq. 5.85 is violated (near the caustic). So, the alternative approach (which will be proven to be the correct choice) is to increase the magnitude of ρ_{1r}^R (see Eq. 5.85). Physically, this can be understood as moving the caustic associated with ρ_{1r}^R away from the subreflector, in which case the rays reflected by the subreflector near point R leave this surface almost parallel to each other. This scattering resembles a plane-wave propagation, and the large roll-off is then naturally obtained.

As mentioned at the end of Sect. 5.4.2, ρ_{1r}^R can be controlled from Eqs. 5.86–5.88, with the help of the two configurations previously analyzed in Sects. 5.6.2 and 5.6.3. From Eq. 5.86 and assuming that $\rho_{1r}^R \to \infty$, the condition to achieve the desirably high roll-off is then given by

$$\sqrt{\left|\frac{\rho_{2r}^R}{R_{RU} + \rho_{2r}^R}\right|} \approx \left|\frac{E_A^{GO}(\rho_A = D_M/2)}{E_F(\theta_F = \theta_E)}\right| . \tag{5.103}$$

Since $D_M = 100\lambda$, $D_S = 15\lambda$, and estimating $\theta_2 \approx -74°$ from the last two geometries (the actual value for the final configuration is $\theta_2 = -73.9°$), Eqs. 5.87 and 5.88

give $R_{RU} \approx 44.21\lambda$ and $\rho_{2r}^{R} \approx 7.80\lambda$, respectively (their actual values are 44.23λ and 7.81λ, respectively). The feed electric field $E_F(\theta_F = \theta_E)$ is directly obtained from the RCF model of Eq. 4.59, where $h = 16$, $\theta_F = 35°$, and $r_F = R_{OR} = 13.08\lambda$ for the present case, yielding $|E_F(\theta_F = 35°)| = 3.14 \times 10^{-3}$ V/λ. Finally, the substitution of these values into Eq. 5.103 yields $|E_A^{GO}(\rho_A = 50\lambda)| \approx 1.22 \times 10^{-3}$ V/λ, the required condition to obtain a large value for ρ_{1r}^{R}. The actual value of ρ_{1r}^{R}, obtained after the accomplishment of the final configuration, is about 275λ.

The desired illumination taper at $\rho_A = 50\lambda$ is then determined from the above result and Eqs. 5.1 and 5.12, once $|E_o|$ is known ($|E_o|$ is the peak of the GO aperture electric-field amplitude, accordingly to Eqs. 5.1 and 5.12). This is accomplished by estimating $|E_o|$ as the average between the peak values obtained from the previous configurations of Sects.5.6.2 and 5.6.3, which are 9.69×10^{-3} V/λ and 4.98×10^{-3} V/λ, respectively. The estimated value of $|E_o|$ is then 7.34×10^{-3} V/λ (the analysis of the present configuration indicates that $|E_o| = 6.55 \times 10^{-3}$ V/λ). Since $|E_o| \approx 7.34 \times 10^{-3}$ V/λ and $|E_A^{GO}(\rho_A = 50\lambda)| \approx 1.22 \times 10^{-3}$ V/λ, then the desired illumination taper at $\rho_A = 50\lambda$ is about 15 dB. The derivative of the aperture illumination at this region will be determined later.

The main-reflector radiation towards the subreflector edge is controlled by specifying the blockage diameter D_B and the corresponding aperture illumination at $\rho_A = D_B/2$. However, no closed-form equations are available for this task. So, with $D_B = D_S = 15\lambda$, the aperture taper at $\rho_A = 7.5\lambda$ was arbitrarily set to 20 dB,

which yielded an antenna configuration that did not meet the required specifications. Afterwards, D_B was then arbitrarily increased to 20λ, which finally provided the desired pattern after some cut-and-try.

The derivatives of the aperture illumination at $\rho_A = 10\lambda$ and 50λ are established in order to control the sidelobe levels of the antenna radiation pattern. From Figs. 5.22a and 5.27a, it was observed that the GO aperture far-zone pattern obtained from Eq. 4.62 accurately predicts the sidelobe characteristics close to the main beam. So, with the aperture tapers at $\rho_A = 10\lambda$ and 50λ previously established as 20 dB and 15 dB, respectively (corresponding to $f_B = 0.1$ and $f_M = 0.1778$ in Eqs. 5.12–5.16), Eqs. 4.62, 5.1, 5.7, and 5.12–5.16 were numerically implemented to obtain the desired values of $f'_B = 0.03/\lambda$ and $f'_M = -0.041/\lambda$ for the aperture field derivatives at $\rho_A = 10\lambda$ and 50λ, respectively. The above parameters yield the GO aperture illumination previously depicted in Fig. 5.2a, with the corresponding far-zone radiation pattern shown in Fig. 5.2b, from where one observes that a large margin with respect to the envelope requirements is obtained.

However, it was established in Sect. 5.5 that the subreflector-edge diffraction affects the actual aperture illumination and, consequently, the sidelobe-envelope decay (and this effect should be included in the design process). From Eq. 5.91 it is observed that the subreflector-edge diffraction reduces by about 6 dB the aperture illumination expected from the GO at $\rho_A = 50\lambda$. This indicates that (with the help of the sidelobe-envelope expression given by Eq. 5.7) the edge diffraction

positively contributes to the faster decay of the sidelobe envelope. From Eq. 5.101, since $\rho_{1r}^{R} \to \infty$ and $R_{RU} \approx 44.21\lambda$, the edge-diffraction effect to the aperture field derivative at $\rho_A = 50\lambda$ is negligible.

The final shaped configuration is obtained from the formulation of Sect. 5.3 with the aperture distribution specified by Eqs. 5.1 and 5.12 and Fig. 5.2a, the feed illumination given by Eq. 4.59 (with $h = 16$), $D_M = 100\lambda$, $\theta_E = 35°$, and $D_B = 20\lambda$. The desired value of $D_S = 15\lambda$ is accomplished by setting $\ell_o = 58.85\lambda$ and $V_S = 7.82\lambda$ (starting from the geometry discussed in Sect. 5.6.3). The end result is depicted (in scale) in Fig. 5.29, with the main-reflector central region extrapolated using the approach of Sect. 5.6.3. The GO efficiency of this configuration is predicted to be $\eta = 82\%$.

The far-zone radiation patterns of the feed/subreflector combination are shown in Fig. 5.30. This figure demonstrates the accomplishment of a large roll-off for the pattern near the subreflector reflection region ($\theta = 106°$), where the gain is about -5 dBi. This large roll-off then reduces the losses and the sidelobe levels associated with the backward subreflector spillover. Furthermore, since the main-reflector edge is expected to provide an extra 6 dB taper to the subreflector radiation, the subreflector spillover is not a concern to the required envelope anymore. Also, from Figs. 5.20a, 5.25a, and 5.30a one observes that all three configurations have the subreflector scattering towards the feed radiating approximately the same levels

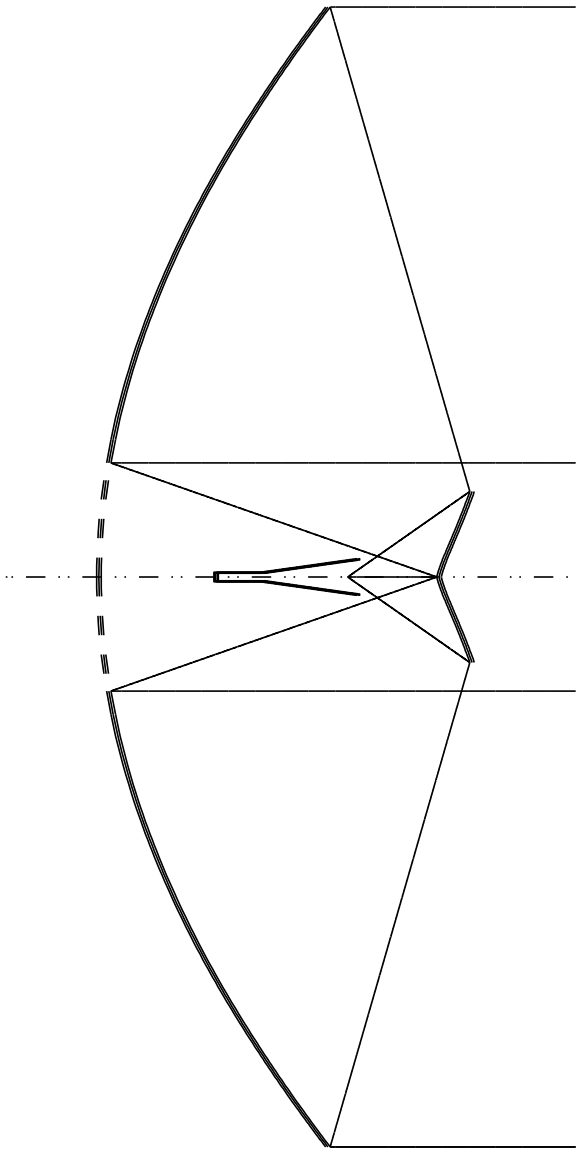

Figure 5.29: Final Shaped Configuration (SG I) with $D_M = 100\lambda$, $D_S = 15\lambda$, $D_B = 20\lambda$, $\ell_o = 58.85\lambda$, $\theta_E = 35°$, and $V_S = 7.82\lambda$.

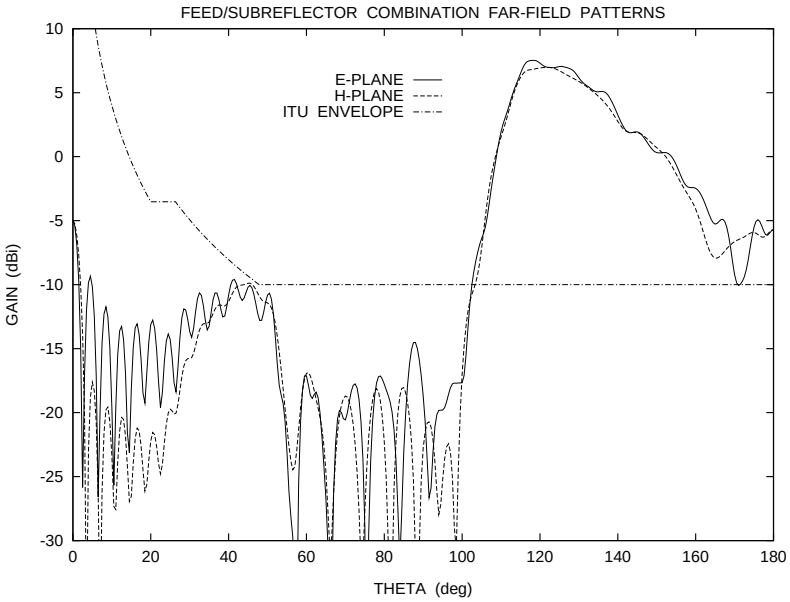

a) With the Horn Feed

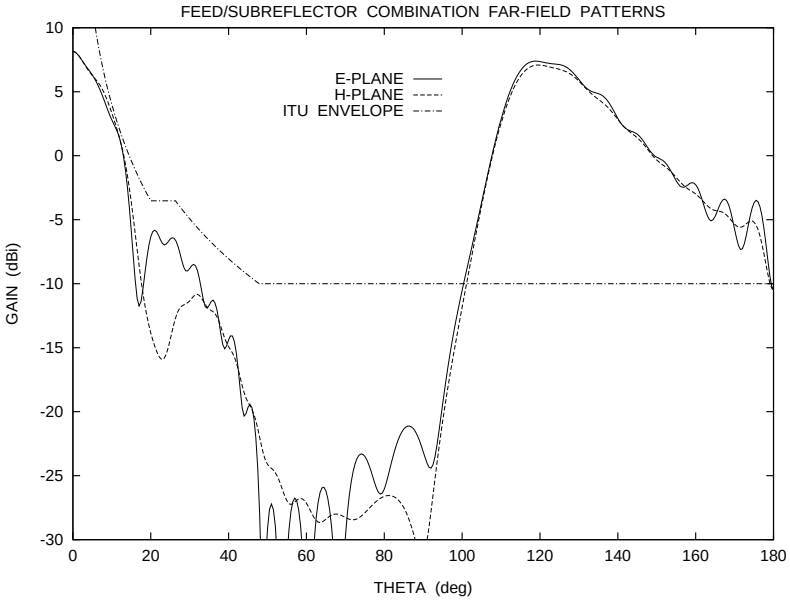

b) With the RCF Model

Figure 5.30: Far-Zone Patterns of the Final Shaped Feed/Subreflector Combination at the E- ($\phi = 0°$) and H- ($\phi = 90°$) Planes.

(around -16 dBi in the present case) over $60^\circ \leq \theta \leq 100^\circ$, indicating that this effect still does not produce high sidelobes.

The aperture electric field (analyzed as in Sects. 5.6.2 and 5.6.3) is illustrated in Fig. 5.31, where the results are normalized with respect to the peak of the GO aperture electric-field amplitude (6.55×10^{-3} V/λ). The GO aperture phase is equal to 54.3°, as $\ell_o = 58.85\lambda$ and $\Phi_G = 0$ (the aperture plane is still at $z = 0$). Again, the oscillatory behavior caused by the diffraction mechanisms is observed. Finally, Figs. 5.32 and 5.33 show the far-zone patterns of the complete antenna. From Fig. 5.32a the antenna gain is evaluated to be 49.00 dBi ($\eta = 80\%$), corresponding to an efficiency just 2% below the one obtained from the GO analysis (as the losses associated with the backward subreflector spillover have been tremendously reduced). It is also observed from this figure that the final configuration has a half-power beam width of about 0.3° and its first sidelobe and cross-polarization peaks are approximately 13 dB and 43 dB below the main-beam level, respectively. Finally, Figs. 5.32 and 5.33 show that the ITU requirements have been met over 90% of the radiation pattern.

The above design process of an axially-symmetric Cassegrain antenna illustrates the usefulness of the rigorous analysis toll provided by the EFIE/MoM technique (which was detailedly discussed in Chapters 2 and 3) and, specially, the closed-form design equations provided in Chapters 4 and 5.

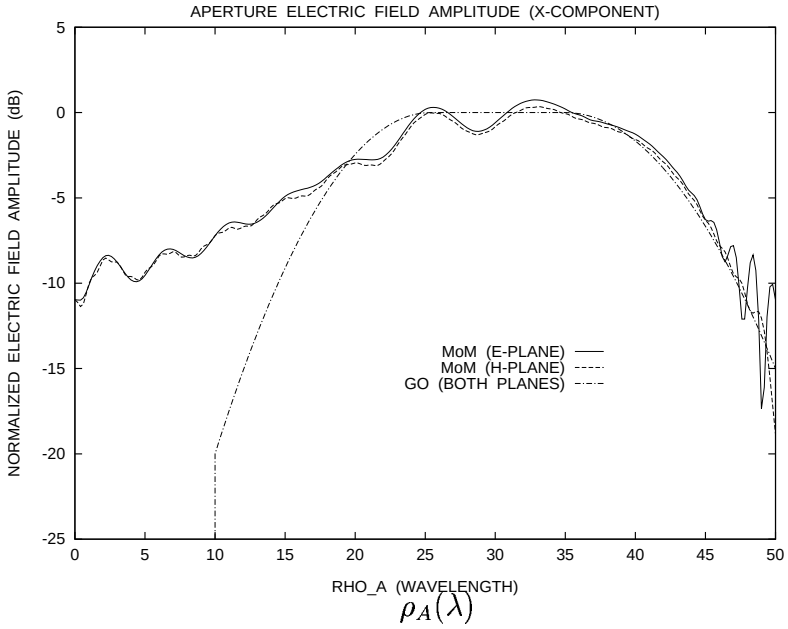

a) Aperture Electric Field Amplitude

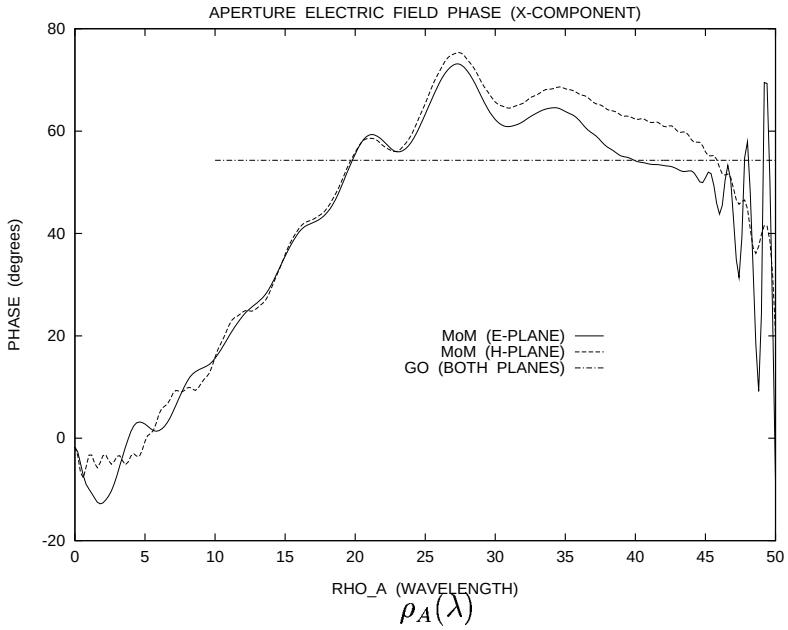

b) Aperture Electric Field Phase

Figure 5.31: Aperture Electric Field x-Component of the Final Shaped Geometry in the E- ($\phi = 0°$) and H- ($\phi = 90°$) Planes.

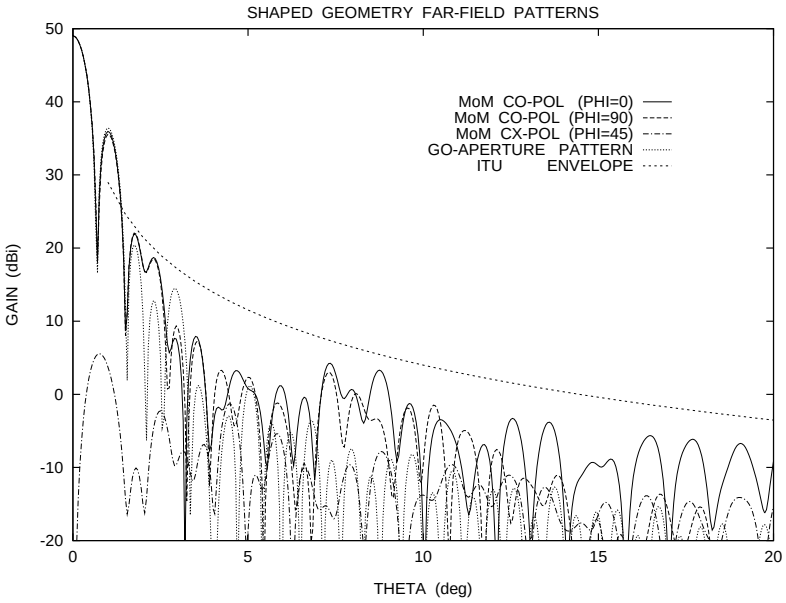

a) With the Horn Feed

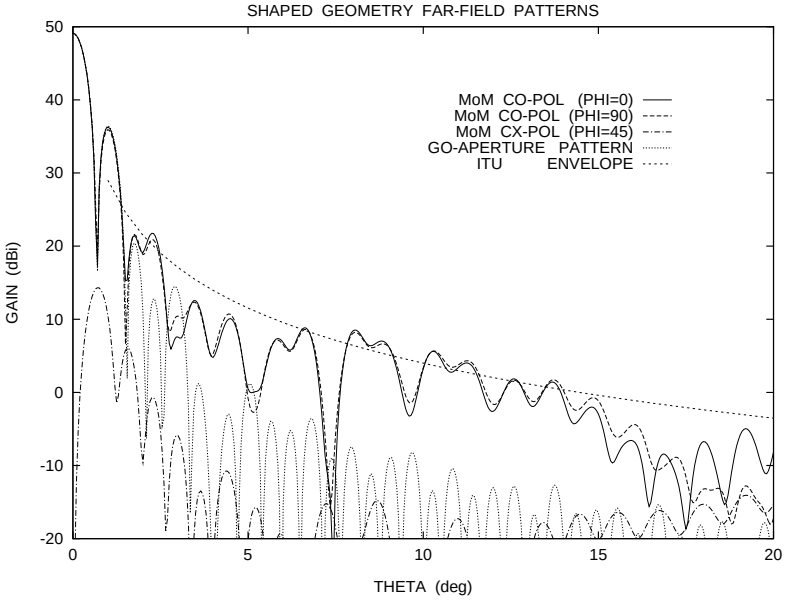

b) With the RCF Model

Figure 5.32: Far-Zone Patterns of the Final Shaped Geometry at $0° \leq \theta \leq 20°$.

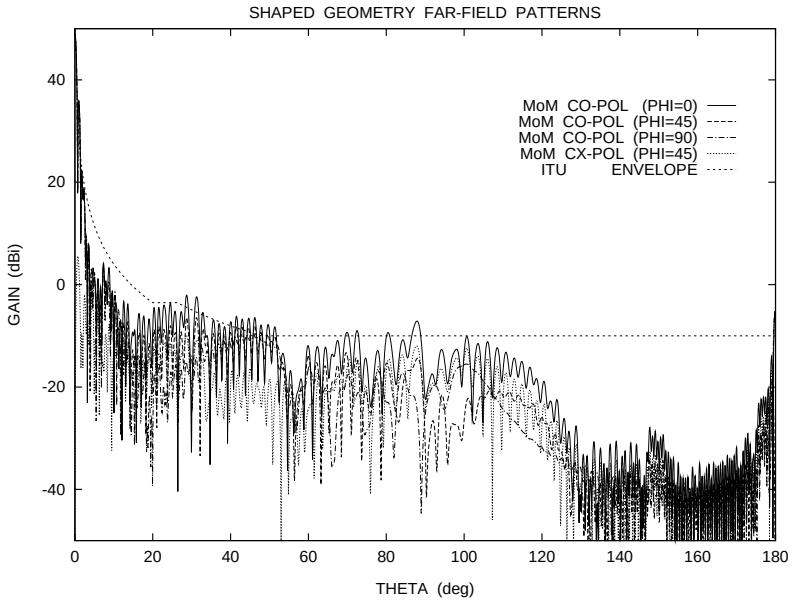

a) With the Horn Feed

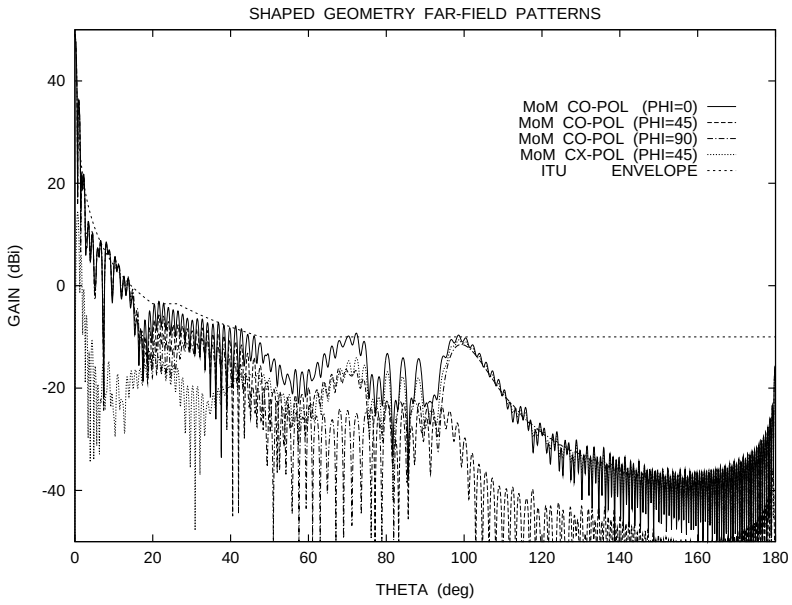

b) With the RCF Model

Figure 5.33: Far-Zone Patterns of the Final Shaped Geometry at $0° \leq \theta \leq 180°$.

Chapter 6
CONCLUSION

Axially-symmetric dual-reflector antennas offer high performance with relatively simple and cost-effective geometries. This fact makes then specially attractive for several applications (e.g., radio astronomy, satellite and mobile communications, radar, remote sensing, etc.). Traditionally these antennas have been designed using Geometrical Optics (GO), and further refined and analyzed using the Physical Optics (PO) and/or Geometrical Theory of Diffraction (GTD) techniques. Although excellent results are provided by both PO and GTD techniques in most cases (particularly for large-reflector configurations), they can not accurately model the mutual couplings among the several antenna components, specially the ones associated with the feed structure. These effects are known to reduce the overall antenna efficiency and increase the sidelobe levels of the radiation pattern. As current technology trends push for even higher communication-system efficiencies, more stringent requirements are constantly being imposed on the performance of reflector antennas. This creates the need for their rigorous modeling, to allow the designer less error margin. Fortunately, modern computational advances permit the entire analy-

sis of axially-symmetric dual-reflector configurations (including the feed structure) using integral-equation techniques, as discussed in this dissertation. These techniques can be used to predict the antenna electrical characteristics with extremely high accuracy, yielding an entirely computer-based design and, consequently, avoiding the costs and hassles associated with laboratory cut-and-try. This dissertation presented a detailed formulation for the rigorous analysis of axially-symmetric dual-reflector antennas based on the Electric Field Integral Equation (EFIE), which was numerically solved by the Method of Moments (MoM) technique. Also, useful guidelines and closed-form equations were derived for the design of these antennas.

Initially, the EFIE/MoM technique for perfectly conducting bodies of revolution (PEC BOR) was discussed in Chapter 2, enabling the analysis of axially-symmetric reflector antennas excited by a spherical-wave point source located at the symmetry axis. Afterwards, the formulation was enhanced in Chapter 3 in order to accommodate a circularly-symmetric feed structure into the reflector-antenna analysis. The feed excitation was provided by equivalent sources located inside the feed circular waveguide and specified to excite only the fundamental TE_{11} mode towards the boresight direction. Also, Impedance Boundary Conditions (IBC) were used to simulate corrugated horns and matched loads for the feed. Furthermore, complete expressions for the radiated near- and far-zone fields were derived. The formulation presented in Chapters 2 and 3 provides the necessary tools to rigorously evaluate the electrical characteristics of axially-symmetric reflector antennas (e.g., radiation

pattern, gain, return loss, etc.) with a single computer run. The application of IBC to characterize the horn corrugations proved to yield extremely accurate predictions of the feed radiation. However, the IBC must be judiciously applied to the precise determination of the feed return loss, as the corrugation simulation does not accurately model the mode conversion at the horn throat. In this case, the correct description of the actual corrugated geometry is highly recommended.

Nevertheless, the above mentioned analysis procedure has some drawbacks that should be further investigated in future studies. The present formulation only allows the analysis of mono-modal feed structures (in practical antenna applications, most of the feeds used fall into this category). A more efficient way to handle the feed analysis is accomplished by the scattering matrix technique [46], which requires a somewhat more involved implementation. Also, the combination of the Electric and Magnetic Field Integral Equations can be incorporated for the feed analysis, which can overcome the hassle associated with the dummy observation surfaces used to prevent the internal resonances (previously discussed in Chapter 3). Furthermore, the present EFIE/MoM formulation does not consider the presence of the supporting struts in the antenna analysis. Although previous works have dealt with this particular problem by approximating the struts as infinitely thin wires [17] or strips [33], the rigorous modeling of struts with arbitrarily shaped cross sections still remains undone. The present analysis technique can also be enhanced

to accommodate the possible presence of axially-symmetric dielectric bodies (e.g., radomes, dielectric cones, dielectric coatings, etc.) in the antenna system [59],[60].

The most commonly encountered axially-symmetric dual-reflector antennas are the classical Cassegrain and Gregorian, in which case part of the main-reflector energy is radiated towards the subreflector, causing efficiency loss and increase of the sidelobe levels. This problem may be reduced by either shaping the reflector surfaces or by using alternative classical configurations where (under a GO perspective) the main-reflector scattering towards the subreflector is minimized. Both possibilities were considered in this dissertation. The antenna design process started in Chapter 4 by presenting the only four possible classical axially-symmetric dual-reflector configurations that reduce the subreflector illumination by the main-reflector radiation while providing a uniform phase distribution for the aperture field. Applying GO principles, general closed-form design equations were derived, together with the associated aperture electric fields. The formulation enabled a parametric study of these configurations (yielding high-frequency upper bounds), and it was determined that efficiencies beyond 90% can be accomplished by some geometries. Although higher efficiencies are obtained with shaped geometries, the generalized classical configurations (and the corresponding closed-form equations) provide useful insights for the design process, besides being an excellent starting point for the shaping procedure.

The maximum possible (theoretical) efficiency is obtained with a uniform aperture field distribution, both in amplitude and phase. However, depending on the particular application and the associated requirements, the use of a uniform amplitude distribution may create intolerable sidelobe levels. The antenna must then be designed to satisfy the required sidelobe envelope while providing the highest possible antenna efficiency, and this topic was treated in Chapter 5. To this purpose, a convenient amplitude distribution for the aperture field was proposed, which is capable of controlling the sidelobe-envelope decay while yielding high efficiencies. To accomplish the proposed amplitude distribution together with a uniform-phase aperture illumination, an effective GO shaping scheme was presented.

Chapter 5 also investigated the impacts of the forward feed spillover and the backward subreflector spillover on the antenna pattern, using GTD asymptotic approximations. The study yield useful insights to define the minimum required feed illumination towards the subreflector edge in order to prevent the forward spillover from violating a particular sidelobe envelope. Also, closed-form expressions were obtained for the specification (before the reflector shaping) of the aperture illumination to accomplish a large roll-off for the subreflector radiation and, consequently, to reduce the backward spillover. Furthermore, the effects of the subreflector-edge diffraction on the aperture illumination were also discussed. However, as the tip diffraction is negligible when compared to the edge one [53], this dissertation did not consider the diffraction effects caused by the subreflector vertex, a topic left

for future works. Finally, as a case study, the complete formulation developed in this dissertation was employed in the design and analysis of a shaped axially-symmetric Cassegrain configuration with main- and subreflector diameters of 100 and 15 wavelengths, respectively. The design yield and antenna configuration with 80% radiation efficiency and satisfying the current ITU sidelobe-envelope requirements for earth-station antennas operating with geostationary satellites [41].

Bibliography

[1] H. Hertz, *Electric Waves*, Macmillan & Co., Ltd, London, 1893.

[2] W. A. Imbriale, "Evolution of the Large Deep Space Network Antennas," IEEE Antennas and Propagation Magazine, **33**, No. 6, pp. 7–19, December 1991.

[3] K. Fujimoto and J. R. James, editors, *Mobile Antenna Systems Handbook*, Artech House, Inc., Boston, 1994.

[4] P. J. B. Clarricoats and G. T. Poulton, "High-Efficiency Microwave Reflector Antennas—A Review," Proceedings of the IEEE, **65**, No. 10, pp. 1470–1504, October 1977.

[5] A. W. Rudge and N. A. Adatia, "Offset-Parabolic-Reflector Antennas: A Review," Proceedings of the IEEE, **66**, No. 12, pp. 1592–1618, December 1978.

[6] W. V. T. Rusch, "The Current State of the Reflector Antenna Art," IEEE Transactions on Antennas and Propagation, **AP-32**, No. 4, pp. 313–329, April 1984.

[7] W. V. T. Rusch, "The Current State of the Reflector Antenna Art—Entering the 1990's," Proceedings of the IEEE, **80**, No. 1, pp. 113–126, January 1992.

[8] W. V. T. Rusch and P. D. Potter, *Analysis of Reflector Antennas*, Academic Press, New York, 1970.

[9] R. G. Kouyoumjian and P. H. Pathak, "A Uniform Geometrical Theory of Diffraction for an Edge in a Perfectly Conducting Surface," Proceedings of the IEEE, **62**, No. 11, pp. 1448–1461, November 1974.

[10] R. F. Harrington, *Field Computation by Moment Methods*, IEEE Press, New York, 1993.

[11] R. Mittra, editor, *Computer Techniques for Electromagnetics*, Pergamon Press, Oxford, 1973, Chap. 4.

[12] J. J. H. Wang, *Generalized Moment Methods in Electromagnetics*, John Wiley & Sons, New York, 1991.

[13] S. M. Rao, D. R. Wilton, and A. W. Glisson, "Electromagnetic Scattering by Surfaces of Arbitrary Shape," IEEE Transactions on Antennas and Propagation, **AP-30**, No. 3, pp. 409–418, May 1982.

[14] Z. Altman, R. Mittra, O. Hashimoto, and E. Michielssen, "Efficient Representation of Induced Currents on Large Scatters Using the Generalized Pencil of Function Method," IEEE Transactions on Antennas and Propagation, **44**, No. 1, pp. 51–57, January 1996.

[15] J. R. Mautz and R. F. Harrington, "H-Field, E-Field, and Combined Field Solutions for Bodies of Revolution," Technical Report TR-77-2, Dept. Electrical and Computer Engineering, Syracuse University, 1977.

[16] J. R. Mautz and R. F. Harrington, "An Improved E-Field Solution for a Conducting Body of Revolution," Technical Report TR-80-1, Dept. Electrical and Computer Engineering, Syracuse University, 1980.

[17] D. C. Jenn, "Application of Integral Equation Theory to Reflector Antenna Analysis," Ph.D. dissertation, University of Southern California, December 1987.

[18] M. R. Barclay and W. V. T. Rusch, "Moment-Method Analysis of Large, Axially Symmetric Reflector Antennas Using Entire-Domain Functions," IEEE Transactions on Antennas and Propagation, **AP-39**, No. 4, pp. 491–496, April 1991.

[19] A. T.-S. Wang, "Transient Scattering from Bodies of Revolution with Applications in Short-Pulse Reflector Antennas," Ph.D. dissertation, University of Southern California, December 1994.

[20] F. L. Teixeira and J. R. Bergmann, "Spatial-Frequency Localized Representations for Integral Equation Reflector Analysis," Proceedings of the 1996 IEEE AP-S International Symposium, Baltimore, Maryland, pp. 890–893, July 1996.

[21] S. Silver, editor, *Microwave Antenna Theory and Design*, Peter Peregrinus, London, 1984.

[22] T. J. Kim and G. A. Thiele, "A Hybrid Diffraction Technique—General Theory and Applications," IEEE Transactions on Antennas and Propagation, **AP-30**, No. 5, pp. 888–897, September 1982.

[23] L. N. Medgyesi-Mitschang and D.-S. Wang, "Hybrid Solutions for Scattering from Perfectly Conducting Bodies of Revolution," IEEE Transactions on Antennas and Propagation, **AP-31**, No. 4, pp. 570–583, July 1983.

[24] U. Jakobus and F. M. Landstorfer, "Improved PO-MM Hybrid Formulation for Scattering from Three-Dimensional Perfectly Conducting Bodies of Arbitrary Shape," IEEE Transactions on Antennas and Propagation, **43**, No. 2, pp. 162–169, February 1995.

[25] P. W. Hannan, "Microwave Antennas Derived from the Cassegrain Telescope," IRE Transactions on Antennas and Propagation, **AP-9**, No. 2, pp. 140–153, March 1961.

[26] W. V. T. Rusch, "Scattering from a Hyperboloidal Reflector in a Cassegrainian Feed System," IEEE Transactions on Antennas and Propagation, **AP-11**, No. 4, pp. 414–421, July 1963.

[27] V. Galindo, "Design of Dual-Reflector Antennas with Arbitrary Phase and Amplitude Distributions," IEEE Transactions on Antennas and Propagation, **AP-12**, No. 4, pp. 403–408, July 1964.

[28] Yu. A. Yerukhimovich, "Analysis of Two-Mirror Antennas of a General Type," Telecommunications and Radio Engineering, Part 2, **27**, No. 11, pp. 97–103, 1972.

[29] Yu. A. Yerukhimovich and A. Ya. Miroshnichenko, "Development of Double-Reflector Antennas with a Displaced Focal Axis," Telecommunications and Radio Engineering, Part 2, **30**, No. 9, pp. 90–94, 1975.

[30] W. Rotman and J. C. Lee, "Compact Dual Frequency Reflector Antennas for EHF Mobile Satellite Communication Terminals," Proceedings of the 1984 IEEE AP-S International Symposium, Boston, Massachusetts, pp. 771-774, June 1984.

[31] F. J. S. Moreira and A. Prata, Jr., "Generalized Classical Axially-Symmetric Dual-Reflector Antennas," Proceedings of the 1997 IEEE AP-S International Symposium, Montreal, Canada, pp. 1402–1405, July 1997.

[32] A. C. Ludwig, "Low Sidelobe Aperture Distributions for Blocked and Unblocked Circular Apertures," IEEE Transactions on Antennas and Propagation, **AP-30**, No. 5, pp. 933–946, September 1982.

[33] T. E. Durham and C. G. Christodoulou, "A Method for Treating Junctions Between Bodies of Revolution and Arbitrary Surfaces," IEEE Transactions on Antennas and Propagation, **42**, No. 2, pp. 213–219, February 1994.

[34] R. F. Harrington, *Time-Harmonic Electromagnetic Fields*, McGraw-Hill, New York, 1961, Chap. 3.

[35] K. A. Iskander, L. Shafai, A. Frandsen, and J. E. Hansen, "Application of Impedance Boundary Conditions to Numerical Solution of Corrugated Circular Horns," IEEE Transactions on Antennas and Propagation, **AP-30**, No. 3, pp. 366–372, May 1982.

[36] J. Flodin, P.-S. Kildal, and A. Kishk, "Moment Method Design of a Large S/X Band Corrugated Horn," Proceedings of the 1996 IEEE AP-S International Symposium, Baltimore, Maryland, pp. 2030–2033, July 1996.

[37] C. Dragone, "Reflection, Transmission, and Mode Conversion in a Corrugated Feed," Bell System Technical Journal, **56**, No. 6, pp. 835–867, July–August 1977.

[38] C. Dragone, "Characteristics of a Broadband Microwave Feed: A Comparison Between Theory and Experiment," Bell System Technical Journal, **56**, No. 6, pp. 869–888, July–August 1977.

[39] P. J. B. Clarricoats and A. D. Olver, *Corrugated Horns for Microwave Antennas*, Peter Peregrinus, London, 1984.

[40] A. Prata, Jr., Lecture Notes of the Graduate Course EE578 - Reflector Antennas, Dept. of Electrical Engineering–Electrophysics, University of Southern California, Spring 1995.

[41] International Telecommunication Union—Radiocommunication (ITU-R), *S Series Recommendations - Fixed Satellite Service.*

[42] J. A. Stratton and L. J. Chu, "Diffraction Theory of Electromagnetic Waves," Physical Review, **56**, pp. 99–107, July 1, 1939.

[43] W. H. Press, S. A. Teukolsky, W. T. Vetterling, and B. P. Flannery, *Numerical Recipes in Fortran*, 2nd Edition, Cambridge University Press, Cambridge, 1992.

[44] I. S. Gradshteyn and I. M. Ryzhik, *Table of Integrals, Series, and Products*, Academic Press, New York, 1980.

[45] A. C. Ludwig, "The Definition of Cross Polarization," IEEE Transactions on Antennas and Propagation, **AP-21**, No. 1, pp. 116–119, January 1973.

[46] E. Kühn and V. Hombach, "Computer-Aided Analysis of Corrugated Horns with Axial or Ring-Loaded Radial Slots," Proceedings of the Third International Conference on Antennas and Propagation (ICAP 83), Norwich, UK, pp. 127–131, April 1983.

[47] R. E. Collin, *Field Theory of Guided Waves*, 2nd Ed., IEEE Press, New York, 1991.

[48] W. V. T. Rusch, J. Appel-Hansen, C. A. Klein, and R. Mittra, "Forward Scattering from Square Cylinders in the Resonance Region with Application to Aperture Blockage," IEEE Transactions on Antennas and Propagation, **AP-24**, No. 2, pp. 182–189, March 1976.

[49] M. Born and E. Wolf, *Principles of Optics*, MacMillan, New York, 1959, Sect. 8.8.4.

[50] C. A. Balanis, *Antenna Theory Analysis and Design*, 2nd Edition, John Wiley & Sons, New York, 1997.

[51] M. Abramowitz and I. A. Stegun, editors, *Handbook of Mathematical Functions*, Dover Publications, Inc., New York.

[52] G. L. James, "An Approximation to the Fresnel Integral," Proceedings of the IEEE, **67**, No. 4, pp. 677–678, April 1979.

[53] K. D. Trott, P. H. Pathak, and F. A. Molinet, "A UTD Type Analysis of the Plane Wave Scattering by a Fully Illuminated Perfectly Conducting Cone," IEEE Transactions on Antennas and Propagation, **38**, No. 8, pp. 1150–1160, August 1990.

[54] P.-S. Kildal, "The Effects of Subreflector Diffraction on the Aperture Efficiency of a Conventional Cassegrain Antenna—An Analytical Approach," IEEE Transactions on Antennas and Propagation, **AP-31**, No. 6, pp. 903–909, November 1983.

[55] P.-S. Kildal and J. J. Stamnes, "Asymptotic Transition Region Theory for Edge Diffraction, Part I: Tracing Transition Regions Via Reflectors," IEEE Transactions on Antennas and Propagation, **38**, No. 9, pp. 1350–1358, September 1990.

[56] P.-S. Kildal, "Asymptotic Transition Region Theory for Edge Diffraction, Part II: Calculation of Diffraction Losses in Multireflector Antennas," IEEE Transactions on Antennas and Propagation, **38**, No. 9, pp. 1359–1365, September 1990.

[57] D. J. Struik, *Lectures on Classical Differential Geometry*, 2nd Ed., Addison-Wesley Pub., Co., Cambridge, 1961.

[58] S. L. Johns and A. Prata, Jr., "An Improved Raised-Cosine Feed Model for Reflector Antenna Applications," Proceedings of the 1994 IEEE AP-S International Symposium, Seattle, Washington, pp. 970–973, June 1994.

[59] J. R. Mautz and R. F. Harrington, "Electromagnetic Scattering from a Homogeneous Body of Revolution," Technical Report TR-77-10, Dept. Electrical and Computer Engineering, Syracuse University, November 1977.

[60] A. A. Kishk and L. Shafai, "Different Formulations for Numerical Solution of Single or Multibodies of Revolution with Mixed Boundary Conditions," IEEE Transactions on Antennas and Propagation, **AP-34**, No. 5, pp. 666–673, May 1986.